RADIATION RESPONSE OF NANOSTRUCTURED CU

by

Cuncai Fan

A Dissertation

Submitted to the Faculty of Purdue University

In Partial Fulfillment of the Requirements for the degree of

Doctor of Philosophy

School of Materials Engineering

West Lafayette, Indiana

August 2019

THE PURDUE UNIVERSITY GRADUATE SCHOOL
STATEMENT OF COMMITTEE APPROVAL

Dr. Xinghang Zhang, Chair
School of Materials Engineering

Dr. Haiyan Wang
School of Materials Engineering/Electrical and Computer Engineering

Dr. Anter El-Azab
School of Materials Engineering/Nuclear Engineering

Dr. David Johnson
School of Materials Engineering

Approved by:

Dr. David Bahr
Head of the Graduate Program

To my parents and little brother

ACKNOWLEDGMENTS

First, I would like to thank my advisor, Dr. Xinghang Zhang for his great patience, kindly encouragement, and instructive guidance. Without him, I cannot complete my Ph.D. studies. I also thank my committee members, Dr. Haiyan Wang, Dr. Anter El-Azab, and Dr. David Johnson for providing me with helpful suggestions. Additional thanks are given to Dr. Wang for the use of her laboratory facilities, and Dr. Anter El-Azab and his student Rayaprolu Goutham Sreekar Annadanam for their regular meeting discussions on my research project.

I thank my collaborators from Argonne National Laboratory and Los Alamos National Laboratory, Dr. Meimei Li, Dr. Mark Kirk, Pete Baldo, Ed Ryan, Dr. Jing Hu, Dr. Wei-Ying Chen, Dr. Yongqiang Wang, and Dr. Di Chen, for their great help in the radiation experiments. I also thank the collaborators from University of Nebraska-Lincoln, Dr. Jian Wang and his students Dongyue Xie, Yanxiang Liang, for their great help in computer simulations.

I really appreciate my friends and coworkers at Purdue University, Zhongxia Shang, Dr. Jin Li, Ruizhe Su, Jie Ding, Qiang Li, Yifan Zhang, Jaehun Cho, Dr. Sichuang Xue, Tongjun Niu, Tianyi Sun, Nicholas Richter, Bo Yang, Han Wang, Dr. Jie Jian, Dr. Jijie Huang, Xing Sun, Zhimin Qi, Bruce Zhang, Xuejing Wang, Di Zhang. I also want to thank our previous group members, Dr. Zhe Fan and Dr. Youxing Chen. Many thanks for their companionship through the pursuit of my doctoral degree. I also appreciate the great help from the staff of School of Materials Engineering (Purdue University), Vicki Cline, Rosemary Son, and Stacey Coar.

I acknowledge the Life Science Microscopy Facility at Purdue University. I also acknowledge the financial support from National Science Foundation's Division of Materials Research (NSF-DMR), and the support from the Bilsland Dissertation Fellowship, granted by the Dean of the Graduate School, Purdue University, in my final academic year (2018-2019) of doctoral degree completion.

Finally, I want to thank my parents, my little brother, and my grandparents for their constant support and understanding.

TABLE OF CONTENTS

LIST OF TABLES

LIST OF FIGURES

ABSTRACT

Author: Fan, Cuncai. PhD
Institution: Purdue University
Degree Received: August 2019
Title: Radiation Response of Nanostructured Cu
Committee Chair: Xinghang Zhang

Irradiation of metals with energetic particles causes heavy damage effects in microstructure and mechanical properties, which is closely associated with irradiation conditions, presence of impurities, and microstructural features. It has been proposed that the radiation tolerance of a certain material can be enhanced by introducing a high density of interfaces, acting as 'sinks' that can frequently involve in attracting, absorbing and annihilating defects. Nanostructured materials with large volume fraction of interfaces, therefore, are assumed to be more radiation tolerant than conventional materials. This thesis focuses on the radiation damage effects in nanostructured Cu via the methods of *in-situ* TEM (transmission electron microscope) radiation experiments, post-irradiation TEM analyses, small-mechanical tests (nanoindentation and micro-pillar compression), and computer simulations (molecular dynamics and phase-field modeling).

We design and fabricate nanostructured Cu using direct current (DC) magnetron sputtering deposition technique, a typica physical vapor deposition (PVD) method and a bottom-up way to construct various nanostructured metals. High-density twin boundaries (TBs) and nanovoids (NVs) are introduced into two distinct nanostructured Cu films, including nanovoid-nanotwinned (NV-NT) Cu (111) and nanovoid (NV) Cu (110). The *in-situ* high-energy Kr^{++} (1 MeV) and *ex-situ* low energy He^{+} (< 200 keV) irradiations are subsequently preformed on the as-deposited Cu samples. On the one hand, the *in-situ* TEM observations suggest that TBs and NVs can influence the formation, distribution and stability of radiation-induced defects. Meanwhile, the preexisting microstructures also undergo structural change through void shrinkage and twin boundary migration. On the other hand, the *ex-situ* micro-pillar compression tests reveal that the He-irradiated NV-NT Cu contains less defect clusters but experiences more radiation-induced hardening. The underlying mechanisms of void shrinkage, twin boundary migration, and radiation-induced hardening are fully discussed based on post-irradiation analyses and computer simulations.

CHAPTER 1. INTRODUCTION

There are grand challenges for developing and advancing nuclear technology in many peaceful applications, such as electricity, industry, medicine, space missions, and so on [1]. This thesis concerns the materials challenges in nuclear energy. A review in this chapter provides the background on fundamentals of ion-solid interactions, radiation damage effects, and recent radiation studies in nanostructured metals.

1.1 Materials Challenges in Nuclear Energy

Nuclear power energy provides about 15 % of electrical power worldwide, and it holds promise as one of the next-generation sustainable energy source [2]. Many of the currently used fission nuclear reactors (Generation II), built in the 1970s and 1980s, are approaching their originally designed lifetime (~ 40 years) [3]. Therefore, it is of great significance to develop new concepts of advanced fusion and fission nuclear energy systems that are expected to be safer, more economic, and more efficient [4]. However, there are a couple of technological challenges in bridging the gap from concept to reality, such as how to design and manufacture structural materials used for building and operating these nuclear reactors [5].

In a nuclear energy system, the structural materials face the most intense radiation environments, especially in the core of a nuclear power reactor where energetic neutrons are continuously created by nuclear reactions [6]. Figure 1.1 shows the temperature and dose requirements for in-core structural materials of the next-generation nuclear power systems [7]. Note that the X-axis in Figure 1.1 refers to the displacement per atom (dpa), a standardized parameter defined to quantify the amount of radiation damage produced in materials. In addition to the high doses and temperatures, in-core structural materials also suffer from high stresses and chemically aggressive coolants [8-10].

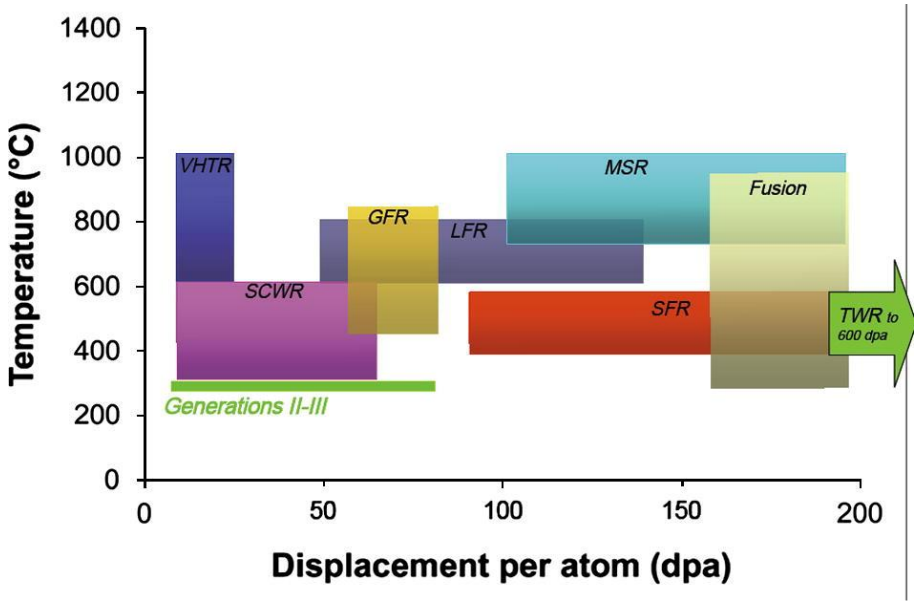

Figure 1.1. Working conditions required for the in-core structural components of the next-generation nuclear power systems. [5].

1.2 Fundamentals of Ion-solid Interactions

To understand the radiation damage effects in materials, it is necessary to investigate the detailed interactions between energetic incident particles (ion or neutron) and target atoms. In this section, general features and fundamental concepts regarding atomic displacements are first introduced, followed by a quantitative description of such damage displacements.

1.2.1 Radiation Damage and Cascade

The radiation damage is initially triggered by incident projectiles into the target atoms, and it concludes in the resulting spatial rearrangement of target atoms [11]. The atomic displacement will occur when the transferred energy exceeds a threshold that is usually called the displacement energy (E_d), approximately 25 - 90 eV for most metals [12]. It is assumed that the displacement damage is confined in a small region. Brinkman [13] first pictured the structure of the region as a displacement cascade (or thermal spike) that is briefly described by a vacancy core and its interstitial shell, as schematically illustrated in Figure 1.2 [14].

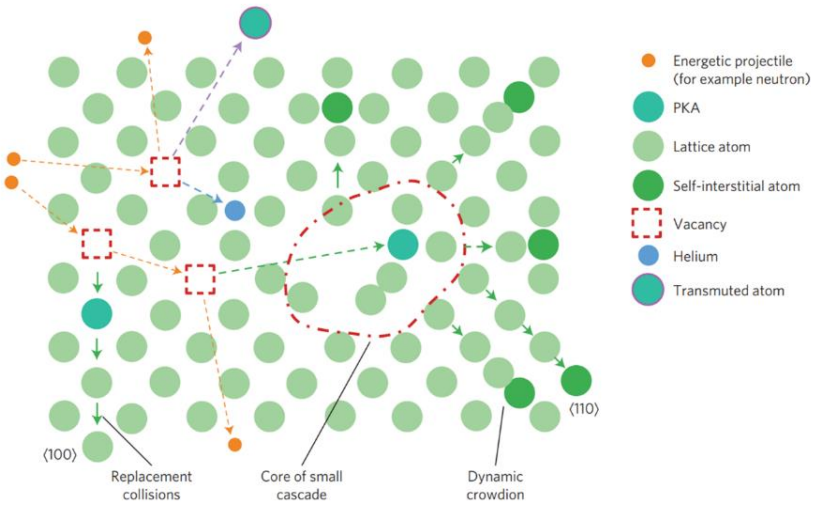

Figure 1.2. Schematic illustration of radiation-induced atomic displacements [15].

The damage cascade creates substantial "Frenkel pairs", the equal numbers of vacancies and self-atom interstitials (SAIs), and it develops rapidly at picosecond scale [15]. In its final stage, the cascade energy drops, and annealing process initiates through the recombination between SAIs and vacancies. Eventually, only part of the displaced atoms can survive the cascade and form individual point defects or defect clusters. The routine way currently used for studying the radiation damage cascades is through the molecular-dynamics (MD) simulations [16], and a typical MD simulation from a 20 keV cascade in iron at 100K is shown in Figure 1.3 [18].

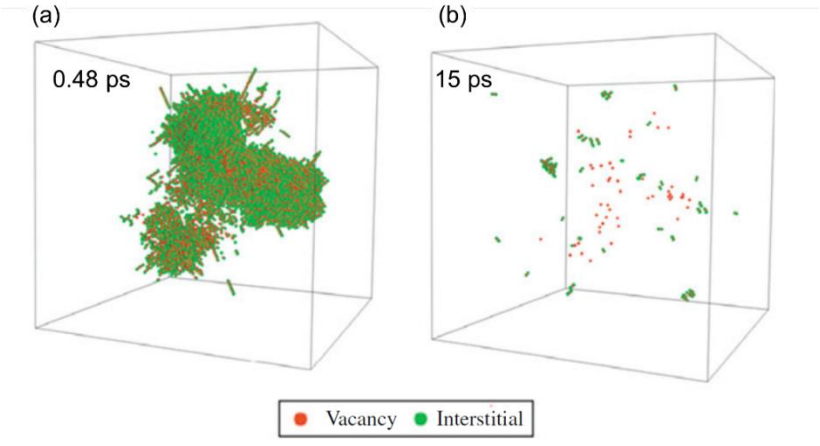

Figure 1.3. A typical MD simulation on 20 keV cascade in iron at 100K [17]. (a) Peak damage state. (b) Residual defect configuration.

1.2.2 Radiation Damage Calculation

The magnitude of radiation damage is indicated by displaced atoms resulting from incident particles (neutrons or ions), in the unit of 'dpa' that is the displacements per atom in the solid. The radiation dpa dose is determined by two key parameters: the fluence (the integration of the flux in a certain period) and the absorbed dose. Therefore, the number of displacements per unit volume per unit time, R, can be described by [11]:

$$R = N\int_{\check{E}}^{\hat{E}}\int_{\check{T}}^{\hat{T}}\phi(E_i)\sigma(E_i,T)\nu(T)dTdE_i \qquad \text{Equation 1.1}$$

where N is the atom number density; E_i is the initial energy of the incident particle, $\check{E}$ and $\hat{E}$ are the minimum and maximum initial energies; T is the transferred energy to the struck atom, $\check{T}$ and $\hat{T}$ are the minimum and the maximum transferred energies; ϕ is the energy-dependent particle flux; σ is the cross section for the collision of a particle of energy that results in a transfer energy to the struck atom; ν is the number of displacements per PKA.

The term $\sigma(E_i,T)$ in Equation 1.1 describes the scattering probability for the incident particle of energy E_i. If a neutron passes through a solid, its collision with nuclei can be presented as colliding hard spheres by virtue of its electrical neutrality. The method in dealing with neutron scattering probability is therefore straightforward. However, if the incident particle is charged, the scattering probability cannot not be certainly determined unless the interatomic potentials are specified. Unfortunately, there is no single potential function that is universal for describing all particle interactions. Appropriate potential functions must be cautiously chosen according to the incident particle energies [18]. Three frequently used potential functions include Born-Mayer potential (for low-energy ions and near head-on elastic collisions) [19], Coulomb scattering potential (for heavy energetic ions) [20], and inverse square potential (for heavy slow ions) [21].

Another term $\nu(T)$ in Equation 1.1 refers to the total number of displacements that the PKA travels through the lattice. Based on hard-sphere assumptions, Kinchin and Pease developed a simple model (often termed as K-P model) to estimate the average number of displaced atoms [22]. According to this model, the displacement is certain to occur when $T \geq E_d$, and then $\nu(T)$ increases linearly with increasing T until it reaches a plateau, as illustrated in Figure 1.4. The term

E_c in Figure 1.4 is the cut off caused by electron stopping beyond which no additional displacements can occur until electron energy losses reduce the PKA energy to E_c. It is worth noting that K-P displacement model is oversimplified without considering the E_d in the energy balance [23], the realistic energy transfer cross sections [24], the energy loss by electronic excitation [25], and the effects of crystallinity [18]. For more accurate calculations, further modifications on the K-P model are necessary.

The analytical solutions for Equation 1.1 would be complex for practical problems, and more reliable solutions are hence expected to be based on computer simulations. Currently, the most widely adopted method for calculating radiation damage of ions is through the Stopping and Range of Ions in Matter (SRIM), a computer program developed by Ziegler based on the Monte Carlo [26].

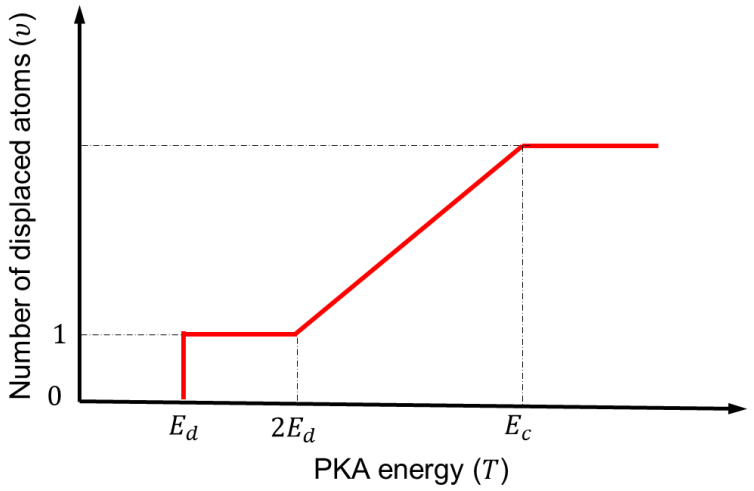

Figure 1.4. The K-P model used for determining the number of displacement atoms in the cascade [22].

1.3 Radiation Damage Effects

A cascade of atomic collisions ends with large numbers of individual vacancies and SAIs that subsequently diffuse and agglomerate into defect clusters. The motion and interaction of these defects in solids lead to significant microstructural alteration, which typically causes degradation in physical and mechanical properties [27-32].

1.3.1 Defect Reaction Rate Theory

The diffusion of point defects is the foundation for understanding the radiation damage effects in materials. According to classical diffusion theory, the flux of atoms through materials is determined by the diffusion coefficient and concentration gradient [33]. For the point defects in crystalline lattice, they can diffuse through several mechanisms [34], including exchange and ring mechanisms, vacancy mechanism, interstitial mechanism, interstitialcy mechanism, dumbbell interstitial mechanism, and crowding mechanism. Therefore, the total and effective diffusion coefficient (D_{rad}) under radiation is the sum of all the operative mechanisms of diffusion, simply written as:

$$D_{rad} = \sum_t f_t D_t C_t \qquad \text{Equation 1.2}$$

where f_t is the correlation coefficient, D_t is the diffusion coefficient of a certain diffusion mechanism, and C_t is the corresponding point defect concentration.

Equation 1.2 indicates that the diffusion process under irradiation is substantially accelerated due to the supersaturated point defects resulting from damage cascade. In irradiated materials, the point concentration at a given time can be determined by the point defect balance equations as follows [35]:

$$\frac{\partial C_v}{\partial t} = K_0 - K_{iv} C_i C_v - K_{vs} C_v C_s + \nabla \bullet D_v \nabla C_v$$
$$\frac{\partial C_i}{\partial t} = K_0 - K_{iv} C_i C_v - K_{is} C_i C_s + \nabla \bullet D_i \nabla C_i \qquad \text{Equation 1.3}$$

where C_v (C_i) is vacancy (interstitial) concentration, K_0 is the defect production rate, K_{iv} is the vacancy-interstitial recombination rate, K_{vs} (K_{is}) is the vacancy-sink (interstitial-sink) reaction rate coefficient, C_s is the defect sink concentration, D_v (D_i) is the vacancy (interstitial) diffusion coefficient. For a given system under irradiation, the concentration of point defects initially builds up rapidly, and then it starts to level off when the system reaches a "quasi-steady-state" with the defect production rate compensated by the recombination rate. On this occasion, the Equation 1.3 can be simplified by setting the left two terms as zero. However, in most cases the equations are stiff, so they can only be properly solved via numerical methods.

The terms of $K_{vs} C_v C_s$ and $K_{is} C_i C_s$ in Equation 1.3 describe the loss of point defects (vacancy or interstitial) to various pre-existing microstructures, namely defect sinks that can be simply divided

into three categories: (1) neutral (unbiased) sinks, (2) biased sinks, and (3) variable sinks [11]. The neutral sinks show no preference for capturing vacancies or interstitials, while the biased sinks could exhibit preferential attraction for one type over the other. Grain boundaries, voids, and incoherent precipitates are classified as neural sinks; dislocations, by contrast, are regarded as biased sinks with a stronger preferential attraction for interstitials. Especially, the coherent precipitates can initially capture a certain type of defect until it is annihilated by the opposite type, so they are regarded as variable biased sinks. The tendency of the loss of defects to sinks is quantified by sink strength, denoted by k_{sv}^2 (or k_{si}^2) and defined as:

$$k_{sv}^2 = \frac{K_{sv}C_v}{D_v} \text{ (or } k_{si}^2 = \frac{K_{si}C_i}{D_i}\text{)} \qquad \text{Equation 1.4}$$

Note that the sink strength has a unit of [cm^{-2}], and k_{sv}^{-1} (or k_{si}^{-1}) has the physical meaning of the mean distance a free vacancy (or interstitial) travels in the solid before it is trapped by a defect sink.

1.3.2 Radiation-induced Defect Clusters

The most profound radiation damage effect on microstructure is the creation of various types of defects, including equal numbers of individual vacancies and interstitials, as well as their clusters, such as loops, voids, bubbles, and stacking-fault tetrahedra (SFT) [36].

1.3.2.1 Characterization of Defect Clusters by TEM

Radiation-induced defect clusters present complicated geometric configurations and range from atomic scale to tens of micrometer in dimensions. Some of them can be clearly identified using appropriate Transmission Electron Microscope (TEM) techniques under certain imaging conditions [37], such as rel-rod imaging condition for characterizing the disc shape (edge-on direction) of Frank loops [38], weak-beam dark filed (WBDF) imaging condition for characterizing triangular shape of SFTs [39], and ‘out-of-focus’ imaging condition for characterizing spherical or faceted cavities (bubbles or voids) [40]. Figure 1.5 compiles the representative TEM micrographs of various defect clusters encountered in some irradiated materials [8].

1.3.2.2 Stability and Mobility of Defect Clusters

The radiation-induced defects present complexed configurations and vary from material to material, depending on radiation conditions and the presence of impurities, like the transmutant elements of Hydrogen or Helium [36]. As shown in Figure 1.5, for instance, the radiation-induced defects show a strong dependence on irradiation temperature [8].

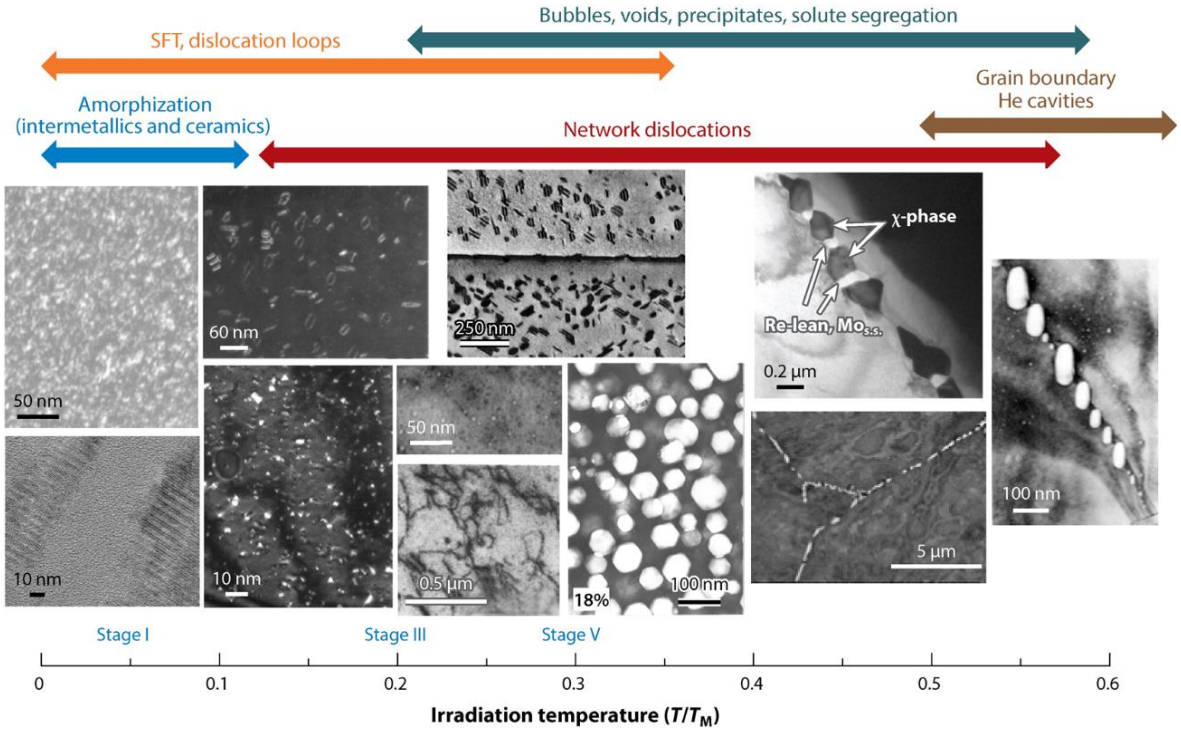

Figure 1.5. TEM micrographs of radiation-induced defect clusters, ordered as a function of homologous irradiation temperature (T / T_M, where T_M is the melting temperature) [8].

For a given material under certain conditions, the configuration stability of defect clusters is related with host material and defect size [36]. From the viewpoint of thermodynamics, defect clusters tend to take up the minimum energy configuration. Therefore, it is reliable to predict their stability by comparing their energy states [41]. For instance, in irradiated face-centered-cubic (FCC) metals a vacancy cluster could exist in the form of a void, SFT, perfect loop, or faulted loop. The energy of a spherical void, E_V, with the radius r_V is given by:

$$E_V = 4\pi r_V^2 \gamma \qquad \text{Equation 1.5}$$

where γ is the surface energy. The energy of an SFT, E_{SFT}, with the edge length L_{SFT} is given by [42, 43]:

$$E_{SFT} = \frac{\mu L_{SFT} b_s^2}{6\pi(1-\nu)}\left[\ln\left(\frac{4L_{SFT}}{a}\right)+1.017+0.97\nu\right]+\sqrt{3}L^2\gamma_{SFE} \qquad \text{Equation 1.6}$$

where μ is the shear modulus, b_s is the Burger's vector of the stair rod dislocation (SFT edge dislocation), ν is the Poisson's ratio, a is the lattice parameter, and γ_{SFE} is the stacking fault energy. The energy of a perfect loop, E_p, with the loop radius r_L is given by [44]:

$$E_p = \frac{2}{3(1-\nu)}+\frac{2-\nu}{6(2-\nu)}\mu b_p^2 r_L \ln\left[\frac{4r_L}{r_c}-2\right] \qquad \text{Equation 1.7}$$

where r_c is the dislocation core radius, and b_p is the Burger's vector of the perfect loop. The energy of a Frank loop, E_F, with the loop radius r_L is given by [45]:

$$E_F = \frac{2}{3(1-\nu)}\mu b_F^2 r_L \ln\left[\frac{4r_L}{r_c}-2\right]+\pi r_L^2\gamma_{SFE} \qquad \text{Equation 1.8}$$

where b_F is the Burger's vector of the Frank loop.

Using Equation 1.5-1.8, the formation energy for various vacancy clusters in Cu is plotted in Figure 1.6 [41]. The calculations suggest that SFT is the most table configuration over the other smaller vacancy clusters (< 1000 vacancies), which is good agreement with post-radiation analyses [46].

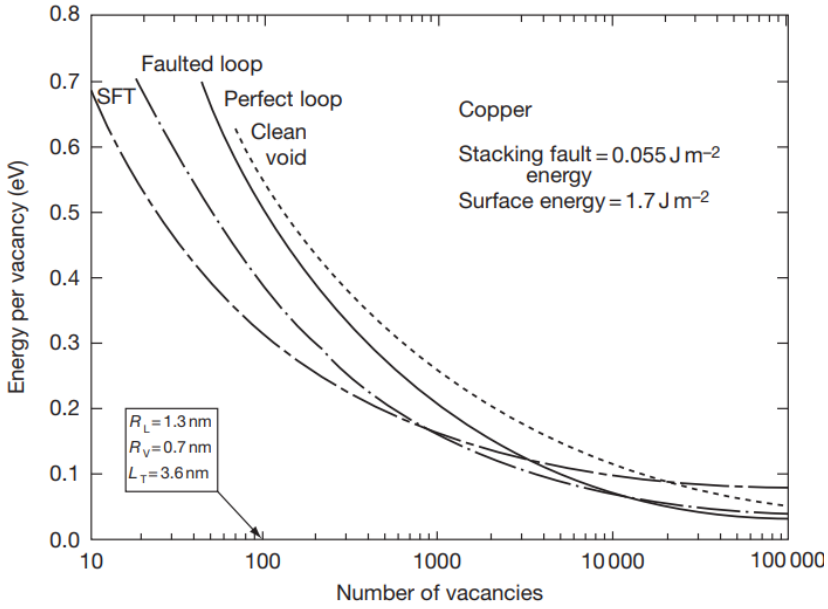

Figure 1.6. Formation energy for various vacancy clusters in copper [41]

In addition, *in-situ* TEM observations show that nanometer-size defect clusters could be highly mobile and migrate frequently in irradiated materials [47, 48]. Figure 1.7(a) shows an interstitial dislocation loop 1/2<111> in Fe that performs one-dimensional migration along its Burger's vector upon heating even in the absence of external and internal stresses [49]. The proposed mechanism for such migration is based on thermally activated dense fluctuation of "crowdions", in the dense packed atomic direction, as schematically shown in Figure 1.7(b) [50]. It is assumed that the defect mobility plays an important role in the microstructure evolution of materials [49, 50]. For instance, the migration of nanovoids (NVs) driven by thermal gradient could account for the formation of central holes and intragranular bubbles in nuclear fuels [51-53].

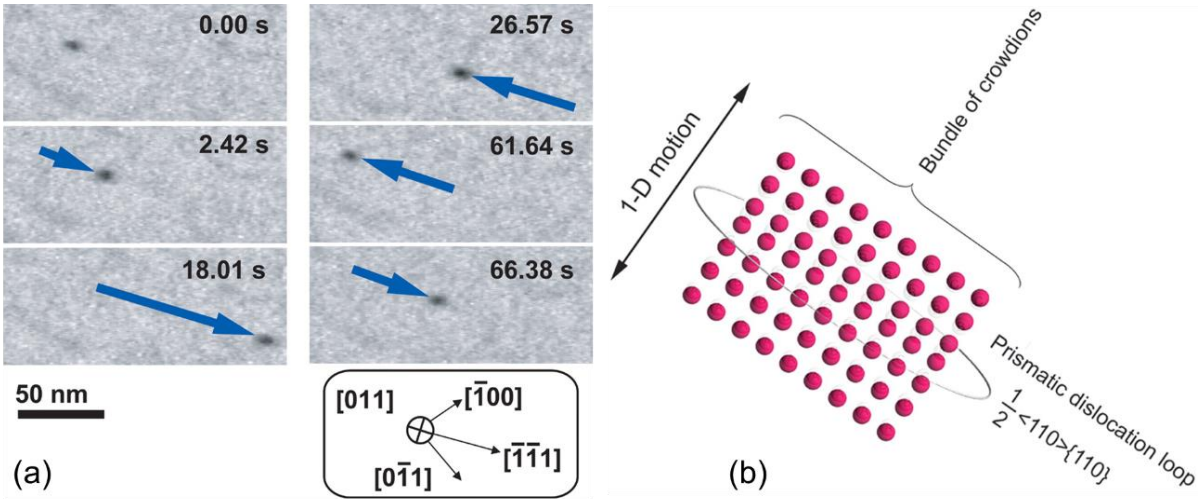

Figure 1.7. (a) One-dimensional migration of an interstitial loops 1/2<111> in Fe at 575 K [49]. (b) Schematic sketch of the migration mechanism for an interstitial loop [50].

1.3.3 Radiation-induced Swelling

Radiation-induced volumetric swelling, caused by voids and bubbles at elevated temperature, is of great interest for the nuclear material community since the first observation of radiation-induced voids in stainless steel in 1967 [54]. Figure 1.8(a) shows one typical example of radiation-induced voids in an 316 stainless steel (SS) bolt from a pressurized water reactor [11]. In this case, the voids are influenced by radiation dose and temperature at different locations, so they vary in size and density along the bolt length. The formation of high-density voids in irradiated components can cause significant dimension changes up to tens of percent in volume [11]. For instance, Figure 1.8(b) compares the intensive volume change of 316 SS rods before and after irradiation at 533 ^{o}C to a fluence of 1.5×10^{23} neutrons/m^2 in a faster reactor [55].

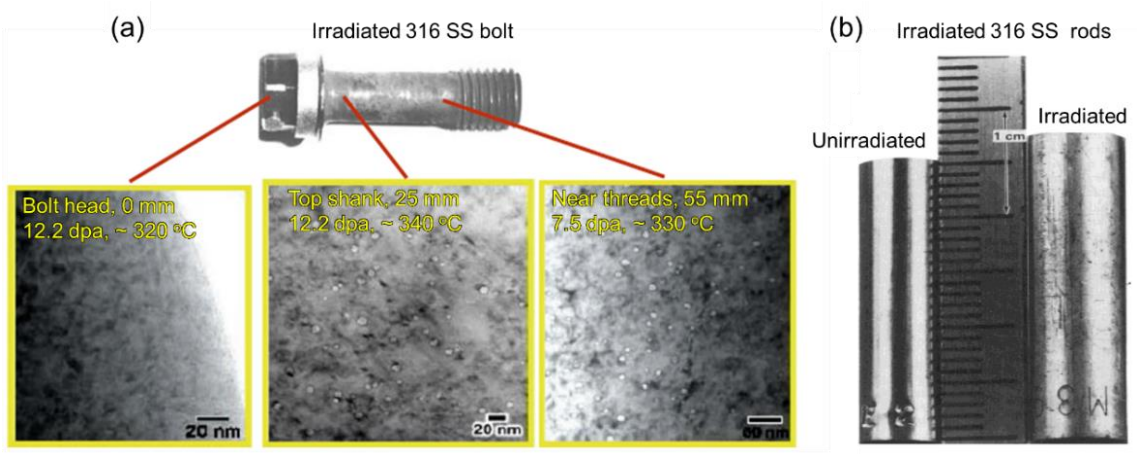

Figure 1.8. Irradiation-induced void swelling. (a) Void distribution along the bolt length in an irradiated cold-worked 316 SS baffle bot [11]. (b) 316 SS steel rods before and after irradiation in a fast reactor [55].

The driving force for the void nucleation in metals is the vacancy supersaturation, given by:

$$S_v = \frac{C_v}{C_v^0} \qquad \text{Equation 1.9}$$

where C_v^0 is the thermal equilibrium concentration of vacancies, and C_v is the vacancy concentration in matrix. The growth (or shrinkage) of voids is determined by absorption or emission of point defects (interstitials or vacancies), and the void growth (or shrinkage) equation in a common form is given as:

$$\frac{dR}{dt} = \dot{R} = \frac{\Omega}{R}[D_v(C_v - C_v^V) - D_i C_i] \qquad \text{Equation 1.10}$$

where R is the void radius, Ω is the atomic volume, D_v and D_i are the vacancy and interstitial diffusivities, C_v is the vacancy concertation in matrix, C_v^V is the vacancy concentration at void surface, and C_i is the interstitial concentration in matrix. Equation 1.10 yields the volumetric swelling arising from void growth as follows:

$$\frac{dV}{dt} = 4\pi R^2 \dot{R} \qquad \text{Equation 1.11}$$

The void evolution is a complicated kinetic process that involves thermodynamic factors and considerations of interfacial reactions [56-59]. For simplicity, Equation 1.10 can be rewritten as:

$$\dot{R} = \dot{R}_0 F(\eta) + \dot{R}_{th} \qquad \text{Equation 1.12}$$

The first term $\dot{R}_0 F(\eta)$ in Equation 1.12 refers to the growth rate of voids arising from a net absorption of vacancies, and the second term $\dot{R}_{th}$ refers to the reduction rate due to thermal emission of vacancies. At low temperature, vacancies are practically immobile, so $\dot{R}_0 F(\eta)$ is low in value. With increasing temperature, the growth rate increases, while the emission rate, the second term in Equation 1.12, also increases and counterbalances the net vacancy influx. As a result, the Equation 1.12 predicts that the plot of void swelling should be characterized by a peak at intermediate temperature. Such prediction has been confirmed by experimental evidences, as typically demonstrated in Figure 1.9 [40, 60]. In addition to temperature, other influential factors of void swelling include the effect of inert gas [61] and impurity atoms [62], role of biased sinks [63], dose and dose rate dependence [64], as well as stress dependence [65].

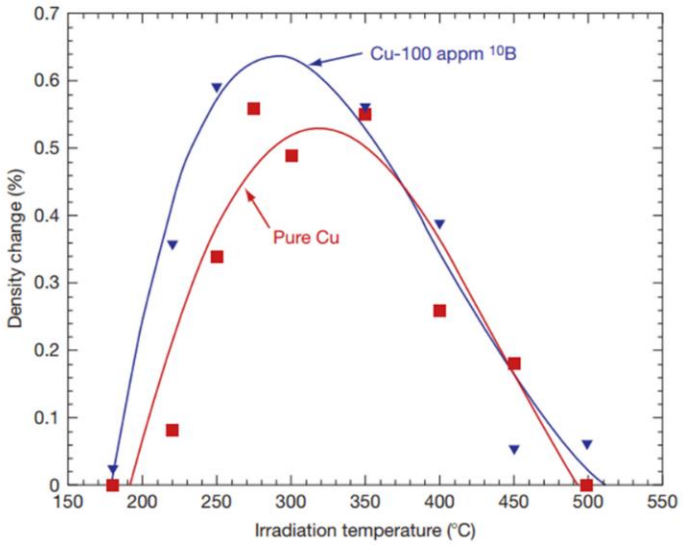

Figure 1.9. The peak swelling of irradiated Cu and Cu-B alloy at ~ 300 ^{o}C [40, 60].

Recently, phase-filed (PH) modeling has been proved successful in understanding and unravelling the underlying mechanisms of void swelling in irradiated metals [59, 66-70]. Figure 1.10 illustrates a simulation result regarding the void nucleation and growth in irradiated polycrystalline metals subjected to on-going vacancy concentration due to cascades [67]. In this study, the void surfaces and the grain boundaries act as sinks for supersaturated vacancies, so a void denuded zone (VDZ) surrounding the peripheries of grains are present in Figure 1.10(f).

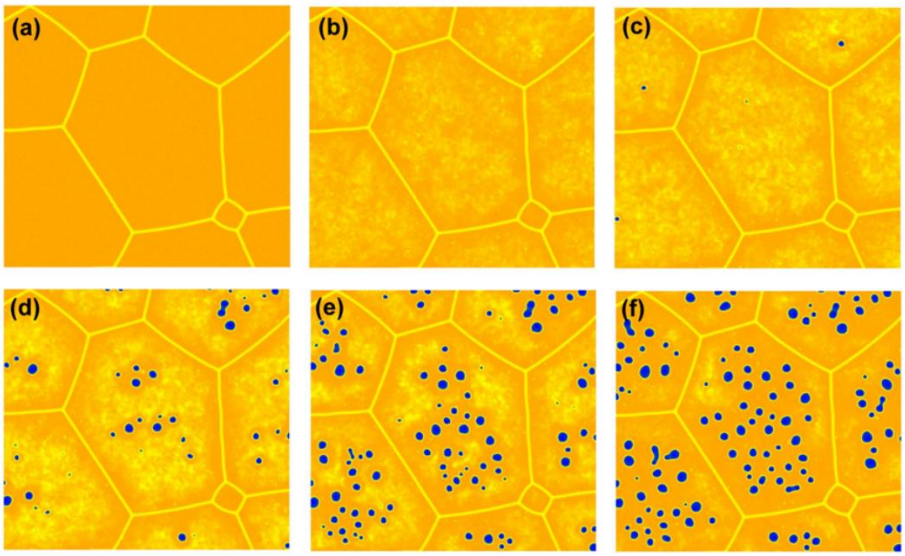

Figure 1.4. The phase-field simulation illustrates void evolution within polycrystalline grains at progressive instances in time [67].

1.3.4 Radiation-induced Hardening and Embrittlement

The radiation damage effects on microstructure directly result in significant damage effects on the physical and mechanical properties of the irradiated material [71]. For crystalline metals that deform plastically through dislocation multiplication and migration, radiation-induced defects can act as barriers against dislocation movement, and thus controlling deformation mechanism and causing strengthening and hardening [72]. Figure 1.11 shows one typical example of the radiation effect on the stress-strain behavior in 316 SS [11].

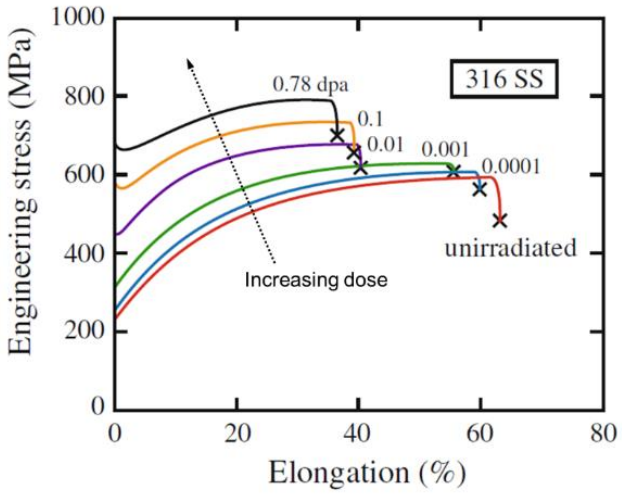

Figure 1.5. Radiation-induced strengthening (hardening) in 316 SS [11].

Note that the yield strength (σ_y) of irradiated 316 SS increases with increasing radiation dose. To describe such strength increment ($\Delta\sigma_y$) in irradiated metals, two approximate dislocation barrier models have been developed [73]. On the one hand, for strong obstacles, such as precipitates, dislocation loops or SFTs, their strengthening effect can be well described by the dispersed barrier hardening model [74], according to which the magnitude of strength increment is described by [75]:

$$\Delta\sigma_y = \alpha M \mu b \sqrt{Nd} \qquad \text{Equation 1.13}$$

where α is a parameter depending on the average barrier strength of radiation-induced defect clusters, and a perfectly hard barrier would have a value of $\alpha = 1$; M is the Taylor factor, a ratio of uniaxial yield strength to resolved shear strength with an average value of 3.06 for both face-centered-cubic and body-centered-cubic lattices [74]; μ and b are material shear modulus and Burgers vector; N and d are density and size of radiation-induced defect clusters. Equation 1.13 simply derives from the dispersed barrier hardening model with little considerations for the defect structure. In addition, the defect clusters must be so 'strong' that moving dislocations would bow out in order to continuously migrate through the lattice. On the other hand, however, for large voids or under-pressurized bubbles that are classified as weak barriers, moving dislocations can directly cut through them. To describe their strengthening contribution, Friedel-Kroupa-Hirsch

established an alternative model, known as FKH model, according to which the strength increment is given by [76]:

$$\Delta\sigma_y = \frac{1}{8} M \mu b d N^{2/3} \qquad \text{Equation 1.14}$$

where M, μ, b, d, and N are the same parameters defined in Equation 1.13.

In addition to strength (or hardness) increment, Figure 1.11 also suggests that the elongation of irradiated 316 SS decreases with increasing dose. From the viewpoint of mechanics, the strength and toughness are generally mutually exclusive [77]. The increment in hardness and strength is accompanied with the reduction in material ductility and toughness [78]. As a result, radiation invariably renders irradiated metals less ductile, in other words more brittle, than the unirradiated condition [79]. The notched bar impact test is the conventional way to quantify the embrittlement characteristics of irradiated metals [11]. In the test, the notched specimen is impacted by a heavy swinging pendulum as shown in Figure 1.12(a). After breaking, the pendulum continues to move until it stops somewhere, through which the energy absorbed in fracturing the specimen can be measured. The radiation effects on ductility is then assessed based on the magnitude of energy absorbed. Figure 1.12(b) illustrates a typical example of the effect of irradiation on steel. It is clear that there is a shit of the curve to higher temperatures after irradiation, indicating a reduction in the upper shelf energy (USE), in other words the trend for embrittlement.

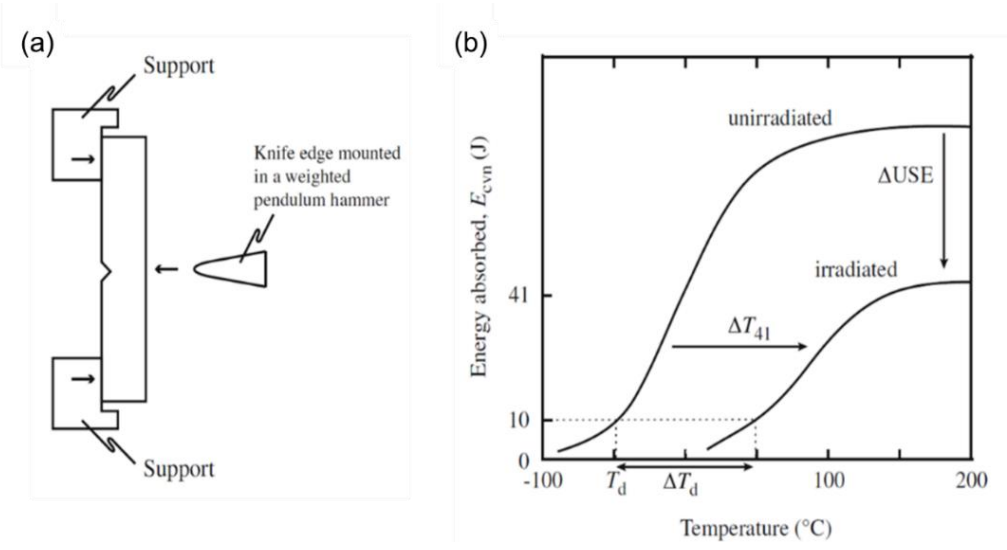

Figure 1.6. (a) Notched bar impact testing. (b) Radiation-induced the reduction in energy absorbed [11].

1.4 Radiation Damage Tolerant Nanostructured Materials

In the past few decades, nanostructured materials have been of great interest to material scientists and engineers due to their superior properties over conventional materials [80]. The superiority arises from high density of intrinsic interfaces introduced during materials processing and manufacturing, such as grain boundary (GB), phase boundary, twin boundary (TB), and free surface [81]. In radiation studies, such interfaces are often referred as defect sinks that are frequently involved in defect production, diffusion, and annihilation process [82, 83]. There are increasing evidences that show nanostructured materials exhibit enhanced radiation tolerant in terms of lower defect density [84], less radiation hardening [85] and swelling [30]. Figure 1.13 illustrates several typical nanostructured materials that contain large volume fraction of interfaces (defect sinks) with enhanced radiation tolerance [86].

Among all the proposed nanostructured materials, nanograined materials are the mostly studied, and their radiation performance shows a strong dependence on grain size [87]. Early in 1997, M. Rose *et al.* found that the radiation-induced defect clusters in ZrO_2 and Pd samples decreases with decreasing gain size [88]. Similar observations are also reported by Zinkle, SJ *et al*. in Cu [89], Edwards *et al*. in stainless steels [38], C. Sun *et al.* in Ni [90] and M. Song *et al*. in T91 steel [91]. In addition, a great many studies on bubbles under Helium irradiation have also confirmed that smaller grains contain lower bubble density [92-96].

The underlying mechanism of such enhanced radiation tolerance for nanograined materials is closed associated with the GB's effect on defect formation and distribution [97]. Post-irradiation analysis revealed a void-denuded zone that is formed along GBs as shown in Figure 1.14(a), suggesting the vacancy supersaturation at GBs is too low to drive void nucleation and growth [60, 67]. Moreover, as shown in Figure 1.4(b), the *in-situ* TEM irradiation captured direct absorption of mobile defect clusters by GBs, which is ascribed to the defect concentration gradient near GBs that serves as the driving force for the directional defect migration towards GBs [90].

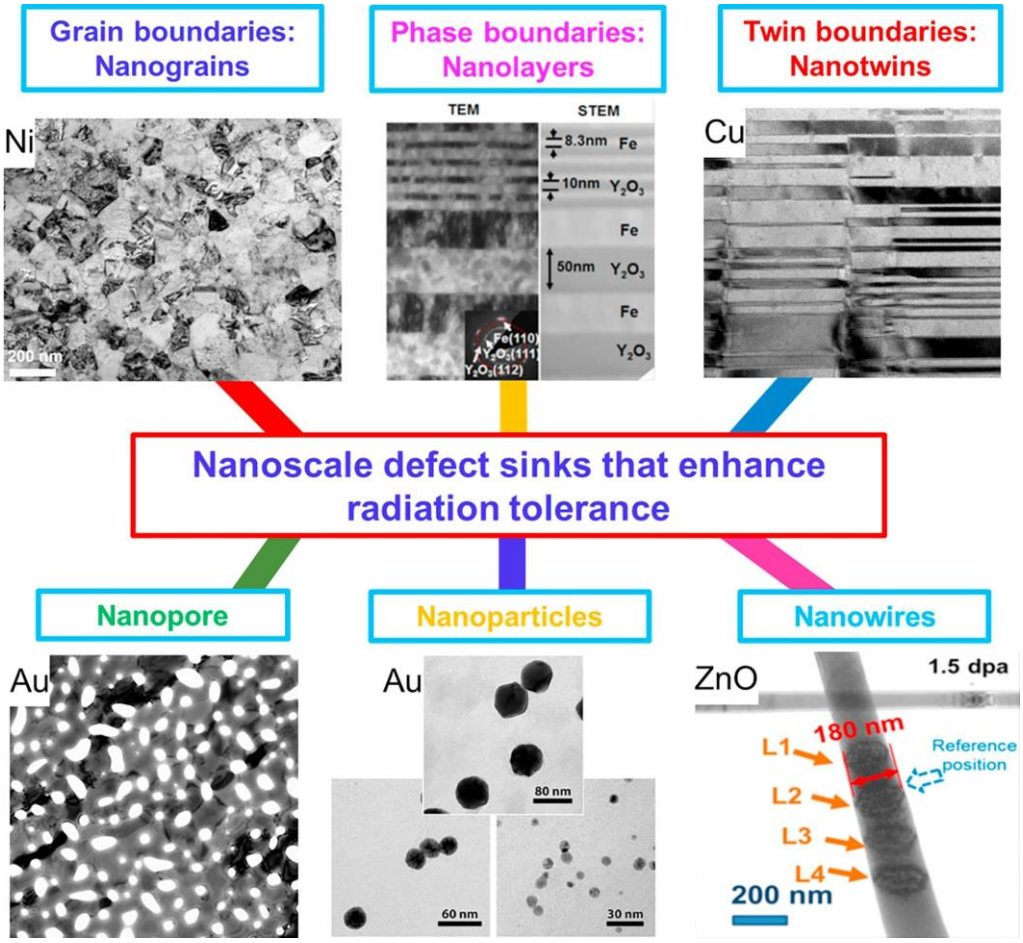

Figure 1.7. Radiation tolerant nanostructured metals with various types of interfaces (defect sinks) [86].

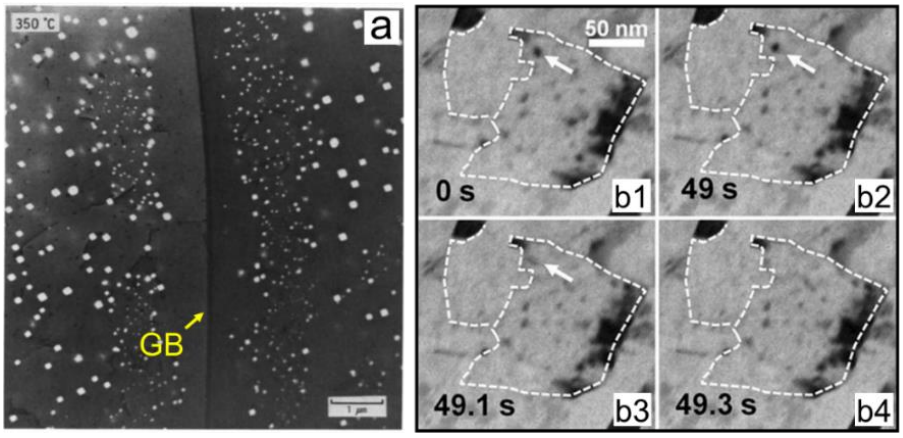

Figure 1.8. GB-defect interactions. (a) Void-denuded zone along a grain boundary in neutron-irradiated copper at 350 ºC [60]. (b1-b4) Absorption of an individual loop (marked by an arrow) by a grain boundary (dashed lines) in heavy ion (1 MeV Kr^{++}) irradiated Ni at room temperature [90].

Theoretically, molecular dynamic (MD) simulation studies demonstrate that GBs can highly promote vacancy-interstitial recombination process while remaining their structural integrity [98]. Figure 1.15 shows the selected snapshots of the MD simulations on damage self-healing near a GB; the smaller black spheres represent pristine atoms, larger green spheres are interstitials, and red cubs mean vacancies. It was found that the GB can first capture interstitials and become overloaded as shown in Figure 1.15B, and then the interstitial-rich GB fire interstitials back into the lattice to annihilate any vacancies that come within a few nanometers of the GBs as shown in Figure 1.15C-I. This 'loading-unloading' mechanism of interstitial emission proves to be highly efficient, because point defect diffusion becomes easier in the interstitial-loaded GB than that in a pristine boundary without initials.

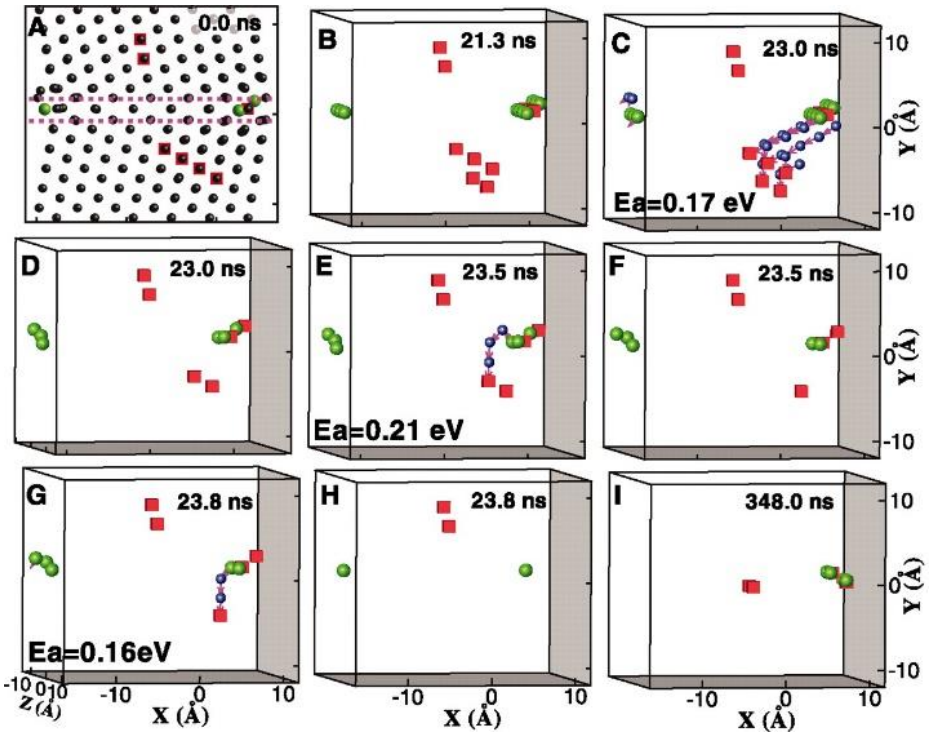

Figure 1.9. MD snapshot showing the damage self-healing mechanism near GB [98].

1.5 Nanotwinned Metals

In spite of their improved radiation tolerance, nanograined metals usually suffer from poor thermal stability due to the high excess energy stored in conventional high-angle grain boundaries [99]. It has been reported that radiation-induced grain-coarsening occurs even at room temperature [27].

In addition, nanograined metals tend to become brittle and show little ductility when the grain size reduces to several and tens of nanometer scale [100]. Comparing with conventional grain boundaries, twin boundaries (TBs) are special high-angle boundaries with peculiar microstructures and lower energies [101]. Nanotwinned (NT) metals have been of great interest to material scientists in the past decade, because of their super thermal stability [102, 103], high electrical conductivity [104, 105], remarkable mechanical properties [106-108], and improved radiation tolerance [109, 110].

Twin structures are widely observed in various face-cubic-centered (FCC) metals with low stacking fault energy (γ_{SF}). Some typical examples are displayed in Figure 1.16, including NT-Cu (γ_{SF} = 45 mJ/m^2) [104, 111, 112], NT-Ag (γ_{SF} = 16 mJ/m^2) [106], NT-Au [113] (γ_{SF} = 32 mJ/m^2) , and NT-austenitic stainless steel [114] (γ_{SF} = 20-50 mJ/m^2). In this section, a review is presented on recent investigations of NT metals with emphasis on their microstructures, mechanical properties, and radiation performance.

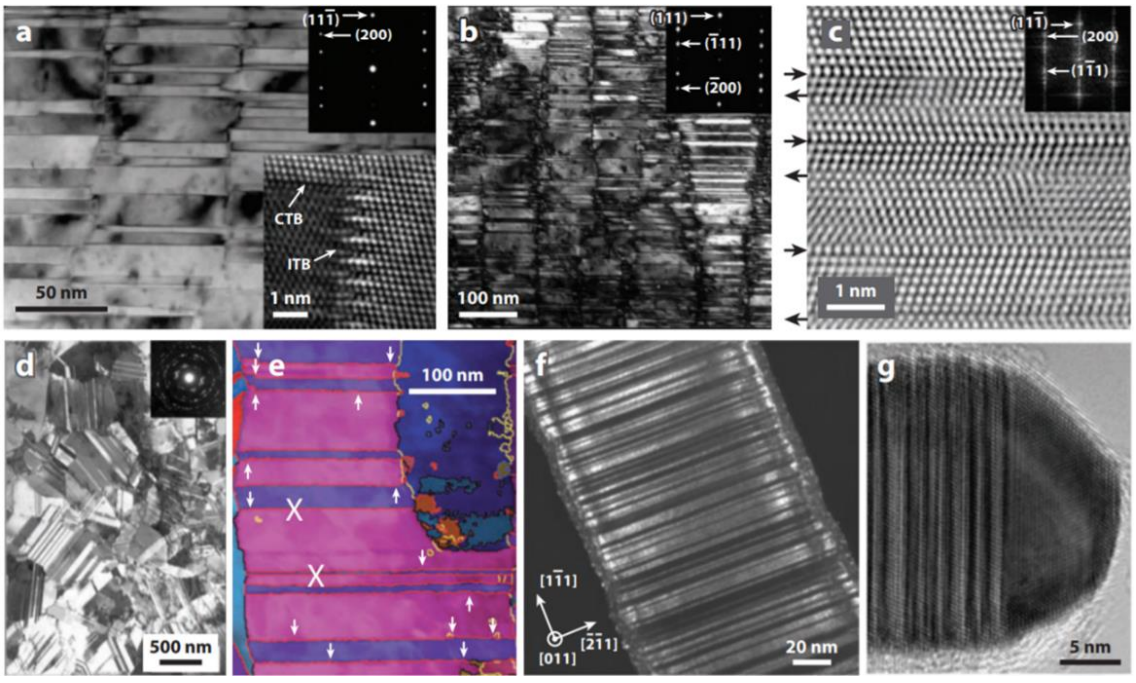

Figure 1.10. Typical examples of nanotwin structures in FCC metals with lower stacking fault energy [104] [106] [114] [105] [113].

1.5.1 Microstructure of Twin Boundaries

Twin structures can be introduced by fabrication processing (growth twins), plastic deformation (deformation twins), or recrystallization (annealing twins) [115]. The NT metals are characterized by a high density of twin boundaries (TBs), including $\Sigma 3\ \{111\}$ coherent twin boundaries (CTBs) and $\Sigma 3\ \{112\}$ incoherent twin boundaries (ITBs). Figure 1.17 shows a cross-sectional TEM micrographs of twin boundaries in epitaxial NT-Cu film [116]. Figure 1.17 (a) is the bright-field (BF) TEM image recorded from the <110> zone axis, and the inset selected area diffraction (SAD) pattern in Figure 1.17 (b) shows typical symmetrical spots of twin structure. The high-resolution (HR) TEM image in Figure 1.17 (c) reveals two distinct twin boundaries of CTBs and ITBs. The CTBs are straight and narrow, located on $\{111\}$ planes with twin and matrix symmetrically aligned on either side. The ITBs, however, exhibit a narrow or diffuse feature depending on the local stress state, as respectively illustrated in Figure 1.17 (d) and 1.17 (e). ITBs are found to be highly mobile under electrical [117], thermal [118], and mechanical [119] extreme conditions, and their migrations lead to detwinning phenomenon accompanied with the reduction of twin boundary density [120].

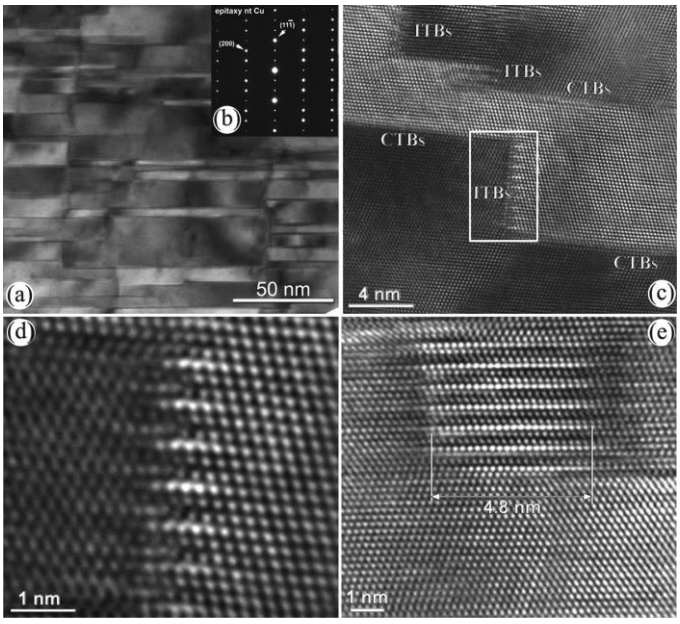

Figure 1.11. HRTEM micrographs of twin boundaries in epitaxial NT-Cu film [116].

To describe the structure and migration behavior of ITBs, a dislocation model is proposed based on atomistic observations [121, 122] and simulations [116, 123], as schematically illustrated in Figure 1.18 [124]. According to this model, the ITBs contain groups of Shockley partial dislocations on successive {111} planes. In Figure 1.18 (a), the three partials are denoted as **A**δ, **B**δ, and **C**δ using the notation of the Thompson tetrahedron, and note that the sum of their Burgers vectors in one triple unit equals zero. Under shear stress, the pure edge dislocation **A**δ is expected to be able to glide individually on {111} plane. **B**δ and **C**δ, however, are two mixed dislocations with opposite sign screw components, and they migrate together due to their mutual attractive forces [123]. Consequently, their migrations give birth to the 9R stacking arrangement of **BCACADABC**, as shown in Figure 1.18 (b).

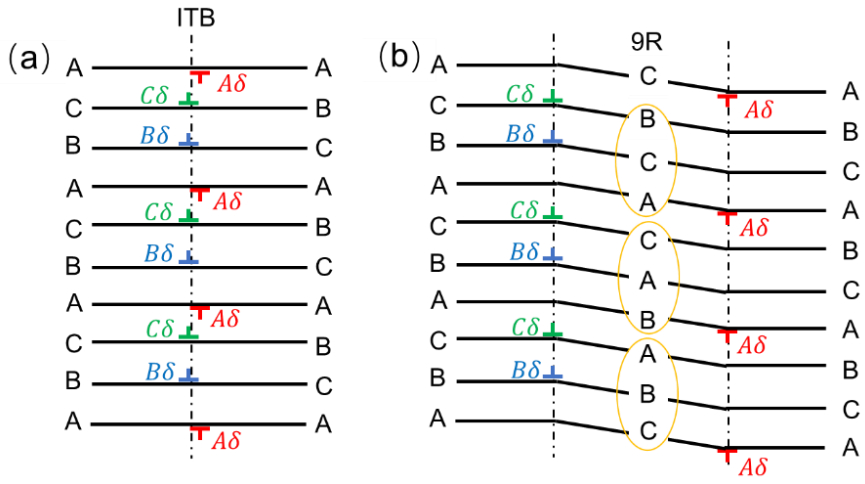

Figure 1.12. Dislocation structures for (a) a narrow ITB and (b) a diffuse and wide ITB with 9R phase.

1.5.2 Mechanical Properties of Nanotwinned Metals

The conventional methods for strength enhancement, such as grain refinement or cold working, unfortunately lead to the reduction in ductility [77, 100, 125]. One of the promising ways to evade such strength-ductility trade-off dilemma is to utilize twin structures [126]. It has been reported that nanotwinned metals are ultra-highly strong, up to 10 times higher than conventional coarse-grained metals in strength, yet considerably ductile compared with nanocrystalline metals [105].

For instance, Figure 1.19 compares the tensile true stress-strain curve of NT-Cu with those of coarse-grained and nanocrystalline (nc) Cu [105].

The strengthening mechanism for nanometals is attributed to the TBs' effective block against moving dislocations in a manner analogous to conventional GBs [127], which has been extensively studied by molecular dynamic (MD) simulations [111, 128-131]. Various plausible dislocation interactions at the twin boundaries could occur depending on the characteristics of the dislocations and the driving stress [132]. Two typical interactions between an incoming 60^{o} dislocation and the CTB in Cu are illustrated in Figure 1.20 [129]. In scenario A, the incoming two dissociated partials of **Dγ** and **γA** (in Thompson tetrahedron notation) first constrict into a perfect dislocation which then cuts through the CTB by splitting into three Shockley partials. Two (**A**`**γ**` and **γ**` **D**`) of them gild in the slip plane of the twin grain, while the third one (**Cδ**) glides along the twin boundary. In scenario B, however, the interaction results in one leading Shockley partial (**γ**` **A**`) and one sessile dislocation left at CTB called 'i-lock', a Hirth lock that is featured by one row of "interstitials".

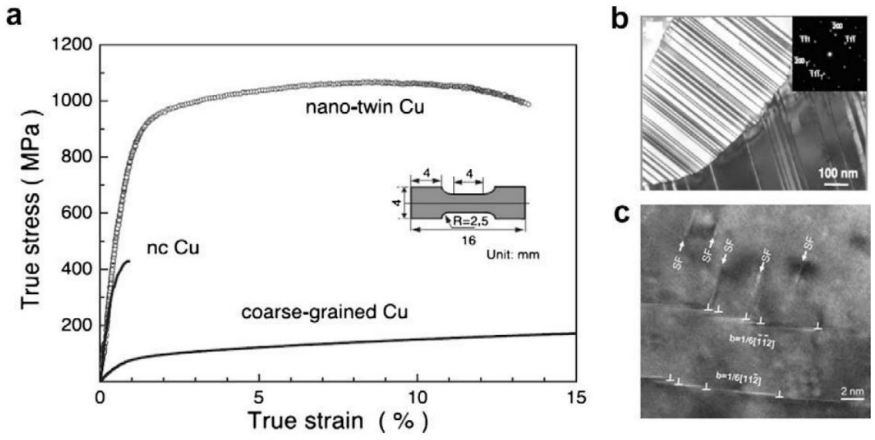

Figure 1.19. Ultra-high strength with high ductility in NT-Cu. (a) Tensile stress-strain curves for a nanotwinned, coarse-grained and nanocrystalline (nc) Cu sample [105]. (b) and (c) TEM micrographs of twin lamellae and deformation-induced dislocations along TBs.

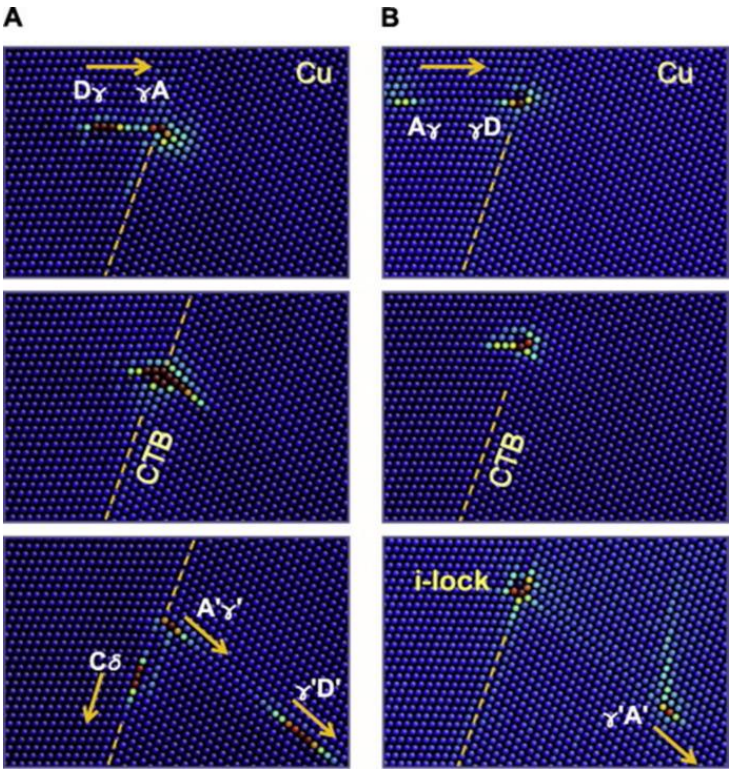

Figure 1.13. MD snapshots illustrating two distinct interactions between an incoming dislocation and a CTB in Cu [129].

The deformation behavior of NT metals is governed by two essential factors: TB orientation [133] and twin thickness [134]. The orientation-dependent plastic response was found in NT samples with preferentially oriented twin structures [135]. Experiments and simulations reveal that the columnar-grained highly textured NT-Cu exhibits the highest strength but least working hardening when the applied stress is oriented at 90^o with respect to TBs [133]. Such mechanical anisotropy is determined by three distinct deformation mechanisms that can be switched when the loading orientation changes [133].

In addition to TB orientation, TB spacing (or twin thickness) also plays an important role in the mechanical behavior of NT metals [134]. Figure 1.21 compiles the yield strength σ_Y of previously reported NT-Cu samples as a function of twin thickness t [136]. When the twin spacing is larger than 15 nm, the yield strength follows the conventional Hall-Petch (H-P) relationship, increasing linearly with decreasing t. However, when the twin thickness decreases down to 15 nm, softening may occur in polycrystalline NT-Cu, presumably because of the dislocation nucleation at grain boundary-twin intersections [130].

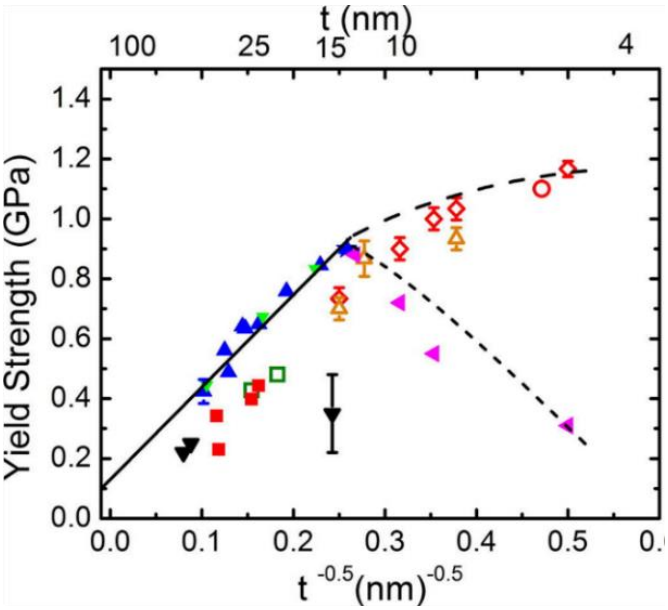

Figure 1.14. The dependence of twin thickness (*t*) on yield strength for NT-Cu [137].

1.5.3 Radiation Response of Nanotwinned Metals

For the irradiated nanotwinned metals that are FCC structure with low-to-intermediate stacking fault energy, their dominant defect clusters are expected to be SFTs at nanometer scale due to their lower formation energy over other defects as predicted by the Equation 1.5-1.8 [36]. As a kind of 3D vacancy clusters, SFTs are stable in structure, and once formed it usually requires high temperature and long time to anneal them out [138]. However, they can be easily destructed and subsequently annihilated through the interactions with TBs [109, 139]. There are increasing evidences that show NT metals are more radiation tolerant than coarse-grained metals in terms of lower defect density [109, 110, 140-144]. The *in-situ* TEM radiation studies on NT-Ag by Yu [109] et al. reveal that SFT density drops significantly with decreasing average twin spacing. Figure 1.22(a) and (b) compare the formation and distribution of SFTs in thick and ultrafine growth twins of irradiated NT-Ag. It is evident in Figure 1.22(c) that no SFTs are formed in twin structures when the twin spacing reduces to several nanometers that are comparable to the size of SFTs. Similar trend has been reported by Chen [110] in *in-situ* TEM radiation studies on NT-Cu. Very recently, the *ex-situ* radiation study on NT-316 austenitic stainless steel by de Bellefon [144] shows that void swelling is highly suppressed in the presence of deformation twin structures, as shown in Figure 1.22(d) and (e).

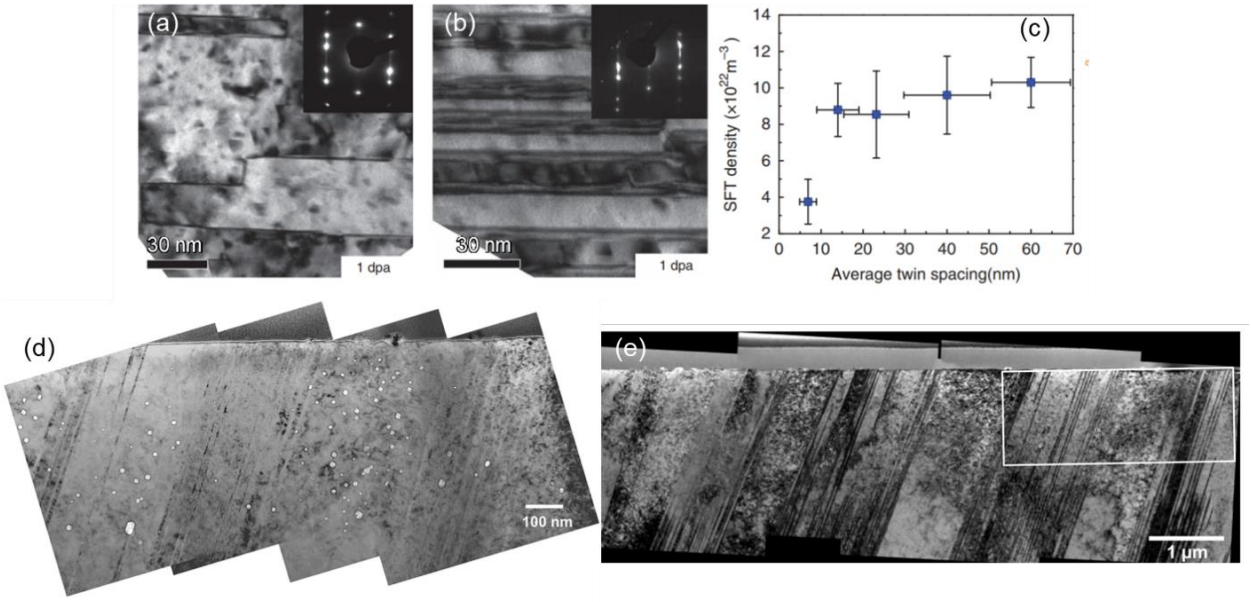

Figure 1.15. Enhanced radiation tolerance in NT metals. (a) and (b) Removal of SFTs by growth twin boundaries in NT-Ag irradiated by 1 MeV Kr^{++} at room temperature [109]. (c) and (d) Suppression of void swelling in NT-316 austenitic stainless after irradiation by 3.5 MeV Fe^{++} at 500 ^{o}C [144].

1.6 Emulating Neutron Irradiation Effects with Heavy Ions

Traditional radiation effect studies are conducted in test reactors, followed by comprehensive post-irradiation analysis [145]. However, in practice such method may impede the advancement for at least three factors. First, there are not enough test reactors available for research purpose. Second, it takes a long time for test reactors to create adequate damage. For instance, two typical test reactors in the US can produce radiation damage at a maximum rate of 8 dpa/year. Third, reactor irradiation is extremely high in cost, and yet usually involved in dealing with radioactive samples. In order to overcome aforementioned issues, heavy ion irradiation technique was developed in the 1960s with an initial purpose of supporting the fast breeder reactor program [146]. The fist consideration of emulating neutron irradiation effects with heavy ions is to identify the distinction between their damage evolution in structures. Figure 1.23 shows a pair of images comparing each feature in both ion- and reactor irradiated samples for ferritic-martensitic alloy HT9 (Fe-12Cr-1Mo) [145]. Qualitatively, they share the same standard microstructural features, such as (a) dislocation segments and loops, (b) G-phase precipitates in matrix, (c) G-phase precipitates along grain boundaries, and (d) voids.

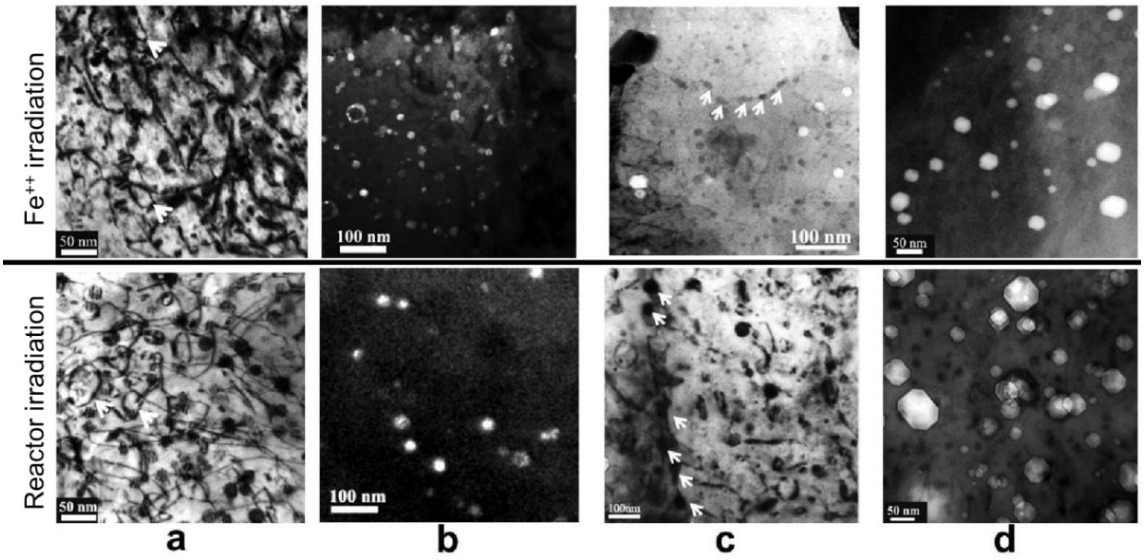

Figure 1.16. Emulating reactor irradiation damage effects (bottom images) using self-ion irradiation technique (top images) [145].

Compared with the test reactor radiation, heavy ion radiations are more efficient, economic, and safer. In addition, heavy ion experiments have the advantages of better control of irradiation parameters over a wide range of values, such as irradiation temperature, dose rate, and damage level [137]. Up to date, it has been widely adopted as an effective surrogate to emulate neutron radiation damage effects for post-irradiation testing [11, 145]. Nevertheless, one must be cautious about some limitations when conducting ion irradiation instead of neutron irradiation. For example, heavy ion irradiations have the lack of Helium, the transmutation product of nuclear reactions, such as the most promising reaction for a commercial fusion power plant [14]. As Helium atoms are hardly soluble in solids, they can rapidly diffuse through the lattice, interact with radiation-induced defects, and play an important role in microstructure evolution. Therefore, it is suggested to implant Helium simultaneously or prior to ion irradiation to take into account the Helium's effect on radiation damage [147]. Table 1.1 summaries several limitations and advantages usually encountered in practice [11].

Table 1.1. Advantages and limitations of irradiations with heavy ions.

Advantages	Limitations
High dose rate (10^{-2} -10^{-4} dpa/s)	Shallow irradiated region
Amendable radiation parameters	Narrow damaged profile
No radioactive injure	Temperature shift caused by high dose rate
	No transmutation (no Helium)
	Potential composition changes at high dose

1.7 Small-scale Mechanical Testing on Irradiated Materials

In radiation studies using heavy ions, the irradiated region is generally limit on sample surface with ion penetration depth at micrometer scale. As a result, the conventional mechanical testing that requires standard specimen in large piece is hardly satisfied. In the past decade, the development and advances in electron microcopy systems make it possible to perform small-scale mechanical testing, which is gaining more and more popularity in the nuclear materials community [148]. Mostly used testing methods include nanoindentation [149], micro bending [150], tension [151], and pillar compression [152]. Figure 1.24 is a typical example about nano-compression testing of irradiated Cu [153]. The samples, with a dimeter of 80-1500 nm, were prepared by focused ion beam (FIB) technique and compressed by a diamond punch inside a TEM, as illustrated in Figure 1.24(a). Before compression, the samples contain a high density of radiation-induced defects, as shown in Figure 1.24(b). The *in-situ* TEM snapshots in Figure 1.24(c)-(f) reveal that deformation and hardening are governed by the bowing and exit of short dislocations, indicated by gentle load drops in Figure 1.24(g).

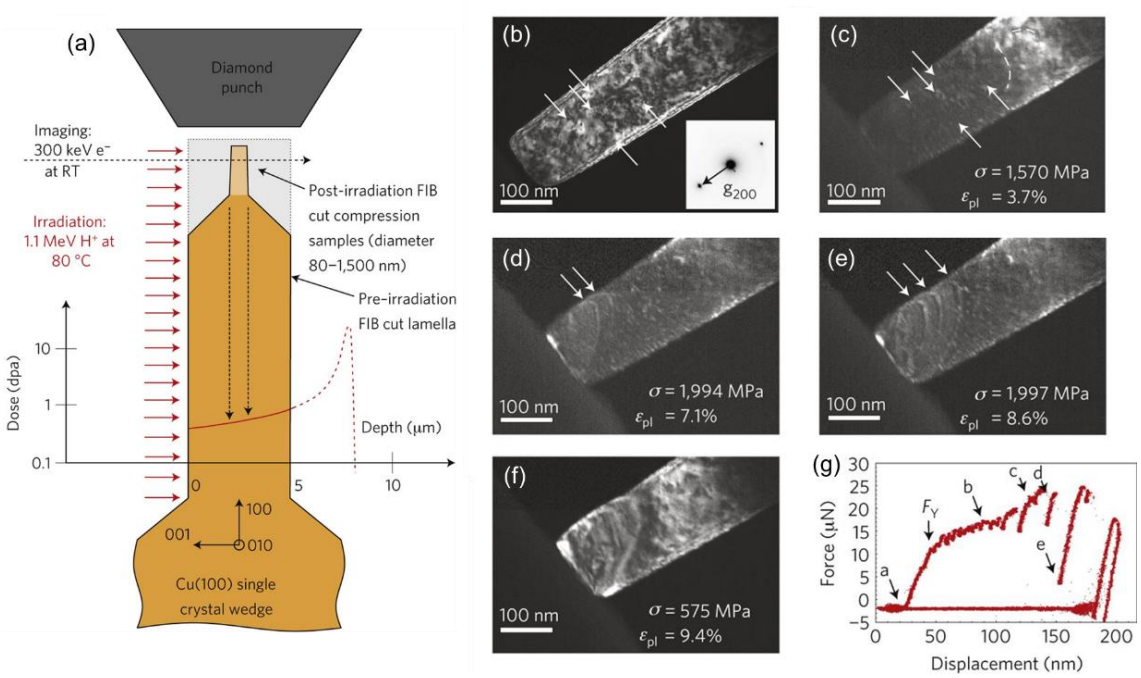

Figure 1.17. Nanocompression testing of neutron-irradiated copper [153]

With appropriate small-scale testing methods, it is possible to evaluate mechanical property changes from small volumes of irradiated components. However, the small-scale mechanical testing inevitably suffers from the so called 'extrinsic size effect', arising from sample dimension change [154]. It has been pointed out that miniature specimens contain too few dislocation sources, so their plastic yielding is much more difficult to be activated until the applied stress approaches the theoretical values of material [155]. Consequently, the measured strength of small-volume specimens at nanometer or micrometer scale tend to be higher than bulk materials [155, 156]. For irradiated samples, their mechanical properties are also influenced by the 'intrinsic size effect' controlled by the size, density and distribution of radiation-induced defect clusters [157]. Figure 1.26 schematically illustrates the intrinsic-extrinsic size effect relationship for microchemical tests on irradiated (fewer obstacles) and unirradiated samples (more obstacles) [157]. The vertical dashed line in Figure 1.26 indicates the transition dimension, beyond which the extrinsic size effect is insignificant for irradiated samples. It is worth noting that, in addition to small-scale mechanical tests, other complementary techniques and further data analysis are necessary in order to obtain bulk emerging like properties and bridge the experimental length-scale gap [158].

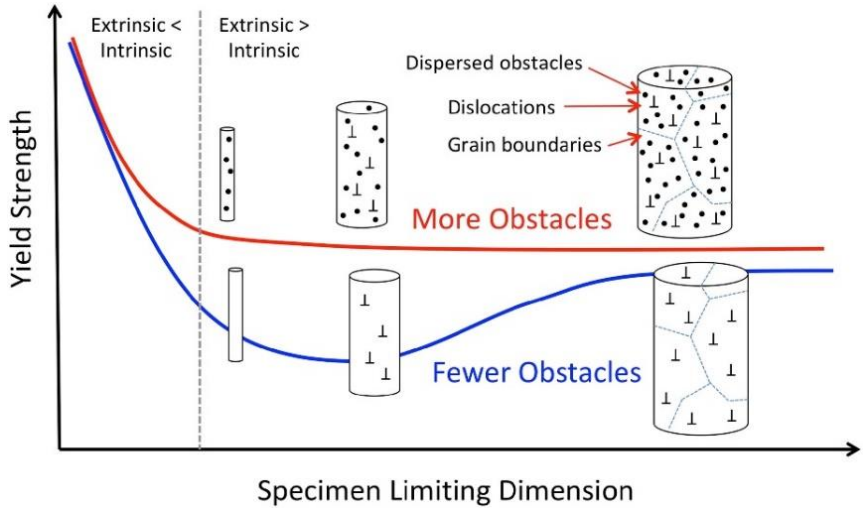

Figure 1.18. Illustration of the specimen size effect and the influence of irradiation [157].

1.8 Motivation and Objective

The motivation and objective of this thesis is to explore the heavy ion radiation damage effects on microstructure and mechanical properties in nanostructured Cu, via the methods of *in-situ* and *ex-situ* radiation experiments, post-irradiation TEM analyses, small-mechanical testing (micro-pillar compression), and computer simulations (molecular dynamics and phase-field modeling).

We chose Cu as our target material for radiation studies, because it is a classical FCC model system that has long been used and extensively studied in both radiation damage effects [46, 60, 87, 159-161] and materials mechanical properties [105, 134]. With the composition little changed, we utilize the direct current (DC) magnetron sputtering deposition technique to design and fabricate two distinct nanostructured Cu films on Si substrates with different orientations: Nanovoid-Nanotwinned (NV-NT) Cu (111) and Nanovoid Cu (110). The microstructures are tailored by controlling the deposition parameters and the orientation of Si substrates. These microstructure differences result in dramatically different mechanical properties and radiation performances. To assemble the influence of nanostructured features (twin boundaries) on material properties, a coarse-grained counterpart Cu is taken as the reference. The conclusions are finally drawn based on the comparisons between our nanostructured Cu and coarse-grained reference, and numerous previous works on Cu.

CHAPTER 2. EXPERIMENTAL

2.1 Magnetron Sputtering

Cu and CuFe (3 at. %) alloy thin films, ~ 2 μm thick, were deposited onto HF acid etched Si substrates via direct current (DC) magnetron sputter deposition technique. Figure 2.1(a) schematically illustrates the basic features of a DC sputter deposition system. Prior to deposition, the chamber is evacuated to a high vacuum state. Then Ar atoms are introduced, ionized, and accelerated toward the target (cathode) at high speed by an imposed electronic field, causing the neural atoms of the target source to be dislodged [162]. These atoms transmit through the discharge and condense onto the substrate (anode), thus resulting in film growth. In addition, a closed magnetic field is superimposed with an electric filed to improve the efficiency of the initial ionization process, so that a plasma can be easily generated at lower pressures. Figure 2.1(b) is the picture of a home-made magnetron sputtering system used in this thesis. It is operated by Zhang Nanometal Group at Purdue University. The system contains four sputtering guns (Kurt J. Lesker, Inc.) and two DC power supplies, pumped by both turbomolecular and cyropumps with a typical base pressure of $< 8 \times 10^{-8}$ torr.

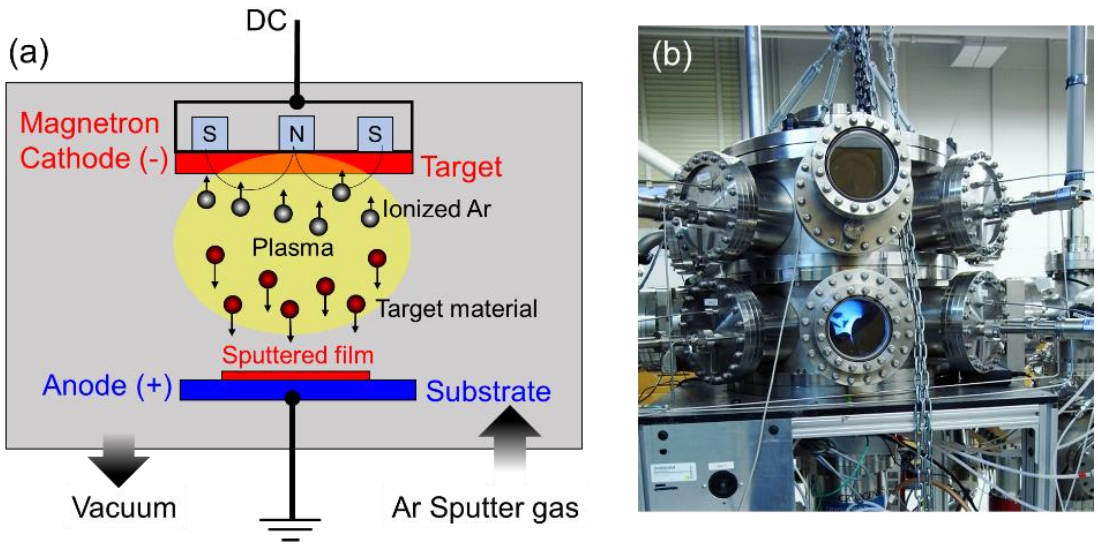

Figure 2.1. (a) Schematic showing the basic features of a DC sputter deposition system. (b) Magnetron sputtering system used for depositing thin films.

2.2 Texture Analysis and Microstructure Characterization

2.2.1 X-ray Diffraction

The microstructure of sputtered films is dependent on film texture [106] that can be examined by X-ray diffraction (XRD). XRD analysis is based on the interaction of X-rays with the atomic structure of a crystalline lattice. In this technique, the incident X-rays are scattered by the atoms at a certain family of crystallographic planes [163]. The diffracted X-rays are collected by a detector and form a unique pattern with discrete diffraction peaks. For parallel planes of atoms, with an interplanar spacing d, a diffraction peak occurs when Bragg's Law is satisfied:

$$n\lambda = 2d\sin\theta \qquad \text{Equation 2.1}$$

where n is an integer referring to the order of the observed peak, λ is the wavelength of the X-ray, and θ is the incident angle between incident X-ray and diffracting planes.

The X-ray scans were conducted at Purdue University using a Panalytical Empyrean X'pert PRO MRD diffractometer with a Cu Kα1 source. Two kinds of X-ray scans (θ-2θ and φ) are used in this thesis, whose operating conditions are schematically illustrated in Figure 2.2. During a θ-2θ scan, the sample stage is fixed, while the X-ray source and detector are moving along a circle, as shown in Figure 2.2(a). The conventional 2θ-scan can only determine the atomic planes parallel with film surface as marked by $\{hkl\}$ in Figure 2.2(a). To measure different crystallographic planes and determine the orientation-relationship (OR) between film and substrate, the φ-scan is also set up as shown in Figure 2.2(b). During a φ-scan, the sample is tilted by χ so that another originally inclined family planes, marked by $\{mnp\}$ in Figure 2.2(b), can become horizontal. Meanwhile, the X-ray incident angle is kept as the diffraction angle of $\{mnp\}$ planes, and the angle value θ_{mnp} can be calculated using the Bragg's Law in Equation 2.1. To complete a φ-scan, the tilted sample stage rotates around its symmetrical axis, while the X-ray source and detector remain stationary, as shown in Figure 2.2(b).

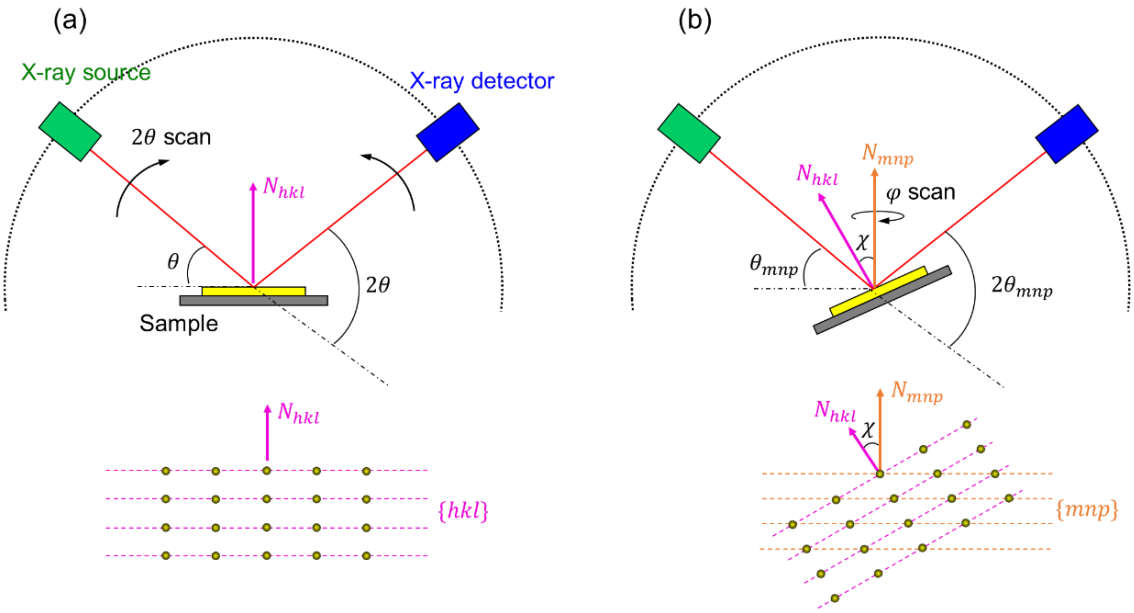

Figure 2.2. Schematic diagrams for (a) 2θ-scan and (b) φ-scan.

2.2.2 Transmission Electron Microscope

Transmission electron microscope (TEM) makes use of the properties of electrons, both as particles and waves, to characterize material microstructure at nanometer scale. The TEM imaging is based on the interaction between incident electrons and target materials through scattering and diffraction. Depending on how the electrons are scattered and diffracted, the electron beam can change both its amplitude and phase when traversing the specimen, and both types of change can give rise to image contrast [164]. TEM has been widely used in the field of radiation damage studies for understanding how microstructures develop under irradiation [165]. However, TEM technique has its own limitations, and various artefacts may occur during an imaging process. In practice, therefore, it is essential to control appropriate imaging conditions for high-quality structural characterizations. Figure 2.3(a) compares the operational modes of two most important imaging conditions: bright field (BF) and dark field (DF). Their conditions are primarily controlled by using of an objective aperture to select transmitted or diffracted beam, resulting in BF or DF TEM image, respectively. Figure 2.3(b) shows the picture of a FEI Talos 200X TEM that is used in this thesis for TEM imaging and post-irradiation analysis.

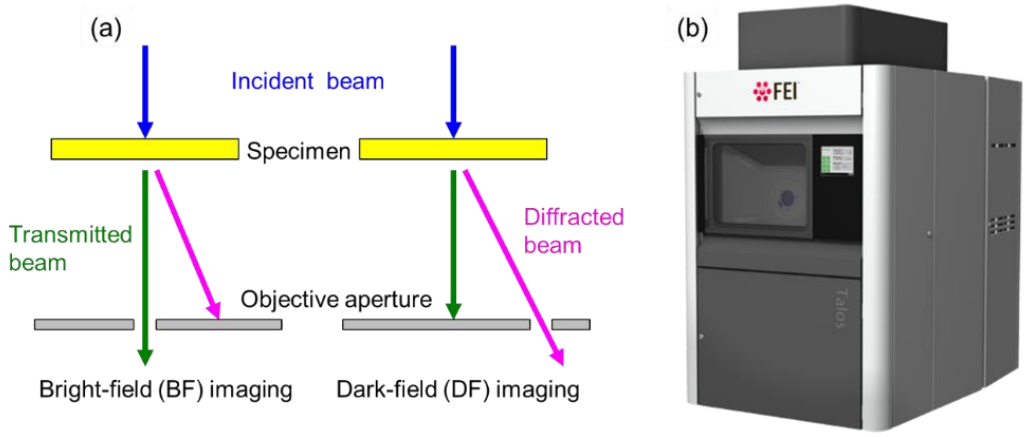

Figure 2.3. (a) Operational modes of BF and DF imaging conditions. (b) Picture of a FEI Talos 200X TEM used in this thesis.

2.3 Heavy Ion Irradiation

2.3.1 *In-situ* TEM Irradiation by 1 MeV Kr^{++}

Compared with conventional *ex-situ* radiation experiments, *in-situ* TEM ion irradiation enjoys the advantage of real time observation of defect formation and evolution under well-controlled radiation conditions, which is essential for understanding fundamentals of radiation damage in materials [166]. The *in-situ* TEM irradiations in this thesis were conducted in the Intermediate Voltage Electron Microscope (IVEM)-Tandem Facility at Argonne National Laboratory (USA), as shown in Figure 2.4(a). The TEM foils, estimated as ~ 100 nm thick and transparent to 200 kV electron beam, were irradiated by 1 MeV Kr^{++} with the ion beam incident at 30^{o} from the electron beam and 15^{o} from the foil normal, as schematically shown in Figure 2.4(b). Radiation damage was calculated using SRIM-2008 [26], with full damage cascades and the displacement energy, E_d = 30 eV for Cu [11]. The calculated depth profiles of ion concentration and radiation damage for 2×10^{14} ions/cm^2 1 MeV Kr^{++} planted in Cu are given in Figure 2.4(c). According to the SRIM calculations, most (~ 95 %) of the Kr^{++} can transmit through the TEM foil and cause ~ 1 dap damage in the foil.

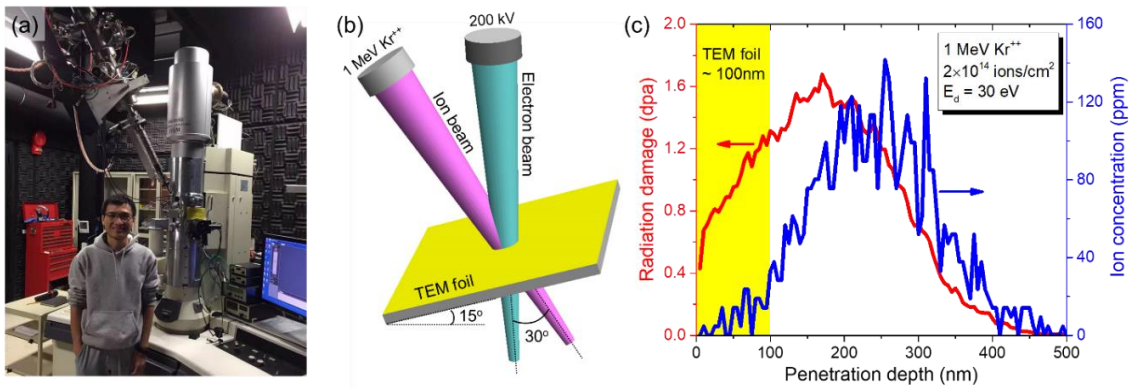

Figure 2.4. *In-situ* 1 MeV Kr^{++} irradiation. (a) The author standing in front of the IVEM-Tandem Facility at Argonne National Laboratory (taken by Jin Li, 2015). (b) Schematic illustration of experimental setup for *in-situ* TEM irradiation. (c) SRIM calculation of radiation damage (in dpa) and ion concentration in Cu caused by 1 MeV Kr^{++}.

2.3.2 *Ex-situ* Multi-He^{+} Irradiation

In addition to *in-situ* TEM irradiations, *ex-situ* irradiations by He^{+} was also conducted at the Ion Beam Materials Lab, Los Alamos National Laboratory (USA), with three sets of He ion beams (with various energies of 50, 100 and 200 keV) sequentially implanted into specimens, as shown in Figure 2.5 (a). The corresponding damage profiles and implanted He concentration are shown in Figure 2.5 (b). Such multi-He irradiation can produce a desirable region with uniform damaged features along the penetration depth, making it more straightforward for conducting and analyzing small-scale mechanical testing afterwards.

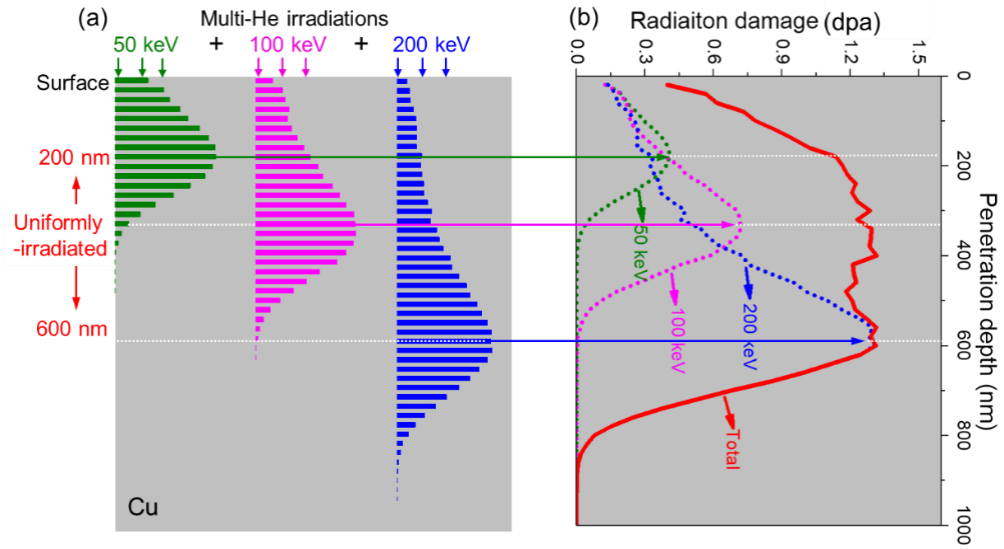

Figure 2.5. He-radiation damage (in dpa) plotted as a function of penetration depth (in nm). (a) Radiation damage of individual He irradiation with various energies of 50, 100, and 200 keV. (b) The total radiation damage profile (red) along ion penetration depth.

2.4 Focused Ion Beam

In the past decade, the focused ion beam (FIB) technique has been developed into a versatile and powerful tool for scientists and engineers, successfully applied in various fundamental materials studies and technological applications, such as TEM sample preparation, nanomachining, and microstructural analysis [167, 168]. In this thesis, the micropillars and TEM samples were fabricated from irradiated materials or deformed pillars using a dual-beam FIB-SEM instrument, as schematically shown in Figure 2.6. It works inside a FEI quanta 3D FEG SEM that consists of a micromanipulator, a highly focused Ga ion beam, and a Pt gas injection. The Ga ion beam is designed for precise machining, while the Pt gas injection is used for local mechanical vapor deposition. The angle between Ga ion beam and electron beam is 52^{o}, and the sample stage is tilted from time to time during an ion milling or lift-out process.

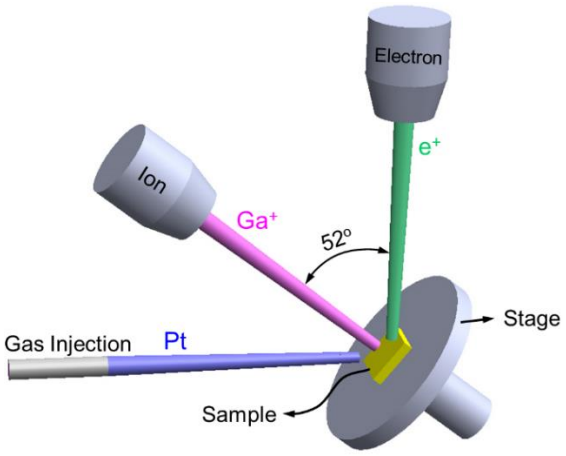

Figure 2.6. Schematic illustration of the dual-beam FIB-SEM instrument used for micropillar and TEM sample preparation.

2.5 Micropillar Compression

The *in-situ* SEM compression tests on FIB-machined micropillars were performed using a 8 μm flat punch on a Hysitron TI 950 TriboIndenter equipped with a transducer with 1 nN load resolution, and the thermal drift rate was below 0.05 nm/s, and monitored for 40 s prior to compressions conducted at a strain rate of 1×10^{-3} /s. Figure 2.7 (a) schematically shows the experimental setup, and Figure 2.7(b) shows a representative as-fabricated micropillar for compression test.

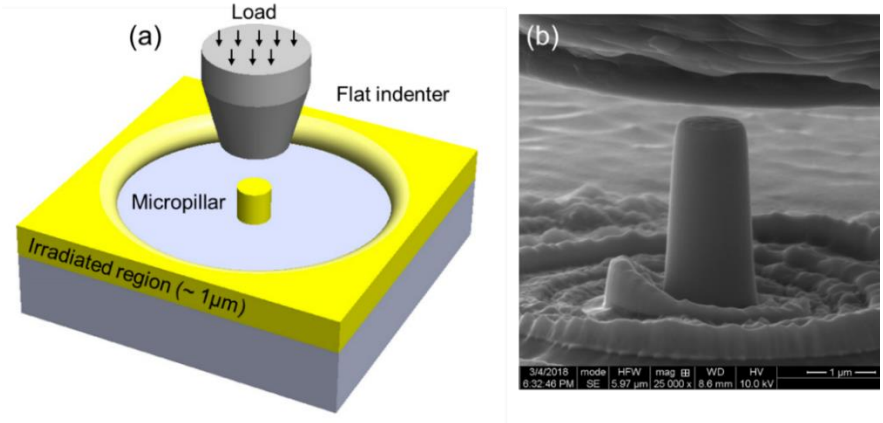

Figure 2.7. *In-situ* SEM micropillar compression test on irradiated materials. (a) Schematic illustration of experimental setup. (b) SEM image of a representative FIB-machined micropillar.

CHAPTER 3. DEFECT EVOLUTION IN HEAVY ION IRRADIATED NANOTWINNED CU WITH NANOVOIDS

The lab work was performed at Argonne National Laboratory by Dr. Youxing Chen and Dr. Jin Li with guidance of Dr. Meimei Li. The data analysis and writing were completed by Cuncai Fan with guidance and editing by Dr. Xinghang Zhang.

3.1 Overview

Our previous *in-situ* TEM radiation studies revealed that the pre-existing nanovoids formed in the nanotwinned Cu can enhance the radiation tolerance [169]. Such capability is assumed to arise from high density of coherent and incoherent twin boundaries that rapidly capture and transport point defects and dislocation loops to nanovoids. To confirm our assumption, this chapter presents a follow-up study about how defects evolve in the presence of nanovoids and twin boundaries. Epitaxial nanotwinned Cu film with abundant nanovoids surrounding domain boundaries was subjected to Kr ion irradiation inside a transmission electron microscope at various dose rates. It was found that irradiation-induced defect clusters distributed preferentially near domain boundaries during the early stage of radiation. Meanwhile, the pre-existing nanovoids continuously shrank. This study suggests that the defect network enabled by the unique combination of nanotwins and nanovoids may significantly enhance the radiation tolerance of metallic materials.

3.2 Introduction

When metallic materials are subjected to irradiations by high-energy ions or neutrons, a large number of vacancy and interstitial clusters are induced in form of Frank (intrinsic or extrinsic) loops, perfect dislocation loops, stacking fault tetrahedrons (SFTs), voids and bubbles[36, 38, 60, 170-176]. These irradiation-induced defects cause dramatic microstructural alteration, leading to the degradation of physical and mechanical properties in irradiated materials [172, 177-179]. For

instance, the irradiation-induced hardening and embrittlement in metallic materials have been frequently reported [180-182]. Therefore, it is of great significance to design advanced materials with excellent radiation tolerance. In general, radiation tolerance of a material is largely determined by its capability to remove point defects[98, 183, 184]. Thus in principle the radiation tolerance of a metallic material can be enhanced by introducing sufficient defect sinks that are capable of annihilating defects and consequently suppressing radiation damage[185, 186]. To date, various types of defect sinks have been investigated, including grain boundary [90, 91, 98, 187-190], phase boundary[191-194], free surface[195, 196] and twin boundary (TB)[109, 110, 197]. Among them grain boundary alleviated radiation damage has been intensively studied, and prior studies revealed that certain nanostructured materials, containing a large volume fraction of GBs, exhibit exceptional radiation resistance [31, 84, 198-201]. However, the grain coarsening of nanocrystalline materials, often observed during irradiation at elevated temperature[27], compromises their radiation resistance.

Recently, nanotwinned (nt) metals have shown superior thermal stability and remarkable radiation tolerance compared to their nanograined counterparts [102-104, 110, 140, 202]. *In-situ* radiation studies in a transmission electron microscope unraveled that irradiated nt Cu and Ag, with a high density of TBs, contained a lower defect density than its bulk counterpart under the same radiation conditions [109, 110, 203]. The *in-situ* observations also confirmed that SFTs, a dominant type of vacancy clusters in various irradiated metals with face-centered-cubic (fcc) structure, can be removed through their frequent interactions with TBs [109]. In addition, TB affected zones were observed in heavy ion irradiated nt Ag, providing direct evidence that TBs can act as an effective defect sinks[140]. Our recent studies on nt Cu showed that its radiation tolerance could be enhanced further by introducing nanovoids (nvs) at domain boundaries[169, 204]. Nevertheless, as defect density evolves rapidly. the early-stage of defect-TB interactions has not yet been fully understood. To elucidate this issue, here we report a follow-up *in-situ* Kr^{++} irradiation study on nanovoid-nanotwinned (nv-nt) Cu. The results show that irradiation-induced defect clusters were non-uniformly distributed inside the specimen at the early stages of irradiation process, lending further evidence for the enhanced radiation tolerance of nv-nt Cu.

3.3 Experimental

An epitaxial nt Cu film, ~1.5 μm thick, was deposited on HF etched Si (110) substrates at room temperature via DC magnetron sputtering technique. The chamber was evacuated to a base pressure of $< 8 \times 10^{-8}$ torr prior to deposition, and the deposition rate was kept at ~ 0.6 nm/s. Plan-view transmission electron microscopy (TEM) samples were prepared by polishing, dimpling and low energy (3.5 keV) Ar ion milling.

In-situ Kr^{++} irradiation was conducted at room temperature in the Intermediate Voltage Electron Microscope (IVEM), at Argonne National Laboratory. The Kr^{++} beam had a high energy of 1 MeV, and the microscope was operated at 200 kV. During radiation, a CCD camera was utilized to capture the microstructural evolution at 15 frames/s. The displacement damage inside TEM foil was estimated using the SRIM (Stopping and Range of Ions in Matter) simulation with the Kinch-Pease method [205, 206].

The dose rate was controlled to be low in order to gain sufficient time for extracting more details on defect-TB interactions and the evolution of defect density during early stage (low dose) of radiation. The entire experiment consisted of two stages: stage 1 ranging from 0 to 0.025 dpa at a low dose rate $K_1 = 2.2 \times 10^{-4}$ dpa/s, and stage 2 over a dose of 0.025 - 0.1dpa at a higher dose rate $K_2 = 6.0 \times 10^{-4}$ dpa/s.

3.4 Results

Figure 3.1 displays the microstructure of as-deposited epitaxial nt Cu film before irradiation. To characterize nanovoids, most of the TEM images were recorded at the under-focus condition ($\Delta f \approx$ - 500 nm), when voids appear as predominantly white dots surrounded by dark Fresnel fringes. The plan-view TEM micrograph examined from Cu <111> zone axis in Figure 3.1 (a) shows abundant nanovoids positioned along columnar domain boundaries, and the inserted selected area diffraction (SAD) pattern confirms the formation of singe crystal Cu. The cross-sectional TEM micrograph examined from Cu <110> zone axis in Figure 3.1 (b) shows a high number density of growth twins with Σ3 {111} coherent twin boundaries (CTBs) and Σ3 {112} incoherent twin boundaries (ITBs). It is worth noting that most of the vertical ITBs are located around domain boundaries and are decorated with nanovoids marked by circles in Figure 3.1(b). Statistic studies

in Figure 3.1(c-e) show the average domain size D_{ave}, void size L_{ave} and twin thickness t_{ave}, are approximately 102, 7 and 7 nm, respectively.

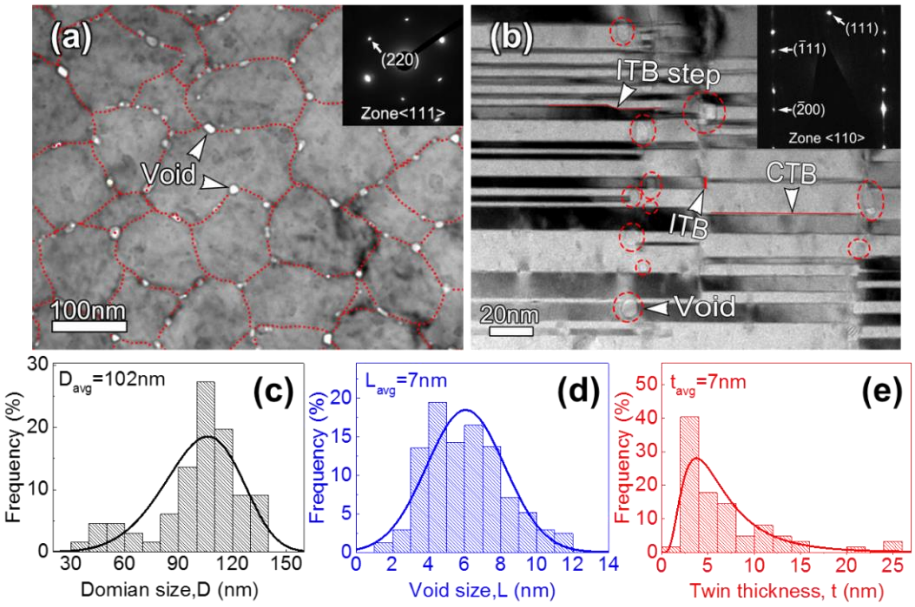

Figure 3.1. Microstructure of nv-nt Cu. (a) Plan-view TEM micrograph showing the epitaxial Cu film containing abundant nanovoids located along columnar domain boundaries (marked by red dotted lines). (b) Cross-sectional TEM micrograph showing the structures of growth twins and nanovoids (red circles). Both coherent twin boundary (CTB) and incoherent twin boundary (ITB) are labeled. (c-e) Histograms showing the statistics of average domain size D_{ave}, void size L_{ave} and twin thickness t_{ave}, measured from TEM.

A series of *in-situ* TEM snapshots in Figure 3.2 demonstrate the defect morphology evolution up to 0.1 dpa at low and high dose rate. These images were taken in a bright-field condition along Cu <111> zone axis to determine defect density. In order to investigate the influence of domain boundaries on defect accumulation and distribution, each domain is divided into three equal-area regions according to their distances to boundaries, Region I located between the red and blue lines is defined as the boundary region. Region II, the intermediate region, is delineated between the blue and green lines. In the center of each domain lies region III, the center region. The width of region I and II is ~9 and 21 nm, respectively. Qualitatively, the TEM micrographs show that a majority of the irradiation-induced defect clusters (black dots) were located near domain boundaries in boundary region II, especially in stage 1 of low dose radiation in Figure 3.2 (a-c).

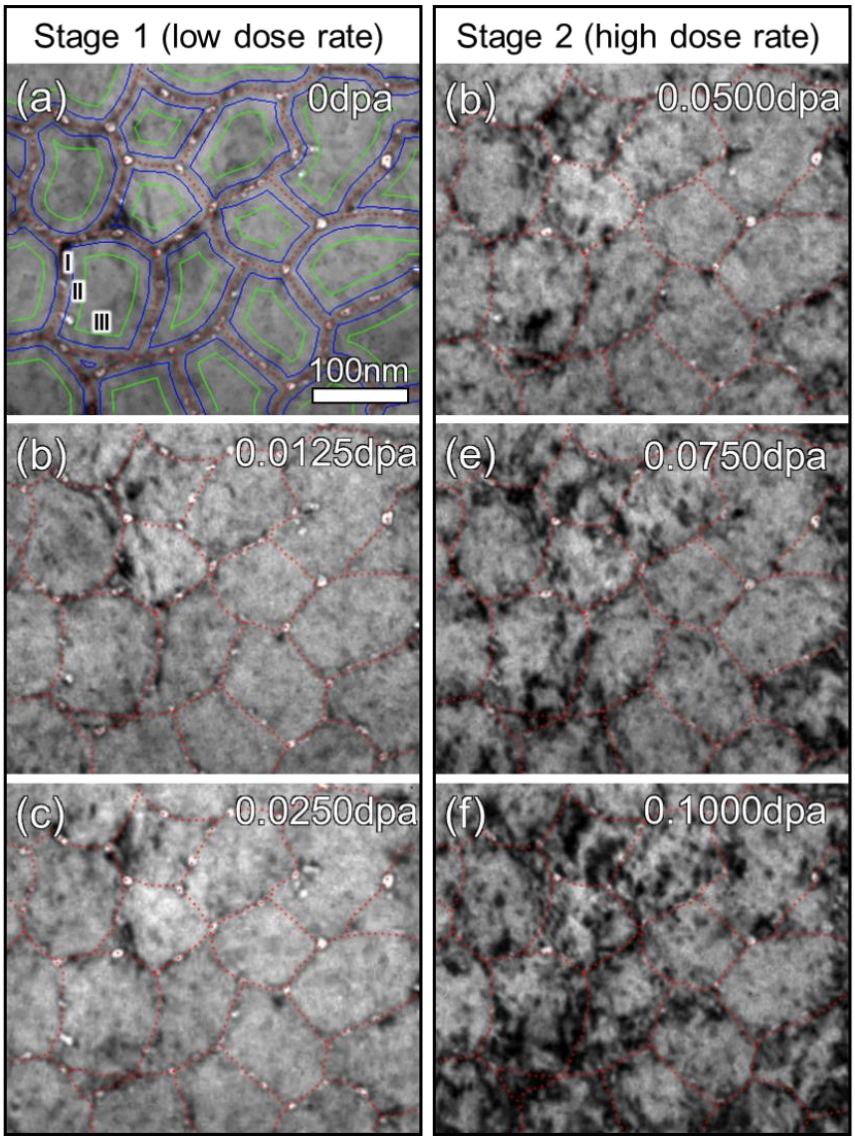

Figure 3.2. Bright-field TEM snapshots showing the accumulation and distribution of defect clusters during *in-situ* Kr^{++} ion irradiation of nv-nt Cu up to a dose of 0.1 dpa. Each doamin is divided into three equal-area regions, as marked in (a) by I, II and III that are bounded by red, blue and green lines, and the irradiation-indcued defects show preferential distribution in Region I. (a-c) The defect evolution in stage 1 of low dose rate from 0 to 0.025 dpa. (d- f) The defect evolution in stage 2 of high dose rate from 0.025 to 0.1 dpa.

The quantitative analysis of defect evolution in each region is shown in Figure 3.3. The defect density in all 3 regions accumulates nearly linearly with increasing dose, and the accumulation rate becomes greater in stage 2 of higher dose rate (Figure 3.3(a)). A linear superposition of defect density in all 3 regions is shown in Figure 3.3(b). Figure 3.3(c) shows the accumulative defect density is the highest in boundary region I, and the lowest in center region III. Figure 3.3(d) shows

the normalized fraction of defect density in each region over two radiation stages. As each region has identical area, a yellow dash line at 33% is shown to indicate the iso-fraction defects level. At stage 1, the density of defects reaches 50% in boundary region I, much greater than that in center region III, merely 20%. However, at stage 2 (a higher dose rate), such a large gap is considerably reduced and defects exhibit a tendency of more uniform distribution as indicated by arrows.

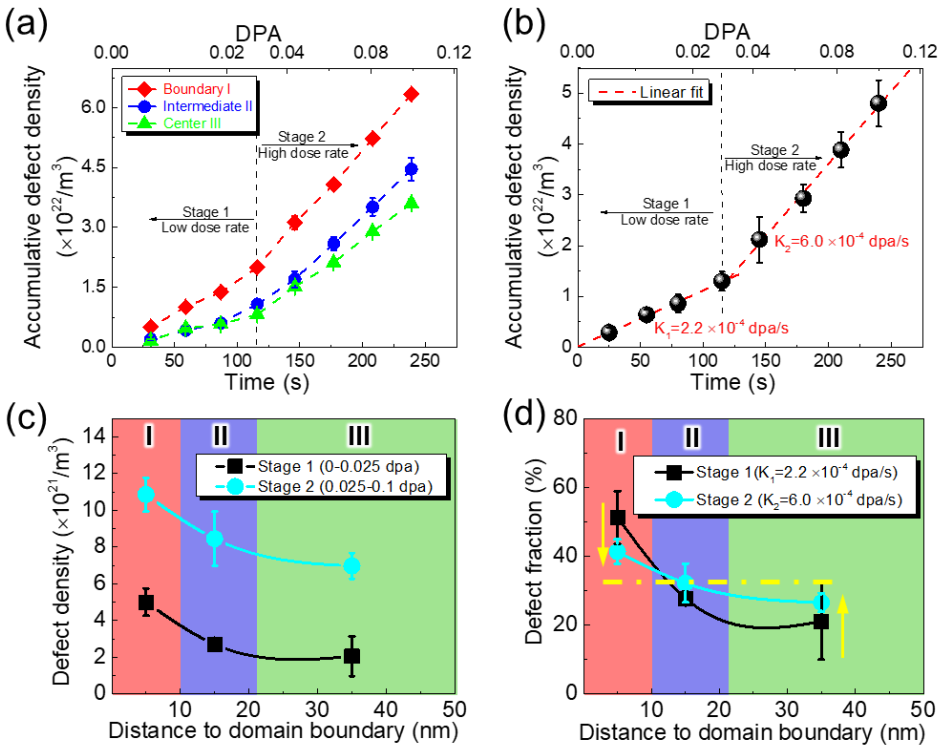

Figure 3.3. Statistics of defect cluster accumulation and distribution. (a) and (b) The defect accumulation with increasing time and dpa for individual regions and the entire area. (c-d) The defect density and fraction at different regions over two stages of low and high dose rate. I, II and III correpond to the boundary, intermediate and center region, respectively.

During irradiation interstitial and vacancy clusters are produced simultaneously in nv-nt Cu. Previous TEM observations indicate that in Cu with low stacking fault energy, a majority of the irradiation induced defects are SFTs, which can be identified by their well-defined triangular shapes in TEM studies[37, 39]. *In-situ* videos captured the morphology evolutions of several SFTs as shown in Figure 3.4. Before irradiation the grain G1 in Figure 3.4(a) was basically free from defects. By 198s (0.075 dpa) in Figure3.4(b), a large number of defect clusters were generated, and two SFTs (SFT1 and SFT2) emerged in the center of G1. At 204s in Figure 3.4(c), the SFT1

reduced its footprint and another SFT, SFT3, was generated adjacent to the slightly enlarged SFT2. During further irradiation at 208 s, SFT1 was eliminated (Figure 3.4(d)). At 213s in Figure 3.4(e), the two SFTs changed their shapes, and SFT2 appeared to be truncated. A few sec later at 217s (0.086 dpa), both SFT2 and SFT3 collapsed into smaller defect clusters (Figure3.4(f)). In comparison to the long-lived SFTs, interstitial loops usually have a shorter life-span[110], and two small circular loops L1 and L2 marked in Figure 3.4(e) were eliminated in merely several sec.

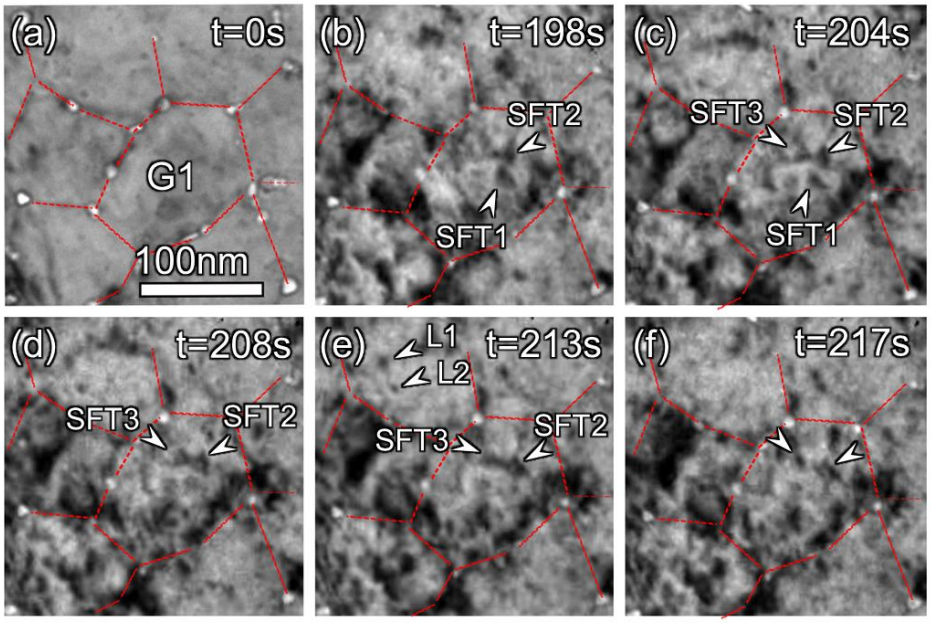

Figure 3.4. *In-situ* TEM observation of morphology evolution of SFTs. (a) Before irradiation, grain G1 contains few defects. (b)-(f) Three triangular defects of SFT1-SFT3 were induced and finally removed in the center of G1. In contrast, two circular interstitial loops of L1 and L2 were generated in (e) and quickly removed after 4 seconds in (f).

Meanwhile, a majority of nanovoids at domain boundaries contracted continuously during irradiation. Typical void shrinkage events captured by *in-situ* TEM experiments are shown in Figure 3.5. At 0 dpa, three representative voids (V1-V3 in red circles) with comparably large diameters of 12.4, 10.8 and 7.6 nm and two relatively small voids (indicated by white arrows) were tracked. After irradiation over 250 s to 0.1 dpa, the dimension of three large voids labeled in circles decreased to 9.4, 9.8 and 5.2 nm respectively, while the two smaller voids (by arrows) almost disappeared. Figure 3.5(e) shows the variation of void size (L) with increasing time and dose for ten nanovoids of various dimensions, with initial diameter ranging from 5 to 12 nm. The void size

decreased slightly during radiation at low dose rate (stage 1), and the void shrinkage rate increased at stage 2 at higher dose rate. The correlation of this phenomenon with the interstitial diffusion and absorption will be discussed later.

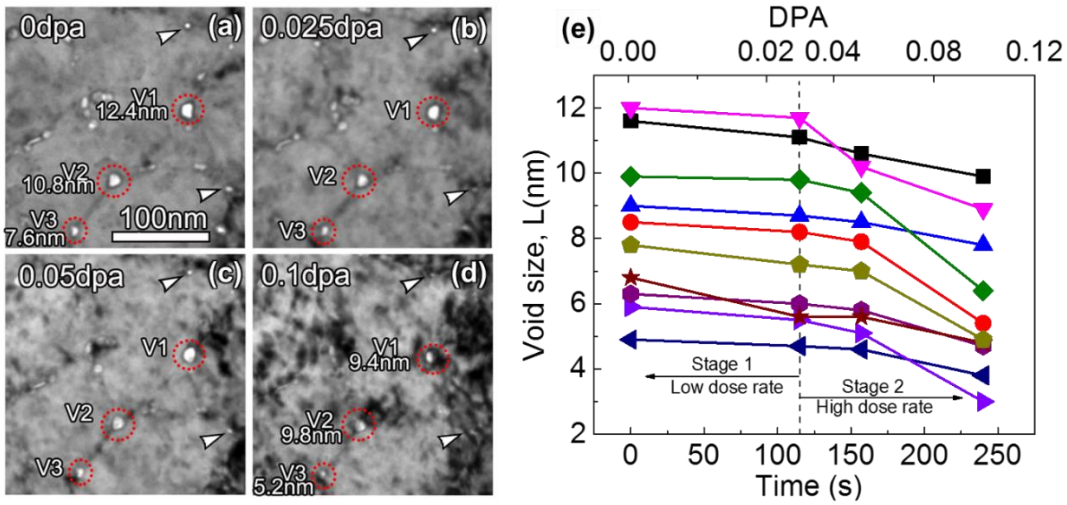

Figure 3.5. Continuous void shrinkage at domain boundaries during *in situ* Kr^{++} ion irradiation. (a-d) Sequential TEM snapshots revealing the typical void shrinkage phenomenon. (e) Compiled chart showing the reduction of void size with increasing dose.

3.5 Discussion

3.5.1 Defect Formation, Diffusion and Distribution in nv-nt Cu

Under heavy ion irradiation, vacancy-interstitial (Frankel) pairs are created by the well-known collision cascade. Compared with vacancies, interstitials have lower migration energy, ~ 0.1eV for Cu at room temperature [172], and once produced they can diffuse rapidly in all directions until they are absorbed by defect sinks [183]. In general, defect sinks, such as high-angle grain boundaries –can efficiently absorb and eliminate irradiation-induced defect clusters, and thus experimentally there are increasing evidences that show defect density (such as void, dislocation loop or He bubble density) is low near grain boundaries [189], and the concept of defect denuded zone has been well adopted [98, 189]. In this sense, the current study is surprising and counterintuitive as it shows clearly the enrichment of dislocation loops near domain boundaries.

To interpret such a phenomenon, several aspects shall be taken into consideration. First, the current study focuses on very low dose of radiation, that is defect density has not been saturated throughout the entire grains. Prior studies on defect denuded zone near GBs primarily deal with heavily

irradiated specimens, wherein defect density has already reached saturation [189]. Second, the nv-nt Cu in this study contains a high number density of TB networks, including CTBs at domain interior and ITBs at domain boundary. On the one hand, it has been reported that the CTBs in Cu can act as fast-diffusion channels [207], through which interstitials migrate rapidly and subsequently be annihilated at defect sinks [169]. On the other hand, the ITBs in Cu can be described as a group of 1/6<112> partial dislocations on three successive $\{111\}$ planes [116, 120]. ITBs are effective sinks for interstitials and vacancies, and MD simulation studies have revealed that the formation energy for an interstitial in ITBs is smaller (~1.3 eV) than that in crystal lattice (~ 3.1 eV) [37, 169], indicating ITBs can provide heterogeneous nucleation sites for self-interstitial atoms. Hence the interstitials produced inside a domain are more likely to be eventually captured by ITBs at domain boundaries. Third, the ITBs are decorated by a large number of nanovoids, which can eliminate a significant amount of interstitials. However, it may take time for interstitials to migrate along ITBs and be eventually captured by the nanovoids.

Based on the current studies, a hypothetical mechanism for defect formation and distribution in nv-nt Cu is schematically illustrated in Figure 3.6. Initially, when a defect cluster is created in domain interior in nv-nt Cu, it inevitably introduces internal stress that deforms the local segment of CTBs, forming curved TBs consisting of ITB steps [202]. The ITB steps may promote defect absorption and migration. Eventually, the radiation-induced defects are transported to nanovoids through TB networks. Such a defect removal process includes two major steps: step 1 is the rapid diffusion of interstitials from domain center to boundary along CTBs, and step 2 is the transportation of interstitials along ITB walls into nanovoids with a net flux of $\boldsymbol{J}_i$, as schematically shown in Figure 3.6(a). Another possible mechanism for the accumulation of such loops at TBs could be due to the migration of these loops. It has been shown that nanometer-sized loops exhibit 1D migration capability [49, 50, 208]. Perfect loops with Burgers vector of ½ <110> may glide along the close packed <110> direction on $\{111\}$ planes (parallel to CTBs) [50, 208]. Consequently, these mobile defect loops may migrate toward and accumulate by domain boundaries (ITBs).

Now we discuss the influence of dose rate on defect distribution from the viewpoint of kinetics. The local change in interstitial concentration $\partial C_i / \partial t$ can be written as its net production rate $\dot{\rho}$, and the diffusion rate into or out of the local volume arising from its flux gradient $\nabla \bullet \boldsymbol{J}$, which can be mathematically described as:

$$\frac{\partial C_i}{\partial t} = \dot{\rho} + \nabla \bullet \boldsymbol{J} \qquad \text{Equation 3.1}$$

In the early stage of radiation, the net defect production rate is dominated by collision cascade and assumed to be uniform throughout domains. However, due to a directed net flow of interstitials from center to boundary (driven by the existence of ITBs and nanovoids as defect sinks) as shown in step 1 in Figure 3.6(a), the diffusion term in domain center, $\nabla \bullet \boldsymbol{J}_{\mathrm{III}}$, is greater than that in boundary region, $\nabla \bullet \boldsymbol{J}_{\mathrm{I}}$. In other words, defects are rapidly transported away from center region (via CTBs), leaving behind less defect clusters. Whereas the defect clusters lined up along ITBs, waiting to be transported by ITBs to nanovoids. It is worth mentioning that although nanovoids are effective interstitial sinks, interstitial clusters landed at ITBs need to go through a diffusion process to locate the nanovoids before being eliminated (as nanovoids are distributed in a scattered way along ITBs). Given the existence of defect absorption time, interstitial clusters may accumulate along the ITBs (boundary region), as shown schematically in Figure 3.6(b). At higher dose rate in stage 2, the defect production rate $\dot{\rho}_2$ is higher, and only a portion of the radiation-induced defects can be instantly transported away from the center, so defect clusters begin to accumulate in both center and boundary and tend to distribute more uniformly. This hypothesis is consistent with our TEM observations as shown in Figure 3.2, and it is further confirmed by the continuous shrinkage of nanovoids in domain boundary (see Figure 3.5) and the emergence of SFTs in domain center (see Figure 3.4).

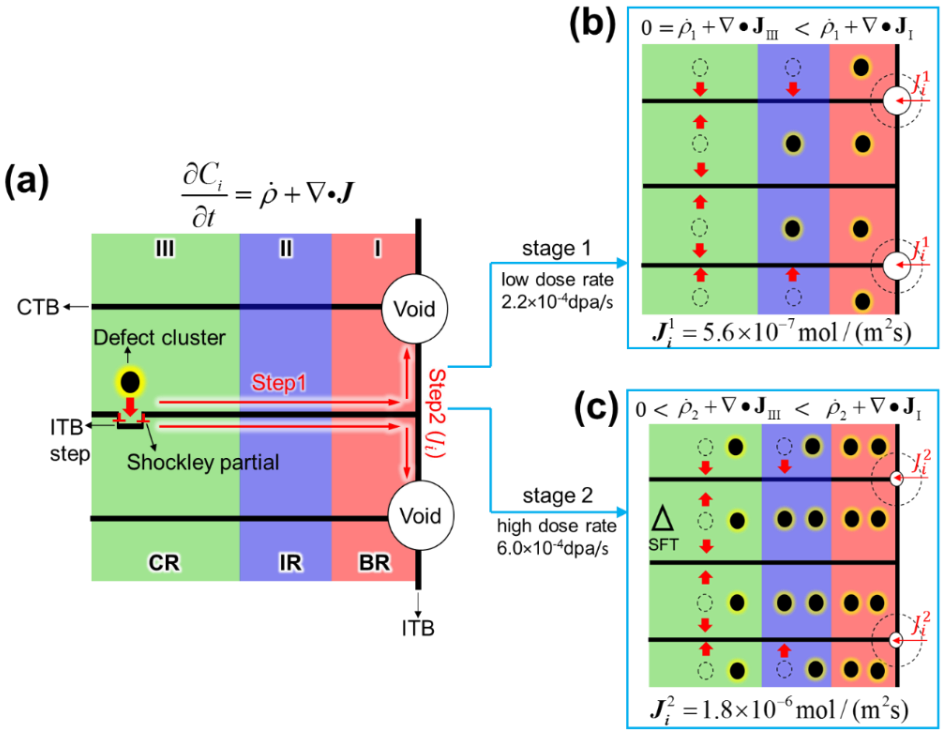

Figure 3.6. Schematic illustration of defects formation and distribution in nv-nt Cu. (a) The microstructure of nv-nt Cu with CTBs and ITBs, as well as nanovoids. Irradiation-induced interstitials are absorbed and removed effectively through two steps: step 1, rapid diffusion along CTB, and step 2, transportation into nanovoids via diffusion in ITBs with a net flux $\boldsymbol{J}_i$, measured as $\boldsymbol{J}_i^1 = 5.6\times10^{-7}$ mol/(m^{2}s) for stage 1, and $\boldsymbol{J}_i^2 = 1.8\times10^{-6}$ mol/(m^{2}s) for stage 2. The interstitial accumulation rate $\partial C_i / \partial t$ is the summation of its net production rate $\dot{\rho}$ and diffusion flux gradient $\nabla \bullet \boldsymbol{J}$. (b) The defect distribution in stage 1 at low dose rate, where the interstitial accumulation rate $\dot{\rho}_1 + \nabla \bullet \boldsymbol{J}$ is almost zero at domain interior. Eventually, most of the self-interstitial atoms are accumulated in domain boundary (labeled as I). (c) The defect distribution at stage 2 of high dose rate, where the interstitial accumulation rate $\dot{\rho}_2 + \nabla \bullet \boldsymbol{J}$ is greater than zero in domain boundary and center (labeled as III) with a more uniform distribution of defects. Meanwhile, a large number of vacancies are left behind in the center and may agglomerate into SFTs.

3.5.2 Shrinkage of Nanovoids Near Domain Boundaries

The nanovoids in boundary regions shrink gradually with increasing dose (see Figure 3.5) through continuous absorption of interstitials. Assume the net radial flux of interstitials towards all nanovoids is a constant, $\boldsymbol{J}_i$ (see Figure 3.6) and its value can be estimated as:

$$J_i = \frac{1}{V_m}\frac{dL}{dt}$$ Equation 3.2

where V_m is molar volume, and the void shrinkage rate dL/dt can be obtained from statistics in Figure 3.5. For stage 1 at low dose rate, $dL/dt = 4\times10^{-3}$ nm/s and we arrive that $J_i^1 = 5.6\times10^{-7}$ mol/(m^{2}s); similarly, for stage 2 at higher dose rate, $dL/dt = 1.3\times10^{-2}$ nm/s and thus $J_i^2 = 1.8\times10^{-6}$ mol/(m^{2}s). The fact that J_2 is ~ 3 times larger than J_1 indicates that nanovoids are efficient in absorbing extra defects generated in the matrix at higher dose rate. Considering the dose rate increased by ~3 times in stage 2, it can be concluded that the sink efficiency in nv-nt Cu remains unchanged and is nearly independent of dose rate. Previous studies show that with increasing dose, the defect density reaches saturation [178]. For coarse-grained Cu, its irradiation-induced defect density reaches a saturation of ~5×10^{23} m^{-3} at a low dose of ~0.01 dpa [84, 209]. For nv-nt Cu in current study, the defect density is ~5×10^{22} m^{-3} at 0.1 dpa (see Figure 3.3(b)), much smaller than that of coarse-grained counterpart, indicating a much better resistance to irradiation of nanotwinned and nanovoid materials.

3.6 Conclusions

In-situ Kr ion irradiation studies at both low and high dose rate on nv-nt Cu were performed to investigate the evolution of defect clusters. The major findings include the followings: (1) Initially at a lower dose rate, defect clusters were distributed preferentially near domain boundaries. However, at a higher dose rate, the defect clusters tended to be distributed more uniformly. (2) Nanovoids at domain boundaries shrank continuously during the radiation process, which was caused by interstitials diffusion and transportation along CTB-ITB networks. The interstitial fluxes to nanovoids are estimated as 5.6×10^{-7}mol/(m^{2}s) and 1.8×10^{-6}mol/(m^{2}s) at low and high dose rate, respectively. These findings provide in-depth understanding for the impact of nanovoid-nanotwin network on the alleviation of radiation damage in nanotwinned metals.

CHAPTER 4. HELIUM IRRADIATION INDUCED ULTRA-HIGH STRENGTH NANOTWINNED CU WITH NANOVOIDS

The radiation experiment was performed at Los Alamos National Laboratory by Dr. Di Chen with guidance of Dr. Yongqiang Wang. The mechanical testing was performed by Cuncai Fan at Purdue University, with great help from Qiang Li, Jie Ding, Zhongxia Shang, Jin Li, Ruizhe Su, Jaehun Cho. The molecular dynamic simulation was performed by Yanxiang Liang with guidance by Dr. Jian Wang at University of Nebraska-Lincoln. The data analysis and writing were completed by Cuncai Fan with guidance and editing by Dr. Xinghang Zhang.

4.1 Overview

There are increasing studies that show nanotwinned (NT) metals have enhanced radiation tolerance. However, the mechanical deformability of irradiated NT metals is a largely under explored subject. Here we investigate the mechanical properties of He ion irradiated NT-Cu with preexisting nanovoids. In comparison with coarse-grained Cu, nanovoid nanotwinned (NV-NT) Cu exhibits prominently improved radiation tolerance. Furthermore, *in-situ* micropillar compression tests show that the irradiated NV-NT Cu has an ultrahigh yield strength of ~ 1.6 GPa with significant plasticity. Post radiation analyses show that twin boundaries are decorated with He bubbles and thick stacking faults. These stacking fault modified twin boundaries introduce significant strengthening in NT-Cu. This study provides further insight into the design of high-strength, advanced radiation tolerant nanostructured materials for nuclear reactor applications.

4.2 Introduction

Nuclear energy holds the promise as a reliable and economic next-generation source of electricity [2, 4]. New concepts of advanced fusion and fission nuclear reactors require structural materials to perform stably in extremely aggressive radiation environment (high dose and high temperature)

[5, 9, 10]. Severe radiation damage often occurs in the core of nuclear power reactors where structural components are subjected to intense fluxes of energetic neutrons [6], resulting in a wide variety of defect clusters [36, 210], such as dislocation loops [38, 46, 196], stacking fault tetrahedrons (SFTs) [39, 211], and cavities (voids or bubbles) [40, 212, 213]. These defects typically cause significant degradation of mechanical properties for irradiated materials [71], including radiation induced hardening, fracture and embrittlement [149, 151, 152, 214, 215]. Design and manufacture of advanced materials that can resist damage at irradiation and mechanical extremes are grand challenges in nuclear energy industry [5, 6, 8, 216].

As a classical model system, Cu has been the subject of numerous studies on both radiation damage effects [46, 60, 87, 159-161] and materials mechanical properties [105, 134]. The typical method to improve its mechanical and physical properties is through grain refinement [99]. For instance, nanocrystalline (NC) metals have significantly improved mechanical strength [100, 125] and radiation tolerance [86, 93] compared with their coarse-grained (CG) counterparts. However, NC metals tend to become brittle with decreasing grain sizes [100, 125]. In addition, NC metals often have poor thermal stability, and radiation-induced grain-coarsening occurs even at room temperature [27]. An alternative approach to tune the mechanical properties of Cu is to utilize twin boundaries (TBs) [99, 101]. It has been found that nanotwinned (NT) Cu exhibits ultrahigh strength and yet considerable ductility [105], as TBs are effective barriers for the transmission of dislocations [127]. Also NT-Cu shows better thermal stability than NC-Cu, and the annealed NT-Cu still retains high hardness [102]. On the other hand, NT-Cu proves to be more radiation tolerant than CG-Cu in terms of lower defect density [110], because TBs can effectively absorb, transport and finally eliminate a large number of radiation-induced defects [109, 140, 142, 217]. The radiation tolerance of NT-Cu can be enhanced further by introducing nanovoids (NVs) that act as ‘storage bins’ for interstitial defects [169, 218]. Though several studies have recently been reported on the microstructural characterizations of irradiated NT-Cu [110, 169, 197, 219, 220], its mechanical response to irradiation remains less well understood.

Heavy ion irradiation technique has been widely used as a surrogate to emulate neutron radiation damage effects on mechanical properties [11, 137, 145]. Nevertheless, the ion-beam-irradiated region is generally shallow on the surface with a penetration depth at micron scale [148, 221]. To investigate mechanical properties of ion irradiated materials, small-scale mechanical testing techniques, such as nanoindentation [149], micro bending [150], tension [151] and compression

[152], have been increasingly applied to nuclear materials [148, 222-225]. In this study, we conduct *in-situ* micropillar compression test inside a scanning electron microscope (SEM) to investigate the mechanical properties of He ion irradiated NV-NT and CG-Cu. The results show that radiation induces less He bubbles in NV-NT Cu, and the irradiated NV-NT Cu has ultrahigh strength and remains significant plasticity.

4.3 Experimental

4.3.1 Materials and Helium irradiations

High purity (99.995%) Cu films, ~ 2.6 μm thick, were deposited on HF-etched Si (110) substrates at room temperature using direct current magnetron sputtering technique. Before deposition, the chamber was evacuated to a base pressure < 8×10^{-8} torr. During deposition, ~ 1.2×10^{-3} torr Ar working pressure was used, and the deposition rate was controlled at ~ 0.6 nm/s.

The as-deposited Cu films were subsequently irradiated at room temperature with Helium ions at the Ion Beam Materials Lab, Los Alamos National Laboratory, USA. To produce a uniform irradiated region, three sets of He ion beams (with various energies of 50, 100 and 200 keV) were sequentially implanted into specimens. The corresponding ion doses are ~ 1×10^{16}, ~ 2×10^{16} and ~ 4×10^{16} ions/cm^2, respectively. Figure 4.1(a) and (b) show the profiles of radiation damage and He concentration along penetration depth (h), calculated using SRIM software with the Kinchin-Pease model [205]. The resultant radiation damage is 0.9 displacements-per-atom (dpa) on average, and almost uniformly distributed across a penetration depth of 200 - 630 nm. The average He concentration is 1.0 at. %, with a peak value of around 1.8 at. % when h = 700 nm. For comparison purposes, bulk CG-Cu, annealed at 800 ºC for 4 hours, was polished and irradiated under the same conditions.

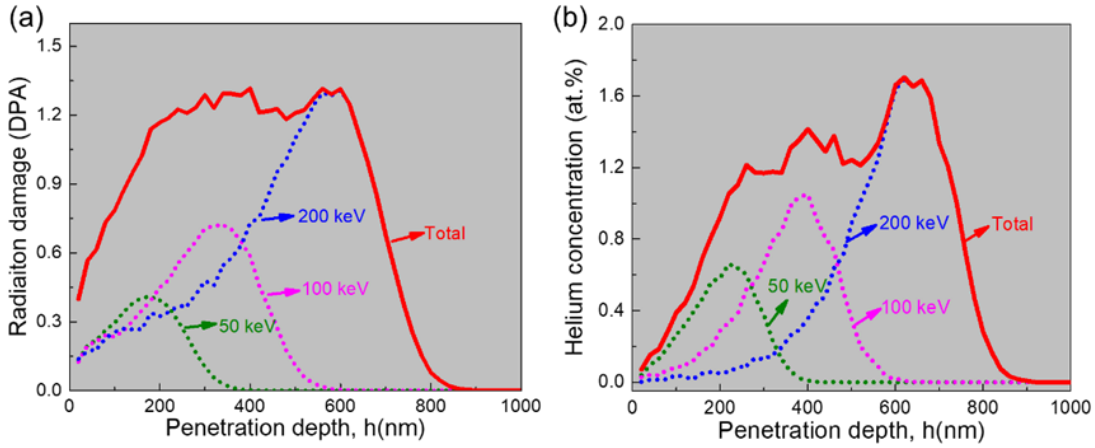

Figure 4.1. SRIM calculations of (a) radiation damage (dpa) and (b) He concentration (at. %), plotted as a function of penetration depth h.

4.3.2 Micropillar Compression

Micropillars were fabricated using the FIB technique , with a height of ~ 2.6 μm and a diameter of ~ 1.2 μm, following a generally preferred aspect ratio (height-to-diameter ration between 2:1 and 3:1) suggested for micro-compression experiment [226]. The test was conducted on a Hysitron PI 88 × R PicoIndenter inside a FEI Quanta 3D FEG SEM. During each compression process, two partial unloading segments were applied while maintaining a constant strain rate of $1\times 10^{-3}\,s^{-1}$, and the maximum displacement was 410 nm. To confirm the repeatability, at least three micropillars were compressed for each sample.

4.3.3 Microstructure Characterization

The texture of as-deposited NV-NT Cu film was analyzed using an X-ray diffraction technique on a Panalytical Empyrean X'pert PRO MRD diffractometer with a Cu $K\alpha_1$ source. Plan-view (PV) and cross-sectional (CS) transmission electron microscopy (TEM) specimens were prepared by mechanical grinding and dimpling, followed by low-energy Ar ion milling. The annealed CG-Cu was characterized by an optical microscope before irradiation. For the irradiated samples before and after compression tests, CS TEM specimens were prepared by FIB technique. All the TEM samples were examined on a FEI Talos 200X TEM microscope operated at 200 kV.

4.4 Results

4.4.1 Radiation-induced Evolution of Microstructures

Figure 4.2 displays the texture analysis of the as-deposited Cu films for He irradiations. Figure 4.2(a) is the θ-2θ XRD spectrum for the epitaxial Cu (111) film on the Si (110) substrate. The φ-scan in Figure 4.2(b) shows diffraction peaks from twin and matrix with nearly identical intensity, indicating the formation of high-density growth twins in the film. Figure 4.2(c) schematically illustrates the film – substrate orientation relationships: Cu (111) // Si (110) and Cu $[01\bar{1}]$ // Si $[1\bar{1}0]$ (matrix).

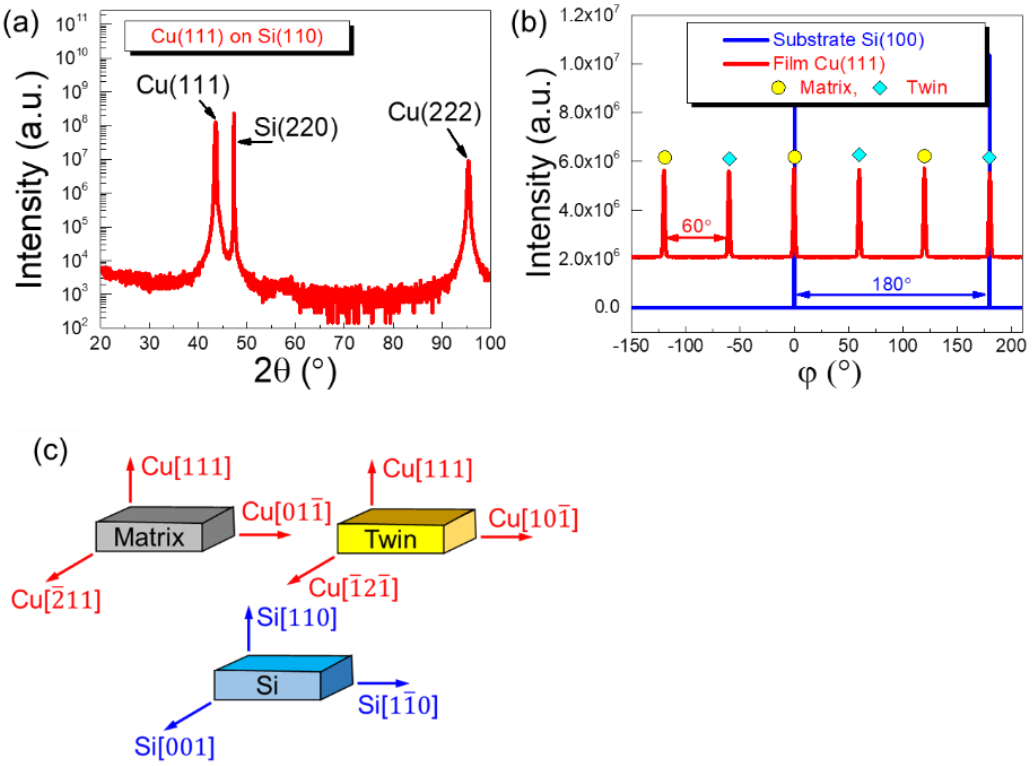

Figure 4.2. Texture analysis of as-deposited NV-NT Cu. (a) and (b) XRD spectra of sputtered films showing the epitaxial growth of NT Cu (111) on Si (110). (c) Schematic illustration of film-substrate orientation relationship.

Figure 4.3 displays the microstructural characterization of the materials for He irradiations. The PV TEM micrograph in Figure 4.3(a) shows polygonal domains formed in as-deposited Cu film, and the inserted selected area diffraction (SAD) pattern confirms the formation of highly-textured Cu (111). The enlarged view in Figure 4.3(b) shows abundant nanovoids (NVs) primarily located

at domain boundaries. The CS TEM micrograph examined from Cu <110> zone axis in Figure 4.3(c) shows columnar domains along growth direction, and the inserted SAD pattern confirms the formation of growth twins. The enlarged view in Figure 4.3(d) reveals high-density growth twins in columnar domains and the NVs (denoted by arrows) at domain boundaries. Statistic studies in Figure 4.3(e-g) show the average domain size D_{NT}, void size d_V and twin spacing t, are approximately 115, 6 and 8 nm, respectively. The void number density N_V is also measured as 4.0 ± 0.5 $10^{21}/m^3$. In contrast, the CG Cu sample contains large grains, ~ 43 μm in size, as shown in Figure 4.3(h) and (i).

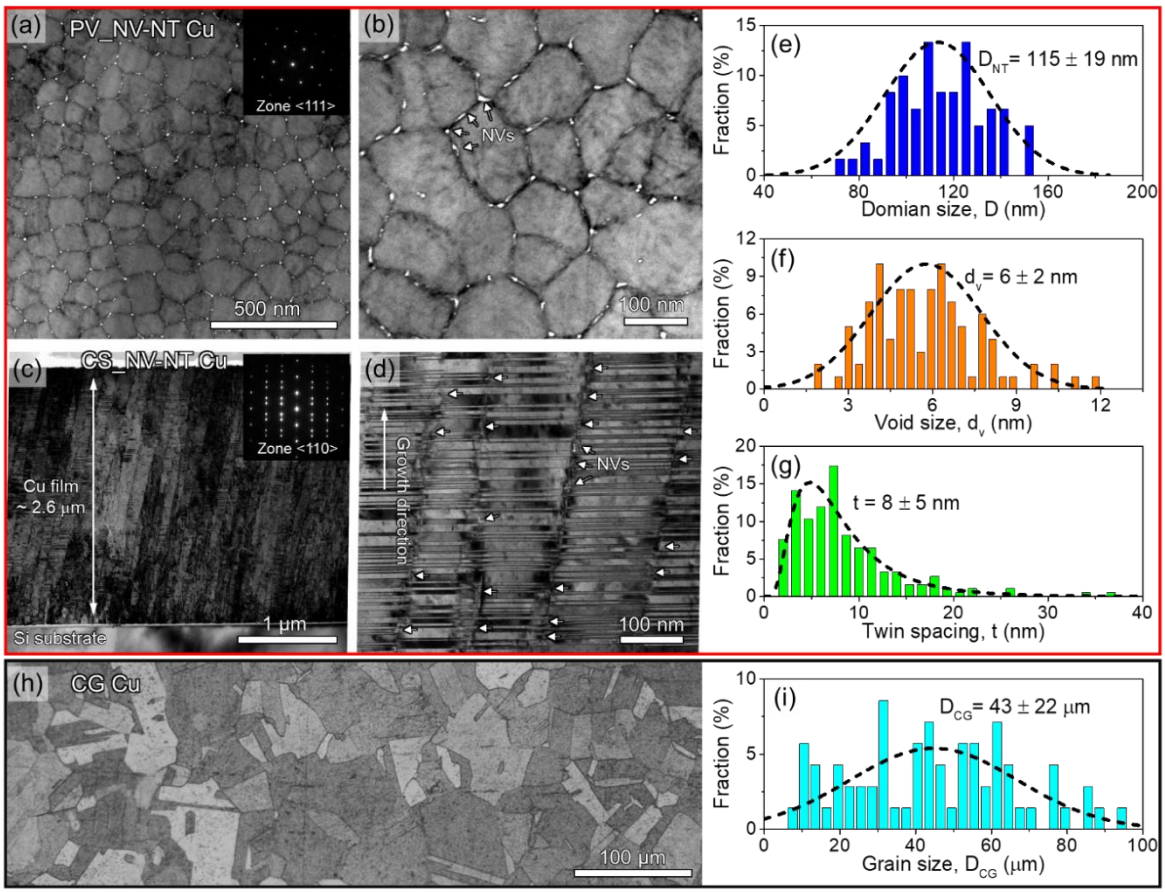

Figure 4.3. Microstructure of as-deposited NV-NT Cu and annealed CG Cu before Helium irradiations. (a) and (b) Plan-view (PV) TEM images showing the (111) textured Cu film containing polygonal domains and abundant nanovoids (NVs) at boundaries. (c) and (d) Cross-sectional (CS) TEM images showing high-density growth twins in columnar domains. Nanovoids are marked by arrows. (e-g) Statistic studies of domain size (N_V), void size (d_V) and twin spacing (t) in NV-NT Cu. (h) Micrograph of coarse-grained (CG) Cu. (i) The grain size (D_{CG}) distribution of CG Cu.

Figure 4.4 shows the microstructure of irradiated NV-NT Cu. The PV TEM images in Figure 4.4(a)-(c) reveal the remaining NVs, radiation-induced defect clusters, and He bubbles. Figure 4.4(d) is the panoramic cross-sectional view of irradiated NV-NT Cu, superimposed with solid curve showing the calculated damage profile. The enlarged view of irradiated region in Figure 4.4(e), taken along <110> zone axis, shows the retention of high-density nanotwins. The magnified views at different penetration depths in Figure 4.4(f-i) reveal high-density He bubbles when h = 400 and 600 nm, but lower-density bubbles when h = 200 and 800 nm. In comparison, Figure 4.5 shows the microstructure of He-irradiated CG Cu. The overview of a CS TEM micrograph in Figure 4.5(a) shows the radiation-induced dislocation loops, and the magnified views in Figure 4.5(b)-(e) show the He bubbles at various penetration depths. Note that there are more radiation-induced bubbles in CG Cu than in NV-NT Cu at the same penetration depth.

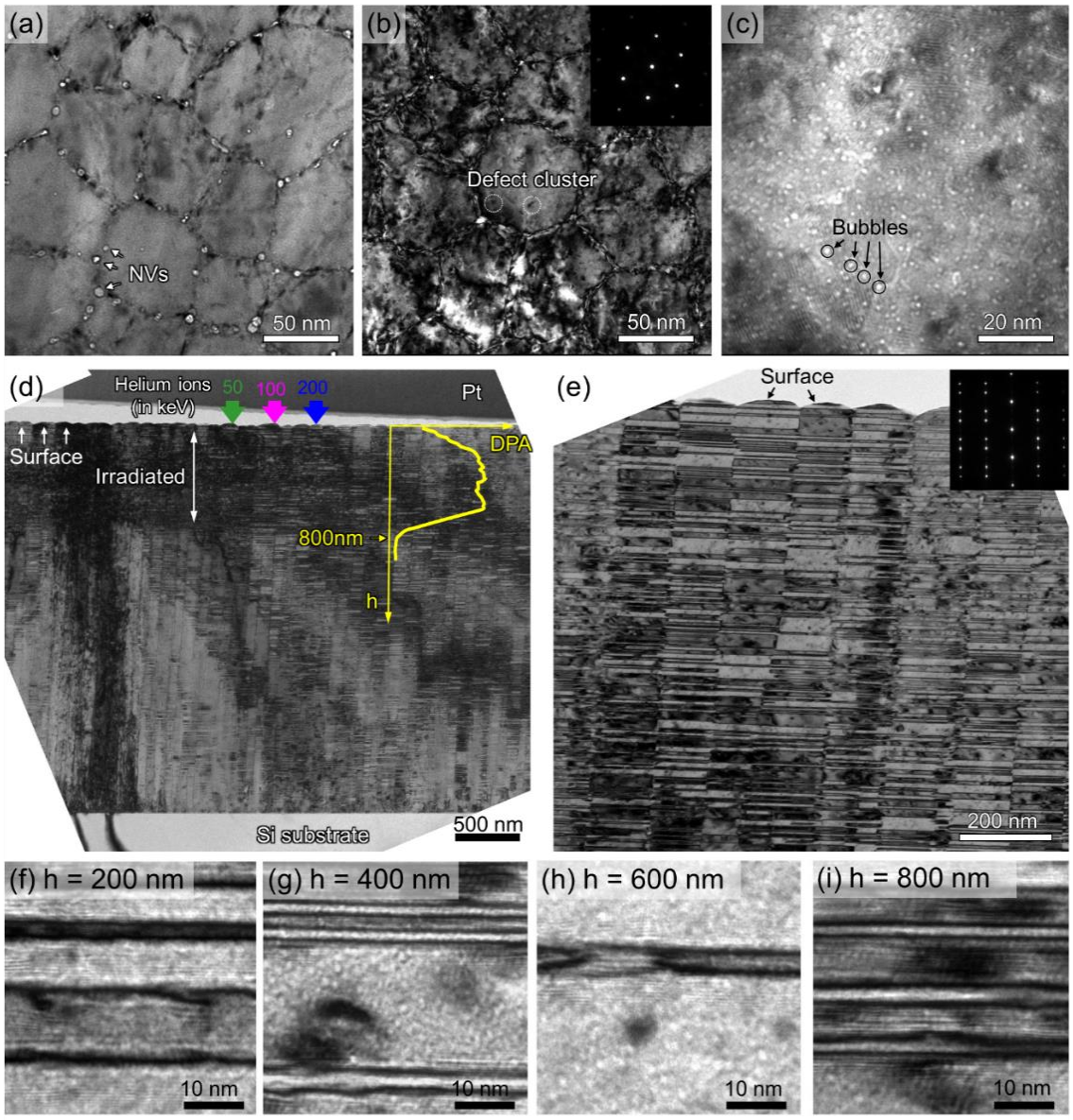

Figure 4.4. Microstructure of He ion irradiated NV-NT Cu. (a)-(c) Plan-view TEM images showing surviving NVs at domain boundaries and radiation-induced defect clusters, as well as He bubbles. (d) Cross-sectional overview of the irradiated specimen superimposed with the depth-dependent DPA profile. (e) Enlarged view of the irradiated region close to film surface showing defect clusters. (f)-(i) Radiation-induced He bubbles at various radiation depths.

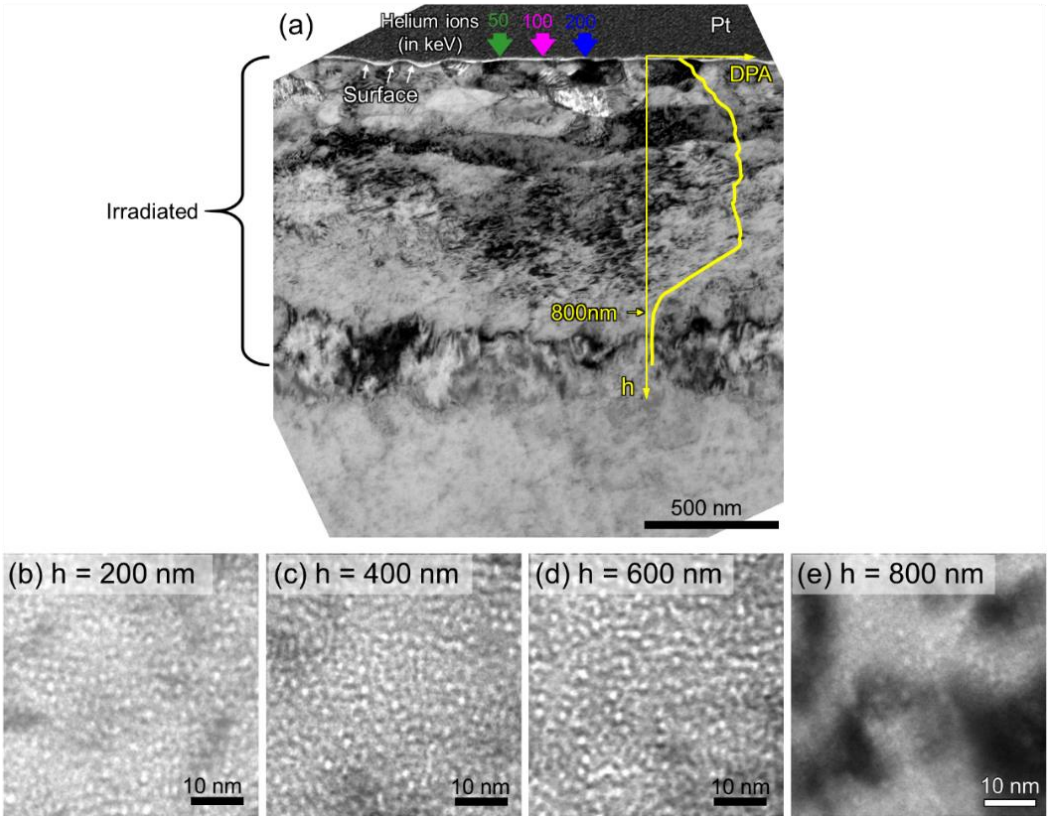

Figure 4.5. Microstructure of He ion irradiated CG Cu. (a) Cross-sectional TEM image showing the overview of irradiated Cu, superimposed with the depth-dependent DPA profile. (b)-(e) TEM micrographs displaying radiation-induced He bubbles at various depths.

4.4.2 Mechanical properties of He ion irradiated NV-NT Cu

Figure 4.6 compares the deformation behaviors for NV-NT and CG Cu micropillars under uniaxial compression. The load-displacement curves for all the compressed micropillars are compiled in Figure 4.6(a). The as-received CG Cu was soft and the load-displacement curves have long plateaus, and numerous inclined discrete slip bands formed on the surface after deformation, as shown in Figure 4.6(b1-b5). After He ion irradiation, the load increased moderately with displacement. Interestingly, the irradiated CG pillars first experienced barreling deformation near the base part where the material was little irradiated, while the heavily irradiated region on the top portion remained nearly undeformed, as shown in Figure 4.6(c1-c5). In comparison, the pillars of as-deposited and irradiated NV-NT Cu were much harder, and they both experienced substantial plastic deformations primarily at the pillar tops, as shown in Figure 4.6(d1-d5) and Figure 4.6(e1-e5).

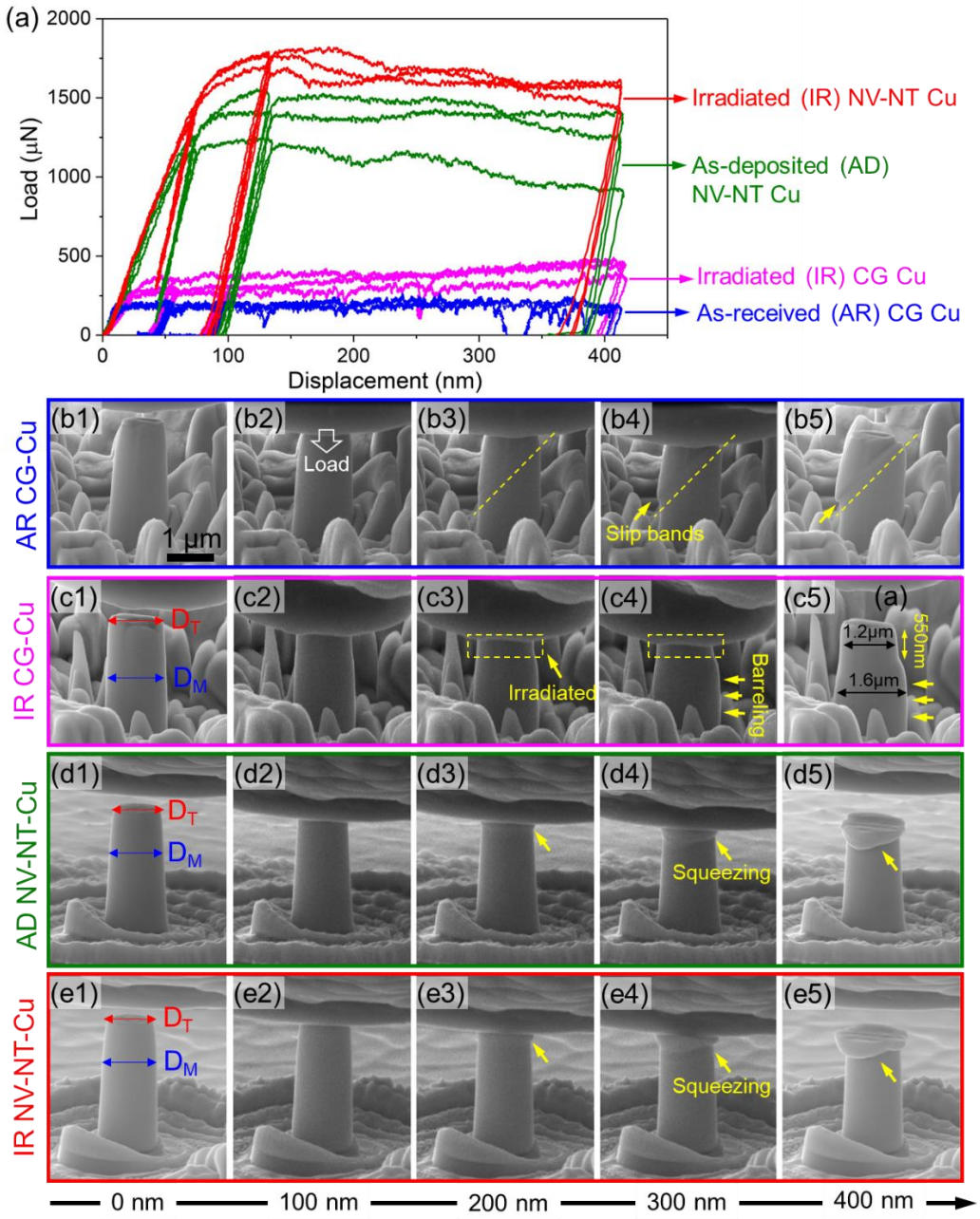

Figure 4.6. *In-situ* micropillar compression studies on CG Cu and NV-NT Cu before and after He ion irradiations. (a) Compilation of load-displacement curves of various specimens under compression. (b1-e5) SEM snapshots of pillars compressed to various strain; (b1-b5) Formation of typical slip bands in as-received (AR) CG Cu; (c1-c5) Micrographs showing base barreling and deformation at unirradiated region in irradiated (IR) CG Cu. (d1-d5) and (e1-e5) Severe squeezing and extrusion on pillar top for as-deposited (AD) and irradiated (IR) NV-NT Cu, respectively. D_T and D_M in (c1), (d1) and (e1) mark the diameters of pillar top and middle, used for compressive stress measurement.

It should be noted that the pillars were deformed nonuniformly, so the compressive stress-strain curves cannot be directly calculated using the typical methodology reported in previous studies [227]. To address the issue and to measure the local stress more accurately, the true compressive stress is calculated by dividing the load by corresponding instantaneous cross-sectional area directly obtained from the sequential snapshots of *in-situ* SEM videos. Details on the true stress measurement are shown in Figure 4.7 and 4.8.

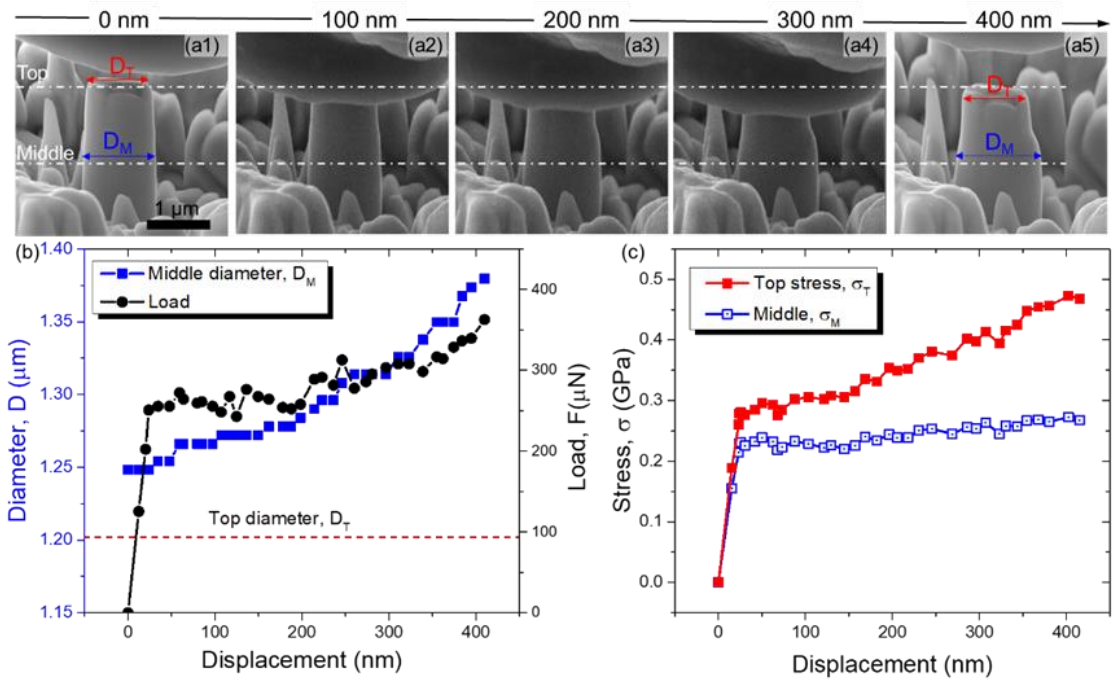

Figure 4.7. Compressive stress measurement for irradiated CG. (a1-a5) Typical SEM snapshots for compressed CG pillar 1. (b) Variations of load (black circles) and middle dimeter D_M (blue squares). The red dashed line denotes the top diameter D_T that barely changes during compression. (c) Variations of stresses for pillar top (solid red squares) and middle (open blue squares), calculated by dividing the instantaneous load by instantaneous cross-sectional area.

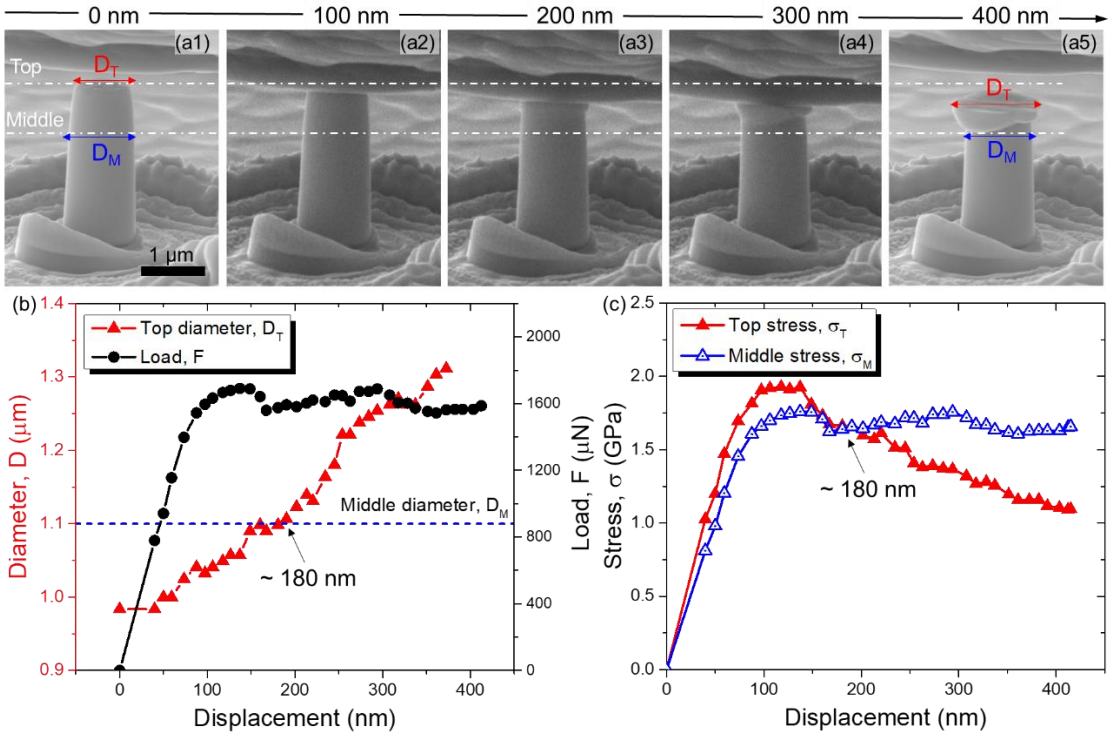

Figure 4.8. Compressive stress measurement for irradiated (or as-deposited) NV-NT Cu. (a1-a5) Typical SEM snapshots for compressed irradiated NV-NT Cu pillar 1. (b) Variations of load (black circles) and top dimeter D_T (red triangles). The blue dashed line denotes the middle diameter D_M just below the plastic deformation zone that barely changes, as shown in (a1-a5). (c) Variations of stresses for pillar top (solid red triangles) and middle (open blue triangles), calculated by dividing the instantaneous load by instantaneous cross-sectional area.

The calculated stress-displacement curves for all the compressed pillars are compiled and plotted in Figure 4.9. The stresses-displacement curves for as-received (AR) Cu pillars (solid lines) show nearly elastic initial loading, followed by long stress plateaus with numerous discrete strain bursts in Figure 4.9(a). The true stresses for irradiated (IR) CG pillars were calculated at two positions, the irradiated pillar top (solid data points) and the unirradiated region – the middle portion of the pillar (shown as open data points). The open data points match well with the solid lines, while the solid data points show considerable hardening with increasing displacement compared to unirradiated CG Cu. Furthermore, for as-deposited (AD) or irradiated (IR) NV-NT Cu, only the pillar tops experienced plastic deformations. The true stresses for irradiated NV-NT Cu (solid data points) and as-deposited specimens (open data points) are compared in Figure 4.9(b). The irradiated NV-NT Cu has greater yield strength than the as-deposited counterparts. After yielding,

both types of NV-NT Cu pillars exhibited slight hardening followed by significant softening. Such softening is ascribed to the internal microstructural change that will be analyzed further in the following section.

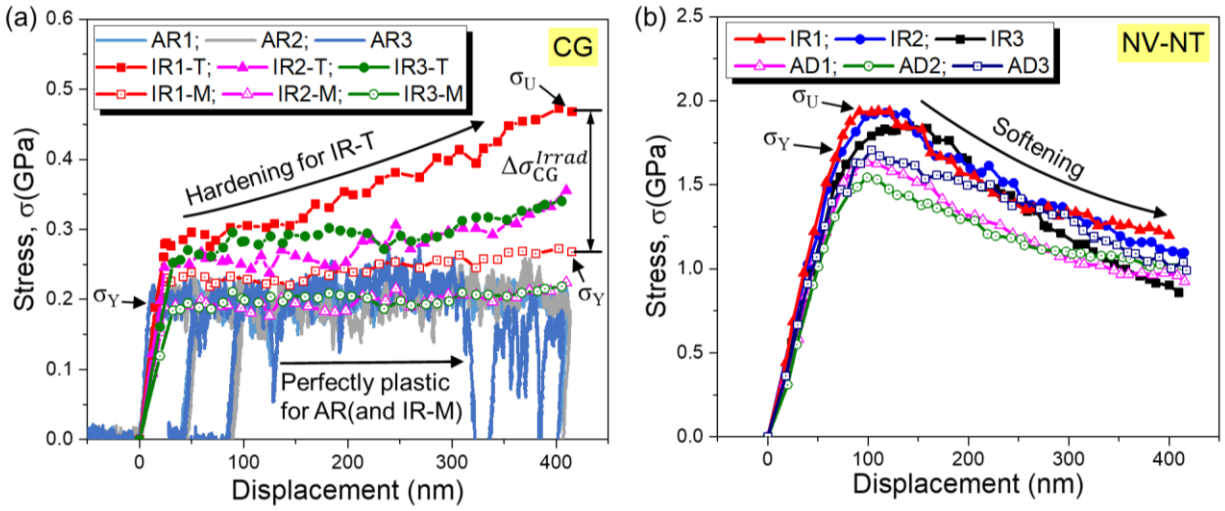

Figure 4.9. Stress-displacement behavior of (a) CG and (b) NV-NT pillars. AR: as-received; IR: Irradiated; IR-T: Irradiated pillar top; IR-M: Irradiated pillar middle; AD: as-deposited. Three pillars (marked as 1, 2 and 3) were compressed for each sample. In (a), AR-CG Cu pillars are perfectly plastic with little hardening, while the IR-CG Cu pillars exhibit considerable hardening at top portion (irradiated region). (b) The softening of top stresses for all the compressed NV-NT Cu pillars (AD or IR).

In order to quantify the radiation-induced hardening, two stresses are defined and marked in Figure 4.9, yield stress σ_Y and ultimate compressive stress σ_U. Table 4.1 summaries the values of σ_Y and σ_U for all the compressed pillars. The radiation-induced strengthening $\triangle\sigma^{Irrad}$ for NV-NT Cu thus was calculated by comparing the σ_Y between the as-deposited and irradiated specimens. For CG Cu, however, each pillar may be a single-crystal-like pillar and thus have a different crystallographic orientation that may affect the yield strength. To avoid such an orientation effect, the $\triangle\sigma^{Irrad}$ for irradiated CG Cu pillar is calculated by the subtraction of its σ_Y measured at the unirradiated (middle) section of the pillar from σ_U measured at its irradiated pillar top, as marked in Figure 4.9(a). The strength increment calculations are summarized in Table 4.2 and will be discussed later in more detail.

Table 4.1. Yield stress σ_Y and ultimate stress σ_U for all the compressed pillars, defined and measured based on the local stress-displacement curves in Figure 4.9. AR – As-received; IR – Irradiated; AD – As-deposited.

Material	Sample		σ_Y (GPa)	σ_U (GPa)
CG Cu	AR	1	0.19 ± 0.03	0.19 ± 0.03
		2	0.20 ± 0.03	0.20 ± 0.03
		3	0.19 ± 0.05	0.19 ± 0.05
	IR	1	0.25 ± 0.03	0.47 ± 0.01
		2	0.20 ± 0.02	0.35 ± 0.01
		3	0.20 ± 0.02	0.34 ± 0.01
NV-NT Cu	AD	1	1.32 ± 0.10	1.68 ± 0.02
		2	1.21 ± 0.13	1.63 ± 0.01
		3	1.21 ± 0.10	1.52 ± 0.01
	IR	1	1.65 ± 0.20	1.94 ± 0.02
		2	1.59 ± 0.16	1.84 ± 0.02
		3	1.56 ± 0.08	1.85 ± 0.01

Table 4.2. Comparisons of radiation-induced microstructure evolution and strength increment, between CG Cu and NV-NT Cu. d_B – bubble size; ρ_B – bubble density; d_D – dislocation loop size; ρ_D – dislocation loop density. $\Delta\sigma_B + \Delta\sigma_D$ is the calcualted value using dispersed barrier hardening models, and $\Delta\sigma^{Irrad}$ is the measured value from Table 4.1.

Material	Bubbles		Dislocation loops		Strength increment	
	d_B (nm)	ρ_B (1×10^{24}/m^3)	d_D (nm)	ρ_D (1×10^{22}/m^3)	$\Delta\sigma_B + \Delta\sigma_D$ (GPa)	$\Delta\sigma^{Irrad}$ (GPa)
CG Cu	1.5 ± 0.3	2.3 ± 0.2	9 ± 4	2.0 ± 0.5	~ 0.22	~ 0.17 ± 0.04
NV-NT Cu	1.5 ± 0.3	1.2 ± 0.1	6 ± 2	1.2 ± 0.4	~ 0.14	~ 0.35 ± 0.05

4.4.3 Post-compression analyses

To investigate the deformation mechanisms of NV-NT Cu, post-compression TEM examinations were performed. Figure 4.10(a) displays an overview of the area near pillar top. The TEM sample was tilted to Cu <110> zone axis for the unformed region where high-density growth twins can be clearly seen, while in the plastically deformed region most of the twins have been removed. The SAD pattern for the deformed region in Figure 4.10(b) indicates the crystal rotation induced by heavy plastic deformation. In comparison, the SAD pattern for undeformed region in Figure 4.10(c) shows a typical symmetrical twin pattern, together with extra spots (marked by circles) arising from ITBs. The corresponding dark-field image (DF) TEM micrograph in Figure 4.10(d) confirms

the removal of growth twins in the plastic deformation region. As shown in Figure 4.10(e), the enlarged view of box (e) in Figure 4.10(a) denotes a sharp boundary (dotted line) between the deformed and undeformed region. High-density dislocations were observed along the boundary. The enlarged view in Figure 4.10(f) shows several remaining TBs that have been greatly distorted in the plastic deformation region.

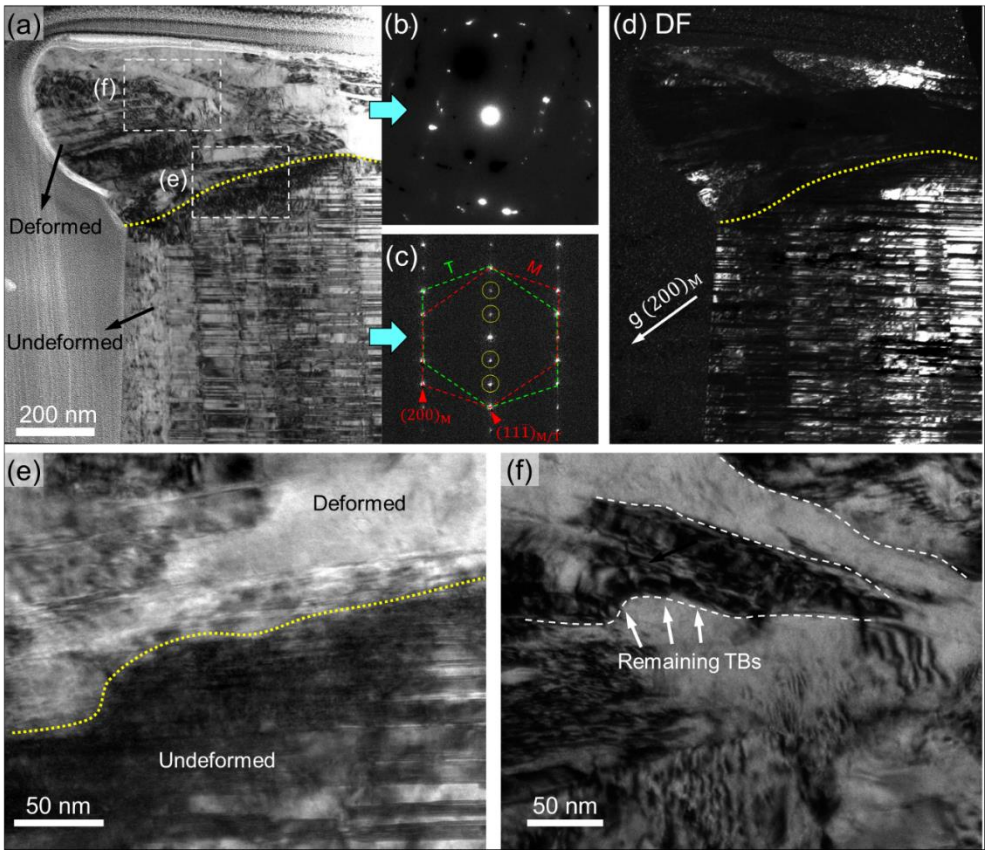

Figure 4.10. The microstructure of a compressed pillar for as-deposited NV-NT Cu. (a) The bright-field TEM image of the deformed pillar showing the detwinning in the plastically deformed region. (b-c) The SAD patterns from deformed and undeformed regions, respectively. (d) Corresponding DF TEM image showing lower twin density in the deformed region. (e-f) Enlarged views of the squares in (a).

Somewhat different microstructures have been observed in the deformed pillar of He-irradiated NV-NT Cu, as shown in Figure 4.11. The overview TEM micrograph in Figure 4.11(a) shows the substantial plastic deformation confined near the pillar top. The SAD pattern in Figure 4.11(b) indicates the retention of twins in the deformed region, and there is much less crystal reorientation

than that in the as-deposited NV-NT Cu. Compared with the SAD pattern from undeformed region in Figure 4.11(c), there are no extra spots from ITBs in the plastic deformed pillar top. The retention of nanotwins in the deformed region is also confirmed by the corresponding DF TEM image in Figure 4.11(d). The enlarged view in Figure 4.11(e) also denotes the sharp boundary between deformed and undeformed region, and the enlarged view in Figure 4.11(f) shows numerous He bubbles and the stacking faults (SFs) along the remaining TBs in the plastic deformation region.

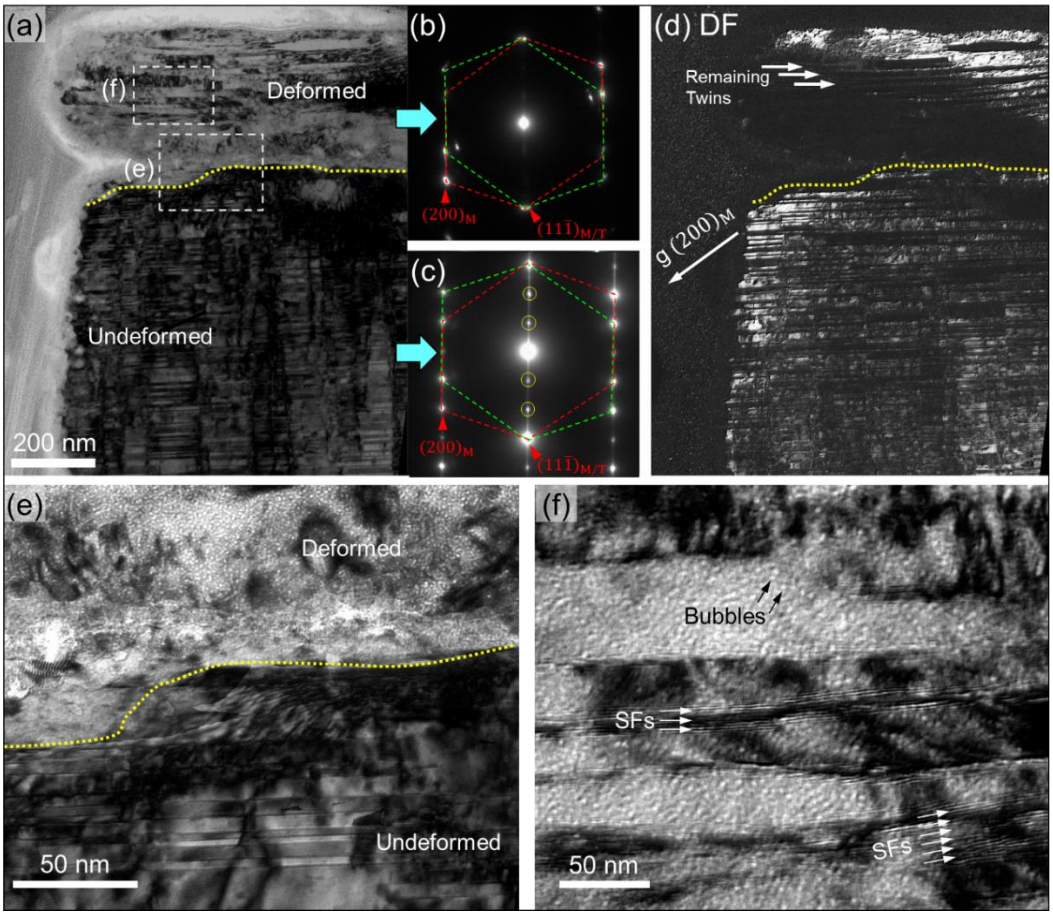

Figure 4.11. Deformed microstructure of a compressed pillar for He-irradiated NV-NT Cu. (a) The bright-field TEM image of the plastically deformed region. (b-c) The SAD patterns from deformed and undeformed regions. The deformed region has CTBs, but little sign of ITBs. (d) Corresponding DF TEM image showing the withholding of twins in the deformed region. (e-f) Enlarged views of the marked boxes in (a) showing formation of He bubbles and SFs along deformed TBs.

4.5 Discussion

4.5.1 Irradiation-induced He Bubbles and Lattice Expansion

At room temperature, He atoms are essentially insoluble in metals [228, 229], and they can easily migrate and combine with radiation-induced vacancies to form bubbles [230, 231]. It has been shown that precipitated He bubbles can significantly distort crystal lattices and cause substantial lattice expansion [182]. In the current study, more bubbles are produced in CG Cu than in NV-NT Cu, as shown in Figure 4.4 and 4.5. The variation of bubble density with increasing penetration depth shown in Figure 4.12 is in good agreement with calculated He concentration profile (black curve). Note that over the depth of 200 - 600 nm, the bubble density, ρ_B, remains a constant, about $2.2 \pm 0.2 \times 10^{24}/m^3$ for CG Cu, twice larger than that in the irradiated NV-NT Cu, $1.2 \pm 0.1 \times 10^{24}/m^3$. The histograms in Figure 4.12(b) show the bubble size (d_B) varies from 1.0 to 2.5 nm in both cases regardless of the radiation depth, and they have nearly the same average bubble size of ~ 1.5 nm. The lattice expansion is evidenced by the shrinkage of SAD (selected area diffraction) patterns, as shown in Figure 4.12(c1) and (c2) examined along <110> zone axis over the depth of 200 - 600 nm. The lattice expansion is calculated to be 1.83 ± 0.76 (%) for CG Cu, much larger than that in NV-NT Cu, 0.84 ± 0.09 (%). The reduced lattice expansion in NV-NT Cu may be related to the pre-existing NVs. Unlike our previous studies that showed preexisting NVs could shrink rapidly after absorbing the interstitials induced by 1 MeV Kr ion irradiations [169, 218, 232], most of the preexisting nanovoids survived He irradiation in the current study. The underlying mechanism is attributed to the effect of He on the kinetics of void growth or shrinkage [231]. With the further addition of He atoms into NVs, the void internal pressure increases until it reaches a stable state. According to the proposed critical bubble model (CBM) [233], the shrinkage rate for nanometer-sized voids will decrease prominently in the presence of internal He pressure. From another point of view, when the He-filled NVs capture interstitials, the internal He pressure will build up even further, and thus He once absorbed by voids will reduce the driving force for NVs to absorb interstitials. Meanwhile, the NVs can reduce He bubble density and alleviate lattice expansion by trapping a large number of Helium atoms. Conversely, for CG Cu, nearly all He atoms may reside in bubbles, leading to higher bubble density and more lattice expansion. He ion irradiation induced lattice expansion has been observed previously in Cu/V nanolayers, and the magnitude of He

bubble induced lattice expansion appears to decrease with decreasing individual layer thickness [182].

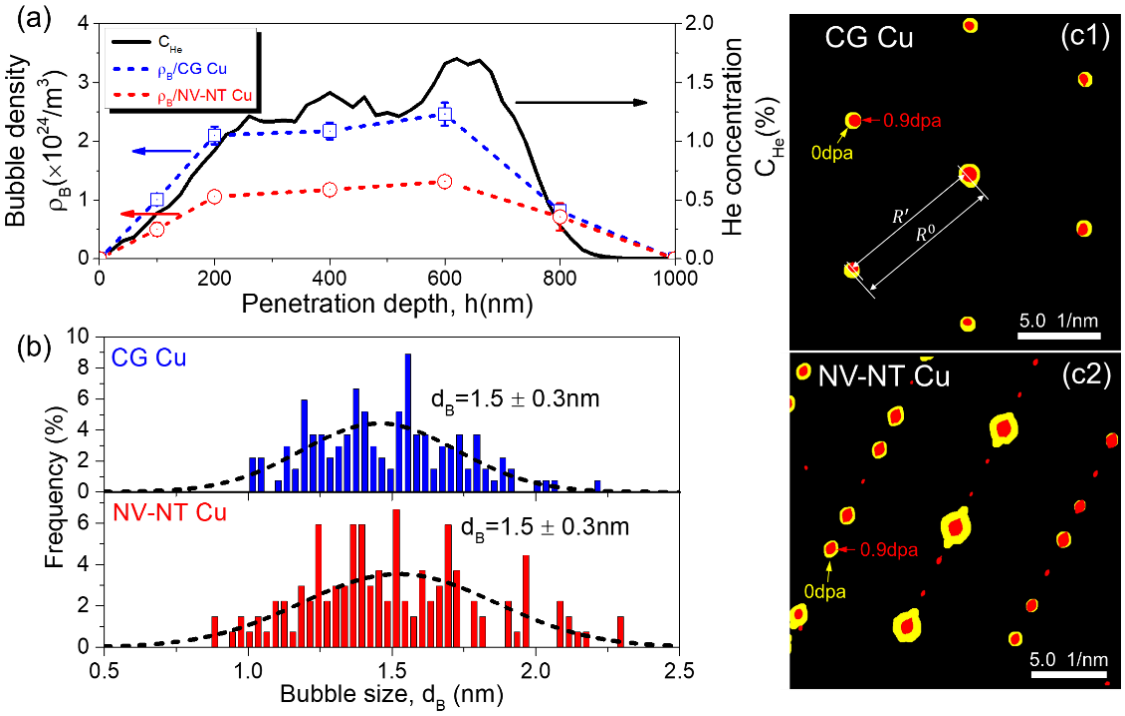

Figure 4.12. He-irradiation induced bubbles and lattice expansion. (a) Comparison of bubble density along ion penetration depth. (b) Bubble size distributions in He-irradiated CG Cu and NV-NT Cu. (c1) and (c2) Overlap of two SAD patterns along [110] zone axis of CG Cu and NV-NT Cu before (yellow) and after (red) Helium irradiations.

4.5.2 Mechanical properties of nanotwinned Cu

It is well known that the strength of micropillars shows a strong size-dependence (extrinsic size effect) [227], and there is a critical pillar diameter beyond which the extrinsic size effect is insignificant, that is the measured properties of pillars are similar to those of bulk materials [154, 155]. It is worth pointing out that the critical pillar size depends on the intrinsic microstructure characteristics and their interactions with mobile dislocations [153]. Previous micro-compression studies on perfect single-crystal Cu revealed that the size effect is exerted on all the micropillars with diameters of less than several μm [234], presumably because of the absence of dislocation sources and obstacles [157]. The flow stress of CG Cu is ~ 0.2 GPa, comparable to those reported in the literature [74]. Furthermore, for the irradiated materials containing high-density defect

clusters, the transition diameter of pillars of single-crystal Cu pillars has been experimentally estimated to be ~ 400 nm [153, 235]. The measured strengths of irradiated Cu in the current study are based on the compression test on micropillars with 1.2 μm in diameter. Therefore, our measured values can be reasonably compared with previous studies and will be discussed later in detail.

For NT Cu, experiments and simulations reveal that twin-spacing t plays an important role in determining their mechanical properties [130, 134]. Figure 4.13 compiles the yield strength σ_Y versus $t^{-0.5}$ for previously reported studies on NT Cu [102, 104, 105, 108, 127, 133-135, 236-238]. When t > 15 nm, the strength is dominated by the resistance of TBs against slip transmission of dislocations, and σ_Y follows the conventional Hall-Petch (H-P) relationship:

$$\sigma_Y = \sigma_0 + k_{TB} t^{-0.5} \qquad \text{Equation 4.1}$$

where σ_0 is the lattice friction stress, ~ 100 MPa, and k_{TB} is a material constant. However, when t < 15 nm, the size dependent variation of σ_Y appears to be more influenced by texture [135]. On the one hand, for polycrystalline NT Cu with equiaxed grains (Eq-NT Cu), softening occurs with decreasing t, which is governed by the dislocation nucleation at grain boundary-twin intersections [77]. The softening behavior can be described by dislocation-nucleation-controlled (DNC) mechanism [130] that shows:

$$\sigma_Y = \frac{\Delta U}{SV^*} - \frac{k_B T}{SV^*} \ln\left(\frac{d\nu_D}{t\dot{\varepsilon}}\right) \qquad \text{Equation 4.2}$$

where ΔU is the activation energy, S is a factor presenting local stress concentration and geometry, V^* is the activation volume, k_B and T are the Boltzmann constant and temperature, d is the grain size, ν_D is the Debye frequency, and $\dot{\varepsilon}$ is the macroscopic strain rate.

On the other hand, for the preferentially (111) textured NT Cu with columnar grains (Col-NT Cu) , its σ_Y continues to increase slightly with decreasing t [135]. Considering most TBs are parallel with each other and normal to the loading axis under compression, the strength variation of Col-NT Cu is better described by confined layer slip (CLS) model [239]:

$$\sigma_Y = \sigma_0 + \gamma \frac{\mu b}{t} \ln\left(\frac{\eta t}{b}\right) \qquad \text{Equation 4.3}$$

where μ is the shear modulus, b is the magnitude of the Burgers vector, and γ and η are material constants. For Cu, μ = 48 GPa, b = 0.256 nm, η = 0.16 and γ = 0.40 [135].

According to the CLS model, dislocations are confined by adjacent TBs, plastic deformation occurs by dislocation bowing between TBs [135, 239]. In addition, the model predicts the upper limit of strength for NT Cu is ~ 1.2 GPa, when $t = be/\eta \approx 4$ nm, where e is the nature constant. In reality, if t < 4 nm, the ultrafine NT Cu is most likely to suffer from significant detwinning, driven by strong twin-twin interactions [120]. The strongest NT Cu reported to date has a flow stress of 1.2 GPa, with a twin spacing of ~ 4 nm [108]. In our work, the NV-NT Cu has an average twin spacing of 8 nm, but its yield stress σ_{NV-NT} is ~ 1.25 ± 0.06 GPa (see Table 4.1). Such a high strength arises from two contributions: TBs and nanovoids. The contribution from TBs σ_{NT} is estimated to be 1.09 GPa by substituting t = 8 nm into Equation 4.3, while the strengthening from the nanovoids ($\Delta\sigma_V$) and can be described by the proposed dispersed barrier model [71]:

$$\Delta\sigma_V = \alpha_V M \mu b \sqrt{N_V d_V} \qquad \text{Equation 4.4}$$

where α_V is a parameter depending on the average barrier strength of the irradiation-induced defect clusters, ~ 1 for voids [240, 241], M is the Taylor factor, a ratio of uniaxial yield strength to resolved shear strength and has an average value of 3.06 for both face-centered-cubic and body-centered-cubic lattices [74]; μ and b are shear modulus and Burgers vector as defined in Equation (3); N_V and d_V are void density and size. Setting α_V = 1 and substituting N_V = 4.0 ± 0.5 10^{21}/m^3 and d_V = 6 ± 2 nm into Equation (4) give $\Delta\sigma_{NV}$ = 0.19 ± 0.05 (GPa). Hence the nanovoids reasonably accounts for the extra strengthening observed in NV-NT Cu comparing to NT Cu without nanovoids as shown in Figure 8. In addition, as shown in Table 4.1, after He irradiations, the yield strength of irradiated NV-NT Cu can increase further to 1.60 ± 0.05 (GPa). The strength increment $\Delta\sigma^{Irrad}$ (0.35 ± 0.05 GPa) caused by irradiation must be closely associated with radiation damage, which will be discussed in detail in the following section.

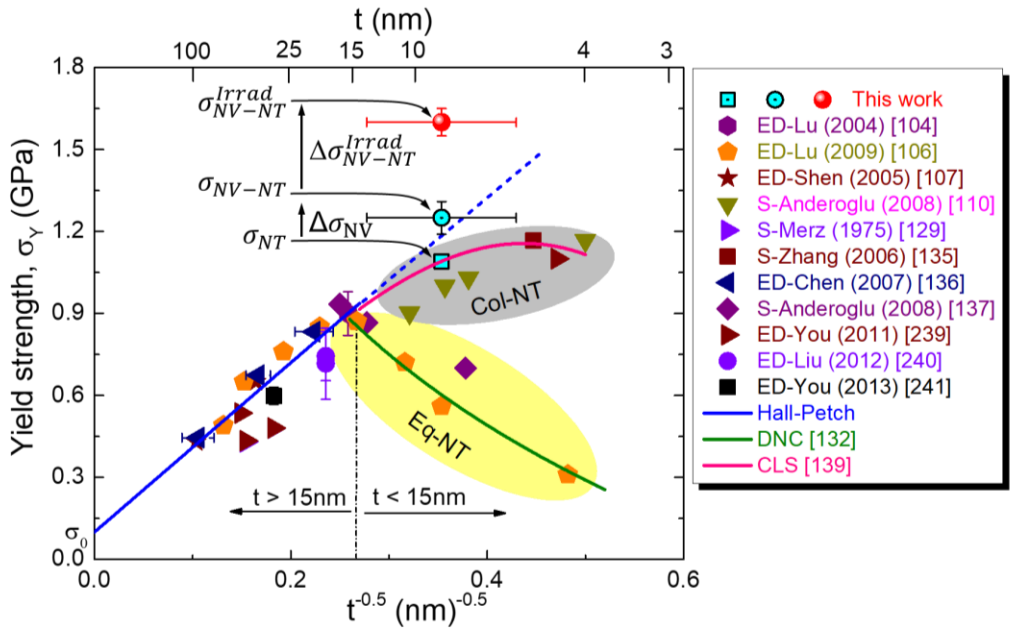

Figure 4.13. Comparison of yield strength σ_Y of He-irradiated NV-NT Cu with previous studies synthesized by electrodeposition and sputtering [102, 104, 105, 108, 127, 133-135, 236-238]. σ_Y shows a strong dependence on twin spacing (t) and reaches a maximum value ~1.2 GPa at $t \approx 4$ nm, while He irradiation can increase the yield strength of NT Cu to 1.6 GPa when $t \approx 8$ nm. The strength data points are obtained from compressive (this work) and tensile tests or estimated as 1/3 of hardness. S, sputtering; ED, electrodeposition; DNC, dislocation-nucleation-controlled [132]; CLS, confined layer slip [139].

4.5.3 Radiation-induced hardening

Strengthening in irradiated metals is caused by the production of various defects and their interactions with mobile dislocations [11]. In He-irradiated metals, the primary defects are dislocation loops and He bubbles [189]. For dislocation loops that are classified as strong obstacles, their contribution to strengthening can also be described by the dispersed barrier model [71]:

$$\Delta\sigma_D = \alpha_D M \mu b \sqrt{N_D d_D} \qquad \text{Equation 4.5}$$

where α_D is the parameter indicating the average barrier strength of the irradiation-induced dislocation loops, approximately 0.2 in Cu [242]; N_D and d_D are density and size of dislocation loops. M, μ and b are the same parameters as defined in Equation 4.4.

For He bubbles, the magnitude of their barrier resistance appears to be dependent on internal pressure [182, 243]. Figure 4.14 compares the high-resolution TEM (HRTEM) micrographs of

nanoscale twins in NV-NT Cu before and after He irradiations. As-deposited NV-NT Cu has nearly perfect (pristine) CTBs in Figure 4.14(a) and (c). In contrast, the CTBs in irradiated NV-NT Cu are decorated with He bubbles in Figure 4.14(b) and SFs in Figure 4.14(d). Also, many of the bubbles are hexagonally faceted rather than spherical, indicating their low internal pressure [244]. It has been demonstrated that under-pressurized He bubbles are weak obstacles to mobile dislocations [243] or crack propagation [150]. To describe the weak strengthening arising from under-pressurized bubbles, $\Delta\sigma_B$, an alternative relationship was developed by Friedel-Kroupa-Hirsch (FKH) [76]:

$$\Delta\sigma_B = \frac{1}{8} M \mu b d_B N_B^{2/3} \qquad \text{Equation 4.6}$$

where M, μ and b are the same parameters defined in Equation (4); d_B and N_B are bubble size and density.

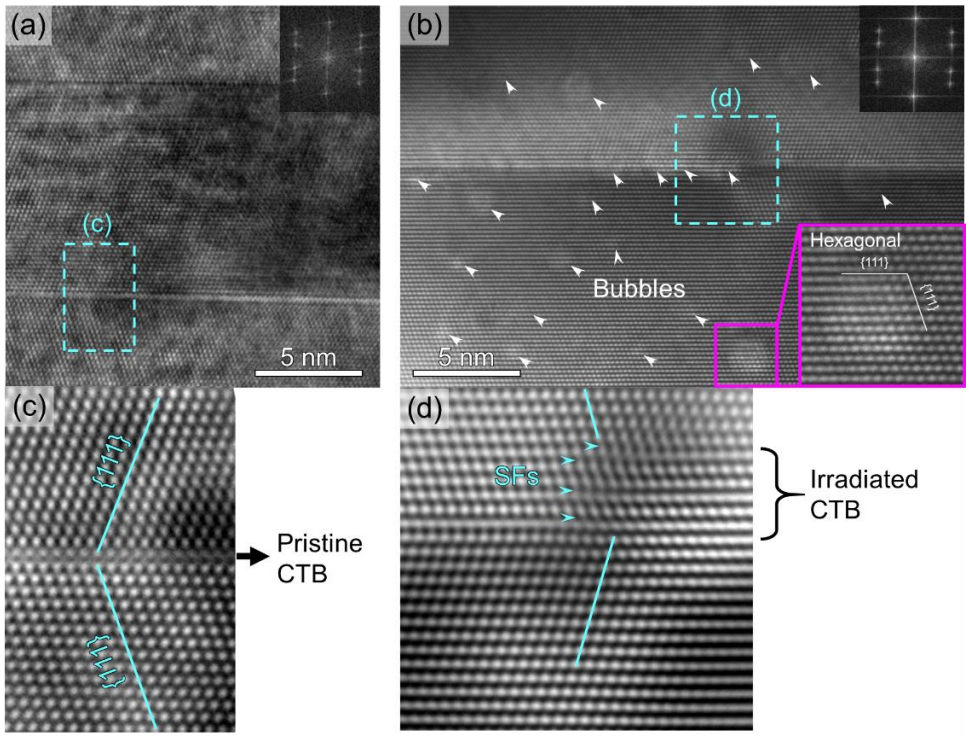

Figure 4.14. HRTEM images comparing the microstructures of pristine and He-irradiated CTBs. (a) Typical nanotwins in as-deposited NT Cu. (b) He-irradiated NT Cu with abundant bubbles distributed in the lattice and along CTBs. The inset shows an HRTEM image of a hexagonally faceted He bubble. (c) Enlarged view of the square in (a) showing a narrow nearly perfect CTB. (d) The enlarged view of the square in (b) showing several SFs along a CTB in irradiated NT Cu.

Table 4.2 summaries the size and density of He bubbles and dislocation loops for irradiated CG Cu and NV-NT Cu over the penetration depth of 200 - 600 nm. These measurements were obtained from our TEM analyses, and more detailed information can be found in Figure 4.15 and Figure 4.16. The measured and calculated strengthening are summarized in Table 4.2. Note that, although the irradiated NV-NT Cu contains a lower density of bubbles and dislocation loops, it experiences a higher strength increment, $\Delta\sigma^{Irrad}$, than irradiated CG Cu does.

The radiation-induced strengthening in CG Cu, $\Delta\sigma_{CG}^{Irrad}$, arises from both the weak obstacles (He bubbles) and strong obstacles (dislocation loops). Its total increment in this scenario is given as [11]:

$$\Delta\sigma_{CG}^{Irrad} = \Delta\sigma_B + \Delta\sigma_D \qquad \text{Equation 4.7}$$

Using Equation 4.5 and 4.6, $\Delta\sigma_B$ and $\Delta\sigma_D$ are calculated as ~ 0.12 GPa and 0.10 GPa, respectively, so the total strengthening $\Delta\sigma_{CG}^{Irrad}$ in CG Cu is estimated as ~ 0.22 GPa. Based on the micropillar compression test in Figure 4.6, the measured value of $\Delta\sigma_{CG}^{Irrad}$ is 0.17 ± 0.04 GPa (see Table 4.1). But considering the pillar base (the unirradiated region) yields first as shown in Figure 4.6(c3), the true strength increment in the top irradiated region should be slightly higher than 0.17 GPa, and it is expected to be comparable with the calculated value.

We now attempt to interpret the radiation-induced strengthening in NV-NT Cu. Before irradiation, the strength of NV-NT Cu can be estimated as:

$$\sigma_{NV-NT} = \sigma_0 + \sigma_{NV} + \sigma_{TB} \qquad \text{Equation 4.8}$$

where σ_0 is the lattice friction; σ_{NV} and σ_{TB} are the contributions from NVs and TBs, respectively. After He irradiations, the strength of NV-NT Cu is determined by:

$$\sigma_{NV-NT}^{Irrad} = \sigma_0 + \sigma_{NV}^{*} + \sigma_{TB}^{*} + \Delta\sigma_B + \Delta\sigma_D \qquad \text{Equation 4.9}$$

where σ_{NV}^{*} refers to the He-filled NVs, and σ_{TB}^{*} refers to the irradiation modified TBs. Combining Equation 4.8 and 4.9 yield the irradiation induced strengthening, $\Delta\sigma_{NV\text{-}NT}^{Irrad}$, in NV-NT Cu:

$$\Delta\sigma_{\text{NV-NT}}^{Irrad} = \Delta\sigma_B + \Delta\sigma_D + (\sigma_{NV}^{*} - \sigma_{NV}) + (\sigma_{TB}^{*} - \sigma_{TB}) \qquad \text{Equation 4.10}$$

As shown in Table 4.2, the measured value of $\Delta\sigma_{NV\text{-}NT}^{Irrad}$ from pillar compression tests is 0.35 ± 0.05 GPa. However, the calculated values of $\Delta\sigma_B$ and $\Delta\sigma_D$ from equations 4.5 and 4.6, add up to only

~ 0.14 GPa, insufficient to account for the measured strengthening in NV-NT Cu. The extra strengthening must come from the irradiation modified NVs and TBs, that is the last two terms on the right side of Equation 4.10. Figure 4.16 compares the plan-view TEM images of as-deposited and irradiated NV-NT Cu, which shows little change on the size or number density of NVs after He irradiation. In other words, the contribution of the third term (irradiation modified NVs) in Equation 4.10 to strengthening maybe insignificant. Therefore, the last term, arising from the irradiation modified TBs, may play a primary role in the irradiation hardening in NV-NT Cu. Furthermore, as shown in Figure 4.14, the irradiated TBs are decorated with bubbles and SFs, thus these defective TBs may be stronger barriers against trespassing of dislocations than pristine (sharp) TBs in as-deposited NV-NT Cu. Such an aspect will be confirmed further by molecular dynamic (MD) simulations in the following section.

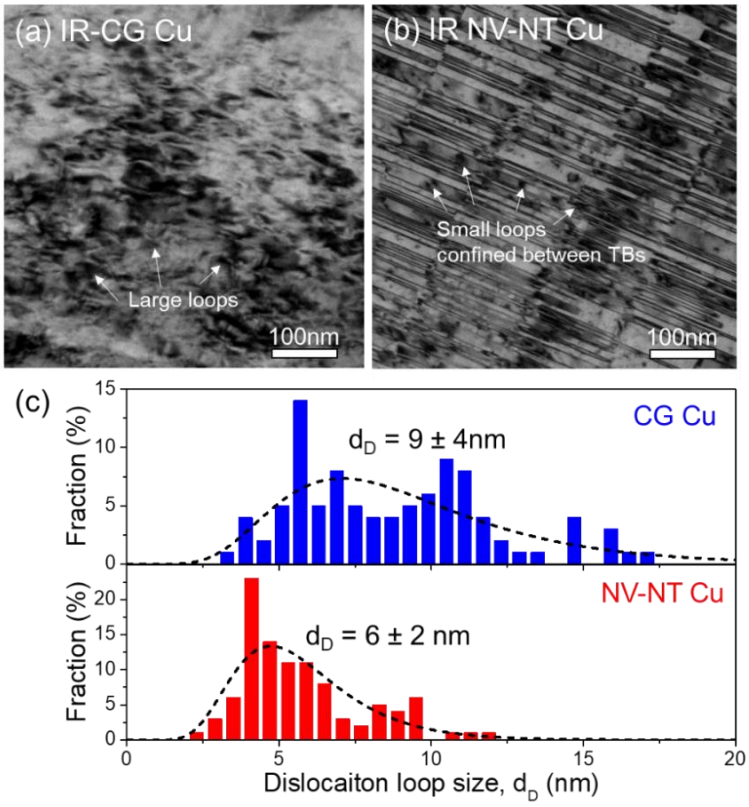

Figure 4.15. Comparison of irradiation-induced dislocation loops in CG and NV-NT Cu. (a) Large dislocation loops randomly distributed in CG Cu. (b) Small dislocation loops confined between parallel TBs in NV-NT Cu. (c) Comparison of loop size for irradiated CG (9 ± 4 nm) and NV-NT Cu (6 ± 2 nm).

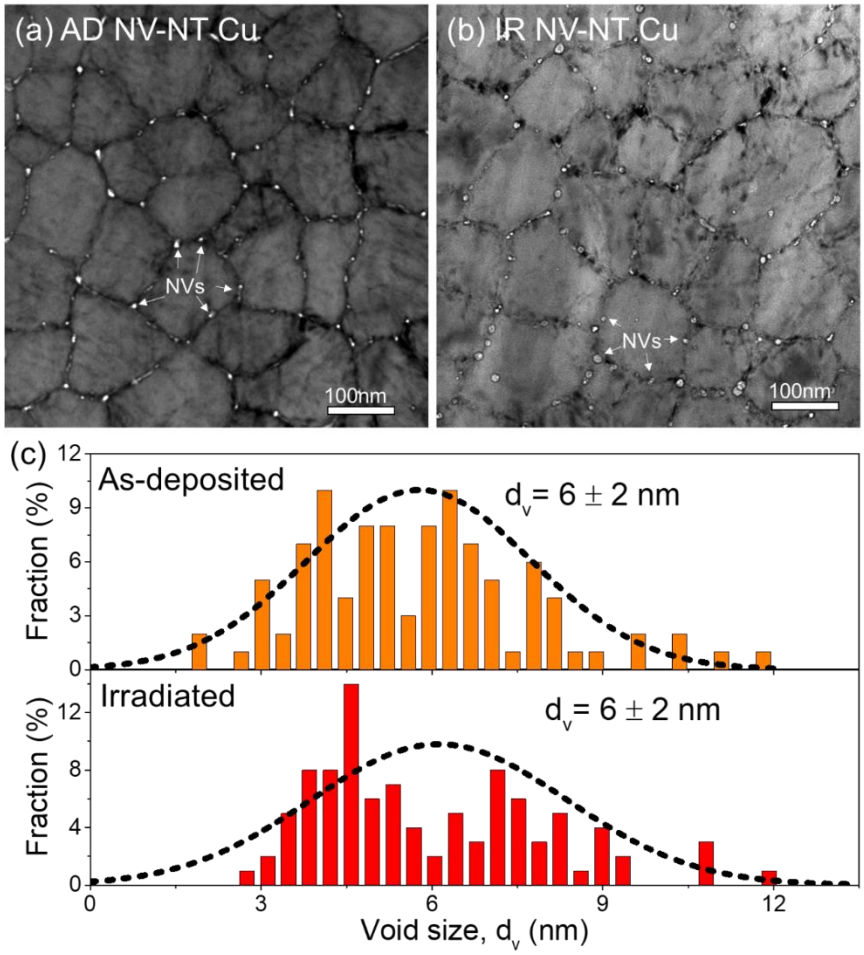

Figure 4.16. Comparison of NVs in as-deposited and He irradiated NV-NT Cu. (a) and (b) Plane-view TEM images, before and after irradiation, showing the same features of NVs primarily positioned at domain boundaries. (c) Comparison of void size for as-deposited and irradiated samples, indicating little change in void size (6 ± 2 nm).

4.5.4 Deformation mechanisms

Based on experiments and discussions above, we finally address the deformation mechanisms of Cu under uniaxial compression. Previous micro-compression test on non-tapered pillars of electrodeposited polycrystalline Cu film revealed a compressive yield stress of ~ 0.3 GPa, when the grain size is around 0.8 μm and the pillar diameter is 10 μm [245]. In addition, for pillars with diameters greater than grain size, the yielding is expected to be followed by an obvious working hardening arising from the grain boundary strengthening [245]. For our CG Cu, the pillars are most likely to be single crystals, because the diameter of micropillars is 1.2 μm, much smaller than its

average grain size (43 μm), as shown in Figure 4.3(h). Therefore, the as-received CG Cu pillars yield at a low compressive yield strength, ~ 0.2 GPa (see Table 4.1). After yielding, there is little work hardening in CG Cu, and the stress-displacement curves are characterized by discrete strain bursts, as shown in Figure 4.6(a). Meanwhile, numerous discrete slip bands are formed on the pillar surface as shown in in Figure 4.6(b1-b5), in agreement with prior studies on single-crystal metals under compression [154, 226, 246]. Figure 4.17 below shows one typical configuration of deformed pillar for as-received CG Cu, from which the corresponding critical resolved shear stress τ_{CRSS} in slip plane is estimated to be ~ 0.1 GPa using Schmid's law. The calculated τ_{CRSS} is in good agreement with previous micropillar compression tests on (100)- or (111)-orientated single-crystal Cu pillars [234]. After irradiation, however, the upper portion of the pillar is strengthened by He bubbles and dislocation loops, so it experiences limited plastic deformation. In contrast, the lower portion is soft, and it yields first and undergoes significant plastic deformation, driven by dislocation multiplication and migration as shown in Figure 4.6(c1-c5).

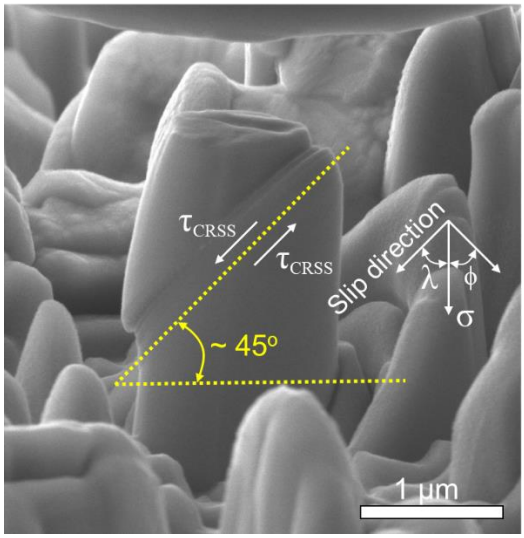

Figure 4.17. SEM image of a compressed pillar for as-received CG-Gu. Discrete slip bands are formed on pillar surface. The critical resolved shear stress τ_{CRSS} is calculated using Schmid's law: $\tau_{CRSS} = \sigma_Y \cos\phi\cos\lambda$. σ_Y, ~ 0.2 GPa , is the compressive yield stress, ϕ (~ 45º) is the angle between the applied stress and normal vector of slip plane, and λ (~ 45º) is the angle between the applied stress and slip direction .

For the as-deposited NV-NT Cu with ultra-fine twins, dislocations are confined by TBs, and the deformation mechanism is dominated by dislocation bowing, resulting in squeezing and extrusion

of the pillar top. After He irradiations at room temperature, the TBs become defective, decorated by He bubbles and SFs. These defective TBs could be stronger barriers to slip transmission via dislocations.

In order to understand the influence of SF-decorated TBs on strengthening mechanisms, MD simulations were performed for Cu with SF-decorated CTBs, as shown in Figure 4.18. Using the Thompson tetrahedron notation and satisfying the conservation law of Burgers vector, we describe the interactions between a dislocation and the three-layer faults. Figure 4.18(a) schematically illustrates the twin/matrix orientation relation and several slip systems that could be involved during deformation [247]. Start with an ideal twin boundary with the stacking sequence of …ABC**A**CBACB…, the three-layer fault can be formed by gliding a Shockley partial on the plane between C and B, i.e, …ABC**ACA**CBA… The underline indicates the fault. The Shockley partial could be one of three Burgers vectors, **Aδ'**, **Bδ'**, and **Eδ'** [120]. Here, a **Bδ'** partial dislocation glides on the (111) plane, creating the three-layer fault.

When a screw dislocation $\mathbf{b_s}$ with Burgers vector **AB** on the slip plane $(1\bar{1}1)$ moves towards the three-layer fault, as shown in Figure 4.18(b1), the planar-extended core condenses at the fault due to the discontinuity of slip systems in Figure 4.18(b2). The screw then dissociates on the secondary (111) plane (between C and A) above the original CTB in Figure 4.18(b3). Figure 4.18(b4) shows the disregistry plot of the dissociated structure with respect to the three-layer fault structure, revealing that the right partial has Burgers vector **δ'B** and the left partial has Burgers vector **Aδ'**. The corresponding reaction can be described by **AB** = **Aδ'** + **δ'B**. The gliding of **δ'B** partial corrects the fault, i.e., **Bδ'** + **δ'B** = **0** in the right side of the intersection. The gliding of **Aδ'** towards the left side also corrects the fault, i.e., -(**Bδ'** + **δ'A**) = -**BA**, corresponding to a full shear.

Figure 4.18(c1) shows a mixed dislocation $\mathbf{b_m}$ with Burgers vector **DB** on the slip plane $(1\bar{1}1)$ moving towards the three-layer fault. Previous studies have revealed two potential reaction processes. First, $\mathbf{DB} = \mathbf{A\delta'}_{(CTB)} + \mathbf{BB'}_{(100)T}$, the slip transmission from $(1\bar{1}1)_M$ to $(100)_T$ [248]; second, $\mathbf{DB} = \mathbf{E\delta'}_{(CTB)} + \mathbf{AD'}_{(1\bar{1}1)\,T}$, the slip transmission from $(1\bar{1}1)_M$ to $(1\bar{1}1)_T$ [129]. In current case, however, the three-layer faults in Figure 4.18(c2) prevent the $\mathbf{b_m}$ from dissociating and transiting through the CTB. This is ascribed to the creation of a high energy SF if the dissociation occurs, as shown in Figure 4.19. The initial fault is associated with a shear **Bδ'**, and the further

shear by **Aδ'** or **Eδ'** will create the high energy stacking fault, corresponding to the change in the stacking sequence from …ABC**ACA**CBA… to …ABC**ACC**BAC….

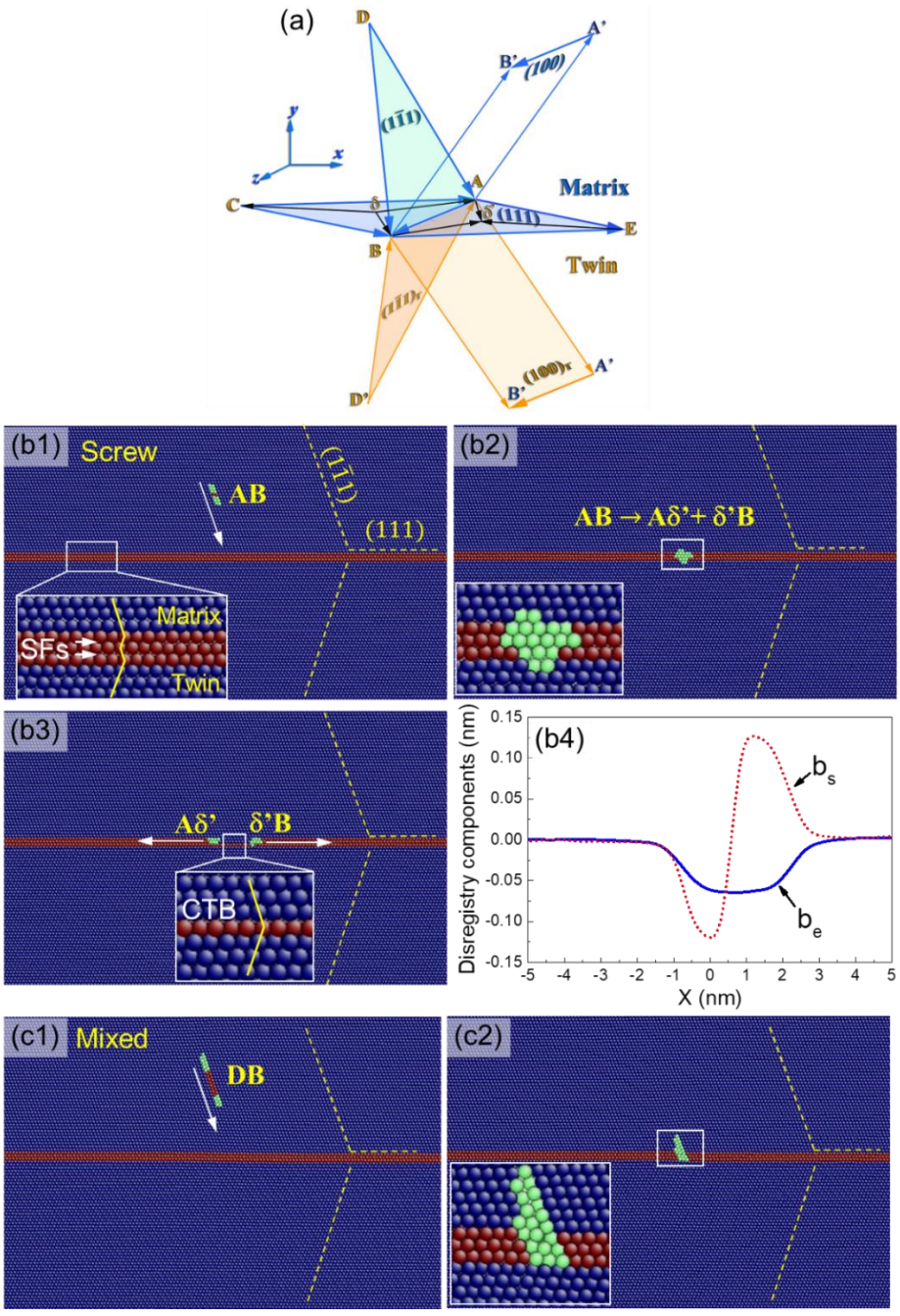

Figure 4.18. MD simulations on dislocation-SF interactions in twin plan. (a) Thompson tetrahedron notation demonstrating the orientation relation and several slip systems between a twin and the matrix. (b1-b3) MD snapshots illustrating the dissociation of a screw dislocation **AB** into two partials (**Aδ'** and **δ'B**). (b4) The corresponding disregistry plot of the dissociated structure in (b3). (c1-c2) MD snapshots illustrating a mixed dislocation **DB** interacting with SFs.

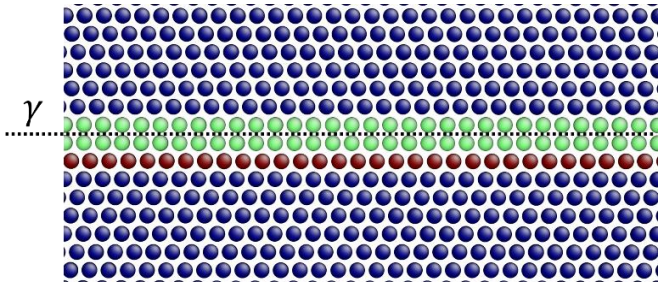

Figure 4.19. High energy stacking fault formed due to the dissociation of the mixed dislocation through Shockley partial glide. The dotted line marks a high energy stacking fault formed due to the dissociation. We found that the system energy increased by 502 eV. Considering the area of the twin plane, the energy of high stacking fault plane was estimated to be γ = 64 mJ/m^2.

In summary, the SFs formed during irradiation act as strong barriers for dislocations in terms of slip transmission with different mechanisms. For a screw dislocation, the faults facilitate the cross-slip of the dislocation onto the CTB. For a mixed dislocation, the faults prevent the dissociation of the dislocation on the CTB, which enhances the energy barrier for slip transmission due to the attraction force of the residual dislocations.

Note that in Figure 4.6(d1-d5), the lower portion of the irradiated NV-NT Cu pillar did not yield preferentially as the irradiated CG Cu did in Figure 4.6(b1-b5). Figure 4.8(c) of irradiated NV-NT Cu pillar 1 indicates that its unirradiated middle portion can sustain a higher applied stress than the pillar top when the displacement goes beyond 180 nm. This is because detwinning and softening occurred near the pillar top, while the nanotwins at the base can still provide significant strengthening, and thus preventing its preferential deformation. The retention of integrity of pillar base for NV-NT Cu could also be induced by the substrate constraints. During compression, the lower portion of the unirradiated region is constrained by the hard irradiated pillar top and the rigid Si substrate. Such constraints may develop a large friction stress along interface and strengthen the unirradiated pillar base. Similar phenomenon has been observed in Cu/amorphous-CuNb multilayers subjected to micropillar compression tests [249]. Consequently, the irradiated top portion of the NV-NT Cu micropillar first yields and undergoes significant plastic deformation. Moreover, post-compression TEM analysis has revealed significant detwinning in as-deposited NV-NT Cu, as shown in Figure 4.10. Detwinning has been frequently observed in NT metals driven by migration of Shockley partials under shear stress [119, 120, 123, 202, 220, 250]. In contrast, moderate detwinning occurred in He-irradiated NV-NT Cu after compression, as shown

in Figure 4.11. The radiation-induced He bubbles and SFs along TBs may retard detwinning and enhance strengthening in NT Cu even further.

4.6 Conclusions

CG and NV-NT Cu were irradiated with He ions at multiple energies to introduce a plateau of radiation damage profile, and the radiation-induced evolution of microstructures and mechanical behavior were analyzed. Our studies show that NV-NT Cu has outstanding radiation tolerance in comparison to CG Cu in terms of lower density of He bubbles and less lattice expansion. The He-irradiated NV-NT Cu reaches an ultra-high flow stress of ~ 1.6 GPa, one of the highest reported to date for Cu. The significant strengthening in He-irradiated NV-NT Cu arises from the defective TBs that are decorated with He bubbles and SFs. MD simulations show that SFs act as strong barriers against dislocation transmission through coherent twin boundaries. Microscopy studies also show that stress-driven detwinning is largely retarded by the He bubbles and defective TBs.

CHAPTER 5. IN SITU STUDIES ON THE RADIATION-INDUCED TWIN BOUNDARY-DEFECT INTERACTIONS IN CU

The lab work was performed at Argonne National Laboratory by Cuncai Fan and Jin Li with guidance of Dr. Meimei Li. The data analysis and writing were completed by Cuncai Fan with guidance and editing by Dr. Xinghang Zhang.

5.1 Overview

Incoherent twin boundaries (ITBs) are highly mobile due to their dislocation structure, as schematically illustrated in Figure 1.18(a). Radiation induces prominent ITB migration and detwinning. In this chapter, polycrystalline Cu films with nanoscale annealing twins are subjected to *in-situ* Kr^{++} irradiation at room temperature inside a transmission electron microscope up to a dose of 1 displacement-per-atom. Depending on twin thickness, three types of twin boundary evolutions are observed, including rapid detwinning, gradual detwinning and self-healing. The mechanism of twin-thickness dependent evolution of microstructures is discussed. This study provides further evidence on twin boundary-defect interactions and may assist the design of radiation-tolerant twinned metallic materials.

5.2 Introduction

Nanotwinned (NT) metals have raised significant attention due to their remarkable electrical conductivity, [104, 105, 251] thermal stability [102, 252] and excellent mechanical properties. [101, 106, 107, 114, 253, 254] Prior studies show that twin thickness (t), the spacing between coherent twin boundaries (CTBs), plays a significant role in determining their physical and mechanical properties. [115, 134, 255] When twin thickness is reduced to a critical value, nanotwins may become unstable as shown by detwinning events occurring under high temperature, [256] electrical field [117] and mechanical stress. [119] The detwinning behavior is directly

correlated to the migration of partials on incoherent twin boundaries (ITBs). [120] According to the experimental studies using high resolution transmission electron microscopy (HRTEM) [121, 122, 124] and atomistic simulations, [116, 123] ITBs are composed of groups of Shockley partial dislocations on three successive {111} planes and tend to glide collectively under shear stress, [116, 119, 123, 257, 258] thereby causing detwinning. [259]

There are increasing investigations on radiation response of nt metals, [109, 110, 140, 169, 197, 202, 260, 261] and radiation-induced detwinning has also been observed. [220] Li et al. [260] reported ITB migration in Cu film after Cu^{3+} ion irradiation, and attributed their migration to the glide of grain boundary Shockley partial dislocations, driven by concurrent reduction in radiation-induced defects. Yu et al. [202] observed continuous migration and recovery of ITB steps at the corners of thick twins in epitaxial nt Ag film under *in-situ* Kr^{++} irradiation and inferred that the TB evolution is due to defect-ITB interactions. Song et al. [261] studied radiation-induced TB migration in Fe using atomistic simulations and demonstrated that the event might be enhanced by local thermal spike and defect clusters. Chen et al. [220] reported that the radiation-induced detwinning in nt Cu depends on twin thickness: the thinner the twins the faster the detwinning process. These studies suggest that radiation-induced detwinning is closely associated with the interaction between ITBs and radiation-induced defect clusters.

In this chapgter, we examined the radiation-induced detwinning for twins of various thicknesses in annealed Cu subjected to *in-situ* Kr ion irradiation experiment. Several distinct types of defect-ITB interactions were identified. The underlying mechanisms of radiation-induced thickness-dependent detwinning are compared. This study contributes to further understanding on heavy ion irradiation response of nt metals.

5.3 Experimental

Cu films, ~ 80 nm in thickness, were DC sputter deposited at room temperature using 99.99% purity Cu target onto sample grids supported with carbon film for transmission electron microscopy (TEM) studies. Prior to deposition, the chamber was evacuated to a base pressure of $\sim 8\times10^{-8}$ torr. Isothermal annealing was then performed for 20 minutes at 300 °C in ultra-high purity Argon gas. After annealing, a large number of annealing twins with various thicknesses were introduced in large grains. *In-situ* Kr ion radiation was conducted at room temperature at the Intermediate Voltage Electron Microscopy (IVEM) facility at Argonne National Laboratory. 1

MeV Kr^{++} ion beam was utilized for the radiation experiment, during which a CCD camera was used to capture microstructural evolution at 15 frame/s. Radiation damage in terms of displacement-per-atom (dpa) inside Cu film was calculated using the SRIM (Stopping and Range of Ions in Matter) simulation with Kinch-Pease method[205, 206]. The average dose rate was controlled at 2.5×10^{-3} dpa/s. The temperature rise of sample during irradiation was measured to be less than 10 °C.

5.4 Results

5.4.1 Irradiation-induced Detwinning

To explore the detailed morphology evolution process, large Cu grains with numerous annealing twins of various thickness were selected for examination. Figure 5.1(a) shows a typical example where 7 well-defined twins (labeled by arrows) in a Cu grain were monitored during their irradiations. All of these twins have one of their ITBs terminated in grain interior, and they are oriented in two sets of {111} planes at an interception angle of 71°. Figure 5.1(b)-(d) show morphology evolutions for several twins up to 1 dpa. Several ultrafine twins 1, 2 and 7 with thickness t < 10 nm, underwent drastic ITB migration and completely detwinned (after irradiation in Figure 5.1(d). Meanwhile, twins 4 and 5 with intermedium thickness (10 < t < 20 nm) experienced incomplete deVItwinning, shortened from their original lengths of 203 and 108 nm to 168 and 82 nm (see Figure 5.1(d)), respectively. However, thicker twins, 3 and 6 (t > 20 nm), survived the heavy ion irradiation with little ITB migration. The detwinning events are summarized and schematically illustrated in Figure 5.1(e), where the areas arising from ITB migrations are outlined by dashed lines. It is worth noting that no significant CTB migrations were observed, and the twins with both ends of ITBs anchored at grain boundaries remained stable after irradiation.

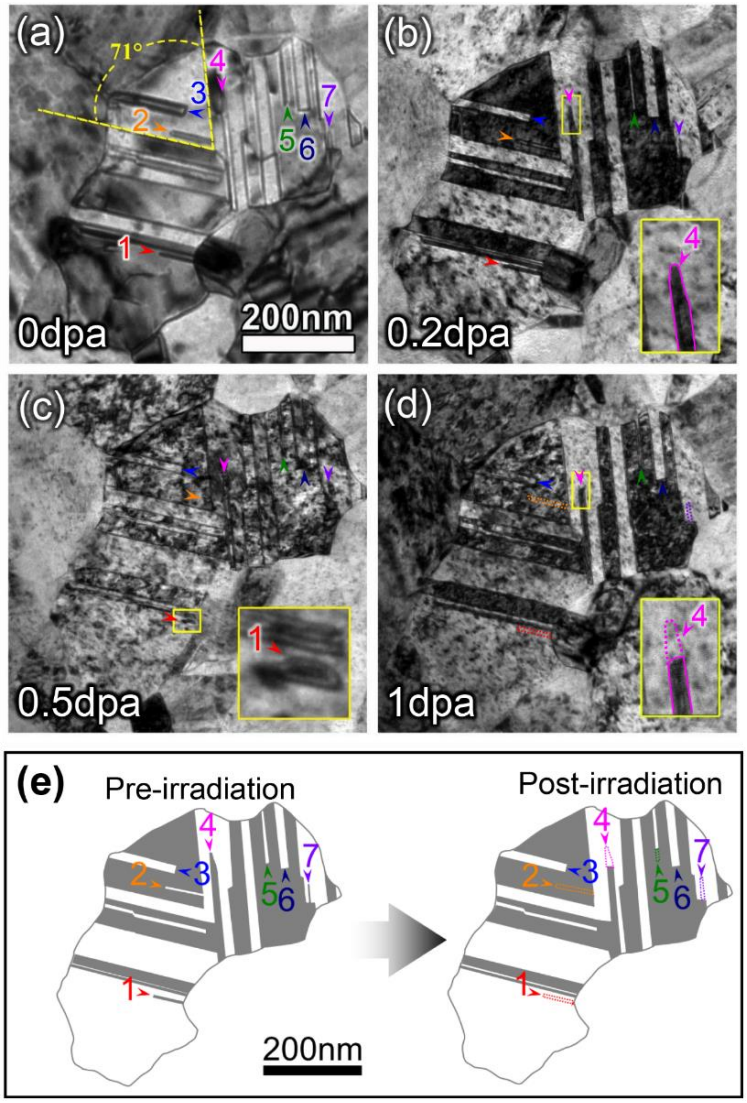

Figure 5.1. *In-situ* TEM snap shots and schematic illustration showing detwinning for various annealing twins inside a large Cu grain subjected to Kr^{++} irradiation up to 1 dpa at room temperature. (a) - (d) Sequential TEM micrographs taken at different doses showing the morphology evolution of several twins labelled as 1-7. The insets in (b) and (d) show the enlarged images of the end of twin 4, and the inset in (c) shows the remaining section of twin 1 at 0.5 dpa. (e) Schematic illustration depicting the morphology variation of the labeled twins.

In-situ TEM studies enable us to track the ITB migration in real time. The reduction of twin length shown in Figure 5.2(a) is a direct consequence of radiation-induced detwinning. Furthermore thinner twins have higher ITB migration velocity (V_{ITB}) as shown by the red circles in Figure 5.2(b), which is consistent with the data (shown as blue squares) derived from our previous studies on radiation-induced detwinning in epitaxial nt Cu films [220]. Moreover, radiation-induced

detwinning also depends on dose rate. The dose rate in the current study is $K_1 = 2.5\times10^{-3}$ dpa/s, higher than our previous study, $K_2 = 0.43\text{-}1.98\times10^{-3}$ dpa/s. A comparison of these two sets of studies reveals that V_{ITB} increases with increasing dose rate for the twins that are less than 20 nm in thickness. However, when the twins are thicker than 20 nm, there are little ITB migrations. In fact, ITBs tend to migrate at room temperature even without irradiation, which is driven by the excess energy stored in CTBs. Atomistic simulations have revealed that when the twin thickness is less than 2 nm, the driving force becomes so large that detwinning process can easily occur (in Cu) at room temperature (without irradiation) [120]. The value of V_{ITB} of non-irradiation case can be calculated based on annealing experiment [256], and it is also plotted as a reference in black in Figure 5.2(b). In contrast, radiation has prominently accelerated detwinning velocity.

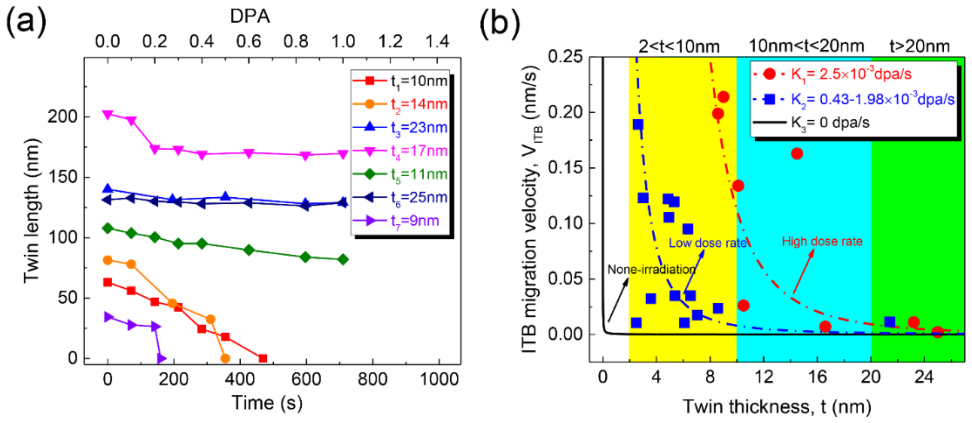

Figure 5.2. The dependence of ITB migration on twin thickness and dose rate at room temperature. (a) The plot of twin length over radiation dose for numerous twins. (b) The average ITB migration velocity (V_{ITB}) of the current study (plotted in red) decreases rapidly with increasing twin thickness at a high dose rate of $K_1 = 2.5\times10^{-3}$ dpa/s. The reference data of a low dose rate [220] ($K_1 = 0.41\text{-}1.98\times10^{-3}$ dpa/s) and non-irradiation($K_3 = 0$ dpa/s) are also plotted in blue and black, respectively [256].

5.4.2 Defect-ITB interactions and morphology evolutions

Heavy ion irradiation induces a large number of defect clusters in annealed Cu, and Figure 5.3 shows the statistics on the distributions of size (D) and lifetime (T) of defects. The defects have an average diameter (D_{avg}) of 5 nm and an average lifetime (T_{avg}) of 15.0 s.

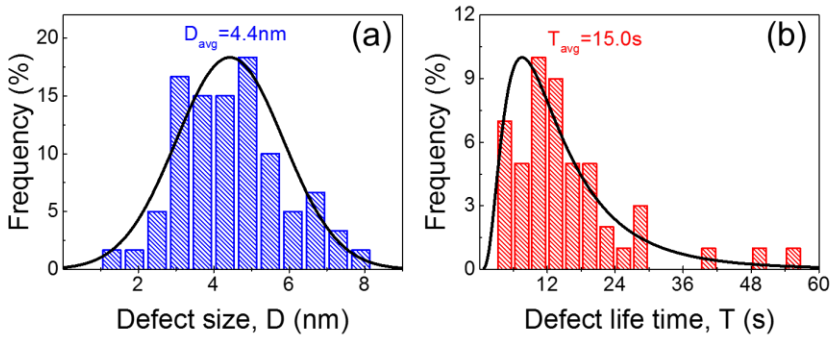

Figure 5.3. Histograms showing the statistics of (a) diameter D and (b) lifetime T of radiation-induced defect clusters in twinned Cu. The average defect size (D_{avg}) and lifetime (T_{avg}) are measured to be 5 nm and 15.0 s, respectively.

In addition, frequent defect-ITB interactions were observed by carefully examining the *in-situ* TEM videos. Figure 5.4 shows two distinct types of defect-ITB interactions for a twin T4, consisting of an ultrafine tip T4^a with a thickness t_4^a of 8 nm, and a medium-thick twin base T4^b with a thickness t_4^b of 17 nm. The defect-ITB interactions led to the removal of T4^a through two steps: a sharpening process as shown in Figure 5.4(a)-(c), and a collapsing process as shown in Figure 5.4(d)-(f). At 78s in Figure 5.4(a), T4^a had a flat end and a dislocation loop L1 was formed in its vicinity. At 80s in Figure 5.4(b), L1 began to grow and approached T4^a, and a direct contact (DC) occurred afterwards. At 94s in Figure 5.4(c), L1 was entirely absorbed and T4^a became quite pointed. The tip remained sharp for ~46s, see Figure 5.4(d). However, once L2 emerged near T4^a at 139.13s in Figure 5.4(e), the sharp T4^a collapsed as evidenced by instant detwinning at 139.40s in Figure 5.4(f); in other words, a non-contact (NC) defect-TB interaction had occurred. The detwinning velocity is ~ 80 nm/s.

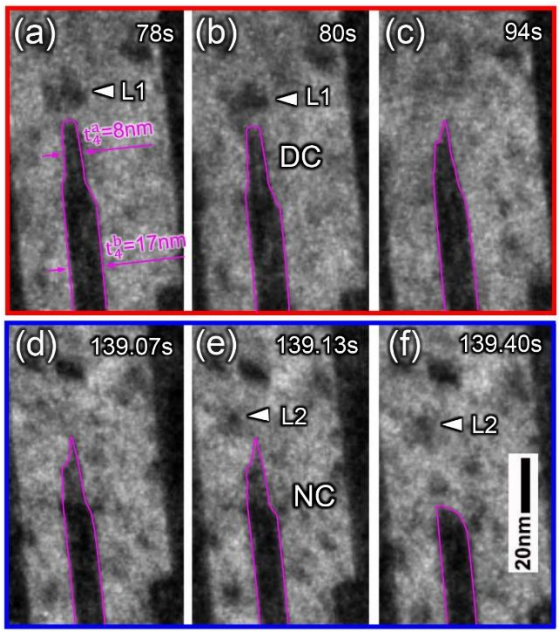

Figure 5.4. A series of TEM snap shots taken during *in situ* irradiation of nt-Cu over 0.1-0.2 dpa, showing the detwinning process for twin T4. Its tip section $T4^a$ is 8 nm in thickness, whereas the base portion, $T4^b$, is 17 nm thick. Two radiation-induced dislocation loops interacting with the ITB are indicated by L1 and L2. (a) - (c) The sharpening process of $T4^a$ caused by its direct contact interaction (DC) with L1. (d) - (f) The subsequent collapsing process of $T4^a$ triggered by its non-contact interaction (NC) with L2.

In addition to the drastic detwinning at the tip of ultrafine twin T4, a gradual detwinning event was observed. Figure 5.5(a)-(c) demonstrate the morphology evolution of twin T1 (t_1 = 10 nm) with increasing dose. At 50 s in Figure 5.5(a), T1 was 60 nm long. During irradiation, it was shortened to 41 nm in 30 s (Figure 5.5(b)), and then shrank to 18 nm in length at 370 s as shown in Figure 5.5(c). Meanwhile, frequent defect-ITB interactions were also captured, and two typical defect clusters that interacted with ITB are marked as L3 and L4. The average detwinning velocity for T1 is calculated to be ~ 0.12 nm/s. In comparison, a thick twin T6 (t_6 = 25 nm) showed self-healing capability. As shown in Figure 5.5(d), the corners of T6 were very sharp at 50 s, but they became blunted at 86 s (Figure 5.5(e)). By 156 s as shown in Figure 5.5(f), the two blunted corners became sharp (orthogonal) again.

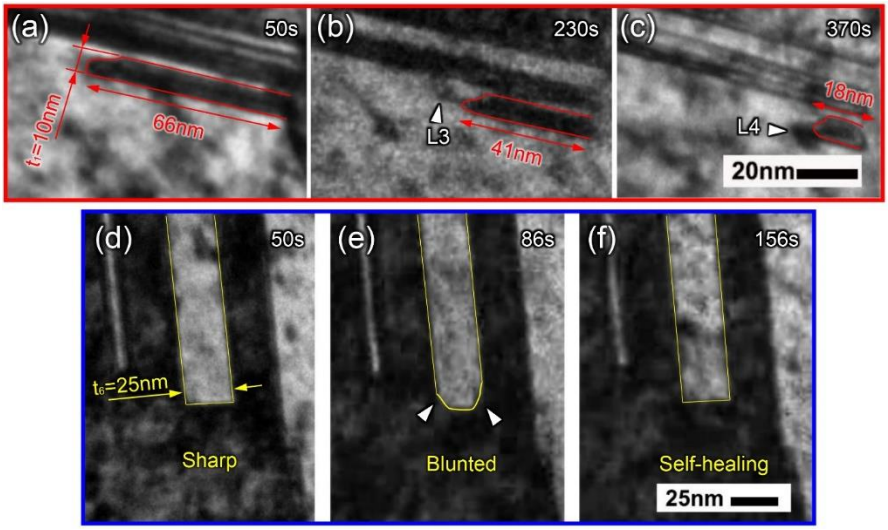

Figure 5.5. *In-situ* TEM observations showing the gradual detwinning of twin T1 and the self-healing capability of twin T6. (a)-(c) The length of twin T1 (thickness t_1 = 10 nm) decreased from 66 nm to 41 nm by 230s, and to 18 nm by 370s. Meanwhile, two typical defect clusters that interacted with the ITB were captured, marked as L3 and L4. (d)-(f) Twin T6 (t_6 = 25 nm) had two sharp corners at 50 s, and by 86 s both corners became blunted. However, by 156 s, the TBs with blunted corners have recovered, exhibiting a self-healing ability.

5.5 Discussion

5.5.1 Radiation-induced detwinning

To understand the detwinning behavior under irradiation, it is necessary to examine the ITB microstructure and its migration mechanism. Most twinning or detwinning processes typically occur via collective glide of multiple twin dislocations (TDs) in ITBs [120, 123, 257]. In face-centered cubic (FCC) metals, ITBs are composed of a set of three Shockley partial dislocations 1/6<112> on adjacent {111} planes [116]. These partials can migrate under applied shear stress, resulting in ITB migration [119, 247, 258] with a velocity V that can be expressed as [256]:

$$V = \frac{2\gamma}{t} M_0 e^{(-\frac{\Delta Q}{kT})} \qquad \text{Equation 5.1}$$

where t is the twin thickness, ΔQ is activation energy, k is Boltzmann's constant, and T is temperature. $M_0 e^{(-\frac{\Delta Q}{kT})}$ is defined as the ITB migration mobility, and $\frac{2\gamma}{t}$ is the net pressure or the main driving force of detwinning arising from the excess CTB energy γ, about 24 mJ/m^2 for Cu [262].

For the case of non-irradiation detwinning at room temperature as shown in Figure 5.2(b), its activation energy has been measured as ~0.90 eV/atom [256]. Under irradiation, ITB migration velocity accelerates significantly, especially for the twins thinner than 20 nm. Using Equation 5.1, we can determine that the average activation energy for the current radiation-induced TB migration is much lower, ~0.42 eV/atom. The reduced activation energy is attributed to the local shear stress τ arising from radiation-induced defect clusters [261]. According to the defect reaction rate theory, [263] ΔQ can be expressed in terms of shear stress τ as:

$$\Delta Q = \Delta Q_0 \left(1 - \frac{\tau}{\tau^c}\right)^{\alpha} \qquad \text{Equation 5.2}$$

where ΔQ_0 is the activation energy at τ = 0, and τ^c is the critical stress and α is a dimensionless exponential factor. MD simulations have revealed that the activation energy barrier and critical activation stress can be lowered in the existence of radiation-induced defect clusters [261]. Under heavy ion irradiation, numerous defect clusters are generated, and they can continuously impinge ITBs (see Figure 5.4) and apply shear stress on Shockley partials along ITBs. Consequently, the activation energy is reduced and the ITB migration velocity is increased.

5.5.2 Defect-ITB interactions

Figure 5.4 shows two distinct types of defect-ITB interactions that are defined as DC and NC. On one hand, DC occurs when a defect cluster is in direct contact with an ITB and is subsequently absorbed by the ITB. In FCC metals, heavy ion irradiation generates point defect clusters in form of dislocation loops, stacking fault tetrahedron (SFT) and voids [16, 36, 60]. Among them, dislocation loops are the most commonly observed, including both faulted and perfect loops [37, 175, 264-266]. The perfect dislocation loops are glissile and able to diffuse very fast in the densely packed <110> direction along their Burgers vector [47, 50, 267]. The mobility of perfect dislocation loops inevitably facilitates their interactions with ITBs, which may lead to the formation of Frank partials by:

$$\frac{1}{2}[\bar{1}\bar{1}0] + \frac{1}{6}[112] \rightarrow \frac{1}{3}[\bar{1}\bar{1}1] \qquad \text{Equation 5.3}$$

The Frank partials formed in ITBs are sessile and cannot glide under shear stress, but they may migrate back and forth via dislocation climb by absorbing vacancies or interstitials. This

mechanism can partially explain the ITB's sharpening process observed in Figure 5.4(a)-(c) and its self-healing capacity shown in Figure 5.5(d)-(f). On the other hand, these Frank partials can further absorb perfect loops with the opposite Burgers vector, resulting in their reverse transformation into Shockley partials through the following reaction:

$$\frac{1}{2}[110]+\frac{1}{3}[\bar{1}\bar{1}1]\rightarrow\frac{1}{6}[112] \qquad \text{Equation 5.4}$$

When ITBs are decorated by Shockley partials, they become mobile again and can migrate rapidly through stress-driven dislocation glide. NC can now occur through the mechanical impingement of adjoining defects on ITBs, as shown in Figure 5.4 (d) - (f).

In addition, it is worth pointing out that the characteristic of defects size and lifetime plays an important role in defect-ITB interactions. Statistic studies in Figure 5.3 show that the dimension of defect clusters is smaller than 10 nm and their lifetime is shorter than 60 s. This observation leads us to hypothesize that the influence of a defect cluster on an ITB may be limited by both space and time scale. For a thick twin, larger than 20 nm in thickness, there would be 4 representative scenarios of defect-ITB interactions, shown schematically in Figure 5.6(a), including A - corner twinning, B - middle detwinning, C - middle twinning, and D - corner detwinning. Here twinning (detwinning) refers to the extension (contraction) of an existing twin. Note that the first three scenarios, A, B and C, lead to the increase of the length of CTBs. Considering the small size and short lifetime of defect clusters, the scenarios of A, B and C are less energetically favorable over the scenario D in Figure 5.6(a). Consequently, the defect-ITB interactions for a thick twin may lead to detwinning process from the corner, as shown in Figure 5.6(b).

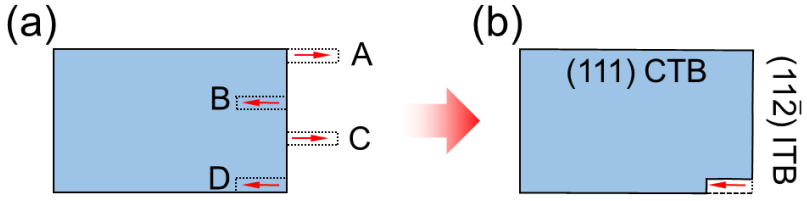

Figure 5.6. Schematics illustrating how a thick twin engages defect clusters (not shown here) and starts its detwinning from the corner. (a) Four potential scenarios of ITB migration are presented, including A - corner twinning, B - middle detwinning, C - middle twinning, and D - corner detwinning. (b) The corner detwinning of scenario D is more energetically favorable than the others, and it occurs more frequently in reality.

5.5.3 Thickness-dependent detwinning

We finally discuss the thickness-dependent detwinning mechanism for twinned Cu under Kr^{++} irradiation. The mechanism is schematically illustrated in Figure 5.7 and summarized as follows:

1. The ultrathin twins (t < 10 nm) in Figure 5.7(a1) - (a2), with thickness comparable to the size of radiation-induced defect clusters, may be more likely to undergo drastic detwinning via the glide of Shockley partials on ITBs. The drastic detwinning event may be triggered by local shear stress (τ) arising from a dislocation loop that is not in direct contact with the ITB (NC mode).
2. The twins with medium thickness (10 < t < 20nm) shown in Figure 5.7(b1) -(b3) may first experience a thinning process at twin corners. Then the sharpened tip may go through a rapid collapsing process resulting in a gradual detwinning.
3. The thick twins (t > 20 nm) shown in Figure 5.7 (c1) -(c2), are only subject to detwinning at twin corners through DC or NC interactions. After DC interactions, Frank partials are formed in ITBs, which are immobile and can slow down the detwinning process significantly. Meanwhile, Frank partials can have positive or negative climb by absorbing vacancies or interstitials, and Shockley partials can glide back and forth in accordance to the direction of local shear stress. As a result, thick twins can recover from their blunting outlines and possess a self-healing capacity.

The aforementioned detwinning mechanism is concluded based on defect-ITB interactions, which implies that the defect density around an ITB plays an important role in its migration. There are two factors that can influence the defect density. First, increasing dose rate can induce more defects, accompanied with more frequent defect-ITB interactions and faster ITB migration velocity as shown in Figure 5.2(b). Second, TBs and grain boundaries (GBs) can act as effective trapping sites that can influence defects formation and distribution [52-54]. For instance, T1, T7 and T5 have similar twin thicknesses, ~ 10 nm, but they have different length reductions after irradiation. Note that T5 is sandwiched between two TBs, but only one side of T1 and T7 has a TB. It can be inferred that less defects were formed in the matrix around T5, causing less detwinning, while more defects interacted with T1 and T7, leading to their full detwinning. In addition, thinner twins of T1, T2 and T7 in Figure 5.2(a) became rather unstable when their lengths were shortened down to 25 nm. As they became shorter, their ITBs migrated rapidly towards the GBs. Twin T5 had an

original length over 100 nm, and it detwinned much less than the shorter twins (T1 and T7 with a length of ~ 63 and 35 nm respectively) did under the same irradiation condition.

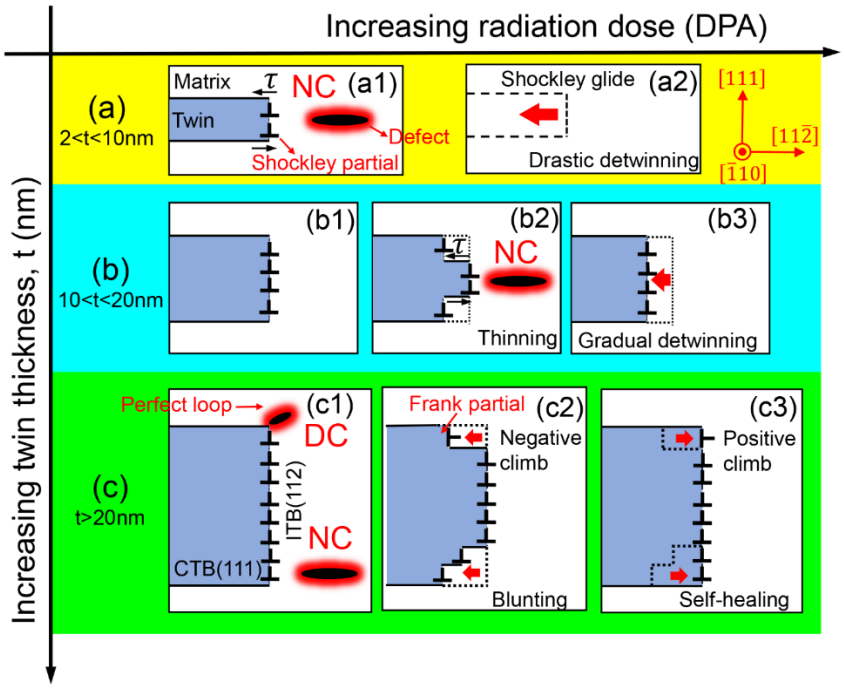

Figure 5.7. Schematic illustration of twin thickness-dependent detwinning during radiation. Two types of defect-ITB interactions, direct contact (DC) and non-contact (NC) interaction are marked. (a1) - (a2) The drastic detwinning of ultrathin twins (t < 10 nm) occurs via the glide of Shockley partials on ITBs. (b1) - (b3) The gradual detwinning of medium-thick twins (10 < t < 20nm), which starts from corner (sharping or thinning of the twin) and subsequent collapses of the sharpened tip. (c1) - (c3) The self-healing capacity of thick twins (t >20nm) occurs through climb of Frank partials or glide of Shockley partials from their ITB corners.

5.6 Conclusions

Using *in-situ* Kr ion irradiation, we have studied the radiation-induced detwinning in Cu containing high density annealing twins. The detwinning event exhibits dose-rate-dependence and thickness-dependence. Higher dose rate accelerates detwinning. Moreover, for thinner twins, less than 20 nm in thickness, radiation significantly accelerate the TB migration velocity. However, when the twin thickness exceeds a critical value, ~ 20 nm in the current study, twins tend to show self-healing capability as evidenced by back-and-forth migration of ITBs from corners. Two types of defect-ITB interaction modes, direct and non-direct contact, have been observed and account for the thickness-dependent detwinning mechanism.

CHAPTER 6. 9R PHASE ENABLED SUPERIOR RADIATION STABILITY OF NANOTWINNED CU ALLOYS VIA *IN SITU* RADIATION AT ELEVATED TEMPERATURE

The lab work was performed at Argonne National Laboratory by Cuncai Fan and Jin Li with guidance of Dr. Meimei Li. The data analysis and writing were completed by Cuncai Fan with guidance and editing by Dr. Xinghang Zhang.

6.1 Overview

Though nanotwinned metals exhibit outstanding radiation tolerance, our studies in Chapter 5 reveal that radiation can induce ITB migration and detwinning, which may reduce the radiation tolerance associated with twin boundaries, especially at elevated temperatures. In this chapter, we show, via *in-situ* Kr ion irradiation inside a transmission electron microscope, that 3 at. % Fe in epitaxial nanotwinned Cu ($Cu_{97}Fe_3$) significantly improves the thermal and radiation stability of nanotwins during radiation up to 5 displacements-per-atom at 200 ^{o}C. Such enhanced stability of nanotwins is attributed to a diffuse 9R phase resulted from the dissociation of incoherent twin boundaries in nanotwinned $Cu_{97}Fe_3$. The mechanisms for the enhanced stability of twin boundaries in irradiated nanotwinned alloys are discussed. The stabilization of nanotwins opens up opportunity for the application of nanotwinned alloys for aggressive radiation environments.

6.2 Introduction

Energetic particle irradiation of metallic materials produces large amounts of point defects (interstitials and vacancies), which can further aggregate into extended defect clusters in the form of dislocation loops [16, 37, 46, 159, 268], stacking fault tetrahedrons (SFTs) [89, 175, 176, 196, 269, 270] or cavities [30, 58, 60, 91, 229, 271-277], resulting in microstructural evolution and degradation of mechanical properties [11, 36, 83, 86, 210, 278]. It has been proposed that the

radiation tolerance of materials can be significantly improved by using defect sinks [169, 183, 185, 216, 279, 280]. Nanostructured materials contain abundant defect sinks and have shown enhanced radiation tolerance [83, 281-284]. Grain boundaries (GBs) are one of the effective defect sinks [98], and nanograined (NG) materials show enhanced radiation tolerance compared with their coarse-grained (CG) counterparts as evidenced by fewer defects [88, 181], reduced radiation hardening [85], stronger resistance to amorphization [31] and much less void swelling [91, 96]. However, due to the high excess energy of conventional high-angle GBs, NG materials often suffer from poor thermal stability [285], and radiation-induced grain coarsening can occur even at room temperature [27]. Design of nanomaterials that can survive harsh radiation environments at elevated temperatures remains a major challenge [5, 216].

Nanotwinned (NT) metals have raised significant interest due to their unique combination of remarkable mechanical properties [105-108, 114] and superior thermal stability [102, 136], as well as enhanced radiation tolerance [109, 142, 220, 286]. *In-situ* studies have revealed that twin boundaries (TBs) can frequently interact with radiation-induced defects and tailor their formation and distribution [109, 140, 141, 219, 220]. For instance, fewer defects are formed in NT Cu than in CG Cu under the same radiation conditions [220]. In addition, SFT, a notorious defect, can be destructed and removed by interacting with TBs [109].

In NT metals with face centered cubic (FCC) structure, there are two major types of TBs: $\Sigma 3$ $\{111\}$ coherent twin boundaries (CTBs) and $\Sigma 3$ $\{112\}$ incoherent twin boundaries (ITBs) [115, 287]. Extensive studies have shown that ITBs, containing arrays of Shockley partials, can migrate under irradiation [288], stress [119], heating [256] and electrical field [117]. As a result, detwinning occurs through ITB migration, decreases twin density, and compromises the performance of NT materials [202, 260]. Therefore, to further improve the radiation tolerance of NT metals, it is of great significance to stabilize TBs, especially the highly mobile ITBs.

In this study, we successfully synthesized epitaxial NT-$Cu_{97}Fe_3$ and compared its radiation response to that of NT-Cu by using *in-situ* Kr^{++} irradiation at 200 ℃ inside a transmission electron microscope (TEM). The *in-situ* studies show that, in contrast to rapid detwinning in NT-Cu, the sharp ITBs in NT-$Cu_{97}Fe_3$ evolve into diffuse 9R phase and are highly stable against radiation at elevated temperatures. ITB migration velocity in NT-$Cu_{97}Fe_3$ is significantly lower than that in NT-Cu, lending experimental support for stabilizing NT structures via the introduction of certain

solutes. *In-situ* studies also show that ITBs and CTBs in NT-$Cu_{97}Fe_3$ actively engage and eliminate radiation-induced defects.

6.3 Experimental

Highly-textured NT-Cu and NT-$Cu_{97}Fe_3$ alloy films, ~ 2 μm thick, were deposited on HF etched Si (110) substrates by using direct current magnetron sputtering technique at room temperature. Purchased pure Cu (99.995%) and Fe (99.99%) targets were used for sputtering, and the chamber was evacuated to a base pressure ~ 5×10^{-8} torr prior to deposition. During deposition, ~ 1.2×10^{-3} torr Ar working pressure was used, and the deposition rate was controlled at ~ 0.6 nm/s. After depositions, the TEM specimens for irradiations were prepared by polishing, dimpling and low energy (3.5 keV) Ar ion milling. Subsequent heavy ion (1 MeV Kr^{++}) irradiations on the cross-sectional TEM samples were conducted in the Intermediate Voltage Electron Microscope (IVEM) at Argonne National Laboratory, where an ion accelerator was attached to a Hitachi-9000 TEM microscope. More specific information regarding such *in-situ* heavy ion irradiation technique has been described elsewhere [166]. Before irradiation, the TEM specimens were annealed at 200 ºC inside the IVEM column for 30 minutes. Then it was followed by heavy Kr^{++} ion irradiations at 200 ºC. During the irradiation, a CCD camera was utilized to capture videos at 15 frames/s.

The texture of as-deposited films was analyzed using an X-ray diffraction technique on a Panalytical Empyrean X'pert PRO MRD diffractometer with a Cu $K\alpha_1$ source. All the as-prepared and irradiated TEM samples were examined by a Thermo Fischer Scientific/FEI Talos 200X microscope with Super-X EDS detectors. The Stopping and Range of Ions in Matter (SRIM) simulation with Kinch-Pease method was used to estimate the radiation damage in unit of displacements-per-atom (dpa) [205, 206]. As the Fe content is pretty low in NT-$Cu_{97}Fe_3$, the radiation damage was estimated based on pure Cu. SRIM simulations calculated for pure Cu (Supplementary Figure S1) show that ~ 99% of Kr ions have penetrated through TEM foils, leaving most radiation damage behind. The average ion dose rate was ~ 2.5×10^{-3} dpa/s, and the maximum radiation damage was 5 dpa with a total fluence of 1×10^{15} ions/cm^2.

6.4 Results

Figure 6.1 demonstrates the texture analysis of as-deposited Cu and Cu-Fe films. The conventional two-theta scans in Figure 6.1(a) show both films are highly {111} textured along growth direction. The Phi scans in Figure 6.1(b) show the diffraction peaks from both twin and matrix orientations with nearly identical intensity, indicating the formation of significant growth twin structures.

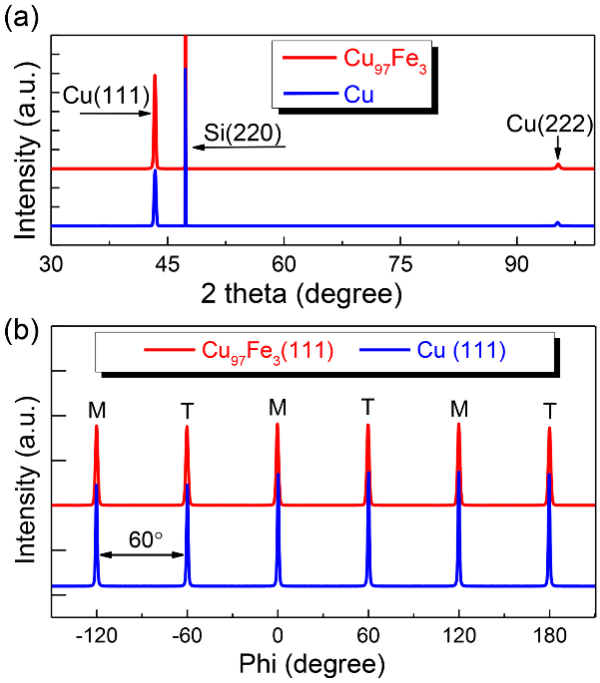

Figure 6.1. Texture analysis of XRD profiles of sputtered Cu (blue) and $Cu_{97}Fe_3$ films (red) on Si (110) substrates. (a) Two-theta scans showing strong (111) texture along growth direction for both films. (b) Phi-scan profiles with a six-fold symmetry, indicating a significant fraction of twins in both Cu and $Cu_{97}Fe_3$ films. M and T denote three matrix and twin peaks, respectively.

Figure 6.2 compares the microstructural evolution of NT-Cu and $Cu_{97}Fe_3$. Cross-section TEM micrographs show that nanotwins in Cu have a smaller average twin spacing, ~ 5 nm, comparing with ~14 nm for the NT-$Cu_{97}Fe_3$. The twin spacing here is defined as the distance between two adjacent CTBs [220]. No obvious TB migrations were observed during the annealing process at 200 ^{o}C for 30 min. However, once radiation started, detwinning took place in NT-Cu, giving rise to significant increase in twin spacing, as shown in Figure 6.2(a1-a4). In contrast, nanotwins in NT-$Cu_{97}Fe_3$ exhibited superior stability, and most of TBs survived after irradiation to 5 dpa, as shown in Figure 6.2(b1-b4). Statistic studies in Figure 6.2(c1) and (c2) show the irradiation-

induced prominent increase of average twin spacing (λ_{ave}) in NT-Cu from 5 to 29 nm (after 5 dpa), while the λ_{ave} in NT-$Cu_{97}Fe_3$ increased slightly from 14 to 16 nm.

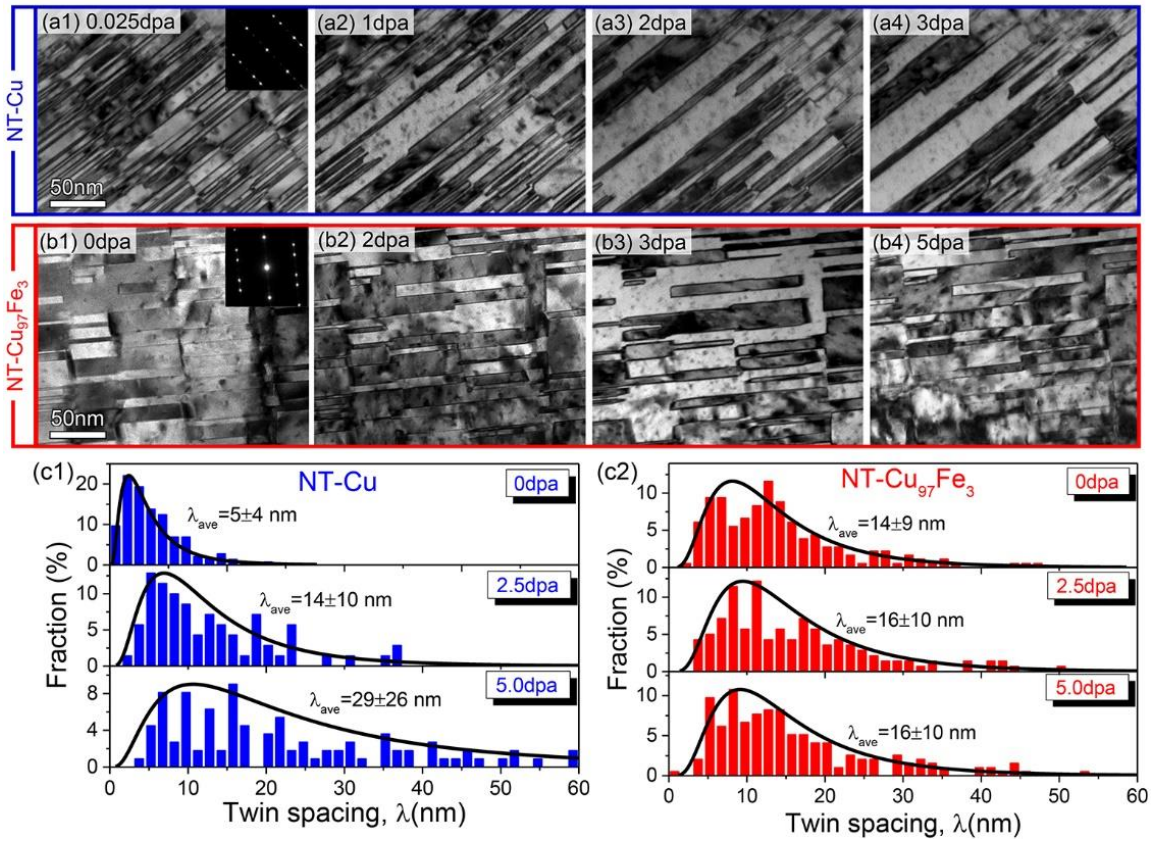

Figure 6.2. Evolution of nanotwins in NT-Cu and NT-$Cu_{97}Fe_3$ under Kr^{++} irradiation at 200 °C. (a1-a4) Irradiation-induced significant decrease of twin density in NT-Cu. (b1-b4) Superior stability of nanotwins against irradiation in NT-$Cu_{97}Fe_3$ to 5 dpa. (c1-c2) Statistical distributions show that the average twin spacing (λ_{ave}) of irradiated NT-Cu increases significantly from 5 to 29 nm, whereas the λ_{ave} in NT-$Cu_{97}Fe_3$ increases slightly from 14 to 16 nm.

The irradiation-induced detwinning event is attributed to defect-TB interactions. Figure 6.3 compares the irradiation response of CTBs. It has been found that CTBs can become curved to accommodate defect clusters formed in the vicinity. Since defect clusters are often small and have transient lifetime [110, 219], they introduce local and temporary distortion (in form of curvatures) along CTBs. As shown in Figure 6.3, the local curved CTBs were frequently observed in both cases and they exhibited surprising resilience and self-healing ability. In NT Cu at ~ 1.8 dpa in Figure 6.3(a1), the CTBs in the twin appeared straight at 0 s. At 6 s in Figure 6.3(a2), the CTB became curved. However, by 19 s in Figure 6.3(a3), the distorted CTB had recovered and restored

its straight appearance. Similarly, in NT $Cu_{97}Fe_3$, the upper CTB appeared straight at 0 s (~ 2.5 dpa) in Figure 6.3(b1). At 6 s in Figure 6.3(b2), a local distortion was identified at position 1. By 25 s in Figure 6.3(b3), the distortion 1 had recovered, while a new distortion at position 2 occurred due to the interaction between the CTB and a defect cluster. At 27 s in Figure 6.3(b4), the distortion 2 also recovered.

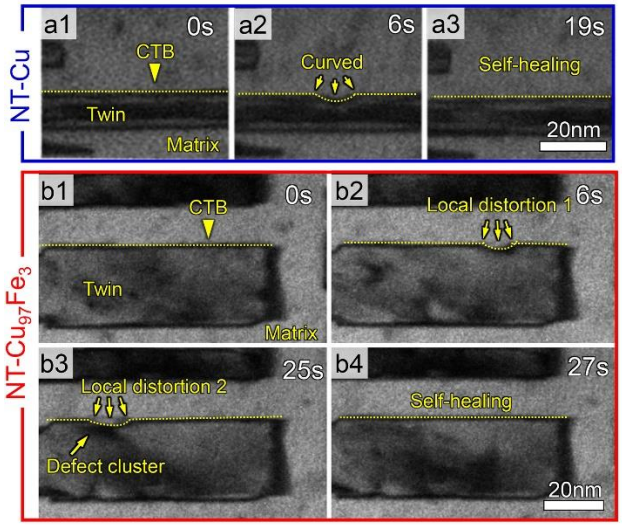

Figure 6.3. Local distortion and self-healing capacity of CTBs in NT Cu (a1-a3) and NT $Cu_{97}Fe_3$ (b1-b4).

By comparison, the ITBs in irradiated NT-Cu frequently migrated and showed prominent thickness-dependence. When the twin thickness (t) is several nanometers, ITBs migrate drastically. As shown in Figure 6.4(a), an ultrafine twin (3 nm in thickness) was 79 nm long at 0 s (~ 0.1 dpa). At 2 s in Figure 6.4(b), its ITB migrated abruptly by 38nm. By 10 s in Figure 6.4(c), the twin had fully retracted (disappeared).

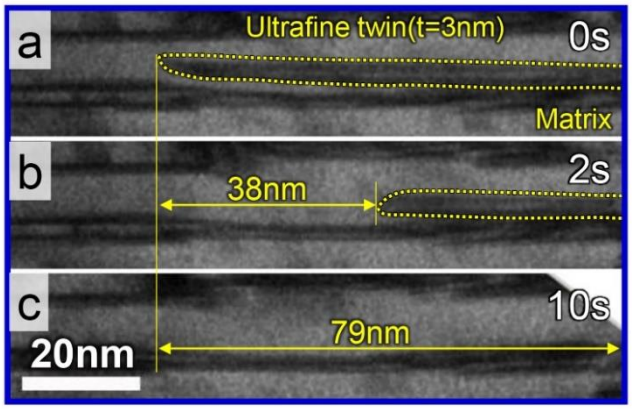

Figure 6.4. The drastic ITB migration of an ultrafine twin (~3 nm in thickness) in NT-Cu.

However, when t > 10 nm, ITB migration often starts from twin corners. As shown in Figure 6.5(a1) at ~ 3.1 dpa, T1 (t_1 = 13 nm) had a vertical ITB with two right corners. In 65 s in Figure 6.5(a2), the lower right corner retracted leftward by 10 nm and continued to retract by 13 nm after 69 s in Figure 6.5(a3). Meanwhile, the upper corner experienced detwinning by 6 nm by 65 s, and recovery by 76 s as shown in Figure 6.5(a4). With further irradiation to 126 s, both corners retracted by 14 nm and 20 nm, respectively, leading to a sharp tip in the middle of the ITB as shown in Figure 6.5(a5). The protrusion remained unchanged, until significant detwinning occurred instantaneously at 160 s in Figure 6.5(a6).

By comparison, the ITBs in NT-$Cu_{97}Fe_3$ remained stable regardless of twin thickness. For instance, three typical twins (T2, T3 and T4) with various thickness were monitored during irradiation (2.4 - 2.8 dpa) as shown in Figure 6.5(b1-b6). No ITB migration was observed, even for the ultrafine twin T2 (t_2 = 3 nm). Note that the ITB of T3 (t_3 = 12 nm), as shown in the box in Figure 6.5(b1), was initially sharp, but subsequently dissociated into a 3-nm-wide diffuse ITB after 98 s in Figure 6.5(b4). The diffuse ITB extended further to be 4 nm wide, as shown in Figure 6.5(b6). T4 (t_4 = 27 nm) has a diffuse ITB, which is 7 nm wide and its width remained unchanged during irradiation. The diffuse ITB absorbed a large defect cluster, an SFT in its vicinity, as shown in Figure 6.5(b2-b3). Meanwhile, CTBs also actively engaged in absorbing defects and became curved locally, as marked by the green arrows in Figure 6.5(b2-b6).

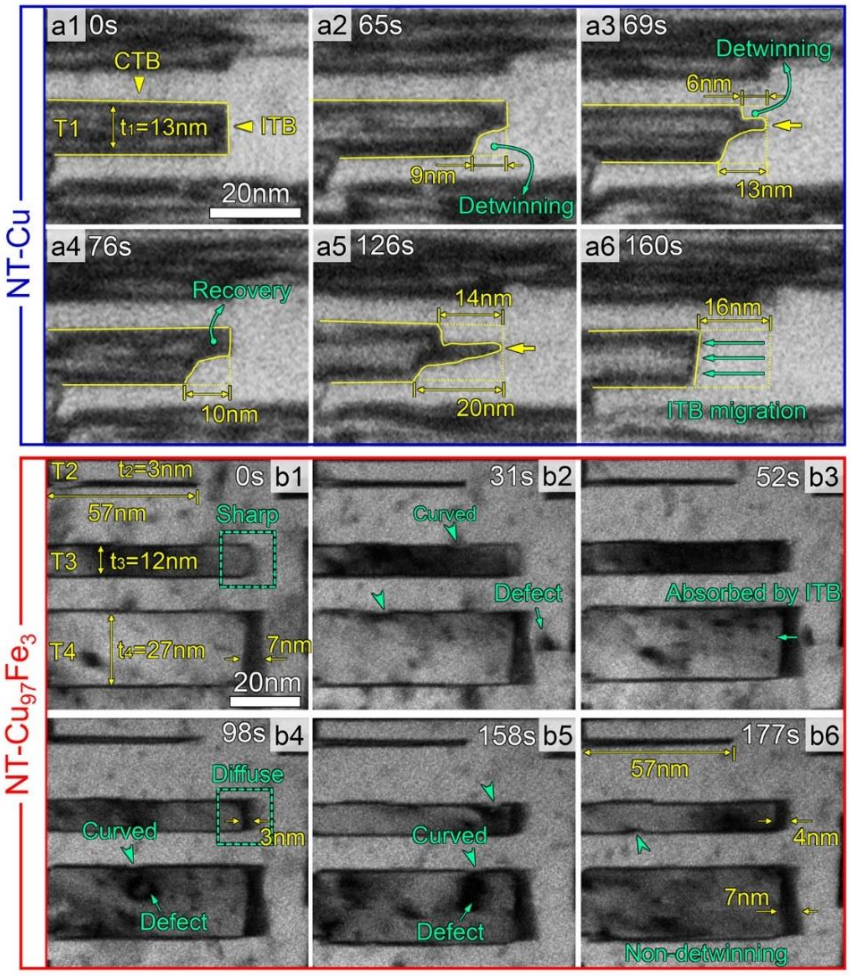

Figure 6.5. *In-situ* TEM snapshots comparing the distinct irradiation responses of ITBs between NT-Cu and NT-$Cu_{97}Fe_3$. (a1-a6) The gradual ITB migration and detwinning of T1 (t_1 = 13nm) in NT-Cu (3.1-3.5 dpa). (b1-b6) The stability of TBs against irradiation (2.4-2.8 dpa) in NT-$Cu_{97}Fe_3$. No detwinning was observed regardless of twin thickness.

High-resolution TEM (HRTEM) experiments were performed to examine the evolution of TBs in irradiated NT-Cu and NT-$Cu_{97}Fe_3$ along <110> zone axis. Before irradiation, as shown in Figure 6.6(a1) and (b1), the CTBs are sharp, and the ITB width is narrow, ~1 nm in both systems. After irradiation to 5 dpa, numerous stacking faults (SFs) emerged in NT-Cu along CTBs, and the thickness of SF ribbon is ~2 nm, whereas the thickness of CTBs in irradiated NT-$Cu_{97}Fe_3$ increases slightly in Figure 6.6(b2). The ITBs of irradiated NT-Cu remain narrow (~1 nm), while the irradiated ITBs in NT-$Cu_{97}Fe_3$ have dissociated into a slab bounded by two curved phase boundaries. A typical example of the dissociated ITB in NT-$Cu_{97}Fe_3$ is shown in Figure 6.6(b2). The lower-left inset shows the dissociated ITB region has a repeatable pattern, identified as 9R

phase, which is also confirmed by the inserted fast Fourier transform (FFT). Note that in Figure 6.5(b6) the dissociated ITB region of T4 is wider than that of T3, and it appears that the width of dissociated ITBs varies with twin thickness as will be shown later. HRTEM images in Figure 6.6(a3) and (b3) also reveal that the defect clusters in NT-Cu are dominated by high-density triangular SFTs, whereas the defects in NT-Cu include SFTs and prismatic dislocation loops.

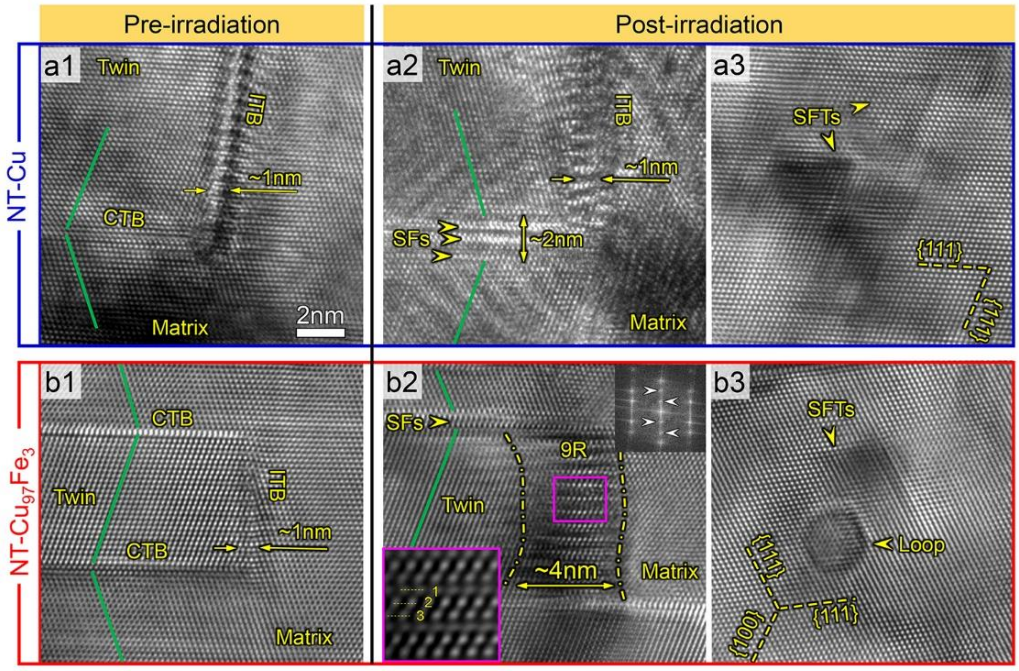

Figure 6.6. HRTEM micrographs of TBs and irradiation-induced defects in NT-Cu and NT-$Cu_{97}Fe_3$ before and after irradiation (5 dpa). (a1) and (b1) TBs are sharp in both systems prior to irradiation. (a2) In irradiated NT-Cu, ITBs remain sharp, but CTBs are decorated with SF ribbons. (a3) Irradiation-induced triangular SFTs in NT-Cu. (b2) Radiation of NT-$Cu_{97}Fe_3$ induces broad ITBs, identified as 9R; but CTBs remain largely unchanged. (b3) The irradiated NT-$Cu_{97}Fe_3$ contains SFTs and prismatic dislocation loops.

In-situ TEM technique permits the determination of ITB migration velocity (V_{ITB}). Figure 6.7(a) indicates that irradiation induces ITB migration in NT-Cu, and the V_{ITB} decreases with increasing thickness (t). Moreover, V_{ITB} of NT-Cu increases significantly with increasing irradiation temperature (to 200 ^{o}C). In contrast, the ITBs in NT-$Cu_{97}Fe_3$ barely migrate during irradiation at 200 ^{o}C. In addition, Figure 6.7(b) illustrates that the ITB width (W_{ITB}) of irradiated NT-Cu has little variation and remains ~1 nm. In comparison, the W_{ITB} of irradiated NT-$Cu_{97}Fe_3$ elevates with increasing t , ranging from 3 to 10 nm.

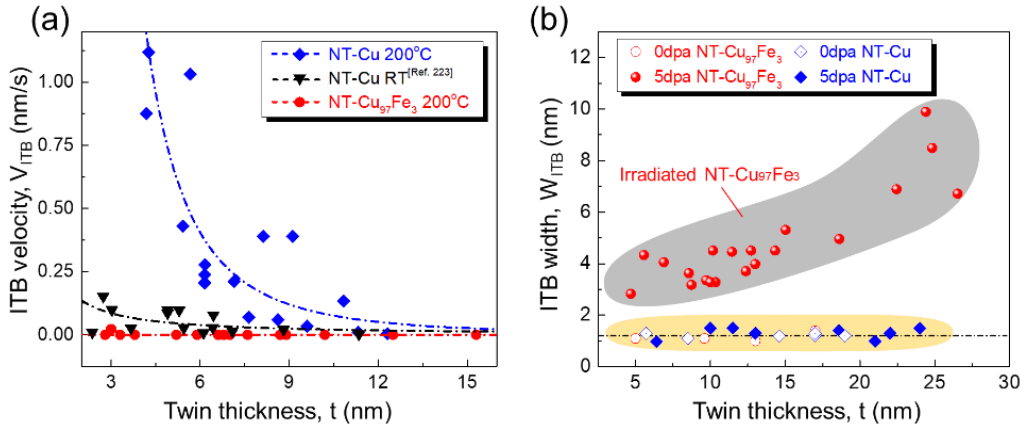

Figure 6.7. Irradiation-induced evolution of ITB velocity (V_{ITB}) and width (W_{ITB}), plotted as a function of twin thickness (t) for NT-Cu and NT-$Cu_{97}Fe_3$. (a) V_{ITB} increases rapidly with decreasing t for NT Cu or at higher irradiation temperature. A reference black data set of NT-Cu irradiated at room temperature (RT) is also plotted [220]. The V_{ITB} is extremely low and barely changes for NT-$Cu_{97}Fe_3$ even for finest twins (t < 5 nm). (b) W_{ITB} of NT-Cu remains constant, ~ 1 nm, after radiation. However, the W_{ITB} of the irradiated NT-$Cu_{97}Fe_3$ increases monotonically with t.

6.5 Discussion

6.5.1 Thickness and temperature dependent detwinning in NT-Cu

Our *in-situ* TEM observations reveal that CTBs exhibit surprising resilience and self-healing ability in response to irradiation, as shown in Figure 6.3. This is determined by the nature of irradiation-induced defect clusters and interactions with CTBs. Since defect clusters are often small and have transient lifetime [110, 219], they introduce only local and temporary distortion (in form of curvatures) along CTBs. Moreover, previous studies show that the SFT-CTB interactions can lead to the formation of multiple SFs [109, 110]. This is also confirmed by our post-radiation HRTEM analysis in Figure 6.6(a2) and Figure 6.6(b2), which show that CTBs appear 'thicker' after irradiation.

Our *in-situ* observations also show that irradiation-induced detwinning occurs primarily through ITB migration. The ITBs in FCC Cu are composed of three types of mobile Shockley partials on successive (111) planes [116, 121, 122]. Figure 6.8(a1) schematically illustrates the ITB structure, including one pure edge partial (b_1) and two mixed partials (b_2 and b_3). This dislocation model has the advantage of relating ITB structure to its migration or dissociation.

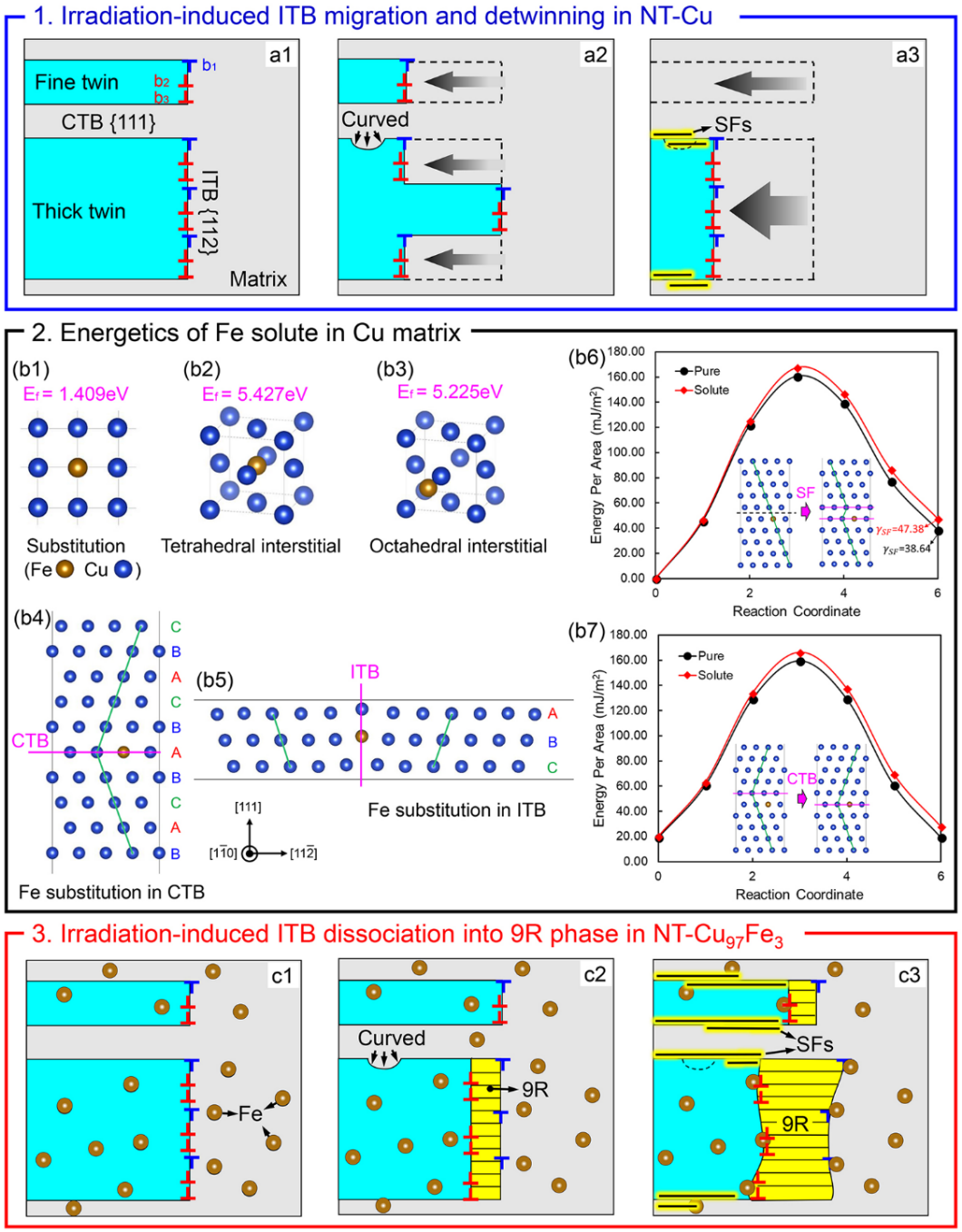

Figure 6.8. Irradiation responses of TBs in NT-Cu and NT-$Cu_{97}Fe_3$. (a1-a3) Irradiation-induced ITB migration and detwinning in NT-Cu. (b1-b7) DFT calculations of the energetics of Fe solute in Cu lattice, SF plane, CTB and ITB. (c1-c3) Irradiation of NT-$Cu_{97}Fe_3$ induces dissociation of ITBs into 9R phase, which is pinned by Fe solute atoms, and thus prohibit detwinning. In addition, irradiation can cause CTB distortions in form of curved TBs in both NT-Cu and NT-$Cu_{97}Fe_3$.

ITBs in pure metals can migrate under shear stress through the collective glide of partials [258, 289], known as the phase-boundary-migration (PBM) mechanism [120, 123]. Impingement of defect clusters during radiation can enhance TB migration by lowering the activation energy barrier for dislocation glide [261]. Consequently, heavy ion irradiation induces ITB migration and detwinning in NT-Cu, as shown schematically in Figure 6.8(a1-a3). The ITB migration velocity, V_{ITB}, in NT-Cu is closely associated with twin thickness (t). The driving force, $2\gamma_{Twin}/t$, for ITB migration increases with decreasing t [220], and γ_{Twin} is twin boundary energy for $\Sigma 3\ \{111\}$, approximately ½ of γ_{SF}, with γ_{SF} being the stacking faulty energy (SFE). When t is comparable to the size of defect clusters, the entire ITB can migrate rapidly (see Figure 6.4), and thus a fine twin is more likely to undergo detwinning, as shown in Figure 6.8(a2-a3). For a thicker twin ($t >$ 10 nm), however, detwinning often starts from twin corners, presumably because the migration of ITBs from corners does not change the total length or energy of the TBs [256]. If this analysis is correct, the reverse process, twinning from corner should also occur when local shear stress reverses its sign. Indeed, this hypothesis has been confirmed by our *in-situ* TEM observations in Figure 6.5(a3-a4). At elevated temperatures, the Shockley partials possess higher mobility due to a reduced friction stress, and the driving force for detwinning also increases, and thus the ITB migration velocity increases further in NT-Cu.

6.5.2 Energetics of Fe solutes in Cu

In-situ studies show that a small amount of Fe solute atoms (~3 at. %) in NT-Cu can significantly enhance TBs stability against irradiation at elevated temperatures. First, there is much less detwinning in the irradiated NT-$Cu_{97}Fe_3$ alloy irrespective of original twin thickness (see Figure 6.2). Many fine twins survived irradiation, in drastic contrast to the rapid detwinning in NT-Cu. Second, the TB migration velocity in NT-Cu increases sharply with decreasing twin thickness. In irradiated NT-$Cu_{97}Fe_3$, however, TBs barely migrate. Third, our study shows that ITB migration velocity in NT-Cu increases significantly during irradiation at elevated temperatures. Irradiation of NT-$Cu_{97}Fe_3$ at the same temperature leads to little sign of detwinning.

To understand the influence of Fe on TB stability, we examined the energetics of Fe solute in Cu lattice with respect to their locations according to density functional theory (DFT) calculations. The detailed calculation procedure can be found in the Supplementary Information. The Vienna ab-initio simulation package (VASP) is used to perform calculation with projector augmented

wave (PAW) method[290] and generalized gradient approximation (GGA) approach[291]. During the calculation, spin polarization is considered, and the Perdew-Burke-Ernzerhof (PBE) function[292] is employed. The pseudopotential with electron configuration $3d^{10}4s^1$ and $3d^7 4s^1$ is used to describe the behavior of Cu and Fe ion, respectively[293]. The bulk properties are computed with a 3×3×3 supercell containing 106-108 Cu atoms and 0-4 Fe atoms. The slab models for a coherent twin boundary (CTB) and stacking fault (SF) have 10 layers on (111) plane. In each plane, there are 16 atoms. The (112) ITB slab models are constructed with 3 layers on (111) plane and 6 layers on $(\bar{1}10)$ plane. The model contains 104-105 Cu atoms and 1 Fe atom. The first Brillouin zone of bulk models and slab models are sampled with a 3×3×3 and a 4×4×1 M-P k-mesh[294]. A 400eV cut-off energy is used for all calculations in this study. The convergence criteria of geometry optimizations and self-consistent calculations is 0.01eV/Å and 10^{-5}eV respectively. To verify the rationality of parameters used in computations, the properties of copper and iron are calculated with unit cell sampled with a 9×9×9 M-P k-mesh. For copper, the calculated lattice constant is 3.629 Å and the cohesive energy is 3.48 eV. For BCC iron, the lattice constant is 2.2866 Å and the cohesive energy is 4.855 eV. These properties are consistent with previous studies[295-297].

The results show that the formation energy (E_f) of a single Fe solute is 1.409 eV for substitution site (Figure 6.8(b1)), 5.427 eV for tetrahedral interstitial (Figure 6.8(b2)) and 5.225 eV for octahedral interstitial site (Figure 6.8(b3)). In comparison, E_f of Cu self-interstitial atom for tetrahedral and octahedral site is 3.901 and 3.488 eV, respectively, much lower than that of Fe interstitial. These results show that Fe solute prefers to stay at substitutional site and can hardly diffuse via interstices. E_f of Fe substitutions pair located at different neighboring sites is also calculated. For the first, second, third, and fourth nearest sites, the formation energies are 2.294, 2.744, 2.805 and 2.766 eV, respectively. E_f of four Fe atoms at nearest substitutional sites is 1.533 eV. Therefore, the segregation of Fe atoms is energetically preferred. But, as mentioned earlier, the diffusion of Fe is energetically difficult, so the Fe solutes are expected to be homogeneously distributed in Cu matrix during deposition, which is consistent with our EDS analysis shown in Figure 6.9.

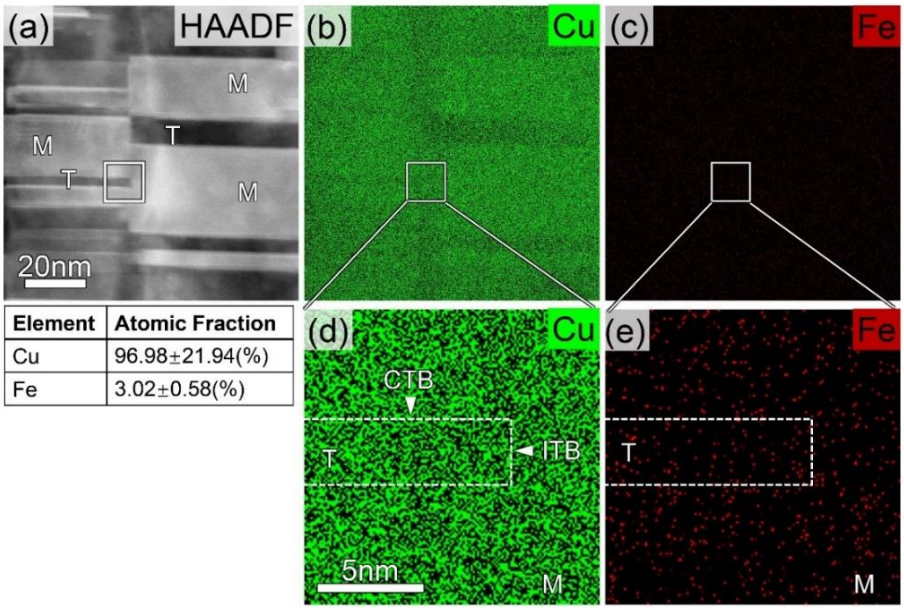

Figure 6.9. Composition mapping of as-deposited NT-$Cu_{97}Fe_3$. (a) Typical STEM HAADF image of the NT-$Cu_{97}Fe_3$. (b) and (c) corresponding EDS elemental maps of Cu and Fe, respectively. The square box focuses on an ITB. (d) and (e) Enlarged view of the square box showing the uniform distributions of Cu and Fe atoms in twin and matrix.

The formation energies of Fe solutes at SF plane, CTB (Figure 6.8(b4)) and ITB (Figure 6.8(b5)) are also calculated. As shown in Figure 6.8(b6), the calculated stacking fault energy (γ_{SF}) of pure Cu is 38.64 mJ/m^2. If one of the 16 Cu atoms on a fault plane is replaced by an Fe atom, the stacking fault energy increases to 47.38 mJ/m^2. For the model with CTB, the segregation energy of Fe, the energy change for moving Fe atom from defect free crystal to the twin boundary, is 0.048 eV, which suggests that the CTB is not the preferred site for Fe solutes. The energy barrier of CTB migration shown in Figure 6.8(b7) increases by adding Fe solutes. In addition, the formation energies of Fe solutes in ITB at substitutional and interstitial sites are 0.623-0.824 eV and 1.669-1.750 eV, respectively. The lower formation energies indicate that ITBs are thermodynamically favorable sites for Fe solutes.

6.5.3 Mechanisms of irradiation stability of nanotwins in NT-$Cu_{97}Fe_3$

Post-radiation TEM studies in Figure 6.6(b2) show that the ITBs in irradiated NT-$Cu_{97}Fe_3$ dissociate into a broad 9R phase, bounded by two phase boundaries. Furthermore, the width of 9R phase increases with increasing twin thickness, as illustrated in Figure 6.7(b). Such an observation

has profound impact on TB stability and radiation tolerance of irradiated NT Cu-Fe alloys and warrants further discussions.

First, the ITB dissociation occurs through the glide of arrays of Shockley partials [116, 298]. When an ITB is subjected to shear, τ_{yx}, the glide force on the partial dislocation b_1 is expressed by [120]:

$$F_x = -\tau_{yx} b_1 + F_{b_1 b_2} + F_{b_1 b_3} + \gamma_{SF} + F_P \qquad \text{Equation 6.1}$$

The first term on the right in Equation 6.1 represents the driving force for migration of b_1 under external shear stress. The resistance for the migration of b_1 arises from $F_{b_1 b_2}$ and $F_{b_1 b_3}$, the attractive force between b_1 and b_2 (b_3); the stacking fault energy, γ_{SF}, and the friction force due to Peierls stress, F_P. During irradiation of monolithic NT-Cu, defect clusters will generate a shear stress that drives the migration of ITBs [140]. The γ_{SF} of Cu is low, and F_P is typically negligible in Cu, and thus the resistance to the migration of TB is relatively low.

Our DFT calculations show that Fe can increase the γ_{SF}, consequently the resistance for ITB migration increases substantially in NT Cu-Fe alloys. Also the growth twin density in as-deposited NT-$Cu_{97}Fe_3$ is lower than that in as-deposited NT-Cu, in agreement with the twin nucleation theory in sputtered films that suggests a higher γ_{SF} leads to a lower probability of twin nucleation [114]. Moreover, post-radiation TEM studies show that a majority of defect clusters in irradiated NT-Cu are SFTs; however, both SFTs and large prismatic dislocation loops are observed in irradiated NT-$Cu_{97}Fe_3$ alloy. Prismatic loops are often observed in irradiated materials with higher γ_{SF} [41].

Second, it has been shown in monolithic NT metals, that the edge Shockley partial and two mixed partials migrate together due to their mutual attractive forces [120]. MD simulations have shown that the edge partial, b_1, tends to migrate first under shear. The attractive force between b_1 and b_2 (b_3) then drag the two mixed partials to move together, leading to the migration of ITBs. The current study shows that radiation of NT-Cu did not change its width of ITBs, ~ 1nm. However, the width of ITBs in irradiated NT-$Cu_{97}Fe_3$ increases rapidly during irradiation to 3-10 nm. Thus, the attractive force between b_1 and b_2 (b_3) decreases, making the migration of ITBs difficult. *In-situ* TEM studies show that broad 9R in twinned Ag is unstable, and can "zip" together into a sharp ITB under e-beam irradiation to relax internal stress, and migrates rapidly thereafter [298]. As the

9R phase is stabilized by Fe solute and remains broad in the irradiated NT-$Cu_{97}Fe_3$, its migration becomes difficult.

Third, our *in-situ* radiation studies in Figure 6.5(b1-b6) show that 9R phase in NT $Cu_{97}Fe_3$ is an excellent defect sink, as it can capture and absorb defect clusters, such as dislocation loops and SFTs. Consequently, the 9R phase becomes broader, as schematically shown in Figure 6.8(c2). Since thicker twins have greater probability to capture defect clusters [110], the width of their 9R increases with twin thickness, as shown in Figure 6.8(c3). 9R and CTBs can thus form an effective defect-sink network, contributing to the remarkable radiation tolerance of NT-$Cu_{97}Fe_3$ alloy.

The dissociation of an ITB into 9R phase has been reported in pure Au [299], Ag [300] and Cu [121] with low γ_{SF} [301]. It has been concluded that the degree to which ITBs dissociate depends not only on the local stress state within specimen but also on the stacking fault energy [124]. Our study suggests that using appropriate solutes may effectively stabilize 9R phase in various metallic materials. Recently, high-density 9R phase has also been reported in sputtered NT Al-Fe [302], Al-Ti [303] and Al-Mg [304] solid solution Al alloys. These studies reveal that 9R phase is also beneficial for improving the mechanical properties (high strength and plasticity) of NT metals. The current study suggests that 9R phase coupled with the selection of appropriate solutes may significantly enhance the radiation resistance and stability of nanotwins in a broad range of metallic materials.

6.6 Conclusions

Nanotwinned Cu and $Cu_{97}Fe_3$ were *in-situ* irradiated using Kr^{++} at 200 ^{o}C under the same condition inside a transmission electron microscope. Monolithic NT-Cu experiences prominent detwinning through ITB migration, whereas the nanotwins in NT-$Cu_{97}Fe_3$ alloy remain stable. The outstanding radiation and thermal stability of TBs in NT-$Cu_{97}Fe_3$ arises from the dissociation of ITBs into a broad 9R phase, which also actively absorbs radiation induced defects. The enhanced twin stability is also attributed to the dragging effect of Fe solutes on the dissociated ITBs. These findings provide an important step forward towards the design of stable radiation resistant nanotwinned alloys under extreme environments.

CHAPTER 7. RADIATION INDUCED NANOVOID SHRINKAGE IN CU AT ROOM TEMPERATURE: AN IN-SITU STUDY

The radiation experiment was performed at Argonne National Laboratory by Cuncai Fan and Zhoangxia Shang with guidance of Dr. Meimei Li. The phase-field simulation was performed by Rayaprolu Goutham Sreekar Annadanam at Purdue University with guidance of Dr. Anter El-Azab. The data analysis and writing were completed by Cuncai Fan with guidance and editing by Dr. Xinghang Zhang.

7.1 Overview

Radiation induced void swelling is widely observed in a variety of metallic materials. In this chapter, by using sputtering deposition technique, we have introduced faceted nanovoids into Cu films. *In-situ* Kr ion irradiation was subsequently performed at room temperature to investigate the evolution of nanovoids. Most nanovoids were found to shrink gradually with increasing dose. Post-irradiation analyses revealed that irradiation induced high-density vacancy clusters in the form of stacking fault tetrahedrons. Phase field modeling revealed that void shrinkage arises from biased absorption of interstitials. These findings provide insights to the physical mechanisms of radiation response of nanovoids in metallic materials.

7.2 Introduction

The irradiation of metallic materials with energetic particles creates atomic displacements in crystalline lattice and results in large concentrations of point defects, including vacancies and self-interstitial atoms (SIAs) [11]. The point defects then agglomerate into defect clusters, such as dislocation loops, stacking fault tetrahedrons (SFTs), and voids [36, 37, 46, 196, 211]. Such defects typically cause microstructural change and lead to significant degradation in the physical and mechanical properties of the irradiated material [181, 278, 305, 306]. To design advanced radiation

tolerant materials, it is essential to explore how such defect clusters evolve and interact with other defects during irradiation [5, 83].

Irradiation-induced voids are of great interest for material performance, because they are directly related to volumetric swelling [62, 212, 275, 307-309]. Extensive efforts have been devoted to investigating void formation and swelling mechanisms [310-312]. Experimentally, it has been demonstrated that void swelling behavior shows strong temperature dependence [40, 60]. At low temperatures, void growth is limited by low vacancy mobility; at higher temperatures, however, void growth is suppressed by vacancy emission from voids [60] and accelerated vacancy-interstitial recombination [11]. Moreover, post-irradiation transmission electron microscopy (TEM) studies have revealed that the void morphology in irradiated metals often exhibits facets corresponding to low-index crystallographic planes [58]. For instance, irradiation-induced faceted voids have been reported in Ni [58], Mg [276], Cu [60], Cu-Ni alloys [313], and stainless steels [314]. However, *in situ* studies on void evolution under irradiation are still limited. Theoretically, the morphology evolution of voids is a complicated process, which involves thermodynamic factors of surface energy change and kinetic considerations governed by interfacial reactions [56, 59, 66-68]. Phase-field simulation can capture the morphological evolution of interfaces in various materials and recently it has been successfully applied for describing the void formation and evolution in irradiated metals [59, 66-70].

In this study, we applied *in-situ* TEM technique to investigate the evolution of faceted nanovoids in Cu under Kr ion irradiation at room temperature (RT). The nanovoids were introduced prior to irradiation, originating from the diffusion and collection of high concentrated non-equilibrium vacancies during physical vapor deposition (PVD) process [315]. Our studies show that such nanovoids shrink and the aspect ratio of these irregular nanovoids also changes during radiation. It is hypothesized that the shrinkage and aspect ratio change of voids are primarily due to the dominant absorption of interstitials. We used the phase field modeling to gain insight on the role of interstitial in void evolution in irradiated Cu.

7.3 Experimental

2-micron-thick Cu films were sputter-deposited on HF-etched Si (112) substrates at RT. The film texture was analyzed using an X-ray spectroscopy with a Cu $K\alpha_1$ source. Plan-view TEM specimens were prepared by polishing, dimpling and low-energy Ar ion-milling methods. TEM

specimens were then irradiated with 1 MeV Kr ion beam up to a maximum fluence of 1×10^{14} ions/cm^2, at RT at the Argonne National Laboratory. More details regarding such *in-situ* heavy ion irradiation technique has been reported and described elsewhere [166]. The Stopping and Range of Ions in Matter (SRIM) simulation with Kinchin-Pease method was used to estimate the radiation damage in unit of displacements-per-atom (dpa) [205, 206]. According to SRIM simulation results, the maximum radiation damage was around 0.5 dpa with a constant dose rate ~ 0.003 dpa/s. Before and after irradiation the specimen was carefully examined by a Thermo Fischer Scientific/FEI Talos 200X microscope.

7.4 Results

Conventional XRD profile in Figure 7.1(a) shows the epitaxial growth of Cu (110) film on the Si (112) substrate. Plan-view TEM micrographs recorded at under-focus (Δf = -1.5 μm) and over-focus (Δf = +1.5 μm) conditions (Figure 7.1(b-c)) reveal the formation of faceted nanovoids with dark and white Fresnel fringes. The inset selected area diffraction pattern in Figure 7.1(b) confirms the formation of single-crystal-like Cu (110) film. The high-resolution TEM (HRTEM) image in Figure 7.1(d) shows a typical nanovoid with facets on $\{111\}$ planes and elongated along <112> direction. The length (L) and width (W) of such elongated nanovoids are measured as 17 ± 3 and 7 ± 2 nm, respectively.

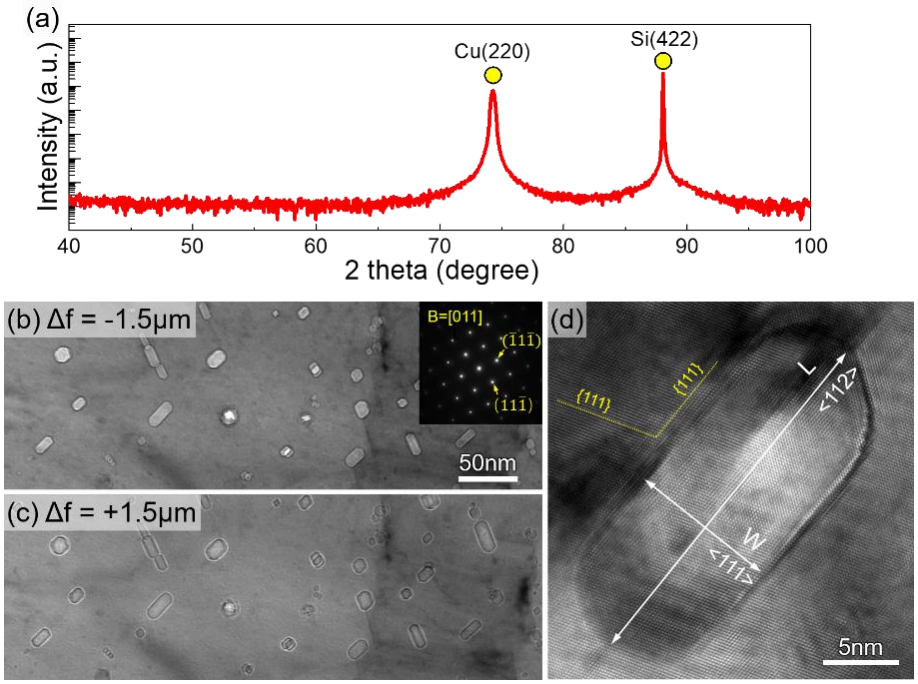

Figure 7.1. Texture analysis, and microstructure characterization of as-deposited Cu (110) with nanovoids. (a) XRD pattern suggests the epitaxial growth of Cu (110) film on Si (112) substrate. (b-c) Plan-view TEM micrographs of faceted nanovoids in Cu films at under-focus and over-focus imaging conditions. (d) HRTEM image of a typical faceted nanovoid with long side parallel to the {111} plane

Figure 7.2(a-e) are sequential TEM snapshots at the same location that show the evolution of nanovoids under irradiation. As shown in Figure 7.2(a), numerous defect clusters are formed surrounding pre-existing nanovoids at 0.1 dpa. During irradiation, these nanovoids shrank gradually. Some small nanovoids, as marked by arrows in Figure 7.2(a) and (b), were eliminated beyond a certain dose level. Some large nanovoids, as marked by circles, survived the irradiation up to 0.5 dpa. The lower right insets in Figure 7.2(a-e) show the enlarged views of a large nanovoid that contracted continuously during irradiation. It is worth mentioning that a large number of defect clusters in Figure 7.2(e) are invisible, as the TEM specimen was tilted away from the standard zone-axis in order to reveal nanovoids. A tilted TEM micrograph in Figure 7.2(f) examined along the <110> zone axis at a similar location clearly resolves a significant amount of defect clusters. Figure 7.2(g-i) show the geometry variation for numerous nanovoids over 0.1-0.3 dpa. As shown in Figure 7.2(g) and (h), both the length and width of nanovoids retract linearly with increasing dose, but the length reduces much more rapidly than the width (26 vs. 8 nm/dpa). For smaller

nanovoids, such as the red triangular data points (L = 9 nm) in Figure 2(i), the aspect ratio (W/L) increases from ~ 0.45 to 0.7. In contrast, for some larger nanovoids, such as the blue diamond data points (L = 18 nm) as shown in Figure 7.2(f), the aspect ratio remains unchanged.

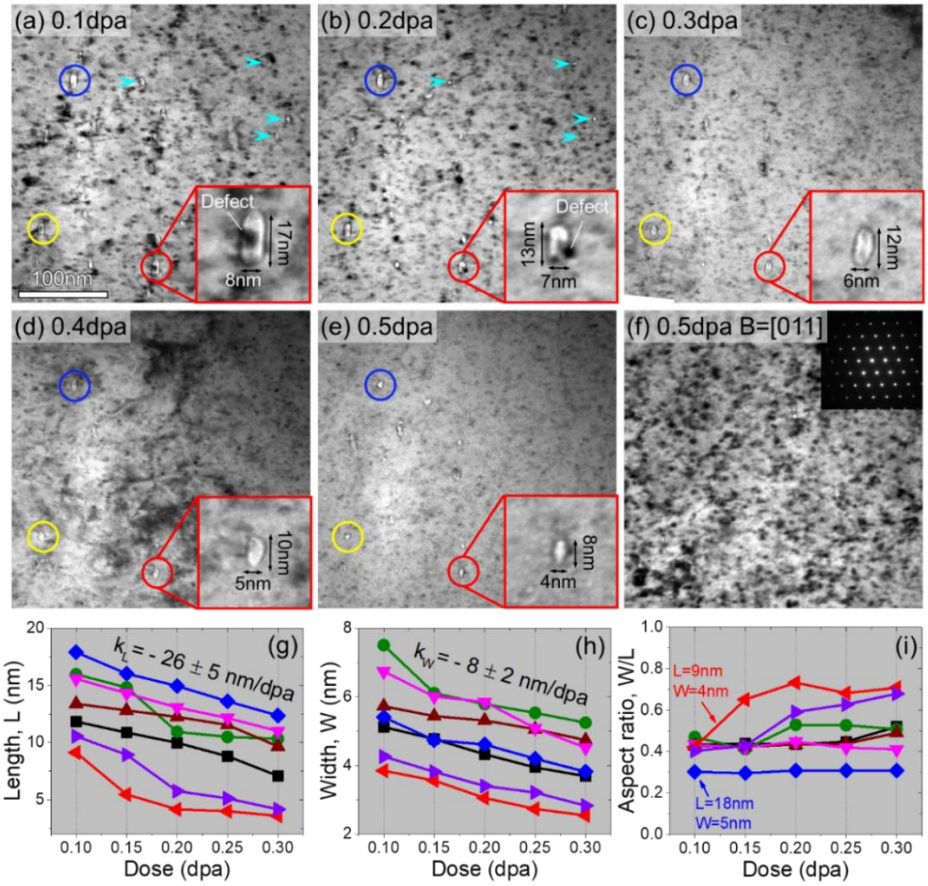

Figure 7.2. (a-e) Sequential TEM snapshots revealing the void shrinkage (0.1-0.5 dpa). (f) TEM micrograph taken at a similar position to (e) but along <110> zone axis reveals a significant number of defect clusters after irradiation to 0.5 dpa. (g-i) Dimension change of nanovoids with increasing dose.

The image characteristics of irradiation-induced defect clusters depend sensitively on the diffraction conditions chosen [37]. During irradiations some of the defects might be invisible because of sample drifting and tilting. To identify the irradiation-induced defect clusters, post-irradiation TEM analysis was performed. Figure 7.3(a) is the bright-field TEM image that shows two remaining nanovoids surrounded by numerous SFTs. SFTs are a general type of 3-dimensional vacancy clusters in irradiated face-centered-cubic (FCC) metals with medium-to-low stacking fault energies [39]. Projected from <110> direction, they often have a triangular shape as

confirmed by the HRTEM observation in Figure 7.3(b). The average density of SFTs is ~ $5.5\times10^{23}/m^3$, and their average edge length (L_{SFT}) is ~ 2.4 nm, as shown in Figure 7.3(c).

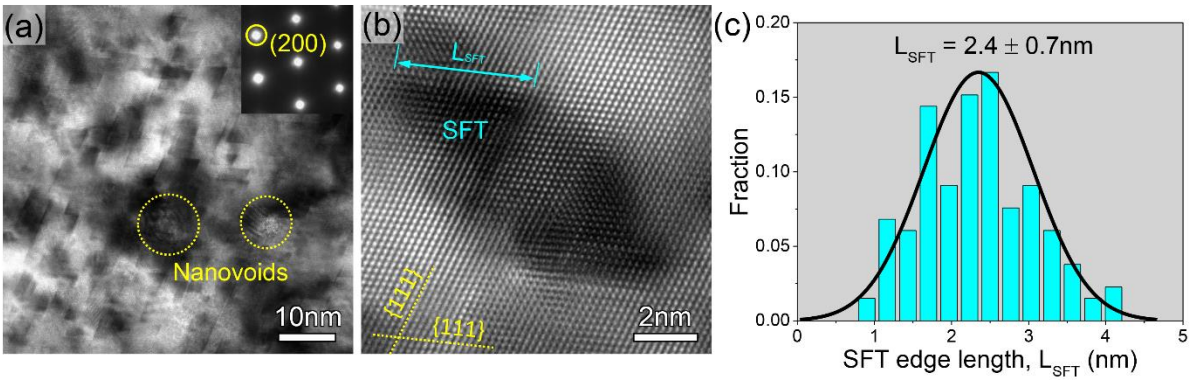

Figure 7.3. (a-b) Post-irradiation TEM analysis identifying the defect clusters in the form of SFTs. (c) The statistic distribution of dimension of irradiation-induced SFTs.

Radiation induced void swelling has been widely observed in irradiated metallic materials [310, 311], and the magnitude of void swelling typically scale with radiation dose and the swelling rate is greater for austenitic stainless steels (~1% /dpa) than that for ferritic/martensitic steels (~ 0.2%/dap) [30, 91]. Swelling was not observed in the current study in Cu (110) with nanovoids. Instead nanovoids shrink continuously during radiation. In what follows we will briefly discuss the mechanisms of void shrinkage and the anisotropic nature of void shrinkage process.

The radiation effect on microstructural evolutions is determined by the kinetic and dynamic process of interstitials and vacancies and their clusters. Heavy ion irradiation creates equal numbers of interstitials and vacancies, and the interstitials are highly mobile at RT due to their low migration energy, ~ 0.12 eV for Cu [11]. Most of the radiation-induced interstitials would be annihilated through interstitial-vacancy annihilation within cascades [316]. The rest can escape from cascade damage zones and diffuse through the sample until they disappear at various sinks. Some of these free interstitials might be absorbed by free surfaces (top or bottom) of TEM foil, and others might diffuse into nanovoids and result in void shrinkage, as reported in irradiated nanovoid-nanotwinned Cu [169, 218]. In comparison, vacancies have a high migration energy, ~ 0.8 eV for Cu, and they become fully mobile only when temperature increases [11]. Therefore at room temperature, instead of long-range migrations, they exist in the form of SFTs [41], a sessile 3-dimensional vacancy cluster with a pyramidal configuration, as shown by their projection images

in Figure 7.3(b). It is worth noting that the SFTs could also act as point defect sinks and continuously grow or shrink by absorbing interstitials or vacancies. According to previous molecular dynamic studies, the interaction of point defects with a SFT is strongly dependent on its position and size [317]. The shrinkage or growth of SFTs is through the nucleation and movement of jogs along a face of tetrahedra. However, such processes are significantly suppressed for small tetrahedra at low temperature [317]. Our post irradiation analysis in Figure 7.3 reveals that a high density of tiny SFTs remains in irradiated samples, indicating their high stability during their interactions with point defects. The free interstitials in current study, therefore, are assumed to be primarily absorbed by free surfaces of TEM foil or preexisting nanovoids.

To validate our hypothesis that the void shrinkage at RT is due to a biased absorption of interstitials, phase-field modeling was applied to determine the void evolution in Cu. The simulation was performed in two-dimensions with a thin film configuration as shown in Figure 7.4(a). The model used was developed and reported elsewhere [318]. The simulation domain has 151 × 101 grid points in total, with the solid region occupying 101 × 101 grid points and the rest being empty space on both sides of the film. Two faceted nanovoids, with the same aspect ratio (0.4) but different sizes, are initialized at the center of the domains. The small void in Figure 7.4(a) is 10 grid points long and 4 grid points wide, and the large void in Figure 7.4(b) is 40 grid points long and 16 grid points wide. The concentration of point defects is initially taken to be equal to the thermal equilibrium concentration. To model the low temperature irradiation scenario, the following ratio of point defect diffusivities is assumed: $D_i / D_v = 60$. This ratio, which indicates that interstitial mobility is much higher than vacancy mobility, is consistent with the diffusion of vacancies and interstitials in FCC metals at low temperature [67]. In order to account for the observed SFTs, the free defects introduced by cascade damage are assumed to follow a biased cascade source – namely, the number of vacancies introduced in each cascade is 90 % of the number of interstitials. The surface energy anisotropy on void shrinkage is also included in the simulation model by making the gradient coefficient of the non-conserved order parameter orientation-dependent, as what has been reported in another study [69]. More detailed information about the phase-field simulation of irradiated metals can be found elsewhere [59, 66].

Figure 7.4 depicts the simulation results on void shrinkage under irradiation. At low temperature, as freely migrating interstitials have higher concentration and greater diffusivity than vacancies, they rapidly diffuse towards the void and deposit at the void surface. As such, the preexisting void

shrinks gradually as shown in Figure 7.4(a-g). Figure 4(h-j) present the time evolution of void geometry. Figure 7.4(h) indicates the small void shrinks much faster than the large one. Note that the void length reduction rate in Figure 7.4(i) is higher than width reduction rate. Consequently, the void aspect ratio in Figure 7.4(f) increases immediately for the small void. In contrast, the large void initially increases slowly in aspect ratio, but in later stages it rapidly becomes spherical when the void size reduces further. These simulation results agree qualitatively with our experimental observations (see Figure 7.2).

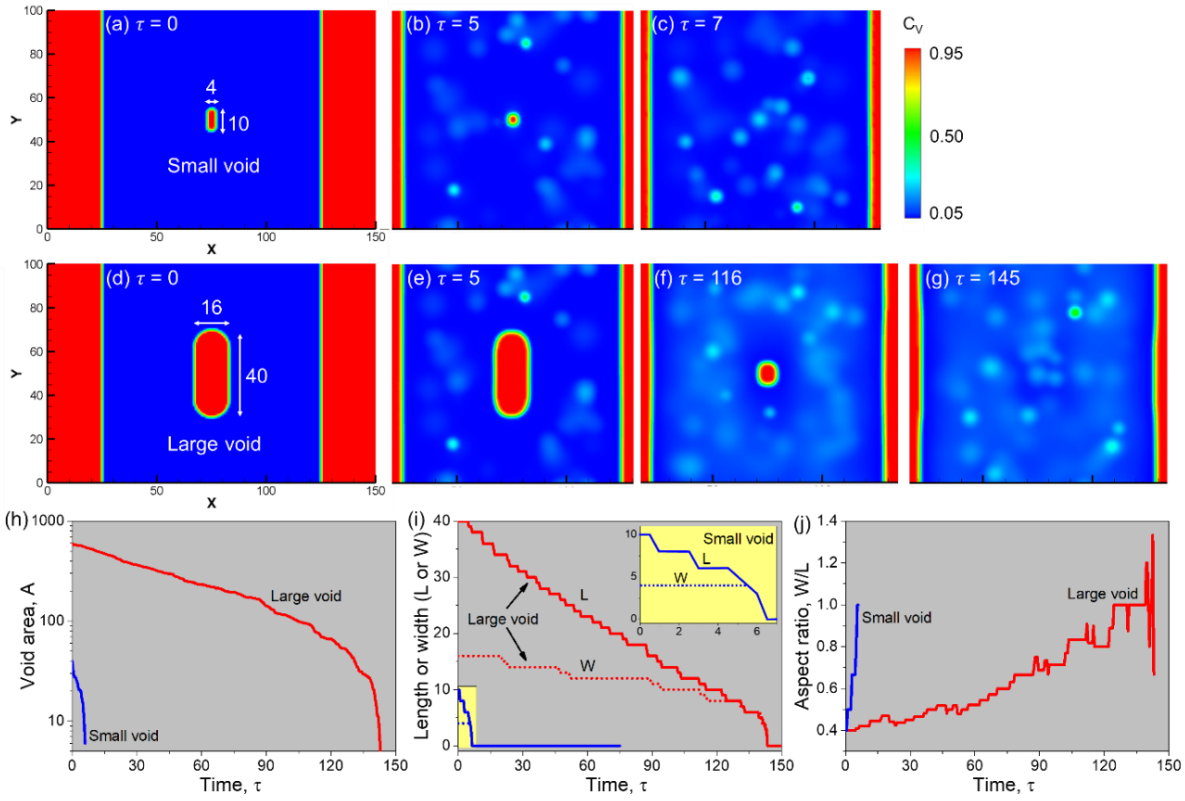

Figure 7.4. Phase-field simulations on the radiation-induced void shrinkage due to a supersaturated self-interstitial concentration at low temperature. (a-g) The evolution of vacancy concentration for a small void in (a-c) and a large void in (d-g). (h-j) Radiation-induced geometrical evolution for the small (blue lines) and large (red lines) void. (h) The reduction of void area (A, in logarithmic). (i) The reduction of void width (W, dotted lines) and length (L, solid lines). (j) The increment of void aspect ratio (W/L).

7.5 Discussion

We now examine the anisotropic shrinkage of nanovoids. *In situ* radiation studies show that the void length shrinks much faster than void width and eventually radiation leads to spheroidization

of nanovoids. The anisotropy is primarily attributed to the effect of void surface curvature. As shown in Figure 7.1(d), the elongated nanovoids are primarily faceted on {111} side walls that have little curvature, while both ends of the voids have a large curvature. The equilibrium interstitial concentration (C_i^{eq}) at the surface can be described by [319]:

$$C_i^{eq} = e^{-\frac{E_i^f + \Omega\kappa\gamma}{k_B T}} \qquad \text{Equation 7.1}$$

where κ is the void surface curvature (with positive sign) that equals the reciprocal of the radius for a spherical void , E_i^f is the interstitial formation energy, Ω is the atomic volume, γ is the surface energy, k_B is the Boltzmann constant, and T is the temperature. The equation indicates that the increase in surface curvature decreases the equilibrium concentration of interstitials at the surface, thus accelerating the diffusion of interstitials to the region of void surfaces with larger curvatures and leading to biased shrinkage (spheroidization) of elongated voids.

Given the curvature's effect on promoting spheroidization, one would anticipate that during radiation, most nanovoids should spheroidize first rapidly and then shrink during irradiation. However, our *in-situ* observations in Figure 7.2 show that large nanovoids (with L > ~ 15 nm) remain their lenticular shape during shrinkage, whereas spheroidization appears to occur faster in voids with smaller L (~10 nm or less). It is likely that the surface tension of smaller nanovoids is greater than that of larger nanovoids, and hence surface tension accelerates the spheroidization of small nanovoids. Chen *et al.* have shown that smaller nanovoids shrink faster in nanotwinned Cu as the tensile stress near the void surface is high [169]. The spheroidization process may also be accelerated at elevated temperatures when the surface mobility increases significantly. However, at elevated temperatures, the void shrinkage rate may decrease. Such a hypothesis requires further experimental validation in our future studies. But recent studies on temperature dependent shrinkage of nanopores in nanoporous Au suggest that higher temperature can indeed reduce the shrinkage rate of nanopores [211].

7.6 Conclusions

A fundamental understanding of void evolution is crucial for the design of advanced radiation tolerant materials with outstanding void swelling resistance. *In-situ* TEM irradiation studies of Cu with nanovoids, performed at room temperatures, show that preexisting elongated and faceted

nanovoids shrink continuously during irradiation. Small nanovoids spheroidize rapidly during radiation, whereas large nanovoids appear to maintain their aspect ratio during shrinkage. The shrinkage mechanism is ascribed to the supersaturated interstitials, while the less mobile vacancies cluster into SFTs. The variation of void aspect ratio is related to the anisotropic diffusion of interstitials into nanovoids and the surface tension of voids.

CHAPTER 8. *IN-SITU* STUDY ON HEAVY ION IRRADIATION-INDUCED NANOVOID EVOLUTION IN CU AT ELEVATED TEMPERATURES

The radiation experiment was performed at Argonne National Laboratory by Cuncai Fan and Zhoangxia Shang with guidance of Dr. Meimei Li. The phase-field simulation was performed by Rayaprolu Goutham Sreekar Annadanam at Purdue University with guidance of Dr. Anter El-Azab. The data analysis and writing were completed by Cuncai Fan with guidance and editing by Dr. Xinghang Zhang.

8.1 Overview

Understanding the radiation-induced void evolutions in metals is of great significance to the design of radiation tolerant materials, as radiation induced voids typically lead to the undesirable degradation of mechanical properties. The study in Chapter 7 shows that faceted nanovoids in Cu (110) shrink instead of swell when irradiated at low temperature. In this follow-up study, we perform *in-situ* Kr ion irradiations in a transmission electron microscope, at elevated temperatures up to 350 ℃. The *in-situ* studies reveal that heavy ion irradiation leads to void spheroidization and shrinkage. Furthermore, the morphology evolution of nanovoids shows a strong dependence on irradiation temperature and initial void size. Post-irradiation analyses identify vacancy clusters in the form of stacking fault tetrahedrons (SFTs), and the remaining large nanovoids faceted on low-index crystallographic planes. The mechanisms of radiation-induced void spheroidization and shrinkage are discussed based on phase field modeling.

8.2 Introduction

In the past several decades, the formation and growth of radiation-induced voids (or bubbles) have been intensively investigated because of their profound impact on the microstructure and mechanical properties of nuclear reactor materials [60, 212, 275, 307, 308, 320-324]. Nanovoids (NVs) are widely observed in metallic materials exposed to energetic electrons, protons, neutrons or heavy ions [30, 36, 86, 211, 311, 325]. The dimensional expansion of irradiated materials accompanied with the significant number of voids is frequently referred to as void swelling, which

usually leads to the degradation in mechanical properties, in form of irradiation hardening, embrittlement, and fracture [11, 72, 181, 326]. To design materials for advanced nuclear reactors, it is essential to explore the void growth and formation mechanisms in materials under radiation environment [5, 6].

A great deal of effort has been devoted to understanding the fundamentals of radiation-induced void swelling, which proves to be a complicated process that involves thermodynamic factors of surface energy variation and kinetic considerations governed by interfacial reactions [56-59]. Prior studies suggest that some key factors must be taken into consideration when dealing with the issue. First, according to post-irradiation transmission electron microscopy (TEM) studies, the geometry of radiation-induced NVs in most cases cannot be simply described as perfect spheres [58]. A couple of sophisticated configurations have been reported, differing in size and shape for various material [56, 313, 327, 328]. For most crystalline metals, NVs often exhibit facets that correspond to low-index crystallographic close-packed planes because of surface energy anisotropy [327]. For instance, faceted NVs were reported in irradiated Ni [58], Al [329], Mg [276], Cu [60], Cu-Ni alloys [313], and stainless steel [314]. Second, the void formation and growth show a strong dependence on irradiation temperature, and void swelling often reaches a peak value at intermediate temperature [40, 60, 310]. In principle, at low temperature the void growth is limited by vacancy diffusivity, but at high temperature it is suppressed by a loss of vacancy supersaturation due to accelerated recombination of opposite type of defects and the approach of the defect concentration to the thermal equilibrium value [11]. Moreover, there are some other factors that may impact the radiation-induced void swelling, including the presence of inert gas [61] and solute atoms [62], biased sinks [63], dose and dose rate [64], as well as internal stresses [65].

Phase-field simulation is an effective method for capturing the morphological evolution of interfaces in various materials science processes [330], and it has been applied successfully to describing the void formation and evolution in irradiated metals [59, 66-70]. Recently, we have used a phase field approach to explain the shrinkage of NVs in (110) Cu observed during *in-situ* (1 MeV) Kr^{++} irradiation at room temperature (RT) [232]. However, a systematic experimental study coupled with phase simulation that considers the influence of temperature on irradiation response of NVs is still lacking. Here we investigated in depth the temperature dependent irradiation damage in Cu (110) films with NVs. *In-situ* heavy ion irradiations in TEM were

performed over 190-350 ℃. The radiation experiments and phase field simulations provide important insight for the further understanding of kinetics of void evolution driven by irradiations.

8.3 Experimental

Ultra-high purity copper films (99.995 wt. %), ~ 2 μm thick, were deposited on HF-etched Si (112) substrates at room temperature (RT) using direct current magnetron sputtering technique. Before deposition, the chamber was evacuated to a base pressure < 8×10^{-8} torr. The deposition rate was controlled at ~ 0.6 nm/s. After deposition, the film texture was analyzed using an X-ray spectroscopy with a Cu Kα1 source. Before and after irradiation the TEM specimens were carefully examined by a Thermo Fischer Scientific/FEI Talos 200X transmission electron microscope operated at 200kV.

Plan-view and cross-section TEM specimens were prepared by polishing, dimpling, and low energy (3.5 keV) Ar ion milling. Subsequent *in-situ* TEM irradiations were conducted in the Intermediate Voltage Electron Microscope (IVEM) at Argonne National Laboratory, where an ion accelerator is attached to a Hitachi-900 TEM. All the radiation specimens were annealed for 0.5 h at 190, 250 and 350 ℃ prior to the 1 MeV Kr^{++} irradiation to a fluence of 2×10^{14} ions/cm^2. The radiation dose (in dpa) was calculated using Stopping and Range of Ions in Matter (SRIM) 2008 with Kinch-Pease method [205, 206], with a displacement threshold energy of 30 eV for Cu [11]. The calculations indicate that > 99 % Kr ions transmitted through the TEM foils, and more detailed SRIM simulation results can be found elsewhere [169]. The maximum dose was 0.5 dpa for the irradiation at 190 ℃, and 1.0 dpa for the cases at 250 and 350 ℃. The dose rate was controlled at ~ 0.0003 dpa/s.

8.4 Results

8.4.1 Faceted nanovoids in as-deposited Cu (110) films

Figure 8.1 displays the texture analysis and microstructure characterization of as-deposited Cu films. Figure 8.1(a) is the θ-2θ XRD profile for the epitaxial growth of Cu (110) film on the Si (112) substrate, and Figure 8.1(b) is the XRD (110) and (100) φ-scan profiles of Si substrate (blue) and Cu film (red), respectively. Figure 8.1(c) summarizes schematically the film–substrate orientation relationship of Cu (110) // Si (112), Cu $[1\bar{1}0]$ // Si $[\bar{1}\bar{1}1]$ and Cu [001] // Si $[\bar{1}10]$.

Plan-view TEM micrographs recorded at under-focus (Δf = -1.5 μm) and over-focus (Δf = +1.5 μm) conditions along beam direction **B** = [110] in Figure 8.1(d) and (e) confirm the formation of faceted nanovoids that exhibit dark or white Fresnel fringes. In addition, the inset SAD pattern in Figure 8.1(e) clearly shows single-crystal-like diffraction spots. The enlarged view of a high-resolution TEM (HRTEM) image in Figure 8.1(f) shows the nanovoid is faceted on [119] crystal planes and elongated along <112> direction. The cross-sectional TEM micrographs in Figure 8.1(g) and (h) taken at under-focus (Δf = -1.5 μm) condition display the cylindrical nanovoids along Cu [110] growth direction. The inserted SAD patterns in Figure 8.1(g) and (h) show clear evidence of single-crystal-like diffraction along beam directions of **B** = [$1\bar{1}0$] (Si [$\bar{1}\bar{1}1$]) and **B** = [001] (Si [$\bar{1}10$]). The HRTEM micrograph in Figure 8.1(i) (recorded along **B** = [001]) characterizes an elongated nanovoid along the growth direction. To describe the configuration of such faceted NVs, three dimensional parameters are defined based on the TEM observations, including the void length L, width W and height H, as marked in Figure 8.1(f) and (i). Statistic studies reveal that the mean value is 17 nm for L, and 7 nm for W, and 20 nm for H. Considering the TEM foil thickness is ~ 100 nm, the introduced NVs are assumed to be embedded inside the TEM specimens.

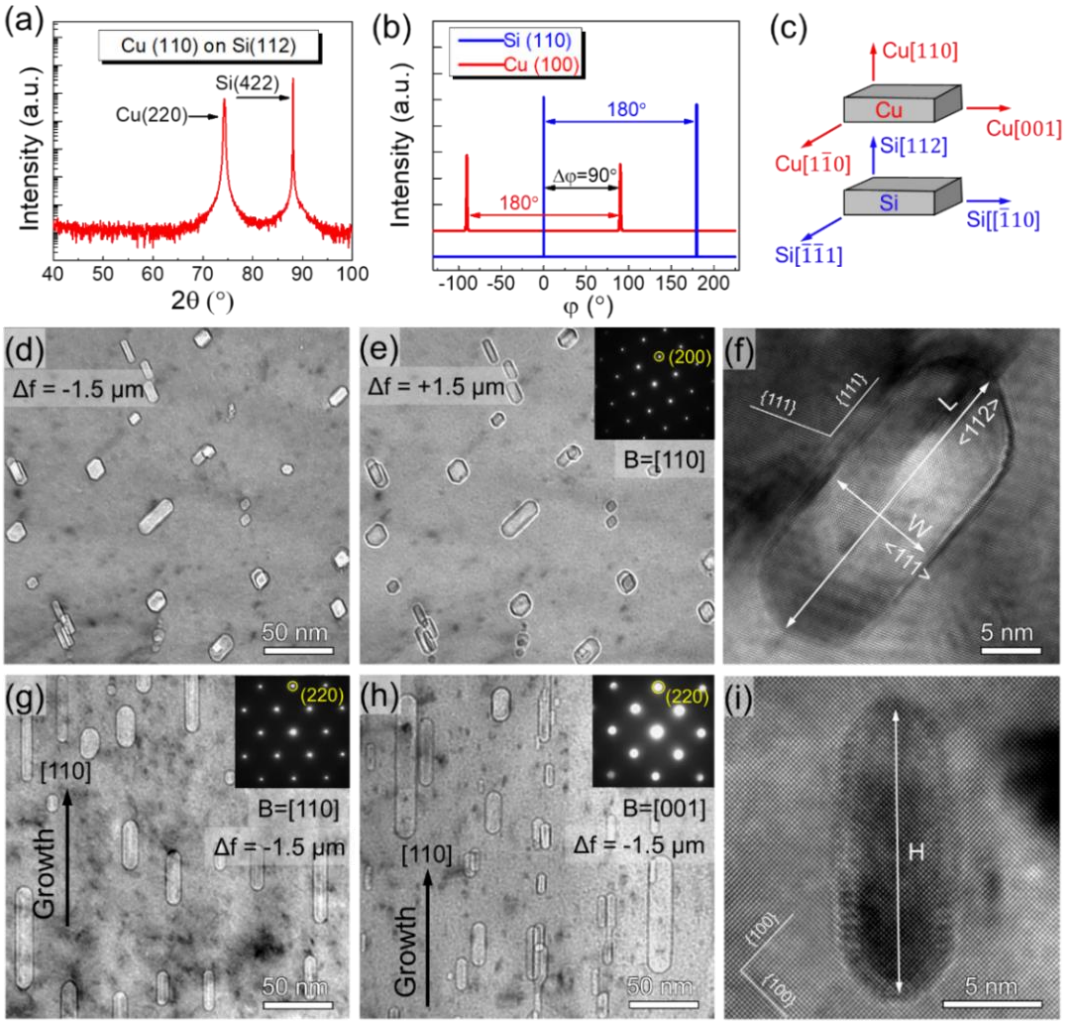

Figure 8.1. Texture analysis, and microstructure characterization of as-deposited NV-Cu. (a) θ-2θ XRD profile of sputtered film showing the epitaxial growth of Cu (110) on Si (112). (b) XRD φ-scan of Cu {100} (red) and Si {110} (blue). (c) Schematic illustration of film-substrate orientation relationship. (d-f) Plan-view TEM micrographs of faceted nanovoids in as-deposited Cu films. L and W in (f) mark the length and width of an elongated nanovoid. (g-i) Cross-sectional TEM micrographs of faceted nanovoids along growth direction. H in (i) denotes the height of a cylindrical nanovoid.

8.4.2 Radiation-induced void spheroidization and shrinkage

In-situ TEM experiments allow direct observation of void morphology evolution in radiation environment. The evolutions of microstructures up to 0.2 dpa at three temperatures are summarized in Figure 8.2. With increasing dose, it is evident that the preexisting faceted NVs undergo a spheroidization process that involves the reduction of void length L and the simultaneous

expansion of void width W . The spheroidization rate tends to increase with increasing temperature. Consequently, by 0.20 dpa, most NVs irradiated at higher temperatures, 250 and 350 ^{o}C, have been fully spheroidized as shown in Figure 8.2(b5) and (c5).

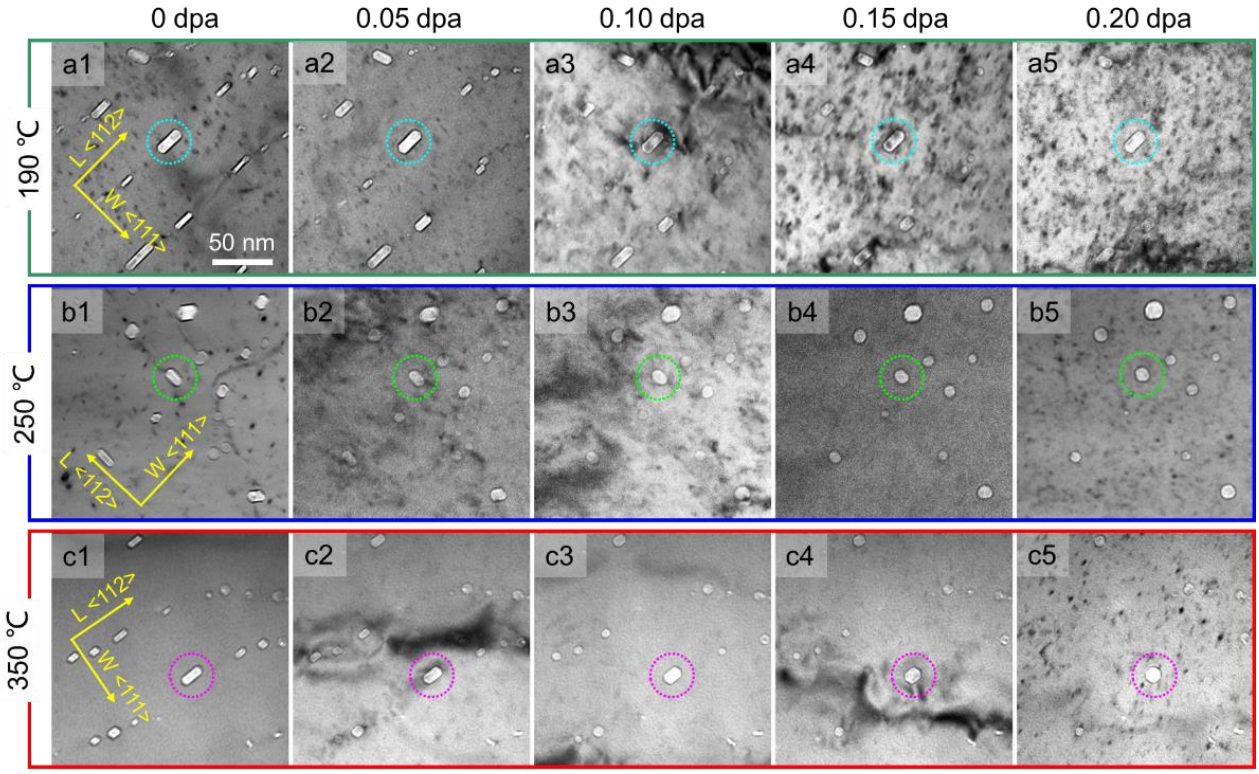

Figure 8.2. TEM sequential snapshots demonstrating the spheroidization process of faceted nanovoids at low dose (to 0.2 dpa) and various temperatures: (a1-a5) 190 ℃, (b1-b5) 250 ℃, and (c1-c5) 350 ℃.

At a higher dose, > 0.30 dpa, the irradiated NVs showed little change in shape, but they kept shrinking gradually. Figure 8.3 compares the TEM micrographs for void shrinkage at different irradiation temperatures over 0.3 to 1.0 dpa. The circles mark three representative NVs that contracted during radiation. During radiation, many NVs shrank continuously until they became too tiny to be visible. Moreover, the shrinkage process also shows a strong dependence on temperature. As shown in Figure 8.3, at a given dose level the mean NV size increases with increasing irradiation temperature, indicting the shrinkage rate is lower at higher temperature.

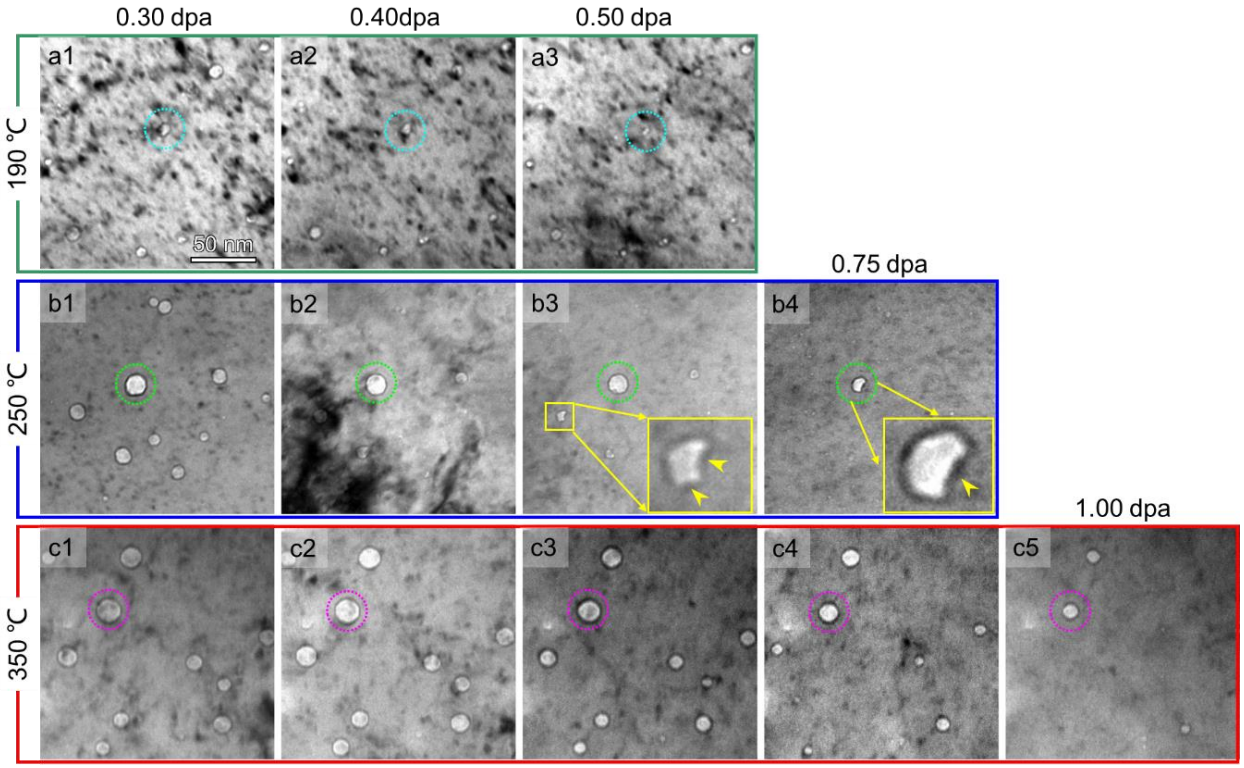

Figure 8.3. TEM snapshots demonstrating the shrinkage process of spherical nanovoids in later irradiation stage over 0.3-1.0 dpa, at various temperatures: (a1-a3) 190 ℃, (b1-b4) 250 ℃, and (c1-c5) 350 ℃. The squares in (b3) and (b4) denote two peculiar NVs that are dented locally at 250 ℃.

As shown in Figure 8.3 (c1-c5), all the NVs irradiated at 350 ℃ remain a perfect circular shape in their projected TEM micrographs while shrinking continuously. However, at 250 ℃ some of the fully spheroidized NVs occasionally exhibited 'craters' on void surface, and two of such peculiar 'imperfect' NVs are marked by the arrows in Figure 8.3(b3) and (b4). It was found that the imperfect voids were capable of self-healing and recovery from such eclipse features. One typical example is shown in Figure 8.4. Figure 8.4 (a1) displays a perfect circular large void around 15 nm in dimeter at 0.559 dpa. The void became concaved on its lower left as marked by the arrow in Figure 8.4(a2), and the concavity erode into the void during radiation (Figure 8.4(a3-a4)). After a while, the void recovered its spherical geometry at 0.656 dpa as shown in Figure 8.4(a5). During subsequent irradiation, a similar concave process repeated from lower right of the void, followed by its recovery as shown in Figure 8.4(b1) -(b5). The geometry change was accompanied with volume shrinkage, and the void diameter decreased from 15 to 12 nm. Meanwhile, some

irradiation-induced defect clusters were captured in the vicinity of the NV, as shown in Figure 8.4(a5) and (b1).

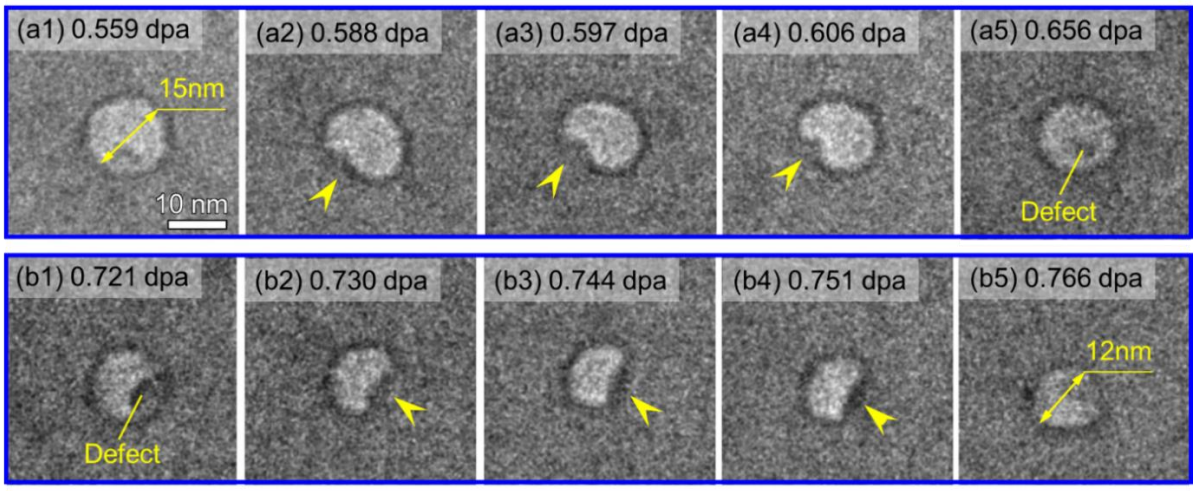

Figure 8.4. Morphology evolution of a void irradiated at 250 ℃. The arrows mark irradiation-induced 'craters' on the void surface.

To quantify the NV morphology evolution at different irradiation temperatures, two parameters are defined as follows. First, the aspect ratio ν (W/L) is used to describe the spheroidization process. Second, to describe the shrinkage process the porosity P is defined by taking into the consideration of both void size D (diameter) and density, given by:

$$P = \frac{\sum V_i}{At} \qquad \text{Equation 8.1}$$

where $\sum V_i$ is the sum of the volume for all the observed NVs, A is the observed area ~ 450 × 450 nm^2, and t is the TEM foil thickness, ~ 100 nm.

Figure 8.5 complies the variations of ν and P with increasing dose Φ at different irradiation temperatures. As shown in Figure 8.2, the void spheroidization occurred primarily at low dose (< 0.3 dpa) through the reduction of void length L and extension of void width W, which leads to the increase of ν in Figure 8.5(a). Before irradiation, ν had an initial value of 0.4 because of the elongation of the NVs along <112> direction, as shown in Figure 8.1(f). During Kr ion irradiation, ν increased gradually, and, by 0.2 dpa, it reached near unity at 350 ℃, 0.96 at 250 ℃, and 0.84 at 190 ℃. In addition to the current studies at high temperatures, a refence of the variation of ν at RT is also plotted in black squares in Figure 8.5(a) [232]. It is worth noting that although ν also

increases slightly at RT, such increment arises from the different reduction rates in both L and W, caused by the effect of void surface curvature on the interstitial diffusion [232]. Figure 8.5(b) shows that the spheroidization rate ($d\nu / d\Phi$) is greater for the smaller faceted NVs. At high dose (> 0.3 dpa), the aspect ratio ν rarely changed, so the void volume can be easily calculated by its projected image. The calculated porosity decreases with escalating dose as shown in Figure 8.5(c). Furthermore, at a given dose level the porosity declines with decreasing temperature, suggesting the void shrinkage process is suppressed at higher temperature. Moreover, the variation of shrinkage rate ($dD / d\Phi$) in Figure 8.5(d) reveals that smaller spherical NVs tend to shrink faster.

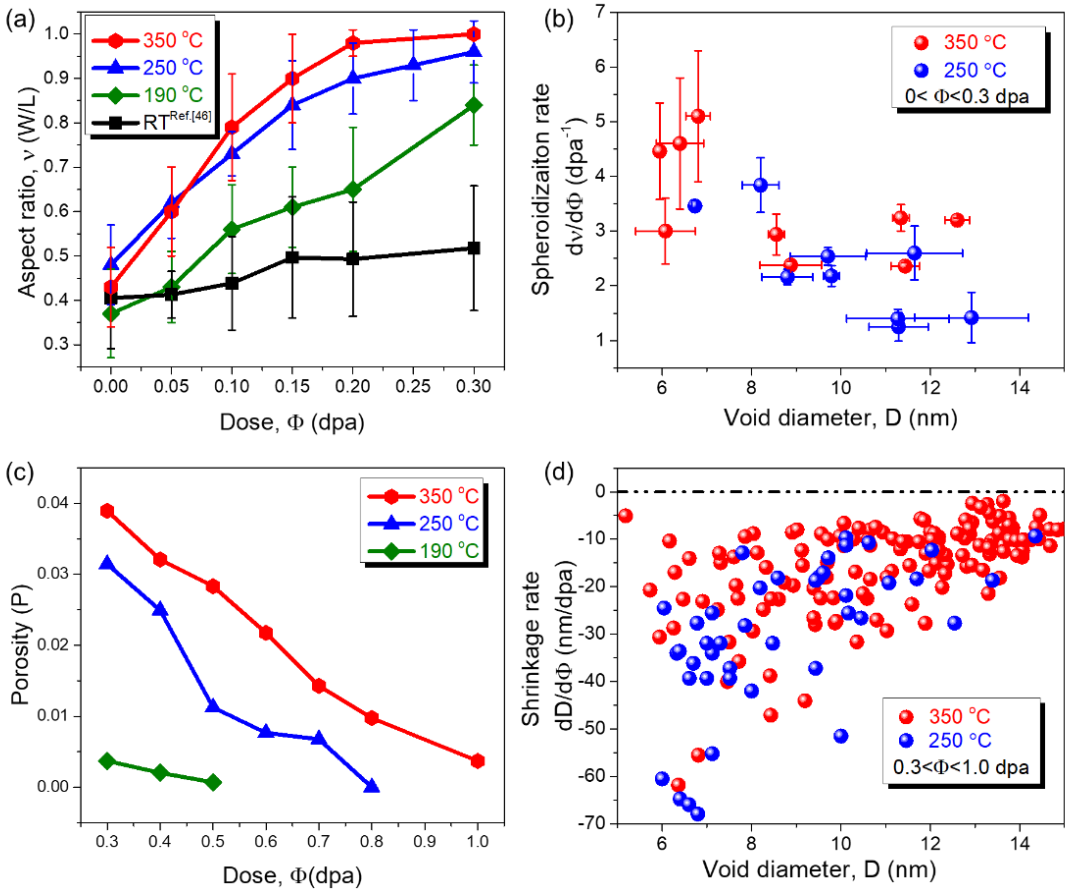

Figure 8.5. The influences of irradiation temperature and void size on void spheroidization and shrinkage. (a) Variations of aspect ratio ν (W / L) with increasing dose Φ to 0.3 dpa. A reference data [232] of RT irradiation is also plotted in black squares. (b) The spheroidization rate ($d\nu / d\Phi$) versus void diameter D. (c) Variations of porosity P with increasing dose Φ over 0.3-1.0 dpa. (d) The void shrinkage rate ($dD / d\Phi$) versus void diameter D.

8.4.3 Post-irradiation analysis

To identify the size and density of radiation-induced defect clusters, post-irradiation experiments were performed. The results revealed that high-density stacking fault tetrahedrons (SFTs) are formed in all irradiated samples regardless of irradiation temperature. Figure 8.6 (a)-(c) are TEM micrographs recorded from <110> zone crystal direction, projected from which SFTs exhibit a peculiar triangular shape as confirmed by the lower-left inset of a high-resolution TEM image in Figure 8.6(a). Figure 8.6(d) compares the SFT edge length (L_{SFT}) distributions at various temperatures. The average value of L_{SFT} increases slightly with increasing irradiation temperature, ranging from 1 to 7 nm and in good agreement with previous observations [39, 41, 46, 138, 217]. Conversely, the SFT density ρ_{SFT} decreases slightly with increasing irradiation temperature, as shown in Figure 8.6(e). SFTs are classified as a type of 3-dimensional vacancy clusters generally observed in FCC (face-centered-cubic) metals with low stacking fault energy [39, 41, 331]. The relation between the SFT edge length (L_{SFT}) and the number of vacancies (N) is given by [41]:

$$N = 3\left(\frac{L_{SFT}}{a}\right)^2 \qquad \text{Equation 8.2}$$

where a is the lattice parameter, about 0.3615 nm for Cu. Using Equation 8.2, the vacancy concentration (C_V) restored in SFTs can be expressed as:

$$C_V = N\frac{\rho_{SFT} M}{\rho N_A} \qquad \text{Equation 8.3}$$

where ρ_{SFT} is the SFT density, N_A is the Avogadro's number, ρ is material density (8.92 g/cm^3 for Cu), and M is material atomic mass (63.55 g/mol for Cu). The calculated C_V is also plotted in Figure 8.6(e), and it decreases with increasing irritation temperature.

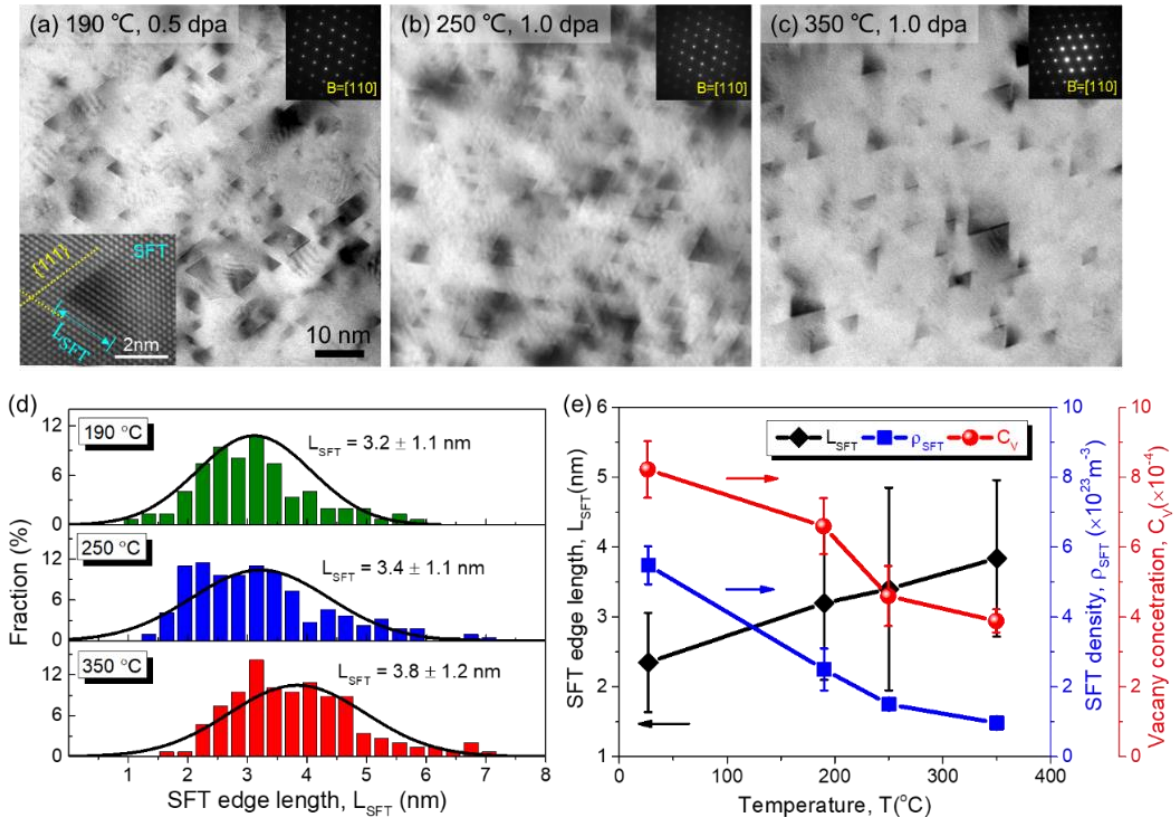

Figure 8.6. Irradiation-induced SFTs. (a-c) Post-irradiation TEM micrographs showing triangular shape SFTs in irradiated Cu samples. All the micrographs were examined along Cu <110> zone axis, as shown by the inset SAD patterns. The lower left inset in (a) is the HRTEM image of a representative SFT with its edge length marked by L_{SFT}. (d) Size distributions of SFTs at various irradiation temperatures. (e) Variations of SFT size (L_{SFT}), density (ρ_{SFT}) and its corresponding vacancy concentration (C_V).

Post-irradiation examination in Figure 8.7 also reveals the effect of void size on the eventual configurations of remaining NVs after irradiation to 1 pda at 350 ℃. Figure 8.7 (a) shows a small NV, around 10 nm in diameter, that is surrounded by numerous SFTs and exhibits a nearly perfect circular shape. Nevertheless, a large NV in Figure 8.7(a), around 23 nm in diameter still presents several facets that are indexed as {111}, {200}, {113} and {510} crystal planes based on the inset SAD pattern.

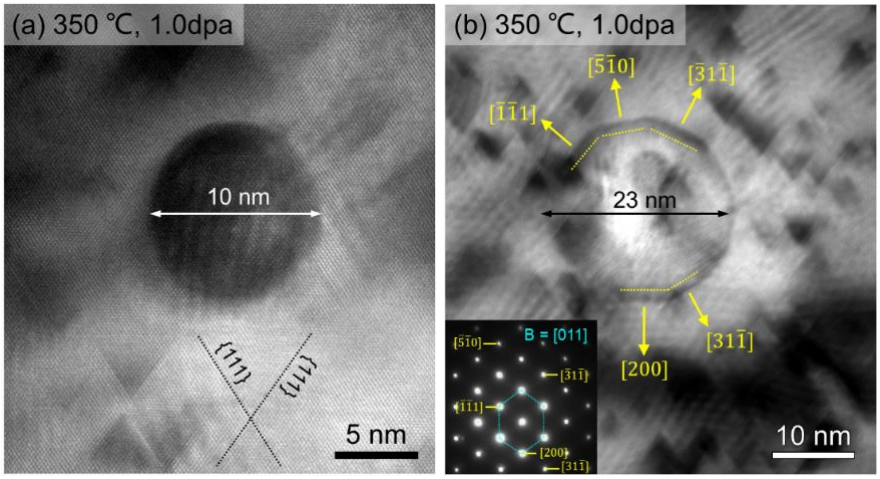

Figure 8.7. Post-irradiation analysis of remaining nanovoids after irradiation to 1 dpa at 350 ºC. (a) A small nanovoid with a dimeter of 10 nm that appears to be circular. (b) A large nanovoid with a diameter of 23 nm that is obviously faceted on several low-index crystallographic planes.

8.5 Phase-field modeling

To understand the underlying mechanism of the void evolution under high-temperature irradiation, we performed phase-field simulations in two-dimensions with a thin film configuration. The simulation domain has a total of 231×151 grid points, with the solid region occupying 151 × 151 grid points and the rest being empty space on both sides of the film. A void which is 30 units long and 13 units wide with an aspect ratio of 0.43 is initialized at the center of the film. The currently used model was developed and reported elsewhere [318]. In our simulations, the concentration of the point defects in the solid region is taken to be thermally equilibrium. The interstitial diffusivity (D_i) is normalized and set as 60 for all simulations, while the vacancy diffusivity (D_v) is set as 1, 20, and 40 to qualitatively model void evolution at low, medium, and high temperature, respectively. Although radiation produces equal numbers of vacancies and interstitials, in Cu some of the vacancies exist in the form of SFTs (see Figure 8.6) that are immobile and cannot interact with preexisting NVs. To account for this effect, we have, in our model, assumed a biased cascade source. For low-temperature irradiation, the number of vacancies introduced in each cascade event is only 90% of the number of interstitials; for the medium and high temperature cases, the number of vacancies introduced in each cascade event is 95% of the number of interstitials. In addition, the surface energy anisotropy is also included in the current model by making the gradient coefficients of the phase field variable orientation dependent, as what has been reported in another independent study [69].

The simulation results are presented in Figure 8.8. Figure 8.8(a1-a5), Figure 8.8(b1-b6) and Figure 8.8(c1-c7) are the snapshots of vacancy concertation C_v that compare the radiation-induced void spheroidization and shrinkage at different temperatures. The corresponding dimensional changes of void length L and width W are plotted as a function of time τ in Figure 8.8(d1-d3). Note that, in Figure 8.8(d1), both L and W decrease with increasing time at low irradiation temperature, but the reduction rate of L is higher than that of W. In figure 8.8(d2) and (d3), however, W initially increases until it reaches L, and then both of them decrease thereafter. As a result, the void undergoes a spheroidization process with its aspect ratio of W/L increasing rapidly from 0.43 to 1.00, as shown in Figure 8.8(e1). Meanwhile, the void keeps shrinking for all the cases, as indicated by the void area A reduction in Figure 8.8(e2). Especially, Figure 8.8(e1) and (e2) also suggest that, with increasing temperature, the radiation-induced spheroidization is to be promoted, while the shrinkage process is to be suppressed. These simulation results qualitatively agree with our experimental findings in Figure 8.2 and 8.3.

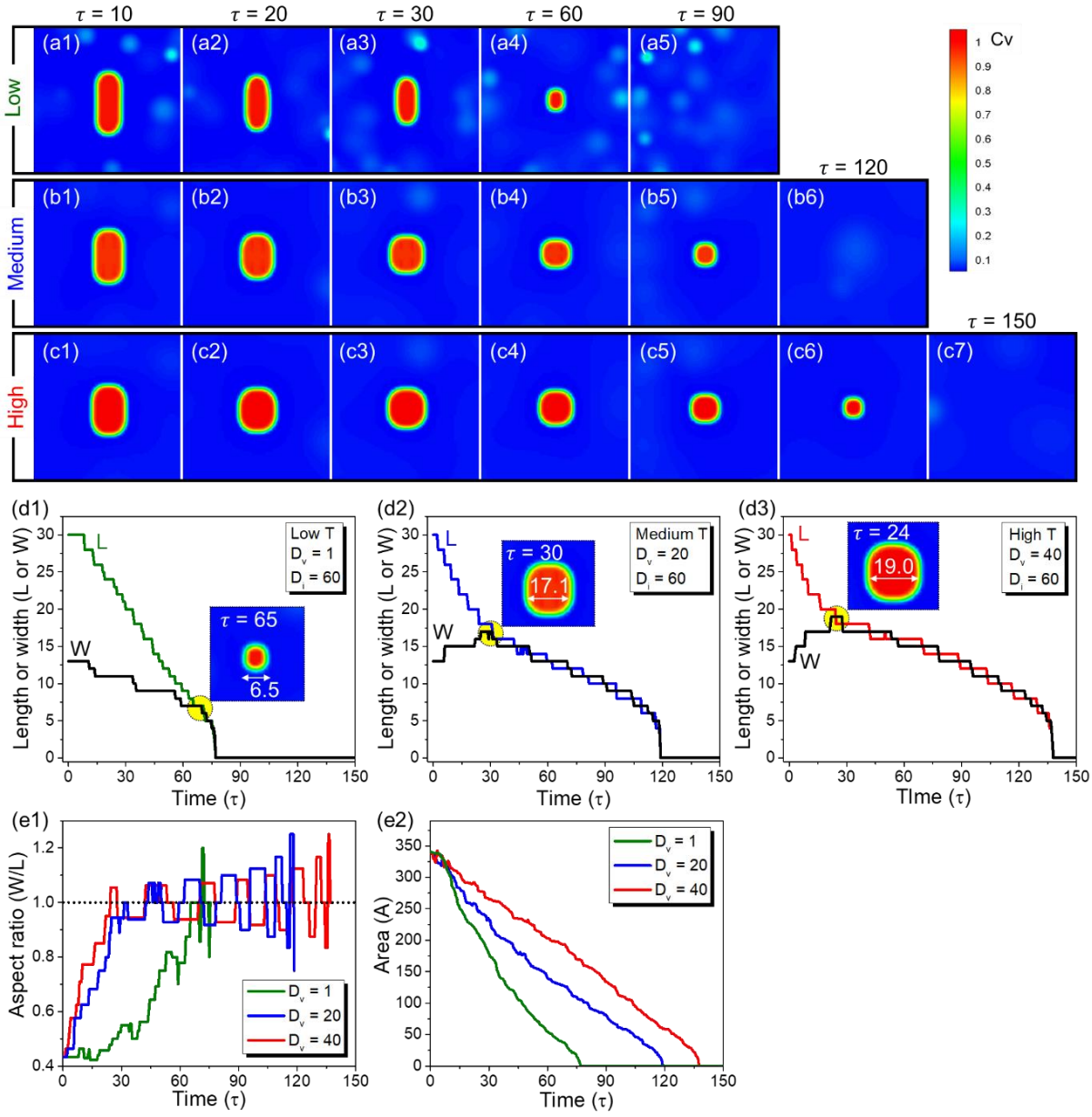

Figure 8.8. Phase-filed modeling on the radiation-induced void spheroidization and shrinkage. The interstitial diffusivity D_i is kept as the constant of 60 for all simulations, while the vacancy diffusivity D_v is set as 1 for low temperature in (a1-a5), 20 for medium temperature in (b1-b6), and 40 for high temperature in (c1-c7). (d1-d3) The evolution of void length (L) and width (W). (e1) and (e2) Temperature's effect on void aspect ratio (W / L) change and area (A) change.

8.6 Discussion

8.6.1 Spheroidization and shrinkage mechanisms

The growth of thin films by sputtering technique is a typical physical vapor deposition (PVD) method, an nonequilibrium process that produces various intrinsic defects, such as NVs [332]. For an individual NV formed in crystalline lattice, it tends to minimize its total surface energy γ that is anisotropic and varies according to crystallographic orientation [333]. The equilibrium shape that satisfies the minimum-energy condition can be described by the so-called Wulff construction [334], according to which the NVs in FCC metals are expected to present {110} and {111} facets [335]. In the current study, the introduced NVs in sputtered Cu film are mostly faceted on {111} planes, as shown in Figure 8.1. Our subsequent *in-situ* TEM observations in Figure 8.2 and 8.3 demonstrated that such {111}-faceted NVs experience geometry change when irradiated at high temperature by heavy ions in two aspects: spheroidization and shrinkage.

At low dose, the elongated NVs obviously tended to become spherical in shape. As shown in Figure 8.5(a), the void aspect ratio ν increases through the reduction of void length L and the extension of width W. Such spheroidization may be caused by two factors: surface migration and diffusion, driven by local curvature (surface tension) and surface energy anisotropy, respectively. On the other hand, the NVs keep shrinking and decreasing in size, as shown in Figure 8.3. The shrinkage phenomenon is attributed to the net flux of interstitials into NVs. Compared with vacancies, interstitials are lower in migration energy but higher in diffusivity [11]. During irradiation, the on-going displacement cascades create supersaturated interstitials that continuously diffuse into NVs, giving rise to void shrinkage. Even though an equal amount of vacancies is created at the same time, some of them exist in the form of sessile SFTs as shown in Figure 8.6. Recent MD (molecular dynamics) simulation studies have shown that a biased formation of vacancies and their emission away from NVs could also lead to void shrinkage when radiation damage cascades occur at the locations that are in the vicinity of NVs [336, 337].

Moreover, the TEM foil used for *in-situ* irradiation experiment is approximately 100 nm in thickness, so the foil surfaces, top or bottom, shall play an important role in absorbing point defects and influence void shrinkage or swelling. Unlike dislocations that are interstitial biased sinks, free surfaces are classified as a type of neutral (or unbiased) sink that can absorb both interstitials and vacancies [338, 339]. On the free surfaces of TEM foil, the vacancy concentration is estimated to

be thermally equilibrium C_v^0. On the NV surface, however, the vacancy concentration C_v^v is related to the surface curvature, and it can be estimated as [319]:

$$C_v^V = C_v^0 \exp\left(\frac{2\gamma\Omega}{RkT}\right) \qquad \text{Equation 8.4}$$

where γ is free surface energy, Ω is atomic volume, R is void radius, k is Boltzmann's constant, and T is temperature. Equation 8.4 suggests that the equilibrium vacancy concentration on the TEM foil surface is lower than that on the void surface, which counterbalances part of the free vacancies in the matrix and facilitates void shrinkage rather than swelling.

8.6.2 Irradiation temperature effect

Our experiments and simulations reveal that the NV spheroidization and shrinkage are heavily influenced by irradiation temperature. First, with increasing temperature, the surface migration and diffusion increase, so the void spheroidization is assumed to be accelerated with increasing temperature. Such hypothesis agrees with our *in-situ* TEM observations in Figure 8.2 and is successfully modeled by our phase-field simulation results in Figure 8.8. In particular, at 250 ℃ the irradiated and fully spheroidized NVs still occasionally presented curving features on void surface, as shown in Figure 8.5. This might result from the interactions between radiation damage cascades and pre-existing NVs. The radiation damage cascade, or displacement spike, is the production of multiple displacement by the primary knock-on atom (PKA) after receiving enough transferred energy from incident particle [22]. It can be simply pictured as a vacancy core surrounded by an interstitial shell [13]. When a cascade occurs in the vicinity of a void, the interstitials on the cascade shell will rapidly flow into the void and deposit on void surface, while the vacancies in cascade core may collapse into sessile clusters of SFTs [331]. Consequently, a 'carter' is formed on void surface. However, considering the dose rate is limited (~ 0.0003 dpa/s) and the cascade lifetime is short (within a few picoseconds) [15], the bean-like void gains enough time to recover from the local curved morphology before another cascade occurs nearby, as what we have found in Figure 8.5. On the other hand, with increasing temperature the NV shrinkage process recedes because of the improvement of vacancy mobility. Therefore, more interstitials are consumed by vacancies through recombination before they can diffuse into NVs. This also leads to the drop of vacancy concentration (stored in SFTs) in specimens at higher irradiation temperature, as shown in Figure 8.6(e).

Besides, it is well known that irradiation-induced void swelling is generally characterized by a peak at intermediate temperature. For Cu irradiated with neutrons, the peak swelling occurs at ~ 325 ^{o}C [60]. In the current study, no NVs showed any obvious swelling, partly because of the TEM foil surface effect mentioned above, and partly because of the peak swelling shift to a higher value due to the heavy ion irradiation effect [340]. We speculate that the void swelling could occur if irradiation temperature is increased high enough, but an incubation period might be required to initiate such swelling. However, considering more significant emission of vacancies by NVs at higher temperature, the pre-introduced NVs might be annealed out before the onset of their swelling [341].

8.6.3 Void size effect

Figure 8.5(b) and (d) demonstrate that the rates of spheroidization and shrinkage are higher for smaller NVs. With decreasing void size, the driving force of curvature for surface mobility increases, so the spheroidization is accelerated for smaller NVs. Besides, as the void shrinkage originates from the net flux of interstitials, the common form of the void size change equation is described by:

$$\frac{dR}{dt} = \frac{\Omega}{R}\left[D_i C_i - D_v (C_v - C_v^V) \right] \qquad \text{Equation 8.5}$$

where D_i and D_v are interstitial and vacancy diffusivity, C_i and C_v are vacancy and interstitial concentration in the solid, and Ω, R and C_v^V are the same parameters defined in Equation 8.4. Combining Equation 8.4 and 8.5, it is concluded that the shrinkage rate of NVs increases with decreasing void radius, consistent with current observations and previous reports [62, 342].

The post-irradiation analysis in Figure 8.7 also indicates that the morphology of remaining NVs shows strong size effect. When the void is less than 10 nm in diameter, it exhibits a perfect spherical shape; while it is larger than 20 nm, it exhibits several well-defined facets of low-index crystal planes. This may result from the competing balance between surface tension and surface anisotropy energy. For small NVs, the surface tension is so high that the NVs tend to become spherical to minimize the total surface area; for large NVs, however, the surface anisotropy comes to be a dominant role, and NVs then tend to become faceted.

8.7 Conclusions

In summary, we successfully introduced faceted NVs in highly textured Cu (110) films using magnetron sputtering technique. Through *in-situ* Kr ion irradiations at elevated temperature, we observed the morphology evolution of such NVs in shape and size (spheroidization and shrinkage). Post-irradiation analysis identified the irradiation-induced defect clusters in the form of SFTs and revealed the size-dependent morphology status for surviving NVs. The major findings are summarized as follows:

1. Spheroidization and shrinkage occur simultaneously for faceted NVs irradiated at elevated temperature.
2. The spheroidization is accomplished via surface migration and diffusion, driven by surface tension and anisotropy energy. After fully spheroidized, the NVs irradiated at 250 ^{o}C still become occasionally curved due to their interactions with damage cascades nearby.
3. The shrinkage is a result of net interstitial flux into NVs, which is enhanced by the damage cascade near NVs and the TEM foil surface effect.
4. Increasing temperature can facilitate spheroidization but impede shrinkage process.
5. Compared with larger NVs, smaller NVs tend to become spherical and shrink more rapidly because of their higher curvature effect.
6. The experimental observations can be well simulated by phase-field modeling by controlling the defect production bias and diffusivity of vacancies.

CHAPTER 9. CONCLUSIONS AND FUTURE WORK

9.1 Conclusions

The major findings and conclusions of this thesis are summarized as follows:

1. Two different nanostructured epitaxial Cu films were successfully grown on Si substrates using DC magnetron sputtering deposition technique. The microstructure features, nanovoids and twin boundaries, can be tailored by controlling the orientation of Si substrates.
2. *In-situ* 1 MeV Kr^{++} irradiations revealed several aspects regarding the defect formation and interaction with nanovoids (NVs) and twin boundaries (TBs). First, defect clusters were preferentially distributed along the domain boundaries in NV-NT Cu (111) (see Chapter 3). Second, the pre-introduced NVs kepy shrinking with increasing dose (see Chapter 3 and 7). Especially, the faceted nanovoids in NV Cu (110) experienced spheroidization when irradiated at high temperature (see Chapter 8). Third, ITB migration and detwinning occurred in pure NT-Cu, while in NT-CuFe (3 at. %) alloy the ITB extended into 9R phase that remained stable (see Chapter 5 and 6).
3. Micropillar compression tests showed that, in addition to the regular strengthening from bubbles and dislocation loops, extra strength increment was caused by He irradiation in NV-NT Cu than in CG Cu, majorly due to the radiation-induced SFs that effectively block dislocation movement from twin to matrix (see Chapter 4).
4. The underlying mechanisms of radiation-induced void spheroidization and shrinkage, TB migration and detwinning as well as hardening, were discussed based on post-irradiation analyses and computer simulations, including density functional theory (DFT), molecular dynamics (MD), and phase-field modeling.

9.2 Future work

The radiation damage effects in nanostructured metals vary from material to material and are influenced by a couple of factors, such as dose, dose rate, sample dimension, irradiation temperature, presence of inert gas and impurity atoms [36]. Though this thesis has been tried to take into consideration of several factors mentioned above, systematic studies are still necessary

in the future. The future work will hopefully include three aspects that will be described in this section below.

9.2.1 Void formation mechanism in the nanotwinned metals

One of the interested nanostructured Cu materials used in this thesis is the nv-nt Cu, namely the nanotwinned Cu with abundant nanovoids at domain boundaries (see Figure 3.1). According to our previous studies [169, 218], such material is more attractive than regular nanotwinned metals in mechanical properties and radiation performance, mostly because of the preexisting nanovoids introduced during sputtering deposition process. However, the void formation mechanism in nanotwinned metals is still unclear. To address this issue, preliminary attempts have been made to tailor its microstructure by changing deposition parameters, including deposition rate ($R_{Dep.}$), film thickness (T_{Film}), and Argonne working pressure (P_{Ar}). Figure 9.1 displays the plan-view TEM micrographs of NV-NT Cu (111) fabricated under different deposition conditions, which demonstrate abundant nanovoids located at domain boundaries. Besides, the corresponding cross-sectional TEM micrographs in Figure 9.2 reveal high-density twin structures inside each columnar domain. The twin spacing is around several nanometers, comparable to the void size. From these observations, it is concluded that nanovoids always present at domain boundaries, when the film is fully nanotwinned and (111)-oriented along the film growth direction. The void size and density, on the other hand, can be controlled by adjusting deposition parameters while remaining the film texture. It seems that the void density significantly increases with increasing Argonne pressure and deposition rate, but it decreases with increasing film thickness.

The void formation must be closely related with sputtering deposition process, a non-equilibrium kinetic method that is widely used for constructing nanostructured materials through a ‘bottom-up’ way. The aforementioned problem cannot be well answered until the nucleation, growth and surface diffusion processes involved in the formation of thin films on substrates are fully explored. More interestingly, no nanovoids were reported in other similar nanotwinned metals, such as Ag that shares the same FCC crystal structure and twin features with Cu, but little nanovoids were found inside its sputtered highly textured (111)-oriented films [106]. Therefore, the void formation may be peculiar to Cu, and it varies for other materials. From this viewpoint, the fundamentals of Cu atomic construction are necessary for understanding the final macroscopic state of the nanotwinned system.

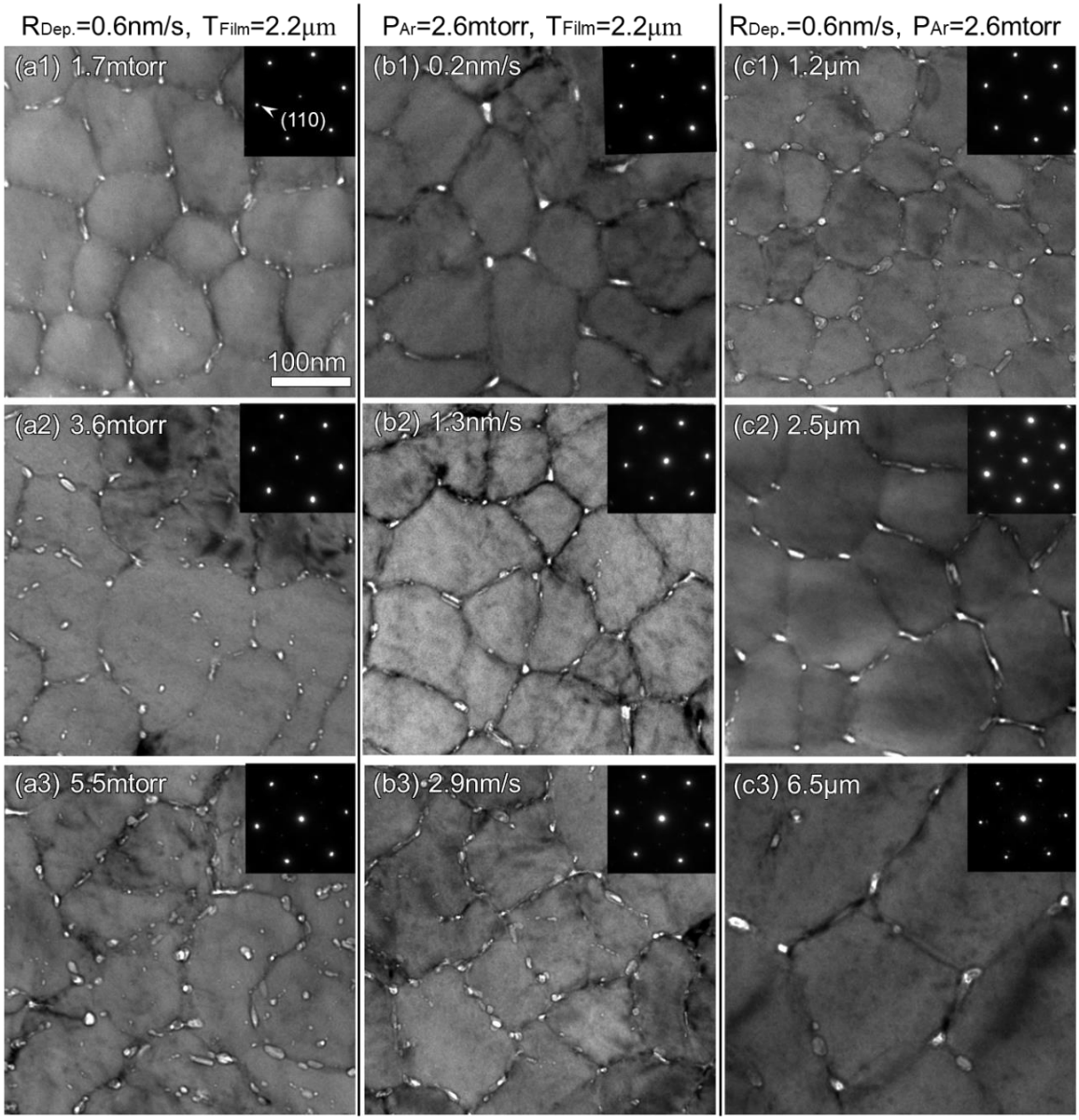

Figure 9.1. Pan-view TEM micrographs displaying abundant nanovoids that are primarily positioned at domain boundaries. The inset SAD patterns clearly show single crystal-like diffraction along the Cu <111> zone axis.

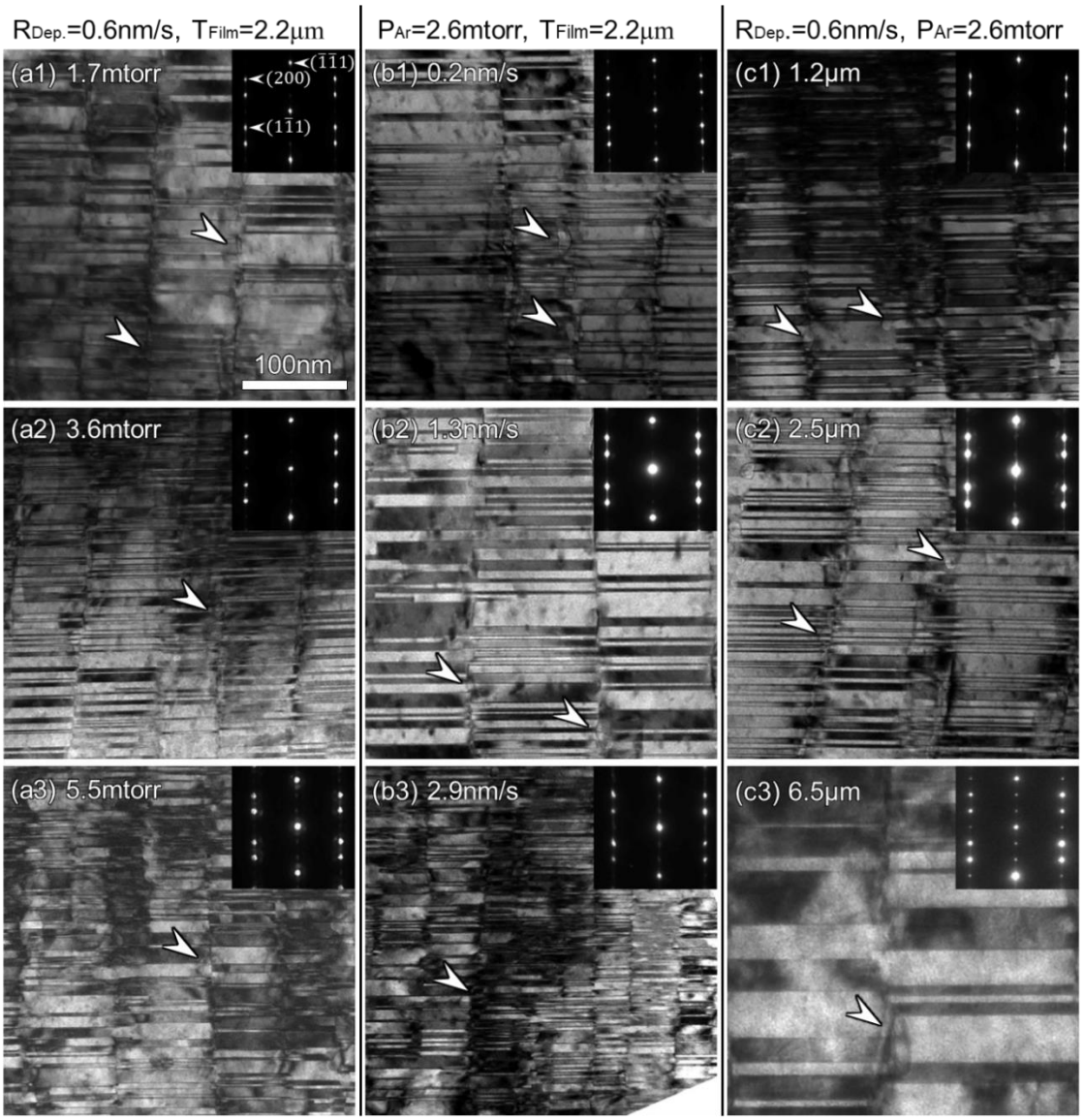

Figure 9.2. Cross-sectional TEM micrographs recorded from Cu <110> zone axis, revealing columnar grains, nanovoids (marked by arrows), and high-density growth twins in epitaxial Cu films. The inset SAD patterns confirm the formation of growth twins.

9.2.2 Radiation-induced void migration

In Chapter 7 and 8, we systematically studied how nanovoids evolved in geometry at different irradiation temperatures. Apart from void spheroidization and shrinkage, void migration is usually predicted in many simulation studies [343-345], but little concrete evidence has been reported because of the experimental difficulties. Fortunately, we captured such phenomenon using *in situ* TEM Kr^{++} irradiation experiment. As shown in Figure 9.3 (a)-(c), the arrow points a typical

example that is shrinking and gradually migrating with increasing dose. The moving void disappears in Figure 9.3(d), and he inset boxes are the complied micrographs at different doses (marked by numbers), which clearly illustrates its trajectory through the crystalline lattice. Figure 9.3(e) shows that most of the irradiated voids can migrate by a long distance (> 20 nm) before they disappear, and their migration behaviors show a strong dependence on void size, as shown in Figure 9.3(f). The future work will be trying to explore the void migration mechanism and to discuss its potential effect on the radiation damage evolution.

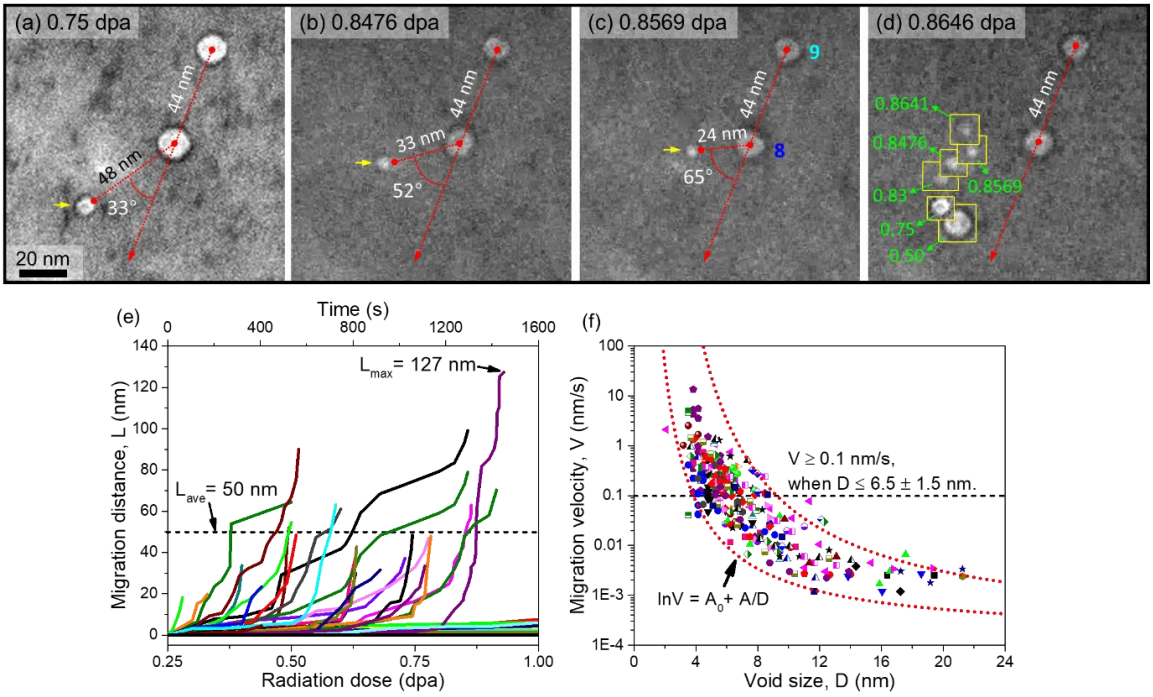

Figure 9.3. (a)-(d) *In situ* TEM observations of irradiation-induced void shrinkage and migration. (e) Void migration distance with increasing time and dose. (f) The logarithmic plot of void migration velocity against void dimeter.

9.2.3 Helium's effect on void nucleation and swelling

One of the ultimate goals of the heavy ion radiation studies is to provide new insights for emulating the neutron irradiation damage that occurs in the nuclear reactors. However, there are several challenges to the use of heavy ion radiation [346]. For instance, it faces the lack of He (Helium) that is introduced inside structural components due to the transmutation reactions, such as the D-

T nuclear fusion reaction, the most promising reaction for a commercial fusion power plant [14]. As an inert gas, He is hardly soluble in solids and plays an important role in microstructure evolution [213, 231, 233, 347]. Therefore, it is suggested to pre-inject or simultaneously implant extra He atoms while conducting regular heavy ion irradiation studies [348]. The nanostructured Cu in this thesis contains nanometer-sized voids that are good candidates for studying the He's effect on their shrinkage or swelling under irradiation environment. Our preliminary work in Figure 9.4 compares the difference of void evolution when irradiated respectively by the dual beams of 12 keV He^{+} and 1 MeV Kr^{++}, and the single beam of 1 MeV Kr^{++}. It has been found that when $R > 5$ nm, the void shrinkage rate decreases with decreasing void size for both cases; when $R < 5$ nm, for single-beam irradiation the shrinkage rate still drops with decreasing void size, while it increases and approaches zero (no shrinkage) at $R \approx 3$nm. The future work will be focused on understanding such He's effect using classical kinetics and phase-field simulations.

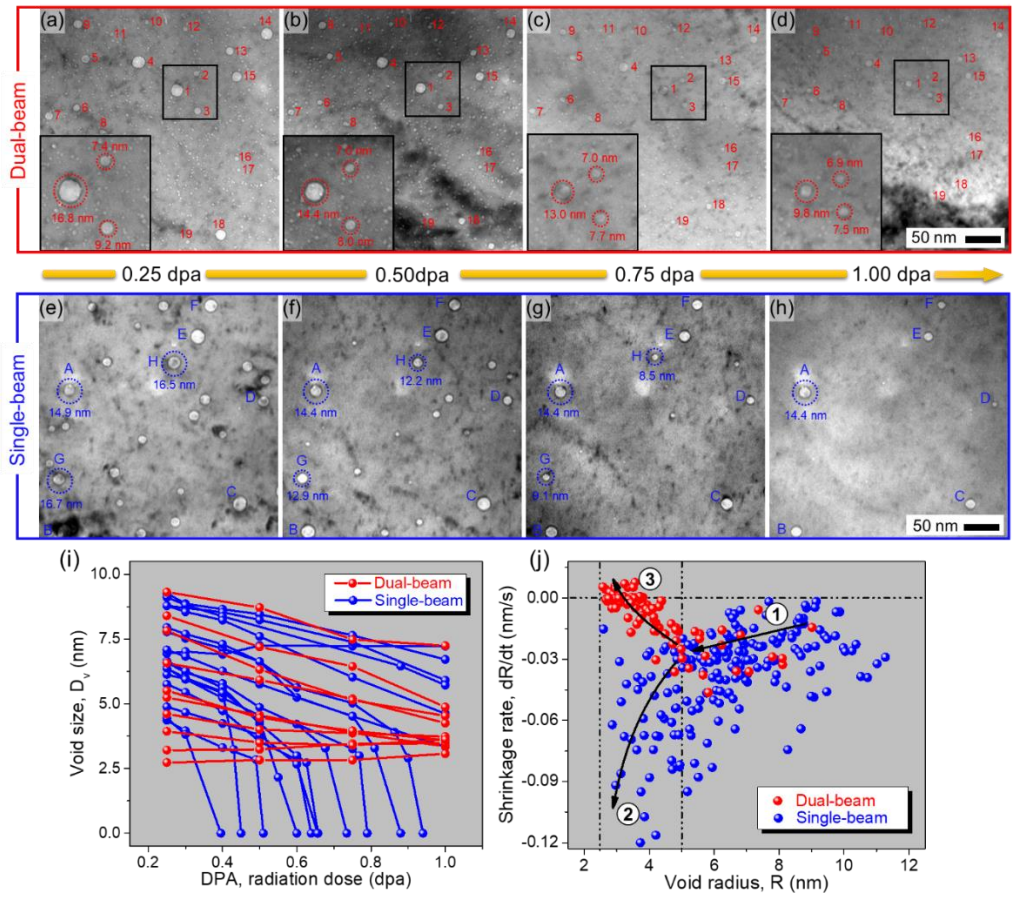

Figure 9.4 Comparison of the void shrinkage between (a)-(d) dual-beam (12 keV He^{+} and 1 MeV Kr^{++}) and (e)-(h) single-beam (1 MeV Kr^{++}) irradiation over 0.25 to 1.00 dpa, at 350 ^{o}C. (i) Void size change with increasing radiation dose. (j) The corresponding void shrinkage rate (in nm/s) plotted as a function of void radius R.

REFERENCES

[1] M. Nastasi, N. Michael, J. Mayer, J.K. Hirvonen, M. James, Ion-solid interactions: fundamentals and applications, Cambridge University Press1996.

[2] S. Chu, A. Majumdar, Opportunities and challenges for a sustainable energy future, nature 488(7411) (2012) 294.

[3] E.A. Marquis, J.M. Hyde, D.W. Saxey, S. Lozano-Perez, V. de Castro, D. Hudson, C.A. Williams, S. Humphry-Baker, G.D. Smith, Nuclear reactor materials at the atomic scale, Materials Today 12(11) (2009) 30-37.

[4] D. Butler, Energy: Nuclear power's new dawn, Nature Publishing Group, 2004.

[5] S.J. Zinkle, G. Was, Materials challenges in nuclear energy, Acta Materialia 61(3) (2013) 735-758.

[6] S.J. Zinkle, J.T. Busby, Structural materials for fission & fusion energy, Materials Today 12(11) (2009) 12-19.

[7] M. Norgett, M. Robinson, I. Torrens, A proposed method of calculating displacement dose rates, Nuclear engineering and design 33(1) (1975) 50-54.

[8] S.J. Zinkle, L.L. Snead, Designing radiation resistance in materials for fusion energy, Annual Review of Materials Research 44 (2014) 241-267.

[9] A Technology Roadmap for Generation IV Nuclear Energy Systems. Generation IV International, Forum, (2002).

[10] GIF R&D Outlook for Generation IV Nuclear Energy Systems. Generation IV International, Forum; 2009.

[11] G.S. Was, Fundamentals of radiation materials science: metals and alloys, Springer2016.

[12] M. Norgett, M. Robinson, I. Torrens, Standard Practice for Neutron Radiation Damage Simulation by Charged-Particle Irradiation, Annual Book of ASTM Standards (1975).

[13] J.A. Brinkman, Production of atomic displacements by high-energy particles, American Journal of Physics 24(4) (1956) 246-267.

[14] J. Knaster, A. Moeslang, T. Muroga, Materials research for fusion, Nature Physics 12(5) (2016) 424.

[15] H. Ullmaier, W. Schilling, Radiation damage in metallic reactor materials, Physics of modern materials. Characterization of materials, defects and mechanical properties1980.

[16] B.D. Wirth, How does radiation damage materials?, Science 318(5852) (2007) 923-924.

[17] R. Stoller, 1.11 Primary Radiation Damage Formation, Comprehensive Nuclear Materials, Elsevier, Oxford (2012) 293-332.

[18] L.T. Chadderton, Radiation damage in crystals, Methuen London1965.

[19] M. Born, J.E. Mayer, Zur gittertheorie der ionenkristalle, Zeitschrift für Physik 75(1-2) (1932) 1-18.

[20] A.A. Abrahamson, Repulsive interaction potentials between rare-gas atoms. Homonuclear two-center systems, Physical Review 130(2) (1963) 693.

[21] M.W. Thompson, Defects and radiation damage in metals, Defects and Radiation Damage in Metals, by MW Thompson, Cambridge, UK: Cambridge University Press, 1974 (1974).

[22] G. Kinchin, R. Pease, The displacement of atoms in solids by radiation, Reports on progress in physics 18(1) (1955) 1.

[23] W. Snyder, J. Neufeld, Disordering of solids by neutron radiation, Physical Review 97(6) (1955) 1636.

[24] P. Sigmund, On the number of atoms displaced by implanted ions or energetic recoil atoms, Applied Physics Letters 14(3) (1969) 114-117.
[25] J. Lindhard, M. Scharff, H.E. Schiøtt, Range concepts and heavy ion ranges, Munksgaard Copenhagen1963.
[26] J.F. Ziegler, M.D. Ziegler, J.P. Biersack, SRIM: the stopping and range of ions in matter, Cadence Design Systems2008.
[27] D. Kaoumi, A. Motta, R. Birtcher, A thermal spike model of grain growth under irradiation, Journal of Applied Physics 104(7) (2008) 073525.
[28] C.M. Barr, G.A. Vetterick, K.A. Unocic, K. Hattar, X.-M. Bai, M.L. Taheri, Anisotropic radiation-induced segregation in 316L austenitic stainless steel with grain boundary character, Acta Materialia 67 (2014) 145-155.
[29] C.M. Barr, L. Barnard, J.E. Nathaniel, K. Hattar, K.A. Unocic, I. Szlurfarska, D. Morgan, M.L. Taheri, Grain boundary character dependence of radiation-induced segregation in a model Ni–Cr alloy, Journal of Materials Research 30(09) (2015) 1290-1299.
[30] C. Sun, S. Zheng, C. Wei, Y. Wu, L. Shao, Y. Yang, K. Hartwig, S. Maloy, S. Zinkle, T. Allen, Superior radiation-resistant nanoengineered austenitic 304L stainless steel for applications in extreme radiation environments, Scientific reports 5 (2015) 7801.
[31] T.D. Shen, S. Feng, M. Tang, J.A. Valdez, Y. Wang, K.E. Sickafus, Enhanced radiation tolerance in nanocrystalline Mg Ga 2 O 4, Applied Physics Letters 90(26) (2007) 263115.
[32] J. Carter, E. Fu, M. Martin, G. Xie, X. Zhang, Y. Wang, D. Wijesundera, X. Wang, W.-K. Chu, S.M. McDeavitt, Ion irradiation induced nanocrystal formation in amorphous Zr55Cu30Al10Ni5 alloy, Nuclear Instruments and Methods in Physics Research Section B: Beam Interactions with Materials and Atoms 267(17) (2009) 2827-2831.
[33] W.D. Callister, D.G. Rethwisch, Materials science and engineering: an introduction, John wiley & sons New York2007.
[34] P. Shewmon, Diffusion in solids, Springer2016.
[35] R. Sizmann, The effect of radiation upon diffusion in metals, Journal of Nuclear Materials 69 (1978) 386-412.
[36] S. Zinkle, 1.03-Radiation-Induced Effects on Microstructure, Comprehensive Nuclear Materials, Elsevier, Oxford (2012) 65-98.
[37] M. Jenkins, Characterisation of radiation-damage microstructures by TEM, Journal of nuclear materials 216 (1994) 124-156.
[38] D.J. Edwards, E.P. Simonen, S.M. Bruemmer, Evolution of fine-scale defects in stainless steels neutron-irradiated at 275 C, Journal of nuclear materials 317(1) (2003) 13-31.
[39] R. Schäublin*, Z. Yao, N. Baluc, M. Victoria, Irradiation-induced stacking fault tetrahedra in fcc metals, Philosophical Magazine 85(4-7) (2005) 769-777.
[40] S. Zinkle, K. Farrell, H. Kanazawa, Microstructure and cavity swelling in reactor-irradiated dilute copper-boron alloy, Journal of nuclear materials 179 (1991) 994-997.
[41] S. Zinkle, L. Seitzman, W. Wolfer, I. Energy calculations for pure metals, Philosophical Magazine A 55(1) (1987) 111-125.
[42] J. Silcox, P. Hirsch, Direct observations of defects in quenched gold, Philosophical Magazine 4(37) (1959) 72-89.
[43] T. J∅ ssang, J. Hirth, The energies of stacking-fault teirahedra in fcc metals, Philosophical Magazine 13(124) (1966) 657-670.
[44] M. Kiritani, Microstructure evolution during irradiation, Journal of Nuclear materials 216 (1994) 220-264.

[45] B.T. Kelly, Irradiation damage to solids, Pergamon Press Oxford1966.
[46] S. Zinkle, R. Sindelar, Defect microstructures in neutron-irradiated copper and stainless steel, Journal of Nuclear Materials 155 (1988) 1196-1200.
[47] H. Abe, N. Sekimura, Y. Yang, Stability and mobility of defect clusters in copper under displacement cascade conditions, Journal of nuclear materials 323(2) (2003) 220-228.
[48] H. Abe, N. Sekimura, T. Tadokoro, Stability and mobility of interstitial-type defect clusters generated from displacement cascades in copper and gold by in-situ transmission electron microscopy, Materials transactions 46(3) (2005) 433-439.
[49] K. Arakawa, K. Ono, M. Isshiki, K. Mimura, M. Uchikoshi, H. Mori, Observation of the one-dimensional diffusion of nanometer-sized dislocation loops, Science 318(5852) (2007) 956-959.
[50] Y. Matsukawa, S.J. Zinkle, One-dimensional fast migration of vacancy clusters in metals, Science 318(5852) (2007) 959-962.
[51] S. Kashibe, K. Une, K. Nogita, Formation and growth of intragranular fission gas bubbles in UO2 fuels with burnup of 6–83 GWd/t, Journal of nuclear materials 206(1) (1993) 22-34.
[52] I. Zacharie, S. Lansiart, P. Combette, M. Trotabas, M. Coster, M. Groos, Microstructural analysis and modelling of intergranular swelling of an irradiated UO2 fuel treated at high temperature, Journal of nuclear materials 255(2-3) (1998) 92-104.
[53] K. Katsuyama, T. Nagamine, S.-i. Matsumoto, M. Ito, Measurement of central void diameter in FBR MOX fuel by X-ray computer tomography, Journal of nuclear science and technology 39(7) (2002) 804-806.
[54] C. Cawthorne, E. Fulton, Voids in irradiated stainless steel, Nature 216(5115) (1967) 575.
[55] L. Mansur, Theory and experimental background on dimensional changes in irradiated alloys, Journal of Nuclear Materials 216 (1994) 97-123.
[56] P. Goodhew, Shapes of pores in metals, Metal Science 15(9) (1981) 377-385.
[57] M.R. Mruzik, K.C. Russell, Equilibrium forms of small voids in metals, Surface Science 67(1) (1977) 205-225.
[58] C. Chen, The shapes of irradiation-produced voids in nickel, physica status solidi (a) 16(1) (1973) 197-210.
[59] P.C. Millett, A. El-Azab, S. Rokkam, M. Tonks, D. Wolf, Phase-field simulation of irradiated metals: Part I: Void kinetics, Computational materials science 50(3) (2011) 949-959.
[60] S.J. Zinkle, K. Farrell, Void swelling and defect cluster formation in reactor-irradiated copper, Journal of Nuclear Materials 168(3) (1989) 262-267.
[61] J.L. Katz, H. Wiedersich, Effect of insoluble gas molecules on nucleation of voids in materials supersaturated with both vacancies and interstitials, Journal of Nuclear Materials 46(1) (1973) 41-45.
[62] J. Evans, Void swelling and irradiation-induced void shrinkage in neutron irradiated molybdenum and TZM, Journal of Nuclear Materials 88(1) (1980) 31-41.
[63] H. Brager, The effects of cold working and pre-irradiation heat treatment on void formation in neutron-irradiated type 316 stainless steel, Journal of Nuclear Materials 57(1) (1975) 103-118.
[64] L. Mansur, Correlation of neutron and heavy-ion damage: II. The predicted temperature shift if swelling with changes in radiation dose rate, Journal of Nuclear Materials 78(1) (1978) 156-160.

[65] B. Singh, M. Eldrup, A. Horsewell, P. Ehrhart, F. Dworschak, On recoil energy dependent void swelling in pure copper Part I. Experimental results, Philosophical Magazine A 80(11) (2000) 2629-2650.
[66] S. Rokkam, A. El-Azab, P. Millett, D. Wolf, Phase field modeling of void nucleation and growth in irradiated metals, Modelling and simulation in materials science and engineering 17(6) (2009) 064002.
[67] P.C. Millett, S. Rokkam, A. El-Azab, M. Tonks, D. Wolf, Void nucleation and growth in irradiated polycrystalline metals: a phase-field model, Modelling and simulation in materials science and engineering 17(6) (2009) 064003.
[68] P.C. Millett, A. El-Azab, D. Wolf, Phase-field simulation of irradiated metals: Part II: Gas bubble kinetics, Computational Materials Science 50(3) (2011) 960-970.
[69] W. Liu, N. Wang, Y. Ji, P. Song, C. Zhang, Z. Yang, L. Chen, Effects of surface energy anisotropy on void evolution during irradiation: A phase-field model, Journal of Nuclear Materials 479 (2016) 316-322.
[70] Z. Xiao, A. Semenov, C. Woo, S. Shi, Single void dynamics in phase field modeling, Journal of Nuclear Materials 439(1) (2013) 25-32.
[71] S.J. Zinkle, Y. Matsukawa, Observation and analysis of defect cluster production and interactions with dislocations, Journal of nuclear materials 329 (2004) 88-96.
[72] R. Barnes, Embrittlement of stainless steels and nickel-based alloys at high temperature induced by neutron radiation, Nature 206(4991) (1965) 1307.
[73] U. Kocks, Theory of an Obstacle-Controlled Yield Strength--Report After an International Workshop, Mater. Sci. Eng. 27(3) (1977) 291-298.
[74] R. Stoller, S. Zinkle, On the relationship between uniaxial yield strength and resolved shear stress in polycrystalline materials, Journal of Nuclear Materials 283 (2000) 349-352.
[75] A. Seeger, Proc. 2nd Int. Conf. Peaceful Uses of Atomic Energy, Geneva, United Nations New York, 1958.
[76] F. Kroupa, P. Hirsch, Elastic interaction between prismatic dislocation loops and straight dislocations, Discussions of the Faraday Society 38 (1964) 49-55.
[77] R.O. Ritchie, The conflicts between strength and toughness, Nature materials 10(11) (2011) 817.
[78] Y. Wang, M. Chen, F. Zhou, E. Ma, High tensile ductility in a nanostructured metal, Nature 419(6910) (2002) 912.
[79] Y.A. Nikolaev, A. Nikolaeva, Y.I. Shtrombakh, Radiation embrittlement of low-alloy steels, International Journal of Pressure Vessels and Piping 79(8-10) (2002) 619-636.
[80] C.C. Koch, Nanostructured materials: processing, properties and applications, William Andrew2006.
[81] X. Li, K. Lu, Playing with defects in metals, Nature materials 16(7) (2017) 700.
[82] I.J. Beyerlein, M.J. Demkowicz, A. Misra, B. Uberuaga, Defect-interface interactions, Progress in Materials Science 74 (2015) 125-210.
[83] X. Zhang, K. Hattar, Y. Chen, L. Shao, J. Li, C. Sun, K. Yu, N. Li, M.L. Taheri, H. Wang, Radiation damage in nanostructured materials, Progress in Materials Science (2018).
[84] N. Nita, R. Schaeublin, M. Victoria, Impact of irradiation on the microstructure of nanocrystalline materials, Journal of Nuclear Materials 329 (2004) 953-957.
[85] G. Cheng, W. Xu, Y. Wang, A. Misra, Y. Zhu, Grain size effect on radiation tolerance of nanocrystalline Mo, Scripta Materialia 123 (2016) 90-94.

[86] X. Zhang, K. Hattar, Y. Chen, L. Shao, J. Li, C. Sun, K. Yu, N. Li, M.L. Taheri, H. Wang, Radiation damage in nanostructured materials, Progress in Materials Science 96 (2018) 217-321.
[87] R. Andrievskii, Effect of irradiation on the properties of nanomaterials, The Physics of Metals and Metallography 110(3) (2010) 229-240.
[88] M. Rose, A. Balogh, H. Hahn, Instability of irradiation induced defects in nanostructured materials, Nuclear Instruments and Methods in Physics Research Section B: Beam Interactions with Materials and Atoms 127 (1997) 119-122.
[89] S. Zinkle, G. Kulcinski, R. Knoll, Microstructure of copper following high dose 14-MeV Cu ion irradiation, Journal of Nuclear Materials 138(1) (1986) 46-56.
[90] C. Sun, M. Song, K. Yu, Y. Chen, M. Kirk, M. Li, H. Wang, X. Zhang, In situ evidence of defect cluster absorption by grain boundaries in Kr ion irradiated nanocrystalline Ni, Metallurgical and Materials Transactions A 44(4) (2013) 1966-1974.
[91] M. Song, Y. Wu, D. Chen, X. Wang, C. Sun, K. Yu, Y. Chen, L. Shao, Y. Yang, K. Hartwig, Response of equal channel angular extrusion processed ultrafine-grained T91 steel subjected to high temperature heavy ion irradiation, Acta Materialia 74 (2014) 285-295.
[92] K. Yu, Radiation damage in nanostructured metallic films, Texas A&M University2013.
[93] W. Han, E. Fu, M.J. Demkowicz, Y. Wang, A. Misra, Irradiation damage of single crystal, coarse-grained, and nanograined copper under helium bombardment at 450 C, Journal of Materials Research 28(20) (2013) 2763-2770.
[94] O. El-Atwani, K. Hattar, J. Hinks, G. Greaves, S. Harilal, A. Hassanein, Helium bubble formation in ultrafine and nanocrystalline tungsten under different extreme conditions, Journal of Nuclear Materials 458 (2015) 216-223.
[95] O. El-Atwani, J. Nathaniel II, A. Leff, J. Baldwin, K. Hattar, M. Taheri, Evidence of a temperature transition for denuded zone formation in nanocrystalline Fe under He irradiation, Materials Research Letters (2016) 1-6.
[96] O. El-Atwani, J. Hinks, G. Greaves, J.P. Allain, S.A. Maloy, Grain size threshold for enhanced irradiation resistance in nanocrystalline and ultrafine tungsten, Materials Research Letters (2017) 1-7.
[97] D. Chen, J. Wang, T. Chen, L. Shao, Defect annihilation at grain boundaries in alpha-Fe, Scientific reports 3 (2013) 1450.
[98] X.-M. Bai, A.F. Voter, R.G. Hoagland, M. Nastasi, B.P. Uberuaga, Efficient annealing of radiation damage near grain boundaries via interstitial emission, Science 327(5973) (2010) 1631-1634.
[99] K. Lu, Stabilizing nanostructures in metals using grain and twin boundary architectures, Nature Reviews Materials 1(5) (2016) 16019.
[100] Y.T. Zhu, X. Liao, Nanostructured metals: retaining ductility, Nature materials 3(6) (2004) 351.
[101] K. Lu, L. Lu, S. Suresh, Strengthening materials by engineering coherent internal boundaries at the nanoscale, Science 324(5925) (2009) 349-352.
[102] O. Anderoglu, A. Misra, H. Wang, X. Zhang, Thermal stability of sputtered Cu films with nanoscale growth twins, Journal of Applied Physics 103(9) (2008) 094322.
[103] D. Bufford, H. Wang, X. Zhang, Thermal stability of twins and strengthening mechanisms in differently oriented epitaxial nanotwinned Ag films, Journal of Materials Research 28(13) (2013) 1729-1739.

[104] O. Anderoglu, A. Misra, H. Wang, F. Ronning, M. Hundley, X. Zhang, Epitaxial nanotwinned Cu films with high strength and high conductivity, Applied Physics Letters 93(8) (2008) 083108.
[105] L. Lu, Y. Shen, X. Chen, L. Qian, K. Lu, Ultrahigh strength and high electrical conductivity in copper, Science 304(5669) (2004) 422-426.
[106] D. Bufford, H. Wang, X. Zhang, High strength, epitaxial nanotwinned Ag films, Acta Materialia 59(1) (2011) 93-101.
[107] J. Wang, X. Zhang, Twinning effects on strength and plasticity of metallic materials, MRS Bulletin 41(04) (2016) 274-281.
[108] X. Zhang, H. Wang, X. Chen, L. Lu, K. Lu, R. Hoagland, A. Misra, High-strength sputter-deposited Cu foils with preferred orientation of nanoscale growth twins, Applied Physics Letters 88(17) (2006) 173116.
[109] K. Yu, D. Bufford, C. Sun, Y. Liu, H. Wang, M. Kirk, M. Li, X. Zhang, Removal of stacking-fault tetrahedra by twin boundaries in nanotwinned metals, Nature Communications 4 (2013) 1377.
[110] Y. Chen, J. Li, K. Yu, H. Wang, M. Kirk, M. Li, X. Zhang, In situ studies on radiation tolerance of nanotwinned Cu, Acta Materialia 111 (2016) 148-156.
[111] Y.M. Wang, F. Sansoz, T. LaGrange, R.T. Ott, J. Marian, T.W. Barbee Jr, A.V. Hamza, Defective twin boundaries in nanotwinned metals, Nature Materials 12(8) (2013) 697.
[112] D. Jang, X. Li, H. Gao, J.R. Greer, Deformation mechanisms in nanotwinned metal nanopillars, Nature nanotechnology 7(9) (2012) 594.
[113] J. Wang, F. Sansoz, J. Huang, Y. Liu, S. Sun, Z. Zhang, S.X. Mao, Near-ideal theoretical strength in gold nanowires containing angstrom scale twins, Nature communications 4 (2013) 1742.
[114] X. Zhang, A. Misra, H. Wang, T. Shen, M. Nastasi, T. Mitchell, J. Hirth, R. Hoagland, J. Embury, Enhanced hardening in Cu/330 stainless steel multilayers by nanoscale twinning, Acta Materialia 52(4) (2004) 995-1002.
[115] I.J. Beyerlein, X. Zhang, A. Misra, Growth twins and deformation twins in metals, Annual Review of Materials Research 44 (2014) 329-363.
[116] J. Wang, O. Anderoglu, J. Hirth, A. Misra, X. Zhang, Dislocation structures of $\Sigma 3$ {112} twin boundaries in face centered cubic metals, Appl. Phys. Lett 95(2) (2009) 021908.
[117] K.-C. Chen, W.-W. Wu, C.-N. Liao, L.-J. Chen, K. Tu, Stability of nanoscale twins in copper under electric current stressing, Journal of Applied Physics 108(6) (2010) 066103.
[118] L. Xu, D. Xu, K. Tu, Y. Cai, N. Wang, P. Dixit, J.H. Pang, J. Miao, Structure and migration of (112) step on (111) twin boundaries in nanocrystalline copper, Journal of Applied Physics 104(11) (2008) 113717.
[119] Y. Liu, J. Jian, Y. Chen, H. Wang, X. Zhang, Plasticity and ultra-low stress induced twin boundary migration in nanotwinned Cu by in situ nanoindentation studies, Applied Physics Letters 104(23) (2014) 231910.
[120] J. Wang, N. Li, O. Anderoglu, X. Zhang, A. Misra, J. Huang, J. Hirth, Detwinning mechanisms for growth twins in face-centered cubic metals, Acta Materialia 58(6) (2010) 2262-2270.
[121] C.B. Carter, D. Medlin, J. Angelo, M.J. Mills, The 112 lateral twin boundary in FCC materials, Materials Science Forum, Trans Tech Publ, 1996, pp. 209-212.

[122] G.H. Campbell, D.K. Chan, D.L. Medlin, J.E. Angelo, C.B. Carter, Dynamic observation of the fcc to 9r shear transformation in a copper∑= 3 incoherent twin boundary, Scripta materialia 35(7) (1996) 837-842.
[123] J. Wang, A. Misra, J. Hirth, Shear response of Σ 3 {112} twin boundaries in face-centered-cubic metals, Physical Review B 83(6) (2011) 064106.
[124] D. Medlin, G. Campbell, C.B. Carter, Stacking defects in the 9R phase at an incoherent twin boundary in copper, Acta materialia 46(14) (1998) 5135-5142.
[125] M.A. Meyers, A. Mishra, D.J. Benson, Mechanical properties of nanocrystalline materials, Progress in materials science 51(4) (2006) 427-556.
[126] Y. Wei, Y. Li, L. Zhu, Y. Liu, X. Lei, G. Wang, Y. Wu, Z. Mi, J. Liu, H. Wang, Evading the strength–ductility trade-off dilemma in steel through gradient hierarchical nanotwins, Nature communications 5 (2014) 3580.
[127] Y. Shen, L. Lu, Q. Lu, Z. Jin, K. Lu, Tensile properties of copper with nano-scale twins, Scripta Materialia 52(10) (2005) 989-994.
[128] Z.-H. Jin, P. Gumbsch, E. Ma, K. Albe, K. Lu, H. Hahn, H. Gleiter, The interaction mechanism of screw dislocations with coherent twin boundaries in different face-centred cubic metals, Scripta Materialia 54(6) (2006) 1163-1168.
[129] Z.-H. Jin, P. Gumbsch, K. Albe, E. Ma, K. Lu, H. Gleiter, H. Hahn, Interactions between non-screw lattice dislocations and coherent twin boundaries in face-centered cubic metals, Acta Materialia 56(5) (2008) 1126-1135.
[130] X. Li, Y. Wei, L. Lu, K. Lu, H. Gao, Dislocation nucleation governed softening and maximum strength in nano-twinned metals, Nature 464(7290) (2010) 877.
[131] T. Zhu, H. Gao, Plastic deformation mechanism in nanotwinned metals: An insight from molecular dynamics and mechanistic modeling, Scripta Materialia 66(11) (2012) 843-848.
[132] Y. Zhu, X. Wu, X. Liao, J. Narayan, L. Kecskes, S. Mathaudhu, Dislocation–twin interactions in nanocrystalline fcc metals, Acta Materialia 59(2) (2011) 812-821.
[133] Z. You, X. Li, L. Gui, Q. Lu, T. Zhu, H. Gao, L. Lu, Plastic anisotropy and associated deformation mechanisms in nanotwinned metals, Acta Materialia 61(1) (2013) 217-227.
[134] L. Lu, X. Chen, X. Huang, K. Lu, Revealing the maximum strength in nanotwinned copper, Science 323(5914) (2009) 607-610.
[135] Z. You, L. Lu, K. Lu, Tensile behavior of columnar grained Cu with preferentially oriented nanoscale twins, Acta Materialia 59(18) (2011) 6927-6937.
[136] X. Zhang, A. Misra, Superior thermal stability of coherent twin boundaries in nanotwinned metals, Scripta Materialia 66(11) (2012) 860-865.
[137] S. Zinkle, L. Snead, Opportunities and limitations for ion beams in radiation effects studies: bridging critical gaps between charged particle and neutron irradiations, Scripta Materialia 143 (2018) 154-160.
[138] B.N. Singh, S.I. Golubov, H. Trinkaus, D.J. Edwards, M. Eldrup, Evolution of stacking fault tetrahedra and its role in defect accumulation under cascade damage conditions, Journal of Nuclear Materials 328(2-3) (2004) 77-87.
[139] M. Niewczas, R. Hoagland, Molecular dynamic studies of the interaction of a/6⟨ 112⟩ Shockley dislocations with stacking fault tetrahedra in copper. Part II: Intersection of stacking fault tetrahedra by moving twin boundaries, Philosophical Magazine 89(8) (2009) 727-746.
[140] J. Li, K. Yu, Y. Chen, M. Song, H. Wang, M. Kirk, M. Li, X. Zhang, In Situ Study of Defect Migration Kinetics and Self-Healing of Twin Boundaries in Heavy Ion Irradiated Nanotwinned Metals, Nano letters 15(5) (2015) 2922-2927.

[141] J. Li, Y. Chen, H. Wang, X. Zhang, In Situ Studies on Twin-Thickness-Dependent Distribution of Defect Clusters in Heavy Ion-Irradiated Nanotwinned Ag, Metallurgical and Materials Transactions A 48(3) (2017) 1466-1473.
[142] J. Li, D. Xie, S. Xue, C. Fan, Y. Chen, H. Wang, J. Wang, X. Zhang, Superior twin stability and radiation resistance of nanotwinned Ag solid solution alloy, Acta Materialia (2018).
[143] S. Jiao, Y. Kulkarni, Radiation tolerance of nanotwinned metals–An atomistic perspective, Computational Materials Science 142 (2018) 290-296.
[144] G.M. de Bellefon, I. Robertson, T. Allen, J.-C. van Duysen, K. Sridharan, Radiation-resistant nanotwinned austenitic stainless steel, Scripta Materialia 159 (2019) 123-127.
[145] G. Was, Z. Jiao, E. Getto, K. Sun, A. Monterrosa, S. Maloy, O. Anderoglu, B. Sencer, M. Hackett, Emulation of reactor irradiation damage using ion beams, Scripta Materialia 88 (2014) 33-36.
[146] D. Mazey, Fundamental aspects of high-energy ion-beam simulation techniques and their relevance to fusion materials studies, Journal of nuclear materials 174(2-3) (1990) 196-209.
[147] E. Wakai, K. Kikuchi, S. Yamamoto, T. Aruga, M. Ando, H. Tanigawa, T. Taguchi, T. Sawai, K. Oka, S. Ohnuki, Swelling behavior of F82H steel irradiated by triple/dual ion beams, Journal of nuclear materials 318 (2003) 267-273.
[148] P. Hosemann, Small-scale mechanical testing on nuclear materials: bridging the experimental length-scale gap, Scripta Materialia 143 (2018) 161-168.
[149] A. Lupinacci, K. Chen, Y. Li, M. Kunz, Z. Jiao, G. Was, M. Abad, A. Minor, P. Hosemann, Characterization of ion beam irradiated 304 stainless steel utilizing nanoindentation and Laue microdiffraction, Journal of Nuclear Materials 458 (2015) 70-76.
[150] W.-Z. Han, M.-S. Ding, Z.-W. Shan, Cracking behavior of helium-irradiated small-volume copper, Scripta Materialia 147 (2018) 1-5.
[151] H. Vo, A. Reichardt, D. Frazer, N. Bailey, P. Chou, P. Hosemann, In situ micro-tensile testing on proton beam-irradiated stainless steel, Journal of Nuclear Materials 493 (2017) 336-342.
[152] W.Z. Han, M.S. Ding, R.L. Narayan, Z.W. Shan, In Situ Study of Deformation Twinning and Detwinning in Helium Irradiated Small-Volume Copper, Advanced Engineering Materials 19(12) (2017) 1700357.
[153] D. Kiener, P. Hosemann, S. Maloy, A. Minor, In situ nanocompression testing of irradiated copper, Nature materials 10(8) (2011) 608.
[154] M.D. Uchic, D.M. Dimiduk, J.N. Florando, W.D. Nix, Sample dimensions influence strength and crystal plasticity, Science 305(5686) (2004) 986-989.
[155] Z. Shan, R.K. Mishra, S.S. Asif, O.L. Warren, A.M. Minor, Mechanical annealing and source-limited deformation in submicrometre-diameter Ni crystals, Nature materials 7(2) (2008) 115.
[156] W.D. Nix, H. Gao, Indentation size effects in crystalline materials: a law for strain gradient plasticity, Journal of the Mechanics and Physics of Solids 46(3) (1998) 411-425.
[157] J.P. Wharry, K.H. Yano, P.V. Patki, Intrinsic-extrinsic size effect relationship for micromechanical tests, Scripta Materialia 162 (2019) 63-67.
[158] S. Pathak, S.R. Kalidindi, Spherical nanoindentation stress–strain curves, Materials science and engineering: R: Reports 91 (2015) 1-36.
[159] J. Silcox, P. Hirsch, Dislocation loops in neutron-irradiated copper, Philosophical Magazine 4(48) (1959) 1356-1374.

[160] A. Stathopoulos, The study of heavy-ion damage in pure copper, Philosophical Magazine A 44(2) (1981) 285-308.
[161] Z. Fan, C. Fan, J. Li, Z. Shang, S. Xue, M.A. Kirk, M. Li, H. Wang, X. Zhang, An in situ study on Kr ion–irradiated crystalline Cu/amorphous-CuNb nanolaminates, Journal of Materials Research (2019) 1-11.
[162] L.B. Freund, S. Suresh, Thin film materials: stress, defect formation and surface evolution, Cambridge University Press2004.
[163] B.D. Cullity, Elements of X-ray Diffraction, (2001).
[164] D.B. Williams, C.B. Carter, The transmission electron microscope, Transmission electron microscopy, Springer1996, pp. 3-17.
[165] M.L. Jenkins, M.A. Kirk, Characterisation of radiation damage by transmission electron microscopy, CRC Press2000.
[166] M. Li, M. Kirk, P. Baldo, D. Xu, B. Wirth, Study of defect evolution by TEM with in situ ion irradiation and coordinated modeling, Philosophical Magazine 92(16) (2012) 2048-2078.
[167] C.A. Volkert, A.M. Minor, Focused ion beam microscopy and micromachining, MRS bulletin 32(5) (2007) 389-399.
[168] L.A. Giannuzzi, F.A. Stevie, A review of focused ion beam milling techniques for TEM specimen preparation, Micron 30(3) (1999) 197-204.
[169] Y. Chen, K.Y. Yu, Y. Liu, S. Shao, H. Wang, M. Kirk, J. Wang, X. Zhang, Damage-tolerant nanotwinned metals with nanovoids under radiation environments, Nature communications 6 (2015).
[170] J. Gibson, A.N. Goland, M. Milgram, G. Vineyard, Dynamics of radiation damage, Physical Review 120(4) (1960) 1229.
[171] D. Bacon, F. Gao, Y.N. Osetsky, The primary damage state in fcc, bcc and hcp metals as seen in molecular dynamics simulations, Journal of Nuclear Materials 276(1) (2000) 1-12.
[172] G.S. Was, Fundamentals of radiation materials science: metals and alloys, Springer Science & Business Media2007.
[173] K. Nordlund, F. Gao, Formation of stacking-fault tetrahedra in collision cascades, Applied physics letters 74(18) (1999) 2720-2722.
[174] D. Maher, B. Eyre, Neutron irradiation damage in molybdenum, Philosophical Magazine 23(182) (1971) 409-438.
[175] M. Jenkins, A weak-beam electron microscopy analysis of defect clusters in heavy-ion irradiated silver and copper, Philosophical Magazine 29(4) (1974) 813-828.
[176] S. Kojima, Y. Satoh, H. Taoka, I. Ishida, T. Yoshiie, M. Kiritani, Confirmation of vacancy-type stacking fault tetrahedra in quenched, deformed and irradiated face-centred cubic metals, Philosophical Magazine A 59(3) (1989) 519-532.
[177] P. Okamoto, L. Rehn, Radiation-induced segregation in binary and ternary alloys, Journal of Nuclear Materials 83(1) (1979) 2-23.
[178] M. Victoria, N. Baluc, C. Bailat, Y. Dai, M. Luppo, R. Schaublin, B. Singh, The microstructure and associated tensile properties of irradiated fcc and bcc metals, Journal of nuclear materials 276(1) (2000) 114-122.
[179] J. Carter, E. Fu, M. Martin, G. Xie, X. Zhang, Y. Wang, D. Wijesundera, X. Wang, W.-K. Chu, S.M. McDeavitt, Ion irradiation induced nanocrystal formation in amorphous Zr 55 Cu 30 Al 10 Ni 5 alloy, Nuclear Instruments and Methods in Physics Research Section B: Beam Interactions with Materials and Atoms 267(17) (2009) 2827-2831.

[180] G. Odette, G. Lucas, Embrittlement of nuclear reactor pressure vessels, JOM 53(7) (2001) 18-22.
[181] K. Yu, Y. Liu, C. Sun, H. Wang, L. Shao, E. Fu, X. Zhang, Radiation damage in helium ion irradiated nanocrystalline Fe, Journal of Nuclear Materials 425(1) (2012) 140-146.
[182] E. Fu, A. Misra, H. Wang, L. Shao, X. Zhang, Interface enabled defects reduction in helium ion irradiated Cu/V nanolayers, Journal of Nuclear Materials 407(3) (2010) 178-188.
[183] G. Ackland, Controlling radiation damage, Science 327(5973) (2010) 1587-1588.
[184] M. Samaras, P. Derlet, H. Van Swygenhoven, M. Victoria, Computer simulation of displacement cascades in nanocrystalline Ni, Physical review letters 88(12) (2002) 125505.
[185] A. Misra, M. Demkowicz, X. Zhang, R. Hoagland, The radiation damage tolerance of ultra-high strength nanolayered composites, JOM 59(9) (2007) 62-65.
[186] X. Zhang, E. Fu, N. Li, A. Misra, Y.-Q. Wang, L. Shao, H. Wang, Design of radiation tolerant nanostructured metallic multilayers, Journal of Engineering Materials and Technology 134(4) (2012) 041010.
[187] O. El-Atwani, J. Hinks, G. Greaves, S. Gonderman, T. Qiu, M. Efe, J.P. Allain, In-situ TEM observation of the response of ultrafine-and nanocrystalline-grained tungsten to extreme irradiation environments, Scientific reports 4 (2014) 4716.
[188] D. Chen, J. Wang, T. Chen, L. Shao, Defect annihilation at grain boundaries in alpha-Fe, Scientific reports 3 (2013).
[189] W. Han, M. Demkowicz, E. Fu, Y. Wang, A. Misra, Effect of grain boundary character on sink efficiency, Acta materialia 60(18) (2012) 6341-6351.
[190] M. Dollar, H. Gleiter, Point defect annihilation at grain boundaries in gold, Scripta metallurgica 19(4) (1985) 481-484.
[191] E. Fu, J. Carter, G. Swadener, A. Misra, L. Shao, H. Wang, X. Zhang, Size dependent enhancement of helium ion irradiation tolerance in sputtered Cu/V nanolaminates, Journal of nuclear materials 385(3) (2009) 629-632.
[192] R. Klueh, A. Nelson, Ferritic/martensitic steels for next-generation reactors, Journal of Nuclear Materials 371(1) (2007) 37-52.
[193] M. Demkowicz, A. Misra, A. Caro, The role of interface structure in controlling high helium concentrations, Current opinion in solid state and materials science 16(3) (2012) 101-108.
[194] X. Zhang, E. Fu, A. Misra, M. Demkowicz, Interface-enabled defect reduction in He ion irradiated metallic multilayers, Jom 62(12) (2010) 75-78.
[195] C. Sun, D. Bufford, Y. Chen, M. Kirk, Y. Wang, M. Li, H. Wang, S. Maloy, X. Zhang, In situ study of defect migration kinetics in nanoporous Ag with enhanced radiation tolerance, Scientific reports 4 (2014).
[196] J. Li, C. Fan, J. Ding, S. Xue, Y. Chen, Q. Li, H. Wang, X. Zhang, In situ heavy ion irradiation studies of nanopore shrinkage and enhanced radiation tolerance of nanoporous Au, Scientific reports 7 (2017).
[197] M.J. Demkowicz, O. Anderoglu, X. Zhang, A. Misra, The influence of$\sum$ 3 twin boundaries on the formation of radiation-induced defect clusters in nanotwinned Cu, Journal of Materials Research 26(14) (2011) 1666-1675.
[198] Y. Chimi, A. Iwase, N. Ishikawa, M. Kobiyama, T. Inami, S. Okuda, Accumulation and recovery of defects in ion-irradiated nanocrystalline gold, Journal of Nuclear Materials 297(3) (2001) 355-357.
[199] S. Wurster, R. Pippan, Nanostructured metals under irradiation, Scripta Materialia 60(12) (2009) 1083-1087.

[200] B.N. Singh, A. Foreman, Calculated grain size-dependent vacancy supersaturation and its effect on void formation, Philosophical Magazine 29(4) (1974) 847-858.
[201] A. Kilmametov, D. Gunderov, R. Valiev, A.G. Balogh, H. Hahn, Enhanced ion irradiation resistance of bulk nanocrystalline TiNi alloy, Scripta Materialia 59(10) (2008) 1027-1030.
[202] K.Y. Yu, D. Bufford, F. Khatkhatay, H. Wang, M.A. Kirk, X. Zhang, In situ studies of irradiation induced twin boundary migration in nanotwinned Ag, Scripta Materialia 69 (2013) 385.
[203] N. Li, J. Wang, X. Zhang, A. Misra, In-situ TEM study of dislocation-twin boundaries interaction in nanotwinned Cu films, Jom 63(9) (2011) 62.
[204] Y. Chen, X. Zhang, J. Wang, Radiation Enhanced Absorption of Frank Loops by Nanovoids in Cu, JOM 68(1) (2016) 235-241.
[205] J.F. Ziegler, M.D. Ziegler, J.P. Biersack, SRIM–The stopping and range of ions in matter (2010), Nuclear Instruments and Methods in Physics Research Section B: Beam Interactions with Materials and Atoms 268(11) (2010) 1818-1823.
[206] R.E. Stoller, M.B. Toloczko, G.S. Was, A.G. Certain, S. Dwaraknath, F.A. Garner, On the use of SRIM for computing radiation damage exposure, Nuclear instruments and methods in physics research section B: beam interactions with materials and atoms 310 (2013) 75-80.
[207] T. LaGrange, K. Arakawa, H. Yasuda, M. Kumar, Preferential void formation at crystallographically ordered grain boundaries in nanotwinned copper thin films, Acta Materialia 96 (2015) 284-291.
[208] Y.N. Osetsky, D. Bacon, A. Serra, B. Singh, S. Golubov, One-dimensional atomic transport by clusters of self-interstitial atoms in iron and copper, Philosophical Magazine 83(1) (2003) 61-91.
[209] R. Schäublin, J. Henry, Y. Dai, Helium and point defect accumulation:(i) microstructure and mechanical behaviour, Comptes Rendus Physique 9(3) (2008) 389-400.
[210] Z. Shang, J. Li, C. Fan, Y. Chen, Q. Li, H. Wang, T. Shen, X. Zhang, In situ study on surface roughening in radiation-resistant Ag nanowires, Nanotechnology 29(21) (2018) 215708.
[211] J. Li, C. Fan, Q. Li, H. Wang, X. Zhang, In situ studies on irradiation resistance of nanoporous Au through temperature-jump tests, Acta Materialia 143 (2018) 30-42.
[212] D. Gelles, Void swelling in binary FeCr alloys at 200 dpa, Journal of nuclear materials 225 (1995) 163-174.
[213] D. Brimbal, B. Décamps, J. Henry, E. Meslin, A. Barbu, Single-and dual-beam in situ irradiations of high-purity iron in a transmission electron microscope: Effects of heavy ion irradiation and helium injection, Acta Materialia 64 (2014) 391-401.
[214] K. Yu, Y. Liu, C. Sun, H. Wang, L. Shao, E. Fu, X. Zhang, Radiation damage in helium ion irradiated nanocrystalline Fe, Journal of Nuclear Materials 425(1-3) (2012) 140-146.
[215] Z.-J. Wang, F.I. Allen, Z.-W. Shan, P. Hosemann, Mechanical behavior of copper containing a gas-bubble superlattice, Acta Materialia 121 (2016) 78-84.
[216] I. Beyerlein, A. Caro, M. Demkowicz, N. Mara, A. Misra, B. Uberuaga, Radiation damage tolerant nanomaterials, Materials today 16(11) (2013) 443-449.
[217] C. Fan, D. Xie, J. Li, Z. Shang, Y. Chen, S. Xue, J. Wang, M. Li, A. El-Azab, H. Wang, 9R phase enabled superior radiation stability of nanotwinned Cu alloys via in situ radiation at elevated temperature, Acta Materialia 167 (2019) 248-256.
[218] C. Fan, Y. Chen, J. Li, J. Ding, H. Wang, X. Zhang, Defect evolution in heavy ion irradiated nanotwinned Cu with nanovoids, Journal of Nuclear Materials 496 (2017) 293-300.

[219] C. Fan, J. Li, Z. Fan, H. Wang, X. Zhang, In Situ Studies on the Irradiation-Induced Twin Boundary-Defect Interactions in Cu, Metallurgical and Materials Transactions A (2017) 1-9.
[220] Y. Chen, H. Wang, M. Kirk, M. Li, J. Wang, X. Zhang, Radiation induced detwinning in nanotwinned Cu, Scripta Materialia 130 (2017) 37-41.
[221] Z. Fan, S. Zhao, K. Jin, D. Chen, Y.N. Osetskiy, Y. Wang, H. Bei, K.L. More, Y. Zhang, Helium irradiated cavity formation and defect energetics in Ni-based binary single-phase concentrated solid solution alloys, Acta Materialia 164 (2019) 283-292.
[222] K. Yano, M. Swenson, Y. Wu, J. Wharry, TEM in situ micropillar compression tests of ion irradiated oxide dispersion strengthened alloy, Journal of Nuclear Materials 483 (2017) 107-120.
[223] Y. Zayachuk, P. Karamched, C. Deck, P. Hosemann, D.E. Armstrong, Linking microstructure and local mechanical properties in SiC-SiC fiber composite using micromechanical testing, Acta Materialia 168 (2019) 178-189.
[224] E. Aydogan, J.S. Weaver, U. Carvajal-Nunez, M.M. Schneider, J.G. Gigax, D.L. Krumwiede, P. Hosemann, T.A. Saleh, N.A. Mara, D.T. Hoelzer, Response of 14YWT alloys under neutron irradiation: A complementary study on microstructure and mechanical properties, Acta Materialia 167 (2019) 181-196.
[225] H. Vo, A. Reinhardt, D. Frazer, N. Bailey, P. Chou, P. Hosemann, In Situ Microtensile Testing for Ion Beam Irradiated Materials, Proceedings of the 18th International Conference on Environmental Degradation of Materials in Nuclear Power Systems–Water Reactors, Springer, 2019, pp. 593-603.
[226] M.D. Uchic, P.A. Shade, D.M. Dimiduk, Plasticity of micrometer-scale single crystals in compression, Annual Review of Materials Research 39 (2009) 361-386.
[227] J.R. Greer, W.C. Oliver, W.D. Nix, Size dependence of mechanical properties of gold at the micron scale in the absence of strain gradients, Acta Materialia 53(6) (2005) 1821-1830.
[228] G. Thomas, Experimental studies of helium in metals, Radiation effects 78(1-4) (1983) 37-51.
[229] D. Chen, N. Li, D. Yuryev, J.K. Baldwin, Y. Wang, M.J. Demkowicz, Self-organization of helium precipitates into elongated channels within metal nanolayers, Science Advances 3(11) (2017) eaao2710.
[230] N. Li, M. Nastasi, A. Misra, Defect structures and hardening mechanisms in high dose helium ion implanted Cu and Cu/Nb multilayer thin films, International Journal of Plasticity 32 (2012) 1-16.
[231] Y. Dai, G. Odette, T. Yamamoto, 1.06-The effects of helium in irradiated structural alloys, Comprehensive Nuclear Materials (2012) 141-193.
[232] C. Fan, A. Sreekar, Z. Shang, J. Li, M. Li, H. Wang, A. El-Azab, X. Zhang, Radiation induced nanovoid shrinkage in Cu at room temperature: An in situ study, Scripta Materialia 166 (2019) 112-116.
[233] L. Mansur, W. Coghlan, Mechanisms of helium interaction with radiation effects in metals and alloys: A review, Journal of Nuclear Materials 119(1) (1983) 1-25.
[234] D. Kiener, C. Motz, G. Dehm, Micro-compression testing: A critical discussion of experimental constraints, Materials Science and Engineering: A 505(1-2) (2009) 79-87.
[235] Q. Guo, P. Landau, P. Hosemann, Y. Wang, J.R. Greer, Helium implantation effects on the compressive response of Cu nanopillars, Small 9(5) (2013) 691-696.
[236] M. Merz, S. Dahlgren, Tensile strength and work hardening of ultrafine-grained high-purity copper, Journal of Applied Physics 46(8) (1975) 3235-3237.

[237] X. Chen, L. Lu, Work hardening of ultrafine-grained copper with nanoscale twins, Scripta materialia 57(2) (2007) 133-136.
[238] T.-C. Liu, C.-M. Liu, H.-Y. Hsiao, J.-L. Lu, Y.-S. Huang, C. Chen, Fabrication and characterization of (111)-oriented and nanotwinned Cu by Dc electrodeposition, Crystal Growth & Design 12(10) (2012) 5012-5016.
[239] A. Misra, J. Hirth, R. Hoagland, Length-scale-dependent deformation mechanisms in incoherent metallic multilayered composites, Acta materialia 53(18) (2005) 4817-4824.
[240] Z. Hu, J. Du, P. Wang, X. Wang, Y. Zhang, Y. Qiu, E. Fu, Insight into the impact of nanovoids on the electrical and mechanical properties of nanotwinned copper films, Scripta Materialia 137 (2017) 41-45.
[241] G. Lucas, The evolution of mechanical property change in irradiated austenitic stainless steels, Journal of Nuclear Materials 206(2-3) (1993) 287-305.
[242] N. Hashimoto, T. Byun, K. Farrell, S. Zinkle, Deformation microstructure of neutron-irradiated pure polycrystalline metals, Journal of nuclear materials 329 (2004) 947-952.
[243] M.-S. Ding, J.-P. Du, L. Wan, S. Ogata, L. Tian, E. Ma, W.-Z. Han, J. Li, Z.-W. Shan, Radiation-induced helium nanobubbles enhance ductility in submicron-sized single-crystalline copper, Nano letters 16(7) (2016) 4118-4124.
[244] M.-S. Ding, L. Tian, W.-Z. Han, J. Li, E. Ma, Z.-W. Shan, Nanobubble Fragmentation and Bubble-Free-Channel Shear Localization in Helium-Irradiated Submicron-Sized Copper, Physical review letters 117(21) (2016) 215501.
[245] M. Mutoh, T. Nagoshi, T.-F.M. Chang, T. Sato, M. Sone, Micro-compression test using non-tapered micro-pillar of electrodeposited Cu, Microelectronic Engineering 111 (2013) 118-121.
[246] A.T. Jennings, M.J. Burek, J.R. Greer, Microstructure versus size: mechanical properties of electroplated single crystalline Cu nanopillars, Physical review letters 104(13) (2010) 135503.
[247] N. Li, J. Wang, A. Misra, X. Zhang, J. Huang, J. Hirth, Twinning dislocation multiplication at a coherent twin boundary, Acta Materialia 59(15) (2011) 5989-5996.
[248] J. Wang, H. Huang, Novel deformation mechanism of twinned nanowires, Applied physics letters 88(20) (2006) 203112.
[249] Z. Fan, Q. Li, J. Li, S. Xue, H. Wang, X. Zhang, Tailoring plasticity of metallic glasses via interfaces in Cu/amorphous CuNb laminates, Journal of Materials Research 32(14) (2017) 2680-2689.
[250] D. Bufford, Y. Liu, J. Wang, H. Wang, X. Zhang, In situ nanoindentation study on plasticity and work hardening in aluminium with incoherent twin boundaries, Nature communications 5 (2014) 4864.
[251] X. Chen, L. Lu, K. Lu, Electrical resistivity of ultrafine-grained copper with nanoscale growth twins, Journal of Applied Physics 102(8) (2007) 083708.
[252] X. Zhang, A. Misra, H. Wang, J. Swadener, A. Lima, M. Hundley, R. Hoagland, Thermal stability of sputter-deposited 330 austenitic stainless-steel thin films with nanoscale growth twins, Applied Physics Letters 87(23) (2005) 233116.
[253] M. Dao, L. Lu, Y. Shen, S. Suresh, Strength, strain-rate sensitivity and ductility of copper with nanoscale twins, Acta Materialia 54(20) (2006) 5421-5432.
[254] F. Sansoz, K. Lu, T. Zhu, A. Misra, Strengthening and plasticity in nanotwinned metals, MRS Bulletin 41(04) (2016) 292-297.
[255] X. Li, Y. Wei, L. Lu, K. Lu, H. Gao, Dislocation nucleation governed softening and maximum strength in nano-twinned metals, Nature 464(7290) (2010) 877-880.

[256] J. Miao, Structure and migration of (112) step on (111) twin boundaries in nanocrystalline copper, Journal of Applied Physics 104 (2008) 113717.
[257] G. Van Tendeloo, D. Broddin, H. Zandbergen, S. Amelinckx, Detwinning mechanism, twinning dislocations and planar defects in YBa 2 Cu 3 O 7− δ, Physica C: Superconductivity 167(5) (1990) 627-639.
[258] N. Li, J. Wang, J. Huang, A. Misra, X. Zhang, Influence of slip transmission on the migration of incoherent twin boundaries in epitaxial nanotwinned Cu, Scripta Materialia 64(2) (2011) 149-152.
[259] A. Hodge, T. Furnish, C. Shute, Y. Liao, X. Huang, C. Hong, Y. Zhu, T. Barbee Jr, J. Weertman, Twin stability in highly nanotwinned Cu under compression, torsion and tension, Scripta Materialia 66(11) (2012) 872-877.
[260] N. Li, J. Wang, Y. Wang, Y. Serruys, M. Nastasi, A. Misra, Incoherent twin boundary migration induced by ion irradiation in Cu, Journal of Applied Physics 113(2) (2013) 023508.
[261] D. Song, X. Li, J. Xue, H. Duan, Z. Jin, Irradiation-enhanced twin boundary migration in BCC Fe, Philosophical Magazine Letters 94(6) (2014) 361-369.
[262] D. Xu, W.L. Kwan, K. Chen, X. Zhang, V. Ozoliņš, K. Tu, Nanotwin formation in copper thin films by stress/strain relaxation in pulse electrodeposition, Applied Physics Letters 91(25) (2007) 254105.
[263] T. Zhu, J. Li, A. Samanta, A. Leach, K. Gall, Temperature and strain-rate dependence of surface dislocation nucleation, Physical Review Letters 100(2) (2008) 025502.
[264] Y.N. Osetsky, D. Bacon, A. Serra, B. Singh, S. Golubov, Stability and mobility of defect clusters and dislocation loops in metals, Journal of nuclear materials 276(1) (2000) 65-77.
[265] D.J. Bacon, Y.N. Osetsky, R. Stoller, R.E. Voskoboinikov, MD description of damage production in displacement cascades in copper and α-iron, Journal of nuclear materials 323(2) (2003) 152-162.
[266] M. Jenkins, D. Cockayne, M. Whelan, The determination of the geometry and nature of small Frank loops using the weak-beam method, Journal of Microscopy 98(2) (1973) 155-164.
[267] K. Arakawa, K. Ono, H. Mori, A.S. Avilov, S.L. Dudarev, L.D. Marks, In-Situ Transmission Electron Microscopy of the Dynamics of Point-Defect Clusters in Metals, AIP Conference Proceedings, AIP, 2008, pp. 66-78.
[268] C.J. Ulmer, A.T. Motta, M.A. Kirk, In situ ion irradiation of zirconium carbide, Journal of Nuclear Materials 466 (2015) 606-614.
[269] W. Sigle, M. Jenkins, J. Hutchison, Determination of the nature of stacking-fault tetrahedra in electron-irradiated silver by high-resolution structural imaging, Philosophical magazine letters 57(5) (1988) 267-271.
[270] C. Lu, K. Jin, L.K. Béland, F. Zhang, T. Yang, L. Qiao, Y. Zhang, H. Bei, H.M. Christen, R.E. Stoller, Direct observation of defect range and evolution in ion-irradiated single crystalline Ni and Ni binary alloys, Scientific reports 6 (2016).
[271] B. Singh, On the influence of grain boundaries on void growth, Philosophical Magazine 28(6) (1973) 1409-1413.
[272] B. Muntifering, S.J. Blair, C. Gong, A. Dunn, R. Dingreville, J. Qu, K. Hattar, Cavity Evolution at Grain Boundaries as a Function of Radiation Damage and Thermal Conditions in Nanocrystalline Nickel, Materials Research Letters 4(2) (2016) 96-103.
[273] J. Li, C. Fan, Q. Li, H. Wang, X. Zhang, In situ studies on irradiation resistance of nanoporous Au through temperature-jump tests, Acta Materialia (2017).

[274] D. Chen, N. Li, D. Yuryev, J.K. Baldwin, Y. Wang, M.J. Demkowicz, Self-organization of helium precipitates into elongated channels within metal nanolayers, Science Advances 3(11) (2017).
[275] C. Cawthorne, E. Fulton, Voids in irradiated stainless steel, Nature 216(5115) (1967) 575-576.
[276] W. Xu, Y. Zhang, G. Cheng, W. Jian, P.C. Millett, C.C. Koch, S.N. Mathaudhu, Y. Zhu, In-situ atomic-scale observation of irradiation-induced void formation, Nature communications 4 (2013) 2288.
[277] C. Du, S. Jin, Y. Fang, J. Li, S. Hu, T. Yang, Y. Zhang, J. Huang, G. Sha, Y. Wang, Ultrastrong nanocrystalline steel with exceptional thermal stability and radiation tolerance, Nature Communications 9(1) (2018) 5389.
[278] S. Zinkle, G. Kulcinski, L. Mansur, Radiation-enhanced recrystallization in copper alloys, Journal of Nuclear Materials 141 (1986) 188-192.
[279] M. Demkowicz, R. Hoagland, J. Hirth, Interface structure and radiation damage resistance in Cu-Nb multilayer nanocomposites, Physical review letters 100(13) (2008) 136102.
[280] M. Demkowicz, P. Bellon, B. Wirth, Atomic-scale design of radiation-tolerant nanocomposites, MRS bulletin 35(12) (2010) 992-998.
[281] N. Li, M. Demkowicz, N. Mara, Y. Wang, A. Misra, Hardening due to Interfacial He Bubbles in Nanolayered Composites, Materials Research Letters 4(2) (2016) 75-82.
[282] A. Vattré, T. Jourdan, H. Ding, M.C. Marinica, M.J. Demkowicz, Non-random walk diffusion enhances the sink strength of semicoherent interfaces, Nature Communications 7 (2016) 10424.
[283] M.J. Demkowicz, R.G. Hoagland, J.P. Hirth, Interface Structure and Radiation Damage Resistance in Cu-Nb Multilayer Nanocomposites, Physical Review Letters 100(13) (2008) 136102.
[284] K. Yu, Y. Chen, J. Li, Y. Liu, H. Wang, M.A. Kirk, M. Li, X. Zhang, Measurement of heavy ion irradiation induced in-plane strain in patterned face-centered-cubic metal films: an in situ study, Nano Letters 16(12) (2016) 7481-7489.
[285] K. Lu, Stabilizing nanostructures in metals using grain and twin boundary architectures, Nature Reviews Materials 1 (2016) 16019.
[286] C. Fan, Y. Chen, J. Li, J. Ding, H. Wang, X. Zhang, Defect evolution in heavy ion irradiated nanotwinned Cu with nanovoids, Journal of Nuclear Materials (2017).
[287] D.C. Bufford, Y.M. Wang, Y. Liu, L. Lu, Synthesis and microstructure of electrodeposited and sputtered nanotwinned face-centered-cubic metals, MRS Bulletin 41(4) (2016) 286-291.
[288] J. Du, Z. Wu, E. Fu, Y. Liang, X. Wang, P. Wang, K. Yu, X. Ding, M. Li, M. Kirk, Detwinning through migration of twin boundaries in nanotwinned Cu films under in situ ion irradiation, Science and Technology of Advanced Materials (just-accepted) (2018) 1-23.
[289] N. Li, J. Wang, X. Zhang, A. Misra, In-situ TEM study of dislocation-twin boundaries interaction in nanotwinned Cu films, JOM 63(9) (2011) 62-66.
[290] P.E. Blöchl, Projector augmented-wave method, Physical review B 50(24) (1994) 17953.
[291] D.C. Langreth, M. Mehl, Beyond the local-density approximation in calculations of ground-state electronic properties, Physical Review B 28(4) (1983) 1809.
[292] J.P. Perdew, K. Burke, M. Ernzerhof, Generalized gradient approximation made simple, Physical review letters 77(18) (1996) 3865.
[293] G. Kresse, D. Joubert, From ultrasoft pseudopotentials to the projector augmented-wave method, Physical Review B 59(3) (1999) 1758.

[294] H.J. Monkhorst, J.D. Pack, Special points for Brillouin-zone integrations, Physical review B 13(12) (1976) 5188.
[295] E. Kaxiras, Atomic and electronic structure of solids, Cambridge University Press2003.
[296] W. Schilling, and K. Sonnenberg, Recovery of irradiated and quenched metals, Journal of Physics F: Metal Physics 3(2) (1973) 322.
[297] E. Owen, E. Yates, XLI. Precision measurements of crystal parameters, The London, Edinburgh, and Dublin Philosophical Magazine and Journal of Science 15(98) (1933) 472-488.
[298] L. Liu, J. Wang, S. Gong, S. Mao, High resolution transmission electron microscope observation of zero-strain deformation twinning mechanisms in Ag, Physical review letters 106(17) (2011) 175504.
[299] W. Krakow, D.A. Smith, A high-resolution electron microscopy investigation of some low-angle and twin boundary structures, Ultramicroscopy 22(1-4) (1987) 47-55.
[300] F. Ernst, M.W. Finnis, D. Hofmann, T. Muschik, U. Schönberger, U. Wolf, M. Methfessel, Theoretical prediction and direct observation of the 9R structure in Ag, Physical review letters 69(4) (1992) 620.
[301] P. Gallagher, The influence of alloying, temperature, and related effects on the stacking fault energy, Metallurgical Transactions 1(9) (1970) 2429-2461.
[302] Q. Li, S. Xue, J. Wang, S. Shao, A.H. Kwong, A. Giwa, Z. Fan, Y. Liu, Z. Qi, J. Ding, High-Strength Nanotwinned Al Alloys with 9R Phase, Advanced Materials 30(11) (2018) 1704629.
[303] Y. Zhang, S. Xue, Q. Li, C. Fan, R. Su, J. Ding, H. Wang, H. Wang, X. Zhang, Microstructure and mechanical behavior of nanotwinned AlTi alloys with 9R phase, SCRIPTA MATERIALIA 148 (2018) 5-9.
[304] Q.L. S. Xue, Zhe Fan, Han Wang, Y.F. Zhang, Jie Ding, Haiyan Wang, and , X. Zhang, Mechanical behavior and strengthening mechanisms of nanotwinned AlMg alloys, Journal of Materials Research (In press).
[305] T.D. de la Rubia, H.M. Zbib, T.A. Khraishi, B.D. Wirth, M. Victoria, M.J. Caturla, Multiscale modelling of plastic flow localization in irradiated materials, Nature 406(6798) (2000) 871.
[306] M. Victoria, N. Baluc, C. Bailat, Y. Dai, M. Luppo, R. Schaublin, B. Singh, The microstructure and associated tensile properties of irradiated fcc and bcc metals, Journal of nuclear materials 276(1-3) (2000) 114-122.
[307] M. Cambini, J. Bressers, M. Heerschap, Void swelling upon neutron-irradiation in helium preinjected vanadium, Journal of Nuclear Materials 62(2-3) (1976) 311-313.
[308] E. Little, D. Stow, Void-swelling in irons and ferritic steels: II. An experimental survey of materials irradiated in a fast reactor, Journal of Nuclear Materials 87(1) (1979) 25-39.
[309] B. Singh, A. Horsewell, D. Gelles, F. Garner, Void swelling in copper and copper alloys irradiated with fission neutrons, Journal of nuclear materials 191 (1992) 1172-1176.
[310] A. Brailsford, R. Bullough, The rate theory of swelling due to void growth in irradiated metals, Journal of Nuclear Materials 44(2) (1972) 121-135.
[311] L.K. Mansur, Void swelling in metals and alloys under irradiation: an assessment of the theory, Nuclear Technology 40(1) (1978) 5-34.
[312] R. Bullough, B. Eyre, K. Krishan, Cascade damage effects on the swelling of irradiated materials, Proc. R. Soc. Lond. A 346(1644) (1975) 81-102.
[313] S. Zinkle, B. Singh, Microstructure of Cu–Ni alloys neutron irradiated at 210° C and 420° C to 14 dpa, Journal of nuclear materials 283 (2000) 306-312.

[314] P. Maziasz, Formation and stability of radiation-induced phases in neutron-irradiated austenitic and ferritic steels, Journal of Nuclear Materials 169 (1989) 95-115.
[315] G. Zhigal'Skii, B.K. Jones, The physical properties of thin metal films, CRC Press2003.
[316] M. Kiritani, T. Yoshiie, S. Kojima, Factors controlling the nature and amount of residual defects in neutron irradiated materials, Journal of Nuclear Materials 141 (1986) 625-632.
[317] Y.N. Osetsky, A. Serra, M. Victoria, S. Golubov, V. Priego, Vacancy loops and stacking-fault tetrahedra in copper: II. Growth, shrinkage, interactions with point defects and thermal stability, Philosophical Magazine A 79(9) (1999) 2285-2311.
[318] A. El-Azab, K. Ahmed, S. Rokkam, T. Hochrainer, Diffuse interface modeling of void growth in irradiated materials. Mathematical, thermodynamic and atomistic perspectives, Current opinion in solid state and materials science 18(2) (2014) 90-98.
[319] T. Hochrainer, A. El-Azab, A sharp interface model for void growth in irradiated materials, Philosophical Magazine 95(9) (2015) 948-972.
[320] C. Dennett, K. So, A. Kushima, D. Buller, K. Hattar, M. Short, Detecting self-ion irradiation-induced void swelling in pure copper using transient grating spectroscopy, Acta Materialia 145 (2018) 496-503.
[321] F. Garner, M. Toloczko, Irradiation creep and void swelling of austenitic stainless steels at low displacement rates in light water energy systems, Journal of nuclear materials 251 (1997) 252-261.
[322] D.J. Edwards, E.P. Simonen, F.A. Garner, L.R. Greenwood, B.M. Oliver, S.M. Bruemmer, Influence of irradiation temperature and dose gradients on the microstructural evolution in neutron-irradiated 316SS, Journal of nuclear materials 317(1) (2003) 32-45.
[323] B. Makenas, S. Chastain, B. Gneiting, Dimensional changes in FFTF austenitic cladding and ducts, Proceedings of LMR1991.
[324] E. Little, Void-swelling in irons and ferritic steels: I. Mechanisms of swelling suppression, Journal of Nuclear Materials 87(1) (1979) 11-24.
[325] D. Norris, The use of the high voltage electron microscope to simulate fast neutron-induced void swelling in metals, Journal of Nuclear Materials 40(1) (1971) 66-76.
[326] H. Trinkaus, H. Ullmaier, High temperature embrittlement of metals due to helium: is the lifetime dominated by cavity growth or crack growth?, Journal of nuclear materials 212 (1994) 303-309.
[327] K. Niwase, T. Ezawa, F. Fujita, H. Kusanagi, H. Takaku, Morphology of micro-cavities in nickel during helium bombardment and post-irradiation annealing, Radiation effects 106(1-2) (1988) 65-76.
[328] S. Kondo, Y. Katoh, L.L. Snead, Unidirectional formation of tetrahedral voids in irradiated silicon carbide, Applied Physics Letters 93(16) (2008) 163110.
[329] K. Farrell, J. Houston, Suppression of radiation damage microstructure in aluminum by trace impurities, Journal of Nuclear Materials 83(1) (1979) 57-66.
[330] L.-Q. Chen, Phase-field models for microstructure evolution, Annual review of materials research 32(1) (2002) 113-140.
[331] B. Uberuaga, R. Hoagland, A. Voter, S. Valone, Direct transformation of vacancy voids to stacking fault tetrahedra, Physical review letters 99(13) (2007) 135501.
[332] N. Kaiser, Review of the fundamentals of thin-film growth, Applied optics 41(16) (2002) 3053-3060.
[333] I.-S. Kim, J. Hunn, N. Hashimoto, D. Larson, P. Maziasz, K. Miyahara, E. Lee, Defect and void evolution in oxide dispersion strengthened ferritic steels under 3.2 MeV Fe+ ion

irradiation with simultaneous helium injection, Journal of Nuclear Materials 280(3) (2000) 264-274.
[334] J.W. Christian, The theory of transformations in metals and alloys, Newnes2002.
[335] D.A. Porter, K.E. Easterling, M. Sherif, Phase Transformations in Metals and Alloys, (Revised Reprint), CRC press2009.
[336] N. Lazarev, V. Dubinko, Molecular dynamics simulation of defects production in the vicinity of voids, Radiation effects and defects in solids 158(11-12) (2003) 803-810.
[337] V. Dubinko, N. Lazarev, Effect of the radiation-induced vacancy emission from voids on the void evolution, Nuclear Instruments and Methods in Physics Research Section B: Beam Interactions with Materials and Atoms 228(1-4) (2005) 187-192.
[338] C. Woo, B. Singh, Production bias due to clustering of point defects in irradiation-induced cascades, Philosophical Magazine A 65(4) (1992) 889-912.
[339] N. Doan, G. Martin, Elimination of irradiation point defects in crystalline solids: Sink strengths, Physical Review B 67(13) (2003) 134107.
[340] N. Packan, K. Farrell, J. Stiegler, Correlation of neutron and heavy-ion damage: I. The influence of dose rate and injected helium on swelling in pure nickel, Journal of Nuclear Materials 78(1) (1978) 143-155.
[341] N. Packan, D. Braski, Electron microscope in situ annealing study of voids induced by irradiation in aluminum, Journal of Nuclear Materials 34(3) (1970) 307-314.
[342] J. Fikus, R. Johnson, Effect of surface energy barriers on void growth kinetics, Radiation Effects 40(1-2) (1979) 63-70.
[343] Y. Li, S. Hu, X. Sun, F. Gao, C.H. Henager, M. Khaleel, Phase-field modeling of void migration and growth kinetics in materials under irradiation and temperature field, Journal of Nuclear Materials 407(2) (2010) 119-125.
[344] L. Zhang, M.R. Tonks, P.C. Millett, Y. Zhang, K. Chockalingam, B. Biner, Phase-field modeling of temperature gradient driven pore migration coupling with thermal conduction, Computational Materials Science 56 (2012) 161-165.
[345] S.Y. Hu, C.H. Henager, Phase-field simulation of void migration in a temperature gradient, Acta materialia 58(9) (2010) 3230-3237.
[346] G.S. Was, Challenges to the use of ion irradiation for emulating reactor irradiation, Journal of Materials Research 30(9) (2015) 1158-1182.
[347] S. Zinkle, W. Wolfer, G. Kulcinski, L. Seitzman, II. Effect of oxygen and helium on void formation in metals, Philosophical Magazine A 55(1) (1987) 127-140.
[348] S. Taller, D. Woodley, E. Getto, A.M. Monterrosa, Z. Jiao, O. Toader, F. Naab, T. Kubley, S. Dwaraknath, G.S. Was, Multiple ion beam irradiation for the study of radiation damage in materials, Nuclear Instruments and Methods in Physics Research Section B: Beam Interactions with Materials and Atoms 412 (2017) 1-10.